Medical Ultrasound for Brain Drug Delivery and Rehabilitation Medicine

A Dissertation

Presented to the Faculty of the Graduate School

of Cornell University

In Partial Fulfillment of the Requirements for the Degree of

Doctor of Philosophy

by

George Kenneth Lewis

May 2012

MEDICAL ULTRASOUND FOR BRAIN DRUG DELIVERY AND REHABILITATION MEDICINE

George Kenneth Lewis, Ph.D.

Cornell University 2012

Medical ultrasound, which is routinely used in diagnostic and therapeutic applications, continues to expand into new medical treatments and interventions. However, owing to the cost, size and inefficiency of ultrasound systems currently available, many potential applications of ultrasound in medicine and biology are hindered. We have developed a platform engineering design solution to ultrasound transducers and electronics based on ultralow impedance design principles that effectively reduce the size and voltage requirements of ultrasound systems, while simultaneously improving their efficiencies thereby enabling portable medical ultrasound devices covering the spectrum of therapeutic applications.

We have developed new measurement tools to better understand and characterize ultrasound transducers using impulse response, Fourier analysis and acoustic delay line modeling. Using these techniques we can calculate electrical to acoustic conversion efficiencies and piezoelectric material parameters on a bench top with minimal electronic instruments.

We have engineered ultrasound assisted cannulas' to improve needle based injection therapy. Using ultrasound in combination with diffusion and convection of tracers we are able to increase the distribution volume and penetration of various molecules in a broad spectrum of tissues *ex vivo* and *in vivo*. Specifically, we focused on improving pharmaceutical distribution in neurological tissue using a technique of direct drug injection to the brain parenchyma called "Convection Enhanced Delivery".

We have generated a portable high intensity focused ultrasound system that we tested *ex vivo* and *in vivo* for non-invasive ablation tissues. The technology was specifically adapted for clinical hands as a tool to non-invasively treat venous varicosities and malformations.

This dissertation presents new ideas and engineering principles of ultrasound instrumentation, design, analysis and use in neurological drug delivery and rehabilitation medicine. Furthermore, it discusses future applications of the presented technology and the adjunct projects that evolved from this research.

BIOGRAPHICAL SKETCH[1]

For Dr. George Lewis, perpetual challenges are the beauty of biomedical engineering; they continue to be the benchmark for learning and his drive to succeed as an independent investigator. The question to answer, the puzzle to assemble, or finding the reason, cure or preventative measure, drives him. Solutions are not black and white, but through complex and thoughtful analysis, curiosity and creativity, the answers can be found.

George's extensive research and hands-on experiences have given him critical tools to tackle the challenges. Experience drives the development of new solutions; his doctoral training with skilled scientists and novel technologies have given him the opportunity to study ultrasound-assisted drug transport, improve upon clinical approaches for brain cancer treatment and ultimately generate new tools to inspire biomedical research.

George began studying mechanical engineering at the University of Miami, but soon switched to a biomedical engineering concentration, which combined aspects of both physics and biological sciences. Initially, this combination made him think about heart transplants, prostheses and diagnostic devices. He now understands that biomedical engineering comprises a broad, mesmerizing, spectrum of issues. At the University of Miami, under the mentorship of Dr. Brian Coomes, Professor of Differential Equations, George performed research in hemodynamics and the Lattice Boltzman Method of modeling blood flow. The research was initiated in his sophomore year by his desire to model *in vivo* phenomena, where he connected faculty from the Math and Biomedical Engineering Departments to tackle a fluidics

[1] The biographical sketch of George K. Lewis Jr.'s Ph.D. dissertation "Medical Ultrasound for Brain Drug Delivery and Rehabilitation Medicine" was adapted and edited by Mr. Blaine Friedlander, Cornell University, Ithaca, NY.

physiological issue. George designed and executed a lattice-based computer model that produced characteristic flow patterns, and he was able to contort the model for normal and abstract channel shapes to aid in hemodynamic understanding. The modeling of vascular flow characteristics, smooth, turbulent and vortex, have found direct correlations to heart disease and aneurisms, and this macroscopic approach was one of the first steps in his studies to understand a small picture of complex systems. Although this research was purely computational, it greatly improved his ability to study current literature in the scientific field and it helped combine his knowledge of math, fluids dynamics, software coding and other engineering disciplines to construct a solution to the conceived problem.

In the summer of 2004, George participated in the National Institutes of Health sponsored Bio-Optics Institute at the Massachusetts Institute of Technology and Massachusetts General Hospital. He assisted in the research of Fluorescence Molecular Tomography (FMT), specifically in size quantification and accuracy of imaging cancerous cysts in vivo. A culturally diverse laboratory with broad educational backgrounds, he worked with the group in developing phantoms to calibrate the system. FMT is a new technology where specific cancer targeting dye is injected into the subject. This dye emits non-harmful radiation when excited. The radiation is then collected, made into an image and the size/location of the tumor may be determined. His work in the lab consisted of developing a method to create hollow spheres of 1-3mm diameter, which were then filled with the specific dyes. The phantom tumors where then imaged *in vitro* and implanted for *in vivo* studies. This was done to correlate the intensity of known concentrations of dye with that of actual tumors in situ. The approach George helped to develop was used in future studies to look at new formulations of specific cancer dyes.

In the summer of 2005, George was a student advisor and mentor to the 2005 group of Bio-Optic Scholars, and was granted a NIH/NSF research internship in the Photon Migration Imaging Laboratory at the Martinos Center for Biomedical Imaging at Massachusetts General Hospital. His research internship was also sponsored through the Harvard University-MIT Health Sciences & Technology Program. Under Dr. David Boas, George conducted interdisciplinary research in several areas, including near-infrared spectroscopy and optical breast imaging to image breast cancer tumors based on functional information such as vascularization and oxygen consumption. George developed a breast spectroscopy system, and conducted preliminary clinical trials classifying healthy vs. cancerous (highly vascular, blood filled) tissues. This experience brought George closer to clinical engineering, while also teaching him new skills such as building fibers, aligning optical lenses and tuning high power lasers. He also developed a recipe to create mechanical and optical equivalent breast tissue phantoms. The phantoms where then used in the hospital to calibrate the optical breast imaging device before patient optical-mammography.

In his senior year 2005-06 at The University of Miami, George conducted research and developed a novel ultrasound device to measure the thickness and properties of tissues *in vitro*. Under his thesis committee and senior design advisors Dr. Weiyong Gu, Dr. Jorge Bohorquez and Dr. Ramarathnam Narashimhan, he developed state-of-the-art instrumentation and protocol for analysis of the data sets, this was followed by hardwiring circuit components, soldering and housing design, and initial testing and system calibration as well as various methods of digital signal processing. The 10MHz device was able to measure the thickness of tissues with micron resolution through the bottom of the Petri dish. The project and thesis were submitted, and approved by the department of Biomedical Engineering and Honors

program, for graduation from the University of Miami with summa cum laude honors. George was first in his class.

George attended Cornell University from 2006-10 where he completed his M.S. and Ph.D. in the Department of Biomedical Engineering with minors in Mechanical Engineering and Neurobiology. In his time at Cornell, he has mentored 22 graduate (Ph.D. and M.Eng) and undergraduate students, and introduced them to ultrasound in medical applications. Some 5 students worked on fetal heart rate monitoring, 7 on ultrasound brain drug delivery, 8 on ultrasound based functional hydrogels, and 2 on other medical ultrasound related research.

In George's research at Cornell University covered a wide range of biomedical research with a primary focus on acoustic topics and applications for medicine. His thesis "Medical Ultrasound for Brain Drug Delivery and Rehabilitation Medicine" has three main sections: 1. Development of ultrasound generation technology and ultrasound impedance spectroscopy measurements and 2. Ultrasound-assisted convection enhanced delivery of drugs to the brain. Beyond his primary thesis topics were six additional projects/collaborations: 1. Dr. Jason Spector of Weill Cornell Medical Center using handheld noninvasive ultrasound for cauterization of varicose veins; 2. Dr. Armen Sarvazyan of Artann Labs using developed technology in Time-Reversal Acoustic applications for brain drug delivery; 3. Dr. Steven Gelber of OB/GYN Associates in developing new wide-beam fetal monitoring transducers; 4. Dr. Michael Schuler of Cornell University developing ultrasound-assisted brain cancer treatments, 5. Dr. Lyndon Hernandez and Dr. Yosi Kost from GI Associates and Massachusetts Institute of Technology, respectively in developing ultrasound mediated colonoscopy; and 6. AngioDyanmics Inc. developing tools for deep vein thrombosis treatment.

As featured on the NSF and NIH websites, George conducted research in developing ultra-efficient, pocket-sized ultrasound generation technology throughout his Ph.D. The motivation for the research came from a NIBIB T35 training experience at Weill Cornell Medical College in summer 2007 where he worked with practicing doctors across the New York City medical campus. The T35 training inspired him with innovative ideas of ultrasound-improved treatment options, but he also knew of the current limitations in the size, cost and lack of portability of ultrasound technology. George effectively worked around this barrier by developing the first high-power, battery powered, high intensity focused ultrasound system (HIFU), and by developing an efficient new approach to generating low- and high-power ultrasound energies for a range of therapeutic applications. He characterized the technology in a range of theoretical and experimental applications by using computational modeling of the electronics and developing numerous instruments that work on the technology platform for academic, medical and industrial collaborators.

George transformed his doctoral advisor's lab to include a state-of-the-art acoustics laboratory. There he developed new ultrasound characterization techniques for transducer calibrations and acoustic power measurements. First, he developed a novel electrical impedance spectroscopy technique, using an impulse response and Fourier analysis to map the electrical impedance of ultrasound transducers. He refined the technique to be applicable for various transducer designs as well as for non-acoustic applications in the life sciences, such as measuring the impedance properties of cell suspensions and tissue constructs. Second, he created an algorithm based off of transmission line modeling to accurately predict electrical-acoustic conversion efficiencies for ultrasound therapy.

George also parametrically explored the potential use of acoustics to overcome neurological drug delivery challenges by enhancing the administration and distribution

of drug within the brain during convection-enhanced delivery (CED). In CED drugs are directly infused into the brain to target specific locations; however the control and penetration of infusate is still limited by a variety of reasons as discussed in the dissertation. Using a 3D *ex vivo* model he showed that the transport of various sized molecules under controlled diffusion and convective processes may be dramatically increased by using therapeutic 1-2 MHz ultrasound over a range of powers. The use of ultrasound resulted in a 100-500% enhancement over diffusion alone and convective transport in tissue samples. As hypothesized, penetration was inversely related to the size of the molecule. Additionally, George transitioned this research into *in vivo* studies and found that ultrasound therapy below tissue damage thresholds improved molecular transport in the brain, which is now in the process of clinical translation to the medical campus.

George's unique adventures into engineering, physics, biology, electronics, anatomy, mathematics and computers, make him into a distinctive researcher. He does not shy away from tough medical problems, but drives toward disentangling answers, armed with the self-assurance of his education. Surely others have similar talent, but George has found a way to blend the flavors of science and the physical world into medical solutions for a better tomorrow.

For my father Dr. George K. Lewis, Sr. and mother Mrs. Diane L. Lewis, my hands on practicums with you enabled my engineering inclination, love for ultrasound and respect for life. For my doctoral advisor Dr. William L. Olbricht, your guidance and commitment to my training and research bestowed qualities I will continue to share with the students I teach and mentor. For my fiancé Sabrina Guarino, your love and passion in my life and research endeavors allowed me to flourish and excel on the hill above Cayuga's waters.

ACKNOWLEDGMENTS

Tremendous support from the entire university community provided a superb environment to develop a biomedical acoustic laboratory during my doctoral research. I would like to acknowledge the following people who made this possible over the four years of doctoral research:

George Blasiak: *Patent support and helping us protect the ultrasound inventions from our Cornell engineering laboratories. Two patents down with a back log of more to go at the time of this dissertation.*

Larry Bonassar: *I will never unintentionally misuse synergistic events with additive outcomes. Our conversations on student mentoring and laboratory procedures provided metrics I used with my own students to help them succeed.*

Ronald Booker: *A prospective on academia that caught my attention. Your fun pessimism and inevitable conversion to ultrasound motivated and inspired new frontiers in my thinking process.*

Pat Burke: *Access to equine brain tissue to translate from agarose brain-phantoms to ex vivo research. The necropsy labs support at the College of Veterinary Medicine is very much appreciated.*

Jeff Fearn: *Technology protection and commercialization of ultrasound inventions from the lab. Your willingness to back our ultrasound inventions and advise in confidentiality matters.*

Blaine Friedlander: *Supporting the dissemination of Cornell medical ultrasound research. A friend with a great family, you opened up a completely new door to my research. Special thanks for providing my dissertation biographical sketch.*

Yingxin Gao: *Medical ultrasound research is alive and well at Cornell and we have much potential to conduct innovative research between our two teams. I look forward to working with you and continuing the discourse.*

Steven Gelber: *Supporting engineering creativity and idea to concept in OB/GYN innovation. Your willingness to work with our team and drive to develop practical solutions makes our collaboration strong.*

Patrica Gonyea: *Helping us build a biomedical acoustics laboratory without a budget. Our go to person for supplies, parts and tools especially when we were just starting off. A friendly face always willing to help.*

Sabrina Guarino: *An editor, researcher and partner. Your help with work, as well as allowing me to take a break from it, when I could not see the*

end or overcommitted myself. Winter in Ithaca was not so cold with you.

JoAnne Guarino: *Advisor and friend. Brain storming new ideas, potential applications of ultrasound, mixing thought patterns and off topic discussions with very good cooking. Fun plane and automobile rides for work and pleasure.*

Bryant Guffey: *A fellow schoolmate with drive to translate innovative technology from the lab to the marketplace. A friend to keep me focused on research and its path to the future.*

Peter Henderson: *Collaboration using our engineering tools, our discussions and success in vein ablation, introduced me to clinical practicality and hospital design of technology.*

Charles Henderson: *Last minute grant reviews, 1 am discussions and power calculations. You showed me a statistical prospective with a very positive attitude.*

Lyndon Hernandez: *New ideas and clinical challenges to be faced with ultrasound applications. Support and eagerness to collaborate and shift medical diagnostic tools.*

Anne Ju: *Never scared of ultrasound even with your sensitive skin. Your writing and stories introduced the nation to pocket-sized ultrasound and did so very well.*

George Lewis, Sr.: *The continued support in research tools and ultrasound engineering insight. We make brain storming, idea generation and concept to practice easy in ultrasound.*

David Lipson: *Casual talks, wine and cheese, and slope day hellos. You started me down the path of multitasking on multiple projects while conducting a Ph.D. at the same time. Thanks for your insight.*

Paula Miller: *New collaborations on improving treatment modalities for aggressive brain cancers, helping with setting up my own lab and working with our research team.*

Richard Newman: *Helping us look at the claims and tuning patents to make them worth their costs. Better yet, teaching us the "real" patent process from a global prospective on gaining priority dates and developing IP walls…and looking for the next big thing.*

Nozomi Nishimura: *Training our team for in vivo animal surgery and histology. Your hands on support, friendly face and willingness to lend a helping hand is at the highest levels and allowed ultrasound research to flourish.*

Chris Ober: *For supporting ultrasound research at Cornell, and financial backing our team to translate technology to Weill Cornell Medical College.*

William Olbricht: *Advice, guidance, mentorship, and truly fostering my individual creativity in research endeavors over the broad spectrum of medical acoustic activities.*

Ralf Ortiz: *Your support and clinical prospective catapulted our technology into rapid translation. You had a major impact on helping me understand the clinical impact of my work.*

Susan Pannullo: *Coming up with resources to translate UCED into the rodent and soon the primate. Your drive to improve brain cancer therapy inspires our engineering creativity. Your energy and enthusiasm is contagious.*

M. Carrington Reid: *Translating our inventions to the next level from lab to clinic, and mentoring on grantsmanship and clinical study design. A great person to work with.*

Cindy Reinhart-King: *Your insight into proposal preparation, willingness to collaborate, casual conversations and friendly attitude was very supportive. Special thanks for help with NIH and fetal monitoring projects.*

Chris Schaffer: *Providing the laboratory space to translate in vitro work into the rodent brain in vivo. Feedback on neurological based experimentation and insight into the future.*

David Skorton: *I enjoyed our discussions over the last four years and correspondences. Furthermore, your support and university backing of our biomedical ultrasound research team was gratefully appreciated.*

Zachary Schulz: *Fantastic research partner from circuit building and testing to ultrasound assisted brain drug delivery. We were in it on the ground floor together and the future looks exciting for UCED.*

Jason Spector: *For making the leap of faith to bring high intensity focused ultrasound into your lab at the hospital, and supporting its refinement as a hand on clinical tool.*

Mike Shuler: *For support of biomedical ultrasound research at the departmental level. Significant mentorship, reviews of proposals, collaboration between labs and dedication to innovation and fresh ideas.*

Teresa Southard: *Discussion and review of histological findings in ultrasound assisted brain drug delivery, and collaboration in the future to translate the technology safely to large animal studies.*

Glenn Swann: *From concept to reality in 30 minutes or under, mechanical engineering machine shop support from Olin Hall. In many cases excessively precise, but oh so beautiful.*

Susi Varvayanis: *Presidential Life Science Fellows, CAT support and Jump Start workshops. Always in the know with technology and its translation into the public domain, and a supporter of medical ultrasound.*

Peng Wang: *Always a fun guy to talk to and supporter of some of the very first UCED experiments in 108 Olin hall. From the initial brain phantom to in vivo work, your help is very much appreciated.*

Artann labs: *Armen Sarvazyan, Laurent Filniger and Guarav Gandhi your support in developing time-reversal based UCED and bridging our technologies to develop innovative engineering solutions to ultrasound-assisted drug delivery. We have a strong collaboration, unique ultrasound prospective and imaginative think tank for biomedical acoustics.*

AngioDynamics: *Support and collaboration in developing new biomedical acoustic tools for deep vein thrombosis.*

MIT: *Robert Langer and Avi Schrodenger brain storming and coming up with "the next best thing". Not being scared by engineering hurtles or funding levels.*

Cornell Students: *Tarn Teraphongphom, Saran Baskaran, Brian Aguilar, Jeff Roshko, Dan Currie, Sarah Wheeling, Pooja Umesh, Zach Schulz, Sabrina Guarino, Allison Jagoe, Apeksha Shapeti and others who helped with data collection, analysis and contributed to the body of this dissertation.*

Others: *Many people helped along the way, continue to help now and into the future. Hockey friends, classmates and especially my family: George Sr., Diane, Jennifer, Jillian, Marilyn, Larry, Kim et. al.*

Funding Agencies and Research Support:

This research was supported by the Presidential Life Science Fellowship, National Science Foundation Graduate Research Fellowship and GK-12 Fellowship, National Institutes of Health Grant #5R01NS045236-05 and #1R43NS065524-01, The WCMC Brain Tumor Project, AngioDynamics Inc., Artann Labs Inc, EBL Products Inc., Transducer Engineering Inc, Center for Advanced Technology, New York State Foundation for Science, Technology and Innovation, New York Creative Core, Cornell Center for Materials Research, College of Engineering and Department of Biomedical Engineering.

TABLE OF CONTENTS

LIST OF FIGURES

Figure 4.4 Predictions of the model shown in Figure 3. (4a) through (4d) show the maximum output power as a function of frequency for values of the amplifier source impedance R_s in the range 0.03 to 200 Ω . (4a) 1.5 MHz 10.3 Ω transducer. (4b) 1.5 MHz 1.2 Ω transducer. (4c) 8 MHz 10.6 Ω transducer. (4d) 8 MHz 0.37 Ω transducer

Figure 4.5 (A and B) Measured 1.54MHz output waveform from the ultrasound driver with slight ringing at the corners without and with the ultrasound transducer attached, respectively. (C) The power spectrum of the 1.54 MHz waveform. The drive signals energy concentration is in the early megahertz frequencies. (D) Measured 8.0 MHz signal shows attenuated drive voltage and asymmetry of the waveform with oscillations on both the positive and negative sides.

Figure 4.6 (A and B) Measured 1.54MHz output waveform from the ultrasound driver with slight ringing at the corners without and with the ultrasound transducer attached, respectively. (C and D) Output waveform from the ultrasound driver with 12 Ω impedance matching power resistor attached directly to driver in series to the 12 Ω ultrasound transducer without and with the transducer attached, respectively. (E and F) Output waveform measured with 50 Ω power resistor in series without and with transducer, respectively.

Figure 4.7 Complete high-power ultralow-output impedance ultrasound driver powering a 1.54 MHz ultrasound transducer. (A) Ultrasound driver operating at 28 V_{pp} with a clean waveform and high acoustic energy output causing the water to vaporize. (B) Close-up of the transducer in the water bath levitating and cavitating the water molecules into the air. Cavitation bubbles are visible in the water stream off the front face of the transducer.

Figure 5.1 The experimental setup for the phantom study is shown. The sonicated phantom is immersed in 0.5 wt% diluted dye and pulse sonicated (15 seconds on and off) while simultaneously the transducer is oscillated up and down at 0.25Hz 10mm amplitude. The beginning position of the transducer was 40mm above the agar/dye interface, so that the US focus was placed on the surface. The control setup was the same without US.

Figure 5.2 Top left and right are histology images taken from phantoms with and without applied US TP 1 and 4. Visible is the increase in dye penetration and intensity of the sonicated phantom. Bottom left and right are the corresponding RGB color intensity maps that correspond with the above images.

Figure 5.3 Plot of the theoretical fit to the experimental data for TP 1 and 4. Top left we see good agreement with control (No US) and constant source diffusion Eq. (5.1), note that US experimental data does not fit Eq. (5.1) well. Bottom left we find that Eq. (5.2) fits experimental data with US well but does not fit control. Top right graph shows that simple diffusion does not fit control or US phantom well for TP4.

Bottom right graph shows that Eq. (5.2). fits both control and US phantom well. Overall Figure shows a noticeable increase in dye penetration when US is applied.

Figure 6.1 The experimental setup for the sample study is shown to the left. The sonicated phantom is covered in 0.25 wt% diluted Evans blue dye and sonicated at 100% duty while simultaneously the transducer is oscillated up and down at 0.25Hz 10mm amplitude. The beginning position of the transducer was 40mm above the sample/dye interface.

Figure 6.2 The above Figure shows the sectional images and the results of enhanced EBD delivery into a tissue mimicking phantom, equine horse brain and avian muscle tissues with the application of Therapeutic Ultrasound for two minutes in red, compared with the control in blue. The Figure shows concentration curves of the EBD uptake into the samples and that local delivery of EBD in conjunction with the application of Therapeutic Ultrasound may significantly enhanced the amount of EBD delivery into tissue. Application of US enhanced EBD density of 61.5% (phantom), 93.2% (brain) and 52.8% (muscle) compared to the control.

Figure 6.3 Dimensionless BCNU concentration profiles in tissue following its release from a wafer in monkey brain

Figure 6.4 EBD concentration profiles after 2 min in equine brain tissue without ultrasound (red) and with 1W/cm^2 ultrasound (blue) for 2 min. Ultrasound increases the apparent diffusion coefficient by about 40x.

Figure 7.1 Experimental setup for ultrasound-enhanced convection. A 1.58MHz transducer sonicated the sample for 1-30 min. The pressure gradient across the sample was primarily provided by a vacuum pump, which induced convective flow through the sample.

Figure 7.2 EBD profile of avian muscle tissue after sonication at 1.3 W (top) and 5.25 W (bottom) for 4 min. US combined with CED provided greatest EBD uptake enhancement of 240% (left) and 390% (right) as compared with diffusion alone.

Figure 7.3 EBD profile of equine brain tissue (top) and brain-mimicking phantom (bottom) after 5.25 W sonication for 2 and 1 min, respectively. US combined with CED provided greatest EBD uptake enhancement of 560% (left) and 880% (right) compared with diffusion alone.

Figure 7.4 Compilation of sectional profile images to produce EBD profile curves in Figures 1 and 2

Figure 7.5 Dimensionless concentration profiles of EBD (left) and AcEBD (right) for brain-mimicking phantom after 5.25 W sonication for 1-30 min. US combined

with CED provided greatest EBD and AcEBD uptake enhancement of 277% (left) and 327% (right) compared with diffusion alone.

Figure 8.1 Construction of the transducer cannula assembly. I. Machine the PZT-4 into a disk with center hole. II. Connect a brass tube to front face of ceramic using solder. III. Place the ceramic in a watertight PVC/aluminum housing with sterotaxic guide arm, and connect ground and hot leads to the transducer through the guide arm. V-VI. Attach the guide-cannula and infusion cannula to the transducer and secure to the popper height with epoxy. VII. Actual finished device.

Figure 8.2 Animal experimental setup for using TCA in rat brain. The rat is secured with ear bars in a stereotaxic frame and a small craniotomy is performed on the left hemisphere. The TCA is guided 5.5 mm deep into the caudate of the rat brain.

Figure 8.3 Electrical impedance of TCA. Resonance occurs at 1.18 MHz with 380 Ω impedance. The phase angle (not shown) is approximately 0 degrees at resonance. Parallel resonance occurs at 3.1MHz.

Figure 8.4 Brain sections from the four subgroups of group 2 studied after 30 minutes of Evans blue infusions at 0.5 μL per minute with a 30 gauge cannula. A. Convection enhanced delivery (CED) and B. Convection enhanced delivery with microbubbles (CED+MB) provide similar infusion profiles for the rodents in each group. C. Ultrasound-assisted convection enhanced delivery (UCED) delivers EBD further into the brain and more diffusely spread across the caudate. D. Ultrasound-assisted convection enhanced delivery with microbubbles (UCED+MB) shows further EBD penetration over CED and CED+MB, but is more localized in the rodent caudate versus UCED which spreads EBD out of the caudate region. Backflow of EBD along the needle track into the white matter track of the corpus callosum is reduced with UCED and UCED+MB as compared to controls.

Figure 8.5 3D Infusion reconstruction of the four subgroups of group 2 brain sections from Figure 4. The cannula is in the plane of the Figure and the transducer cannula assembly (TCA) is positioned at the top of each Figure. A. Convection enhanced delivery (CED). B. Convection enhanced delivery with microbubbles (CED+MB). C. Ultrasound-assisted CED (UCED). D. Ultrasound-assisted CED with microbubbles (UCED+MB).

Figure 8.6 Analysis of total EBD volume distribution in the rodent brain with subgroup standard error bars. UCED and UCED+MB increases EBD volume distribution by 2.24x and 1.37x in the left hemisphere and 2.44x and 1.70x in the left caudate, respectively, as compared with CED and CED+MB receiving 0.25μL per min infusions. For 0.5μL per min infusions of group 2,UCED and UCED+MB increases EBD volume distribution by 2.96x and 1.16x in the left hemisphere and 3.25x and 1.54x in the left caudate, respectively. The left hemisphere and left caudate subgroups

LIST OF TABLES

CHAPTER 1

ULTRASOUND: HISTORY, PHYSIC AND MEDICINE

1.1 The History of Ultrasound

The field of acoustics is older than a millennium and continues to evolve at Mores law pace. Sound, vibration and the principles of acoustics were first documented by Pythagoras, a Greek philosopher, mathematician and scientists, in the early 6^{th} century. Acoustic frequency and vibration, musical pitch and tone were later studied by Galileo and his father in the mid-1600s. Galileo's and others scattered studies across Europe were later combined by Lord Raleigh into the "Theory of Sound" in 1877. The "Theory of Sound" connected the mathematics and physics behind acoustics with empirical results. The field of ultrasonics, or the branch of acoustics that deals with mechanical oscillatory waves at frequencies above the human audible range (greater than 20 kHz), was developed during World War I as the first "passive/active sonar" technology capable of detecting enemy vessels using acoustic propeller and hull noise signatures [1, 2]. The first hydrophone for passively detecting submarines was developed by Wood and Gerrard from England. Langevin from France began using piezoelectric materials and vibrating devices for active ultrasonic detecting means of military ocean vehicles. The effort of the two groups opened a new door to measuring and generating mechanical *ultrasonic* vibrations for measurement applications.

Since early war time to current day, ultrasonics is used for sonar and other measurement capabilities. In the more recent decades, ultrasonics has continued to be studied and developed extensively for a vast array of military, medical, and industrial applications some of which are discussed in this dissertation. Ultrasound which is a

mechanical wave can only exist in matter composed of molecules, since the wave is transmitted from one molecule to another by expansion and rarefaction between molecules in direct contact. Due to the mechanical vibratory transmission of ultrasound , the attenuation of the wave is highly dependent on the elastic property of the medium [3]. These properties of ultrasound allow the acoustic wave to travel efficiently through mediums that are relatively dense such as water, tissue and metal because the wavelength of sound is large compared to the spatial position of the molecules. Conversely, ultrasound does not travel well in gasses and air because molecules are too spread out to effectively vibrate and transmit the ultrasonic waves.

1.2 The Physics Behind Ultrasound

The *wave equation* describes the propagation of ultrasound waves in isotropic homogeneous media and in the simplest 1D form it may be derived from hooke's law. In 3D space the wave equation becomes much more complex particularly when taking into account the non-linearity of amplitude and frequency dependence on the propagation of ultrasound waves in certain regimes. The physics behind ultrasound depends on a number of parameters. Here, we review the fundamental equations that describe the ultrasound wave and the elegant physics behind ultrasound. In most of the equations presented the terms within them may be considered constants for most engineering applications; however the non-linearity of the terms should be noted in certain regimes. The ultrasound frequency f is measured in Hertz (Hz). The speed of ultrasound c through a media is a function of elasticity K (N/m^2) and density ρ (Kg/m^3):

$$c = \sqrt{\frac{K}{\rho}} \qquad (1.1)$$

The wavelength λ (m) of ultrasound is calculated as:

$$\lambda = \frac{c}{f} \qquad (1.2)$$

The amplitude *A* of the ultrasound wave is measured in units of length in meters (m) or pressure in Pascale (Pa). Length measurements describe the maximum distance between the molecules in the rest state in relation to the expansion/compression state, while pressure measurements describe the maximum/minimum local pressure within the ultrasound wave.

The velocity of ultrasound in media is temperature dependent and readily available for a wide range of materials in ultrasound texts. It is important to note however, that ultrasound travels faster in well-ordered solid structures such as ceramics, metals and bone, and much slower in non-rigged objects such as water, muscle and fat. As a general rule of thumb, ultrasound in soft tissues for medical applications has a velocity of approximately c_{Med}=1540 m/s [4]. Furthermore, the speed of sound in some cases is frequency and amplitude dependent.

In the linear and elastic range of a medium, the displacement of particles within the ultrasound field is sinusoidal, and the wave amplitude does not affect wave propagation. When two or more waves interfere in this regime their amplitudes add to one another and their frequencies ride on top of each other. In special cases of interference, stationary nodes are formed with no spatial or amplitude displacement. In this case, the ultrasound wave interaction is termed “standing wave”. Standing waves can produce interesting affects in medical ultrasound applications as will be discussed in Chapter 9. Once the interference of two or more waves concludes, the individual waves maintain their initial properties of frequency and amplitude. Should the sum of

the two waves produce pressures and temperature rises above the linear and elastic range of the medium, non-linear effects need to be taken into account.

1.2.1 Ultrasound Energy, Dissipation and Attenuation

The frictional forces between molecules in the transmission path absorb the energy of the ultrasound waves and convert it into heat. This heat can directly affect the speed of propagation in the medium, as well as the quicker dissipation of the ultrasound wave's energy. Mechanical motion of the wave propagation media discussed later can also dissipated energy. The ultrasound intensity of the wave source I_o is thereby exponentially reduced according to the following equation as it propagates into a medium distance x with absorbance coefficient α:

$$I_x = I_o e^{-2\alpha x} \qquad (1.3)$$

where I_x (W/cm^2) is the intensity of the wave at distance x from the initial source. The absorption coefficient is a function of frequency and as frequency increases the absorbance coefficient increases. The pressure amplitude P is identically related to intensity as a function of distance and the absorption coefficient:

$$P_x = P_o e^{-2\alpha x} \qquad (1.4)$$

The total ultrasound power produced by the wave is measured in Watts (w) and calculated by multiplying the intensity I over the surface area it is applied to. The ultrasound power describes the sum of acoustic energy per unit time.

$$Power = I \cdot A \qquad (1.5)$$

The ultrasound energy density *(E)* is a measure of energy per unit volume and calculated by:

$$E = \frac{I}{c} \qquad (1.6)$$

and measured in units of joules per square centimeter (J/cm^2).

An ultrasound wave traveling through a medium is dispersed and absorbed over a period of time due to matter inconsistency, heterogeneities and friction. This combined effect is called attenuation that is measured in (dB) and is estimated along the propagation distance *x* according to:

$$attenuation = \alpha' \cdot x \cdot f \qquad (1.7)$$

where α' is the attenuation coefficient. Values of α' vary multiple fold depending on the media. For water α' is approximately 0.0022 while for bone α' is approximately 20. For various types of soft tissues and fluids α' is approximately 1.0 for muscle and kidney, 0.94 for liver, 0.85 for brain, 0.63 for fat and 0.18 for blood, all in units of dB/(MHz x cm) [5-8]. The attenuation coefficient for skin varies greatly depending on the moisture level of the skin – approximate α' range is 0.7 to 10.

1.2.2 Ultrasound Reflection and Refraction

Reflection and refraction of a sound wave occurs when it propagates across an interface of two different materials of differing acoustic impedance *Z* calculated by:

$$Z = \rho \cdot c \qquad (1.8)$$

where ρ is the density of the material, c is the ultrasound speed and Z is in units of Nepers·seconds per cubic meter ($N \cdot s/cm^3$) or Megaralys. At the boundary of wave propagation and differing acoustic impedances, two or more acoustic waves are produced: one continuing to propagate in the forward direction into the next medium and the other being reflected back into the initial medium. The forward propagating wave changes its transmission angle according to Snell's Law, while the reflected wave's angle is the same as the incident angle. The reflected fraction of energy R, is proportional to impedance mismatch between the first and second mediums Z_1 and Z_2, and calculated by:

$$R = \left[\frac{Z_1 - Z_2}{Z_1 + Z_2} \right]^2 . \qquad (1.9)$$

The acoustic impedance of air is 0.0004 Megarayls while it is 1.70 and 7.80 Megarayls for muscle and bone, respectively [7]. Such large impedance mismatches between bone and soft tissue provide very good ultrasound contrast in medical imaging.

Understanding reflection and refraction along with the exponential attenuation of ultrasound waves in soft tissue is the basic foundation of ultrasound diagnostic techniques used in medicine today. It also plays an important role in measuring the effective treatment area of ultrasound.

1.2.3 Ultrasound Forces and Physical Mechanisms

Ultrasound waves apply a force on objects that they are reflected or absorbed by. When a wave of radiating power W and speed c is completely absorbed by the medium, the irradiating force F *is* measured in Newton's (N) according to:

$$F = \frac{W}{c} . \qquad (1.10)$$

The radiation force on an object is increased by a factor of two, when completely reflected by the object according to:

$$F = 2\frac{W}{c} \qquad (1.11)$$

The acoustic force can cause the motion of particles in fluid, which is called acoustic streaming. The velocity of acoustic streaming v (m/s), is dependent on the viscosity μ and absorption coefficient α, and calculated according to:

$$v = 2\frac{\alpha \cdot W}{\mu \cdot \rho \cdot c} \qquad (1.12)$$

Both the acoustic force and streaming velocity play an important role in many of the medical applications of therapeutic ultrasound. Understanding these basic physical mechanisms and the interactions of ultrasound in medical therapeutic applications *in vivo* still remain unclear and a topic of continued research as well as this dissertation.

1.2.4 Ultrasound Cavitation and Mechanisms

The formation of microbubbles (gas-filled cavities) or the oscillation of microbubbles in an acoustic field is termed "cavitation" [9-11]. Cavitation activity usually involves intrinsic stable bubbles that were already present in the liquid media or were created by the propagation of the acoustic wave itself. In the latter case, the negative pressure of the acoustic wave must be below the vapor pressure of the fluid in order for a cavitation bubble to form [12]. Once formed within the fluid or when found

intrinsically in the fluid, these microbubbles in the acoustic field oscillate and cause local fluid motion, swirling, streaming, and mixing [13]. Microbubbles may also be actively added into the media from external sources, since they are readily available commercially and used as contrast agents in diagnostic ultrasound today.

There are two well documented types of acoustic cavitation: *stable cavitation* and *inertial cavitation* and their interactions with tissues and structures are immensely different as will be discussed later.

Stable cavitation is the continuous oscillation of microbubbles in the acoustic field with a streaming motion in the path of wave propagation. In stable cavitation the microbubble radius will oscillate with the acoustic pressure field during the compression and rarefaction cycle.

Inertial cavitation is also called "transient cavitation" since it ends with a microbubble implosion. Transient cavitation is the highly active oscillation of microbubbles in high amplitude acoustic fields that causes the microbubbles radius to resonate, and reach both very large and small lengths to a point where it rapidly expands beyond a fatal resonance point and then implodes [14].

The resonant radius for implosion of an air filed microbubble in water R_r (mm) is related to the frequency of sound f (kHz) and can be estimated by:

$$R_r \approx \frac{3.29}{f} \quad \text{[14].} \qquad (1.13)$$

The energy released during transient cavitation can produce very high pressures generating significant forces on surrounding media. The collapse of microbubbles also generates very high but short-lived temperature rises. These extreme pressures and temperatures in a temporally compressed window make inertial cavitation activity an adiabatic process [12,15]. The properties of the microbubble

including the gas inside, its radius, shell properties and fluid surround it determine its resonant frequency, resonant radius and inertial cavitation forces generated [14, 16]. Low frequency applications of ultrasound result in large oscillating bubbles that are used in ultrasonic cleaning and transdermal drug delivery. Higher frequency ultrasound may oscillate much smaller microbubbles that may prove useful in enhancing the movement of pharmaceuticals through tissues as discussed in Chapters 5-9.

When a microbubble collapses near a surface a high-velocity “micro jet” of liquid reaching several hundred meters per second, is propelled toward the surface, thereby depositing enormous energy densities at the site of impact [17-19]. The implosion produces a shock wave with the creation of additional microbubbles, which can cause additional cavitation activity in the medium making a cavitation cloud [20].

The Mechanical Index (MI) is an indicator of the onset of transient cavitation in media exposed to ultrasound [21]. MI is calculated according to:

$$\mathrm{MI} = (P_{neg}/f^{0.5}) \qquad (1.13)$$

where P_{neg} is the peak negative pressure, and f is the frequency. When the MI is greater than 0.7 the probability of transient cavitation is high [22]. An acoustic peak negative pressure of 0.2 MPa will cause inertial cavitation in blood at 1 MHz, but much higher pressures are required for inertial cavitation in tissues. The addition of commercially available microbubbles may be used to induce stable and inertial cavitation in the media at much lower acoustic pressures. In this case, the MI is not well defined and is dependent on the microbubble properties.

The Thermal Index (TI) is a measure of acoustic power *W* required to raise the temperature of tissue by 1 degree centigrade (W_{deg}) according to:

$$TI = (W/W_{deg}) \qquad (1.13)$$

For therapeutic applications TI's are generally maintained below 6 according to FDA guidelines.

1.3 Ultrasound in Medical Applications

The use of ultrasound in medicine has evolved over the last 70 years in physiotherapy, simple diagnostics, medical 3D imaging, and drug delivery and novel combination diagnostic-therapeutic applications [23, 24]. Ultrasound has its longest history of use in physical therapy for musculoskeletal disorders. In recent years the medical application of ultrasound has expanded into new applications some of which are discussed in this dissertation. Therapeutic ultrasound is being used, by itself or in combination with drugs, in various clinical applications such as back and knee pain, healing, venous diseases, cancer, cardiovascular diseases, infections, osteoporosis, thrombosis, glaucoma, nerve damage, aging skin, wounds, muscle spasms, and bone fractures. Many FDA approved ultrasound based devices are available already around the world, and countless others are in various preclinical and clinical approval processes. As of today, European and Asian countries have been more progressive in the regulatory approval, acceptance and use of both traditional and the newer applications of therapeutic ultrasound in medical applications. Furthermore, for the last 70 years no adverse bio effects do to ultrasound exposure for short or long treatment durations have been reported beyond thermal and mechanical effects at

relatively high acoustic exposures. The expert consensuses of investigators who use or are involved in ultrasound research believe that ultrasound is safe.

The interaction of acoustic waves microscopically and macroscopically, and the multiplicity of their effects on cells, membranes and tissues provides a range of beneficial interactions that can be utilized in therapeutic medicine. As presented earlier, a medium exposed to ultrasound experiences pressure oscillations and the possibility for cavitation activity. The absorbance of ultrasound and the pressure oscillations in the tissue both thermally and mechanically affect it. Ultrasound has been shown to cause vasodilation and increase tissue plasticity. Additionally, the interaction of ultrasound with tissues increases the permeability of it, and may be used for a variety of drug delivery and therapeutic effects through it that will be discussed.

Though the temperature rise of tissue do to the absorption of the ultrasound wave is important, perhaps the second most significant effect of ultrasound in medical applications is cavitation. Both stable and inertial cavitation have significant mechanical, thermal and macro/micro level effects on cells and tissues including fluid mixing and shear forces on tissue matrixes [25, 26], and disruptive shock waves that can induce chemical changes "sonochemistry" [27]. The ultrasonic waves create a dynamic moving environment in the treatment zone that may be utilized in a variety of medical applications.

Figure 1.1 The action shot of the "ultrasonic fountain" shows the interaction of High Intensity Focused Ultrasound (HIFU) waves with water. The ultrasound transducer is typical of medical physical therapy ultrasound devices; operating at 1.5 MHz and with a diameter of 2.54 cm. The difference in this picture is that the transducer is powered 20x greater than typical, and the energy from the transducer is focused to a 1mm^3 volume creating a HIFU spot near the surface of the water. Since ultrasound is a mechanical wave, the HIFU spot sees large pressure changes as the sound travels via compression and rarefaction in the propagation fluid, which results in cavitation and micro-bubble formation in the water. The transfer of ultrasound energy/momentum into the fluid causes the water to stream and/or move in the direction of the ultrasound field. Combining the cavitation and acoustic streaming, the water molecules are shot into the air (some of which are vaproized by the HIFU) creating a beautiful acoustic fountain.

In sonochemistry, high power ultrasound and cavitation interactions are capable of generating highly reactive species that can induce chemical transformations in the surrounding medium. Effects of ultrasound can also appear at the cellular and tissue-level that will be discussed further in Chapter 8-9. Overall, the effects of ultrasound on tissue are governed by several parameters, primarily the frequency, amplitude and pulse frequency of the ultrasound [28-31]. In the following chapters we discuss the development of ultrasound systems and their application in neurological based drug delivery and rehabilitation medicine.

Figure 1.2 Dr. Monaghan and Dr. Ferrer from the Vein and Laser Centers of Central NY, debuting the Cornell engineering ultrasound technology.

REFERENCES

[1] Suslick, K.S. (1988). *Ultrasound: Its chemical, physical, and biological effects.* New York: VCH Publishers.

[2] Kinsler, L.E., Frey, A.R., Coppens, A.B., & Sanders, J.S. (1980). *Fundamentals of acoustics*. New York: John Wiley and Sons.

[3] Ensminger, D. (1988). *Ultrasonics: Fundamentals, technology, applications.* New York: Marcel Dekker.

[4] Cutnell, J.D., & Johnson K.W. (1989). *Physics.* New York: Wiley.

[5] Hill, C.R., Bamber, J.C., & ter Haar, G.R. (2004). *Physical principles of medical ultrasonics.* New York: John Wiley and Sons.

[6] Goss, S.A., Johnston, R.L., & Dunn, F. (1978). Comprehensive compilation of empirical ultrasonic properties of mammalian tissues. *J. Acoust. Soc. Am., 64*(4), 423–457.

[7] Gibbs, v., Cole, D. & Sassano, A. (2009). *Ultrasound physics and technology.* New York: Elsevier Inc.

[8] Schroeder, A., Kost, J. & Barenholz, Y. (2009). Ultrasound, liposomes, and drug delivery: principles for using ultrasound to control the release of drugs from liposomes *Chem. Phys. Lips., 162*, 1–16.

[9] Flynn, H.G. (1964). *Physics of acoustic cavitation in liquids in physical acoustics.* New York: Academic Press.

[10] Neppiras, E.A., & Noltingk, B.E. (1951). Cavitation produced by ultrasonics: theoretical conditions for the onset of cavitation. *Proc. Phys. Soc,. B 64*, 1032–1038.

[11] Noltingk, B.E., & Neppiras, E.A. (1950). Cavitation produced by ultrasonics. *Proc. Phys. Soc., B 63*, 674–685.

[12] Suslick, K.S., Didenko, Y., Fang, M.M., Hyeon, T., Kolbeck, K.J., McNamara III, W.B., Mdleleni, M.M., & Wong, M. (1999). Acoustic cavitation and its chemical consequences. *Philos. Trans. R. Soc. Lond. A, 357,* 335–353.

[13] Margulis, M.A. (1995). *Sonochemistry and cavitation.*Amsterdam: Gordon and Breach Science Publishers.

[14] Young, F.R. (1989). *Cavitation.* Maidenhead, UK: McGraw-Hill.

[15] Catania, A.E., Ferrari, A., Manno, M., & Spessa, E. (2006). A comprehensive thermodynamic approach to acoustic cavitation simulation in high-pressure injection systems by a conservative homogeneous two-phase barotropic flow model. *J. Eng. Gas Turbines Power, 128*(2), 434-445.

[16] Suslick, K.S., & Nyborg, W.L., (1990). Ultrasound: its chemical, physical, and biological effects. *J. Acoust. Soc. Am., 87*, 919–920.

[17] Hoskins, P., Thrush, A., Martin, K., Whittingam, T. (2002). *Diagnostic ultrasound: physics and equipment.* London: Greenwich Medical Media Ltd.

[18] Catania, A.E., Ferrari, A., Manno, M., & Spessa, E. (2006). A comprehensive thermodynamic approach to acoustic cavitation simulation in high-pressure injection systems by a conservative homogeneous two-phase barotropic flow model. *J. Eng. Gas Turbines Power, 128*, 434.

[19] Krasovitski, B., & Kimmel, E. (2004). Shear stress induced by a gas bubble pulsating in an ultrasonic field near a wall. *IEEE Trans. Ultrasonics. 51*, 973–979.

[20] Margulis, M.A. (1995). *Sonochemistry and cavitation.* Amsterdam: Gordon and Breach Science Publishers.

[21] Apfel, R.E., & Holland, C.K. (1991). Gauging the likelihood of cavitation from short-pulse, low-duty cycle diagnostic ultrasound. *Ultrasound Med. Biol. 17*, 179–185.

[22] Leighton, T.G. (1997). The Acoustic Bubble. New York: Academic Press.

[23] Moore, C., & Promes, S.B. (2004). Ultrasound in pregnancy. *Emerg. Med. Clin. North Am. 22*, 697–722.

[24] Lindner, J.R. (2004). Microbubbles in medical imaging: current applications and future directions. *Nat. Rev. Drug Discov.*, 3, 527–532.

[25] Suslick, K.S. (1998). Ultrasound: Its chemical, physical and biological effects. New York: VCH Publishers.

[26] Pecha, R., & Gompf, B. (2000). Microimplosions: Cavitation collapse and shock wave emission on a nanosecond time scale. *Phys. Rev. Lett. 84,* 1328–1330.

[27] Riesz, P., & Christman, C.L. (1986). Sonochemical free radical formation in aqueous solutions. *Fed. Proc., 45*, 2485–2492.

[28] Xu, X., Fowlkes, J.B., & Rothman, E. (2005). Controlled ultrasound tissue erosion: The role of dynamic interaction between insonation and microbubble activity. *J. Acoust. Soc. Am., 117*, 124-135.

[29] Barnett, S.B., Rott, H.D., ter Haar, G.R., et al. (1997). The sensitivity of biological tissue to ultrasound. *Ultrasound Med. Bio., 23*(6), 805-812.

[30] Linder, J.R., Song, J., Christiansen, J., et al. (2001). Ultrasound assessment of inflammation and renal tissue injury with microbubbles targeted to p-selectin. *Circulation, 104*, 2107-2112.

[31] Schroeder, A., Kost, J., & Barenholz, Y. (2009). Ultrasound, liposomes, and drug delivery: Principles for using ultrasound to control release of drugs from liposomes. *Chem. Phys. Lipids. 162*, 1-16.

CHAPTER 2

COST EFFECTIVE BROAD-BAND ELECTRICAL IMPEDANCE SPECTROSCOPY MEASUREMENT CIRCUIT AND SIGNAL ANALYSIS FOR PIEZO-MATERIALS AND ULTRASOUND TRANSDUCERS[2]

2.1 Abstract

This chapter explains the circuitry, and signal processing to perform electrical impedance spectroscopy on piezoelectric materials and ultrasound transducers. Here, we measure and compare the impedance spectrum of 2-5MHz piezoelectrics, but the methodology applies for 700kHz-20MHz ultrasonic devices as well. Using a 12ns wide 5 volt pulsing circuit as an impulse, we determine the electrical impedance curves experimentally using Ohms law and Fast Fourier Transform (FFT), and compare results with mathematical models. The method allows for rapid impedance measurement for a range of frequencies using a narrow input pulse, digital oscilloscope and FFT techniques. The technique compares well to current methodologies such as network and impedance analyzers, while providing additional versatility in the electrical impedance measurement. The technique is theoretically simple, easy to implement and completed with ordinary laboratory instrumentation for minimal cost.

[2]This work has been published as Lewis, G.K., Jr., Lewis, G.K., Sr., Olbricht, W.L. (2008). Cost-effective broad-band electrical impedance spectroscopy measurement circuit and signal analysis for piezo-materials and ultrasound transducers. Meas. Sci. Technol. 19 105102

2.2 Background

Electrical Impedance Spectroscopy (EIS) of piezoelectric devices and materials, henceforth referred to as PED's, derives from the measurement of the current into and the voltage across the PED as a function of the applied sinusoidal voltage frequency. According to Ohm's Law the impedance can be calculated by complex division of the voltage and current. The impedance of the PED can be calculated by applying a sinusoidal voltage to the PED in series with a resistor, and measuring the voltage across the resistor and across the PED. Performing this measurement by sweeping the frequencies of the applied signal provides the impedance phase and magnitude. The power - voltage multiplied by current - delivered to the PED can also be determined from the voltage and current measurements. The impedance plot, and, more importantly the current and voltage measurements as a function of frequency, provides useful information to builders and users of the piezoelectric device.

EIS provides many piezoelectric properties that are necessary in developing ultrasound transducers for imaging, ablation, level-measurement and other ultrasonic applications [1, 2]. The electrical impedance of piezo-material over a range of frequencies is important in understanding the behavior of the piezoelectric around resonance and parallel resonance. It is also useful to compare different piezoelectric materials such as films, composites and single crystals for their possible uses and electro–acoustic behavior [3].

By analyzing the electrical impedance curve as a function of frequency, one can determine properties of the piezo-material such as impedance *Z*, admittance *Y*, maximum impedance frequency $f_{p,}$ maximum admittance frequency $f_{s,}$ mechanical Q Q_m, and the components of the *RLC* circuit that mimics the material [4-7]. Therefore, a

quick and affordable way to measure the impedance of a piezo-material and ultrasonic devices can be of significant benefit.

Numerous methods have been introduced to measure electrical impedances for transducer sensitivity calibrations [7], maximization of acoustic energy conversion/transfer [8, 9] and to determine other properties of piezoelectric ceramics [1,2]. A good review of standard methods used at different frequencies and in a variety of devices is "*Agilent Technologies Impedance Measurement Handbook*" [10] at the Agilent Technologies website. In practice, EIS of piezoelectrics is easily done using network analyzers and impedance meters. However, these devices generally cost ten to forty thousand dollars, which is prohibitive for many potential users. In this manuscript we demonstrate a practical and affordable pulsing circuit along with the methodology to easily perform EIS for assumed lossless PED's [6, 11] using a well established signal processing approach.

The approach in this paper uses an impulse response to determine the transfer function of a simple circuit or system. An applied pulse to a PED in series with a known impedance source in time results in a measurable response. When the measured response is converted into the frequency domain, Ohm's Law can be used to determine the impedance of the PED as a function of frequency.

2.3 Methods

2.3.1 Pulsing Circuit

The pulsing circuit shown in Figure 2.1 constructed from two common high speed integrated circuits (IC) (Mouser Corporation) mounted on a prototyping board. The first IC was a Hex Inverter (DM74AS04 Fairchild Semiconductor) wired to form a simple 4 kHz square wave oscillator (pins 1-4 and 12-13). The output from the oscillator pin 4 was then sent through even multiples of gates as shown in the Figure

to obtain two equivalent wave forms. The two outputs from the Hex Inverter (pins 10 and 8) were sent to the second IC, a high speed Quad NAND Gate (DM74AS00 Fairchild Semiconductor). The NAND Gate's intrinsic 4ns propagation delay was used to slow the output (pin 8 Hex Inverter) by approximately 12ns. The delayed signal was then logically combined with the non-delayed signal (pins 9 and 10 NAND Gate). The output at pin 8 of the NAND Gate was a 10ns wide 5 volt pulse. Bypass capacitors (pins 14 both IC's) and a pull-up resistor (pin 8 NAND Gate) were used to sharpen the pulse and remove ringing as shown in Figure 2.1.

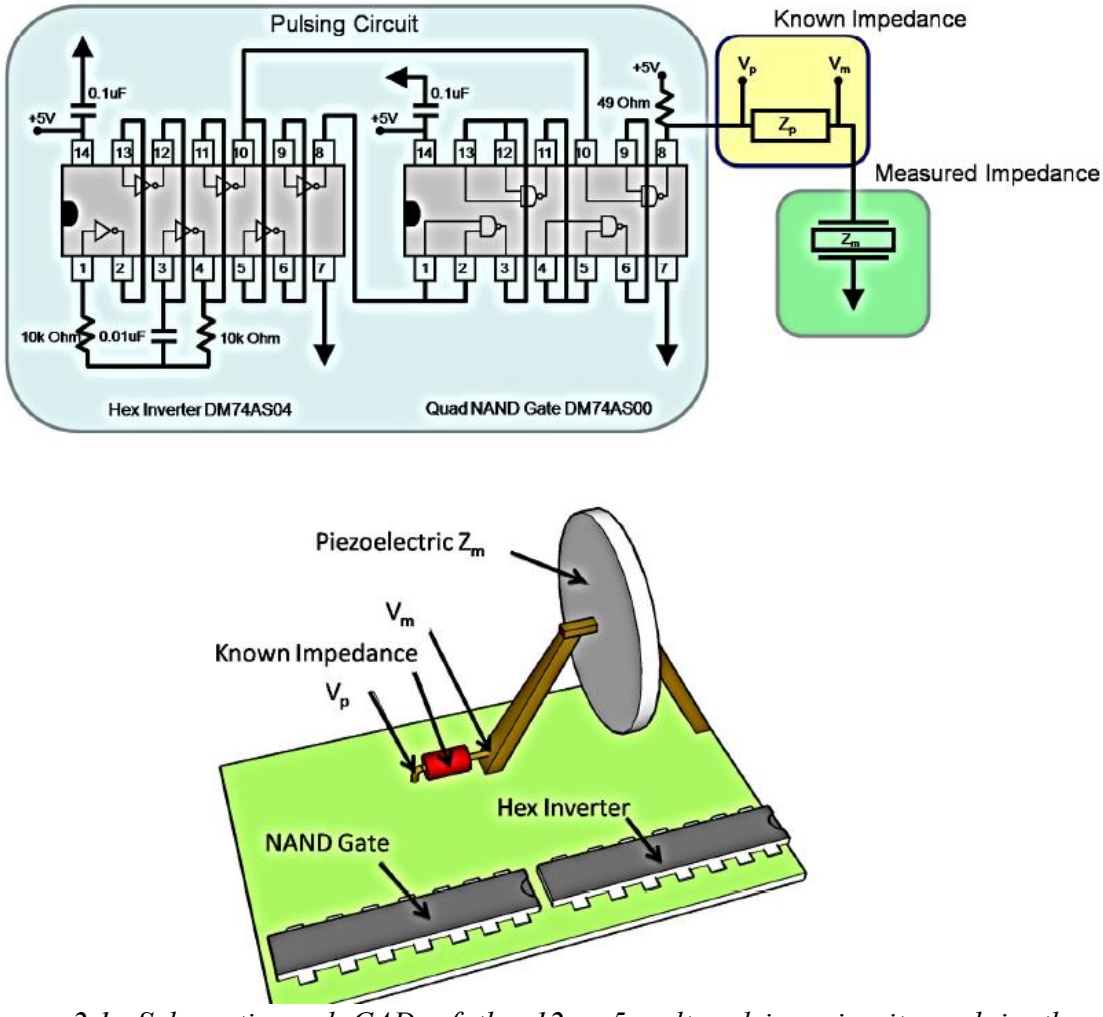

Figure 2.1. Schematic and CAD of the 12ns 5 volt pulsing circuit used in the impedance measurement study.

2.3.2 Experimental Measurements and Analysis

The pulsing circuit in Figure 2.1 was connected in series to a known impedance source Z_p, a simple 49 ohm resistor with 1% tolerance, and the unknown PED electrical impedance Z_m, as shown in Figure 2.1. The transient voltage responses V_p and V_m were measured across Z_p with x10 scope probes triggered off of pin 10 of the NAND Gate. The measured PED's were connected to the pulsing circuit and known impedance source using a two-point copper prong holder (bottom of Figure 2.1). To measure Z_m, the digital wave forms of V_p and V_m were collected using a Tektronics Model# TDS2002B oscilloscope at a sample rate (SR) of 4ns per point. The measurements of V_p and V_m were collected using the screen capture setting on the oscilloscope out to 20μs in time.

For each piezoelectric measured, V_p and V_m were padded with zeros to make the signal $3x10^6$ points long in time, and the Fast Fourier Transform (FFT) was taken in MatLab® (Math Works Corporation, Natick, MA). The FFT of transient voltage measurements V_p and V_m provided the frequency domain content of the signals FV_p and FV_m, respectively. The electrical impedance of the unknown PED as a function of frequency FZ_m was determined according to

$$FZ_m = \frac{FV_m \cdot Z_p}{FV_p - FV_m} \qquad (2.1)$$

The resulting complex impedance vector FZ_m was plotted for its magnitude and phase (y-axis), in conjunction with its frequency vector (x-axis). The per-point frequency step for the x-axis f was given by

$$f = \frac{1}{SR \cdot F} \qquad (2.2)$$

where *SR* is the sample rate and *F* is the number of points for which the FFT was taken.

2.3.3 Impedance Measurement Using Network Analyzer

The impedance phase and magnitude plots were collected with an HP 4194 impedance analyzer and saved into a digital text file for comparison with results from section 2.3.2. The PED's were placed in a two-point holder with leads that connected the PED's to the system. The holder was identical to the impulse measurements holder of section 2.3.1, Figure 2.1.

2.3.4 Impedance Data Fitting

The impedance phase and magnitude plots from the data were fit to the simple model for a piezoelectric using IEEE Standards 1988. The basic model consists of an *RLC* circuit in parallel with another capacitor as shown in Figure 2.2. The impedance and admittance functions for a piezoelectric model can also be represented more precisely by a transmission line equivalent circuit [12, 13].

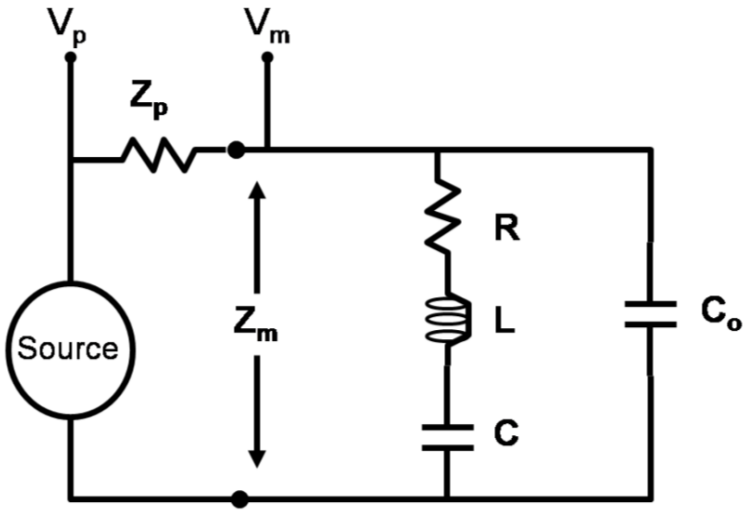

Figure 2.2. Circuit representing a simple model of a piezoelectric and PSpice model

For the circuit shown in Figure 2.2, the relationships among parameters may be determined using Ohm's law and circuit theory. The series resonant frequency for the circuit ω_s is given

$$\omega_s = \frac{1}{\sqrt{L \cdot C}} \qquad (2.3)$$

And the conductance at resonance $G(\omega_s)$ provides the resistance value R for the model according to

$$R = \frac{1}{G(\omega_s)} \qquad (2.4).$$

Manipulating the real and imaginary components of the admittance yields

$$C_o = \frac{B(\omega_s)}{\omega_s} \qquad (2.5)$$

$$\omega_p = \frac{1}{\sqrt{L \cdot C_e}} \qquad (2.6)$$

$$L = \frac{1}{\omega_s^2 \cdot C} \qquad (2.7)$$

Where $B(\omega_s)$ is the maximum value of the susceptance, C_e is the parallel equivalent capacitance of the model and ω_p is the parallel resonant frequency.

Four parameters R, L, C and C_o for the model were estimated using equations 2.4-2.7 and the measured impedance data from the impulse method Fz_m and the network analyzer system. Then a least squares approach was used to fit the model parameters more accurately.

2.3.5 PSpice Model of Impulse Impedance Measurement Method and AC Sweep

Experimental impedance data Fz_m from section 2.3.3 and the model fitting of section 2.3.4 provided the *R, L, C* and C_o parameter values for the simple circuit in Figure 2.2. The corresponding values were then used in a PSpice model (Candence Corporation, San Jose, California) to simulate the impulse method of section 2.3.2, and to perform a standard AC sweep analysis of the circuit. The PSpice model simulated the piezoelectric equivalent circuit shown in Figure 2.2.

For the impulse model the source was defined as a 4 volt 12ns wide pulse with 4ns rise and fall times. Transient analysis was used to simulate the circuit in 0.1ns time steps to 20µs. V_p and V_m were measured in the program and imported into MatLab® for analysis.

The circuit in Figure 2.2 was used in the PSpice AC Sweep analysis. The source was a 4 volt sinusoid that was swept from DC-10MHz in 1kHz increments. The current through Z_p and voltage V_m were measured in the program, and the impedance magnitude and phase were compared with the experimentally measured data.

2.4 Results

2.4.1 Pulsing Circuit Analysis and Performance

Figure 2.3 shows oscilloscope measurements from the pulsing circuit. The green and purple square waves shown in the left side of the Figure were logically combined at pins 10 and 9 of the NAND gate to produce the test signal in yellow at the bottom of the Figure. The signals are shown in more detail on the right side of the Figure where each division corresponds to 10ns.

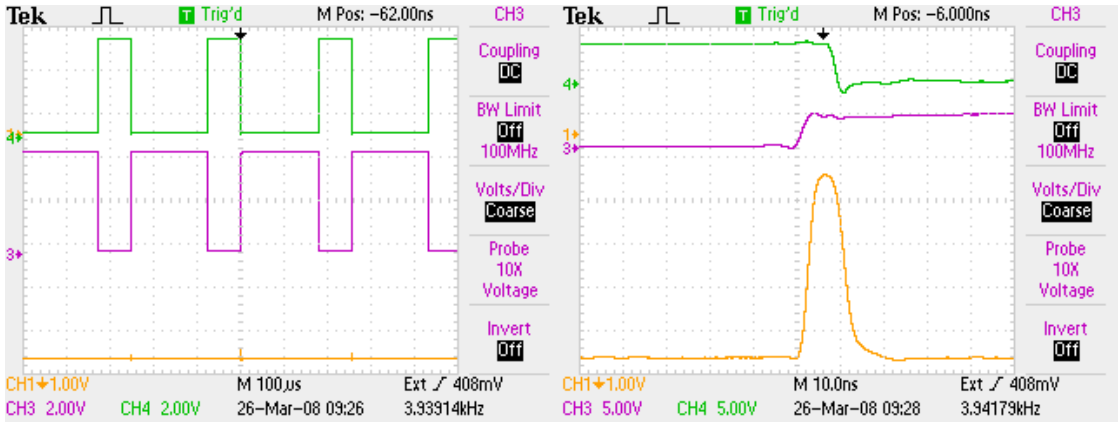

Figure 2.3. Oscilloscope screen capture of a 4kHz Oscillator. The green, purple and yellow curves correspond to the outputs of pin 10, pin 9 and pin 8 of the NAND gates, respectively Left: 100µs per division. Right: 10ns per division.

The high speed NAND Gate produce a stable 12ns wide 4 volt pulse when both green and purple logic signals were "on" as shown in Figure 3.3 on the right. The yellow pulse was the measured output from pin 8 of the NAND Gate. The yellow pulse signal had 5ns rise time and 7ns fall time with minimal ringing around the edges of the signal.

2.4.2 Experimental Analysis of Impedance Measurement Approaches

The following flat disk PED's were tested: a 0.5 inch diameter 5MHz piezoelectric EBL #2 composite, a 0.75 inch diameter 4MHz piezoelectric EBL #1, and a 0.59 inch diameter 2MHz piezoelectric EBL #2 (EBL Products, Hartford, CT). The electrical impedance was measured five times using the impulse approach with a 49 Ohm 1% resistor as Z_p and five times using the network analyzer. Figure 4.4 is a composite of data from the impulse method, the network analyzer and PSpice models. We found good agreement between experimentally measured data for the impulse method (blue line) and network analyzer (blue asterisk) for the three samples. There were no significant variations among measurements using the two techniques. The

impedance calculated from the data and the impedance from the two PSpice models gave similar results for each sample as shown in Figure 2.4. The component values of the piezoelectric equivalent circuit were determined from the PSpice model of the experimental impedance data and compiled in table 2.1. Results for each PED are discussed separately.

5MHz Piezoelectric Composite PZT Disk (Figure 2.4a-b). Figure 2.4a shows the impedance phase measurement obtained from the impulse method, from calculations based on equations 2.3-2.7, from the PSpice model of the impulse measurement, from the PSpice model of an AC sweep and from the network analyzer. The phase shift before resonance occurs at 4.5MHz for the various methods, except for the network analyzer where it occurs at 4MHz. Figure 2.4b shows that the impedance magnitudes determined for the five methods were similar.

4MHz Piezoelectric PZT Disk (Figure 2.4c-d). Figure 2.4c shows the phase shift before resonance is similar for the different methods (4MHz), except that it occurs at a lower frequency (3.7MHz) for the network analyzer. Figure 2.4d shows the impedance magnitudes determined were similar for all five methods, except that the magnitude of the impedance at parallel resonance was greater for the network analyzer (250 Ohm) compared to the other methods (180 Ohm).

2MHz Piezoelectric PZT Disk (Figure 2.4e-f). The phase and impedance plots (2.4e and 2.4f) were similar quantitatively to those obtained for the two other materials, but the data showed small amplitude variations at low frequencies, and through resonance and parallel resonance. The phase shift and resonant frequency were identical for the impulse method and network analyzer (1.98 MHz). This was true for the parallel resonant frequency of 2.2 MHz as well.

Figure 2.4. Impedance phase (on left) and magnitude (on right) plots for five methods and three different piezoelectric materials.
Figure 2.4a-b: 5 MHz 0.5 inch diameter composite piezoelectric impedance plots agree well overall.
The phase shift of the network analyzer around resonance begins at a lower frequency compared to other methods.
Figure 2.44c-d: 4 MHz 0.75 inch diameter piezoelectric impedance plots agree except for the lower frequency phase shift of the network analyzer around resonance compared with the other methods. The network analyzer shows a higher parallel resonant magnitude compared with the other methods.
Figure 2.4e-f: 2 MHz 0.59 inch diameter piezoelectric impedance plots agree well. The phase and magnitude measurements of the network analyzer and impulse method have low amplitude spectral ripples through EIS plots.

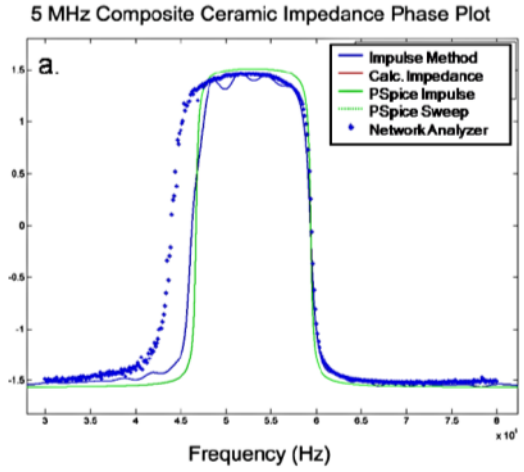
5 MHz Composite Ceramic Impedance Phase Plot
a.
Impulse Method
Calc. Impedance
PSpice Impulse
PSpice Sweep
Network Analyzer
Frequency (Hz)

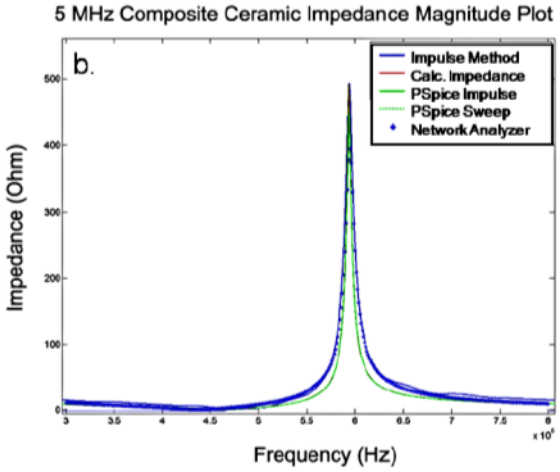
5 MHz Composite Ceramic Impedance Magnitude Plot
b.
Impulse Method
Calc. Impedance
PSpice Impulse
PSpice Sweep
Network Analyzer
Impedance (Ohm)
Frequency (Hz)

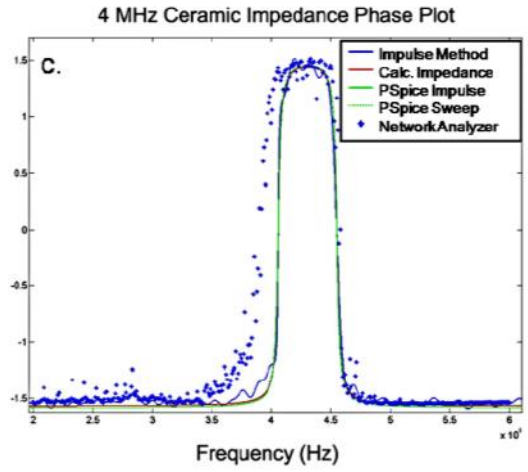
4 MHz Ceramic Impedance Phase Plot
c.
Impulse Method
Calc. Impedance
PSpice Impulse
PSpice Sweep
Network Analyzer
Frequency (Hz)

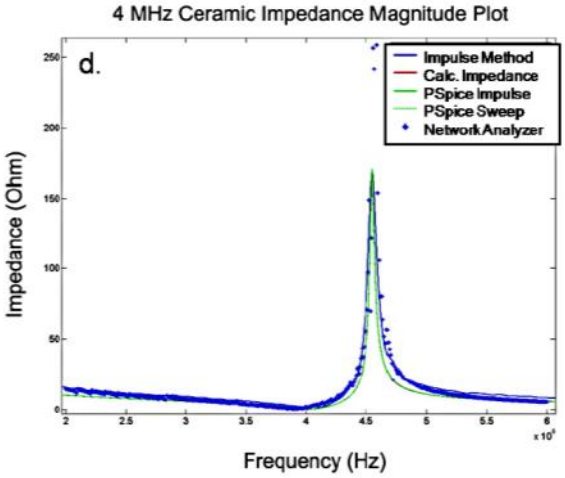
4 MHz Ceramic Impedance Magnitude Plot
d.
Impulse Method
Calc. Impedance
PSpice Impulse
PSpice Sweep
Network Analyzer
Impedance (Ohm)
Frequency (Hz)

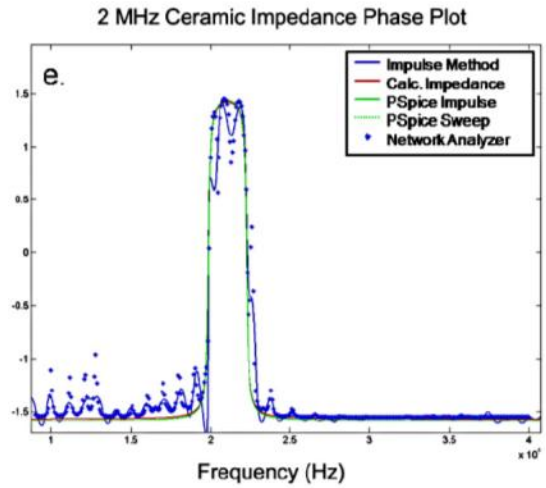
2 MHz Ceramic Impedance Phase Plot
e.
Impulse Method
Calc. Impedance
PSpice Impulse
PSpice Sweep
Network Analyzer
Frequency (Hz)

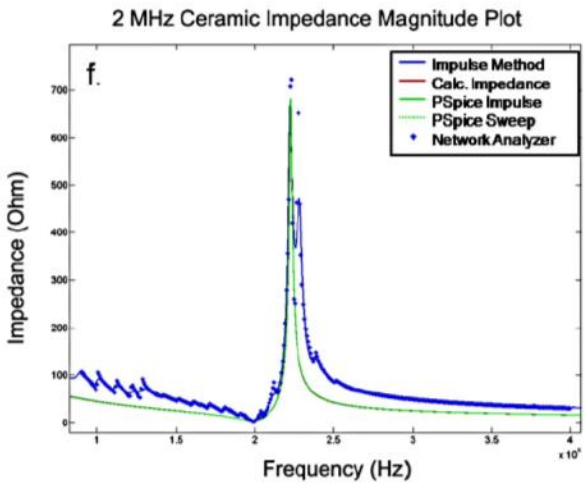
2 MHz Ceramic Impedance Magnitude Plot
f.
Impulse Method
Calc. Impedance
PSpice Impulse
PSpice Sweep
Network Analyzer
Impedance (Ohm)
Frequency (Hz)

Table 2.1. Tabulated model data for piezoelectric materials studied R, L, C and C_O. Also including the resonant and parallel resonant frequencies and impedance magnitudes measured using the impulse and network analyzer methods. The table shows good agreement between the two approaches.

Piezoelectric Material	R	L	C	Co	fs	fp	Magnitue at fs	Magnitue at fp
5 MHz Impulse	0.150 Ohm	0.602 uH	1.93 pF	3.12 pF	4.67 MHz	5.94 MHz	0.15 Ohm	480 Ohm
5 MHz Network Analyzer	0.598 Ohm	0.938 uH	1.36 pF	1.73 pF	4.45 MHZ	5.95 MHz	0.7 Ohm	380 Ohm
4 MHz Impulse	0.203 Ohm	1.00 uH	1.54 pF	5.97 pF	4.06 MHz	4.55 MHz	0.2 Ohm	168 Ohm
4 MHz Network Analyzer	0.170 Ohm	1.00 uH	1.65 pF	4.70 pF	3.92 MHz	4.56 MHz	0.53 Ohm	325 Ohm
2 MHz Impulse	1.06 Ohm	9.36 uH	0.684 pF	2.67pF	1.98 MHz	2.23 MHz	1 Ohm	675 Ohm
2 MHz Network Analyzer	1.06 Ohm	9.35 uH	0.684 pF	2.51 pF	1.99 MHz	2.23 MHz	2 Ohm	720 Ohm

Table 2.1 shows component values for the impedance data determined from the impulse method and network analyzer. Resonant and parallel resonant frequencies f_s and f_p, and magnitudes were similar.

2.5 Discussion

The pulsing circuit comprising the two IC's, four resistors, three capacitors and prototyping board cost ten dollars to build. The simplicity in the design makes it easy to construct in 1 hour. The pulse width can be lengthened or shortened by increasing or decreasing the number of gates through which the signal propagates. The 12ns pulse from the circuit shown in Figure 2.1 provided sufficient bandwidth to measure the impedance of 2-5MHz PED's. A shorter pulse would be required to measure

higher frequency PED's. A longer pulse might be sufficient to measure lower frequency PED's. In practice, we have used the pulsing circuit as presented to perform EIS of ultrasonic probes and piezo-materials with impedance in the range 700kHz to 20MHz.

By applying a voltage pulse into a component with known impedance in series with a PED, and analyzing the transient voltage response across the known component in the frequency domain, we were able to use Ohm's law to accurately measure the impedance magnitude and phase of 2, 4 and 5 MHz piezoelectric disks. The impulse impedance measurement approach agreed well with measurements from a network analyzer system that is often used for these purposes. The resonance and parallel resonance frequencies measured by the approaches were found to be within 5% of each other. The magnitudes of the impedance were also similar, particularly at resonance where the impedance is most important for device design.

Modeling of the impulse measurement method of impedance in PSpice and AC Sweep model agreed closely with the calculated impedance from the piezoelectric equivalent circuit. It was easier to determine the equivalent circuit parameters for the impedance plots using the impulse method, because it provided a high resolution data set (only limited by the length of the recorded signal in time). The network analyzer provided an AC Sweep type of measurement approach for a set 401 points per window. Depending on the characteristics of the PED, the network analyzer may or may not provide enough information to fully characterize the PED.

The network analyzer system was relatively easy to use and provided impedance phase and magnitude curves rapidly. The impulse method required extra time to collect the transient response of the PED and then analyze the signal using the FFT algorithm. The known impedance Z_p in Figure 2.1 may be easily interchanged with a capacitor or PED-equivalent circuit. Using an iterative approach, a simple

known component such as a resistor, as used in this study, maybe refined into a more closely matched impedance to the PED to obtain a more accurate measurement. The approach also has the advantage with the simple circuit: to do signal averaging and to increase the dynamic range of measurement by using a digital scope/acquisition card with higher bit count. Furthermore, the nature of the impulse method may make it particularly suitable in certain applications. For example, to measure the impedance of a transducer in a water tank, the tank must be lined with acoustic absorbing material. Otherwise, reflections from within the tank affect the measured impedance. With the impulse method, data are collected before artifacts from reverberant echoes appear.

2.6 Conclusion

In this chapter a simple pulsing circuit that was used to perform electrical impedance spectroscopy (EIS) with ordinary laboratory instrumentation. The technique is straight forward and useful to laboratories that do not possess a network analyzer or equivalent device. Results showed that, 2, 4 and 5 MHz piezoelectric disk impedance spectra were accurately measured using the impulse impedance approach. The impulse method has been used in our laboratory to measure electrical impedance spectra of ultrasonic transducers and materials from 700kHz-20MHz.

REFERENCES

[1] Schmerr, L., Lopez-Sancheza, A., & Huang, R. (2006). Complete ultrasonic Transducer characterization and its use for models and measurements. *Ultrasonics, 44*(Supplement 1), e753-e775

[2] Kaltenbacher, M., Simkovics, R., Kaltenbacher, B., & Lerch, R. (2001). Determination of piezoelectric material parameters using a combined measurement and simulation technique, *Proc. IEEE Ultrasonics Symp.,* 1023-1026.

[3] Loyaua, V., & Feuillard, G. (2006). Relationship between electrical impedance of a transducer and its electroacoustic behavior: Measurement without primary source, *J. Appl. Phys., 100*(3) 034909.

[4] Maeda, M., Hashimoto, H., & Suzuki, I. (2003). Measurements of complex materials constants of piezoelectrics: extensional vibrational mode of a rectangular bar *J. Phys. D: Appl. Phys., 36*, 176-180.

[5] Kwok, K.., Chan, H., & Choy, C. (1997). Evaluation of the material parameters of piezoelectric materials by various methods. *IEEE Trans. Ultrasonics Ferroelect. Freq. Control., 44*(4), 733-742.

[6] IEEE standard on piezoelectricity *1988 Standards Committee of the IEEE Ultrasonics Ferroelect. Freq. Cont. Soc.*

[7] Lopez-Sanchez, A., & Schmerr, L. (2006). Determination of an ultrasonic transducer's sensitivity and impedance in a pulse-echo setup. *IEEE Trans. Ultrasonics. Ferroelect. Freq. Cont., 53*(11), 2101-2112.

[8] Kim, H., Priya, S., Stephanou, H., & Uchino, K. (2007). Consideration of impedance matching techniques for efficient piezoelectric energy harvesting. *IEEE Trans. Ultrasonics Ferroelect. Freq. Cont., 54*(9), 1851-1859.

[9] Richards, D., Anderson, M., Bahr, D. & Richards, R. (2004). Efficiency of energy conversion for devices containing a piezoelectric component, *J. Micro Mech., Micro Eng., 14*, 717-721.

[10] Agilent Technologies Impedance Measurement Handbook. (2006). Retrieved from the World Wide Web: http://cp.literature.agilent.com/litweb/pdf/5950-3000.pdf

[11] Emeterio, S., Ramos, A., Sanz, P., & Cegarra, M. (2000). Definition and measurement of the normalized electrical impedance of lossy piezoelectric resonators for ultrasonic transducers *Dpto. Señales, Sistemas y Tecnologías Ultrasónicas, Instituto de Acústica (CSIC), 38*(1-8), 140-144.

[12] Mason, W. (1948). Electromechanical transducers and wave filters. New York: Van Nostrand.

[13] Redwood, M., & Lamb, J. (1956). On the measurement of attenuation and ultrasonic delay lines, *Proc. IEEE., 103*(12), 773-780.

CHAPTER 3

DEVELOPMENT OF A PORTABLE THERAPEUTIC AND HIGH INTENSITY ULTRASOUND SYSTEM FOR MILITARY, MEDICAL AND RESEARCH USE[3,4,5,6]

3.1 Abstract

We have developed a portable high power ultrasound system with a very low output impedance amplifier circuit (less than 0.3 Ω) that can transfer more than 90% of the energy from a battery supply to the ultrasound transducer. The system can deliver therapeutic acoustical energy waves at lower voltages than those in conventional ultrasound systems, because energy losses owing to a mismatched impedance are eliminated. The system can produce acoustic power outputs over the therapeutic range (greater then 50 W) from a PZT-4, 1.54 MHz, 0.75 in diameter piezoelectric ceramic. It is lightweight, portable, and powered by a rechargeable battery. The portable therapeutic ultrasound unit has the potential to replace "plug-in" medical systems and RF amplifiers used in research. The system is capable of field service on its internal battery, making it especially useful for military, ambulatory, and remote medical applications.

[3] This work has been published as Lewis, G.K., Jr., Olbricht, W.L. (2008). Development of a portable therapeutic and high intensity ultrasound system for military, medical, and research use Rev. Sci. Instrum. 79, 114302

[4]This work has been published as Lewis, G.K., Jr., Olbricht, W.L. (2008). Development of a portable therapeutic ultrasound system for military, medical and research use. J. Acoust. Soc. Am. 124 2551

[5]This work has been published as Lewis, G.K, Jr., Olbricht, W.L. (2008). Development of a portable therapeutic ultrasound system for military, medical and research use. J. Acoust. Soc. Am. POMA 5 030001

[6] This work has been published as Lewis, G.K., Jr., Olbricht, W.L. (2009). Ultrasound wave generating apparatus. United States PTC Patent Application. PCT/US2009/050297

3.2 Introduction

In the last two decades, researchers and clinicians have shown that therapeutic ultrasound can be an effective tool in relieving arthritis, improving rehabilitation and enhancing wound healing [1-4]. Ultrasound at higher energy has proven useful in surgical applications such as prostate therapy and brain tumor and cardiac tissue ablation [4-7]. Ultrasound may also be useful in improving a variety of drug delivery platforms, including large-molecule transdermal delivery, targeted chemotherapy for brain cancer, and cellular gene transfer [8-11]. In addition, the combination of ultrasound-based imaging with ultrasound-based therapy has potential for important military and medical applications [12-14]. Despite the widespread use of ultrasound, the basic idea in producing ultrasound power has not changed significantly in the past 50 years [6, 13, 15]. Established methods for ultrasound driving systems, such as high voltage switching and RF amplifiers, often require bulky and expensive equipment. Thus, the development of a cost-effective, portable system for delivering ultrasound could greatly enhance the use of ultrasound across a broad range of medical therapies.

In the late 1920's initial studies of the biological effects of ultrasound were performed by Wood and Loomis [16]. Since then, researchers have proposed systems to produce high power ultrasound. In 1942 Lynn et al. introduced an effective 836 kHz high voltage (3000-6000 V) low current (900 mAmp) ultrasound driver for biological research, which was based on vacuum tube technology and radio transmitter design [17]. Since in-house power and very high voltages were used in this design, precautions were taken to avoid electrical shock and RF interference. Lynn's system and power outputs were measured crudely by measuring the rise of a conical oil cone from the radiation force exerted by the focused ultrasound energy. Fry et al. in 1986 presented a focused ultrasound system for tissue volume ablation of brain tumors [18]. The power of the system was supplied by a 990 kHz tuned (impedance matched) 2 kW

amplifier with pre-amplifying circuitry. Lee et al. in 1999 introduced a 64-channel RF driving unit with phase control to produce local hyperthermia *in vitro* and *in vivo* [19]. The amplifier stage of the system used Transistor-Transistor-Logic (TTL) timing with an unspecified in-house built circuit to amplify the drive signal. The 8.0 MHz array Lee et al. developed produced acoustic powers from 0-1 W. Owen et al. in 2003 developed a 12-lb plug-in class D switch-mode amplifier to drive single element high intensity focused ultrasound (HIFU) transducers [15]. The system provided 140 W of acoustic energy from a 70% efficient PZT transducer with 33mm diameter and 55mm radius of curvature. Owen et al. compared the device to products on the market at the time and found their device favorable because of its light weight and ability to cause hemostasis and tissue necrosis.

Commercially available ultrasound drivers and RF amplifiers are generally built with a 50 Ω output impedance that has high voltage amplification and switching of the applied AC signal. To date, many of the developed ultrasound drivers have been impedance matched to enhance power transfer as stated in the maximum power-transfer theorem: *to obtain maximum external power from a source with a finite internal impedance, the impedance of the load must be made the same as that of the source.* The 50 Ω output impedance is matched to the transducer using special impedance-matching circuitry to maximize power transfer and minimize reflections from the ultrasound transducer [6, 13, 15]. From voltage division, the voltage across the transducer is inversely related to the impedance of the source. Therefore, if the source has a 50 Ω output impedance and the transducer has a 10 Ω purly resistive impedance, only 17% of the energy from the source will be supplied to the transducer. The rest will be reflected or lost as heat. When impedance-matching circuitry is used, half of the power from the source is transferred, and the driver becomes more efficient. In matching the characteristic impedance of the driver to the ultrasound

probe, which generally has complex impedance, automatic tuning devices are used that add to the cost and bulk of the system [15].

We have developed a plug-free portable high power ultrasound system with a very low output impedance amplifier circuit (less than 0.3 Ω) that is capable of transferring more than 95% of the voltage from the battery supply to the transducer. Because the output impedance of the drive circuitry and MOSFET switching loss is negligible compared with the ultrasound transducer's impedance, little energy is lost as heat. Furthermore, because the batteries can provide high current, much lower voltages are required to create therapeutic acoustical energy waves than in conventional systems. The system can produce acoustic power outputs over the therapeutic range (greater than 50 W). It is lightweight (under 6 lbs), portable (2 x 6 x 4 in) and powered by a rechargeable battery, which makes it suitable for a variety of military, ambulatory, and field medical applications.

3.3 Methods

The portable therapeutic ultrasound system comprises the low impedance ultrasound driver, accompanying circuitry, and the ultrasound transducer probe. This section describes each part of the apparatus and measurements to determine the power of the device, acoustical driving efficiency, portability and robustness.

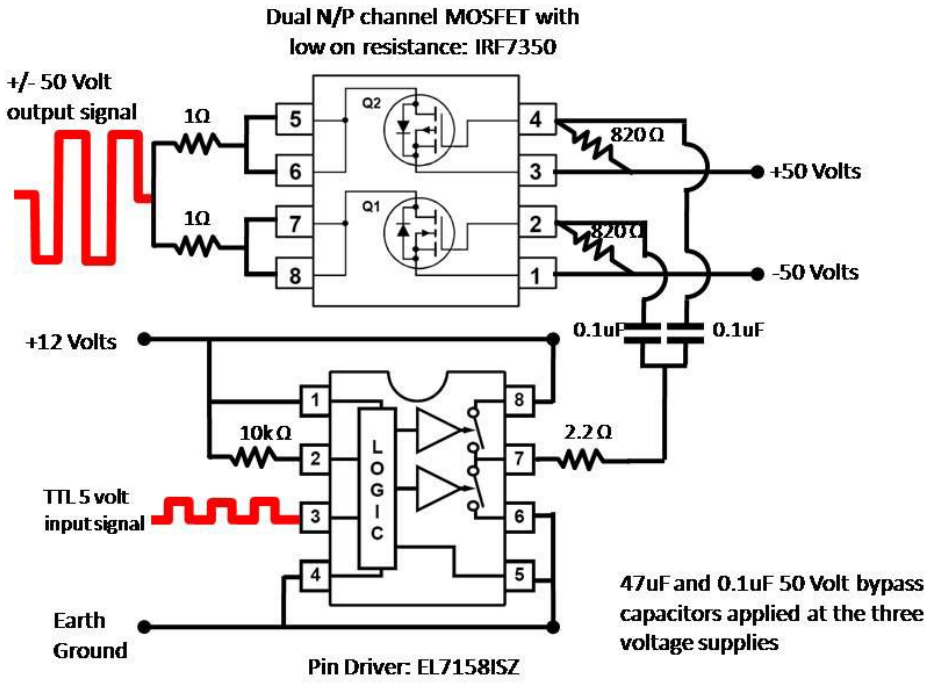

Figure 3.1. Circuit schematic of the low output impedance ultrasound driver. A pin driver is appropriately timed with a TTL 5 volt signal from a 1.54 MHz crystal oscillator that switches the drain of the low output impedance MOSFET from +/- 50 V maximum.

3.3.1 Driving Circuit

The circuit for the low-output-impedance driver is shown in Figure 3.1. A pin driver (EL71581SZ, Intersil Inc.) that is capable of driving high capacitive loads is supplied with a 5 V square wave transistor-transistor logic (TTL) input at pin 3. The input timing signal comes from a 1.54 MHz crystal oscillator (SE1216-ND, Epson Toyocom Inc.) that fits the ultrasound probe's resonant frequency for maximum power transfer. Pins 1 and 8 are held at +12 V with 47 µF and 0.1 µF bypass capacitors to ground. Pin 2 is connected to pin 1 with a 10 kΩ resistor. Pins 4 through 6 are connected to earth ground. Pin 7 of the pin driver is the output that provides a 12 V

square wave to regulate the switching of the MOSFET's voltage drain. From pin 7 of the pin driver a 2.2 Ω resistor splits off with two 0.1 µF coupling capacitors into the input pins 2 and 4 of the low on resistance N/P channel MOSFET (IRF7350, International Rectifier Inc.). Pins 1 and 3 of the MOSFET are held at a maximum of –50V and +50 V, respectively, with 820 Ω resistors across pins 1-2 and 3-4. A 47 µF and a 0.1 µF bypass capacitors to ground are applied as well to pins 1 and 3 of the MOSFET. Pins 5-6 and 7-8 of the MOSFET are tied together and coupled through 1 Ω, 5 W power resistors with the output drive signal applied to the ultrasound transducer through a standard BNC connector.

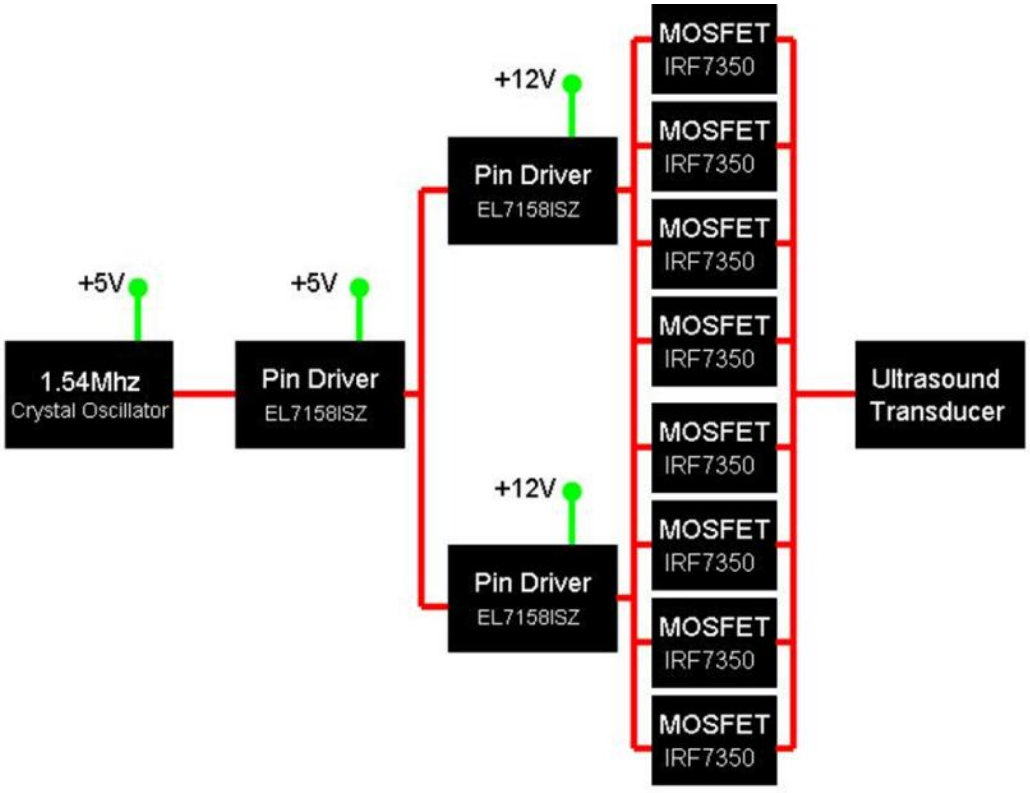

Figure 3.2. Driving circuit used in portable ultrasound system. The working unit of Figure 1 may be applied in parallel stages to reduce the power/heat dissipation in each MOSFET to allow for high current driving to the transducer.

The Intersil Inc. EL7158ISZ pin driver acts as the logic switch for the MOSFETs that supply the power oscillation drive to the ultrasound transducer. For high power continuous wave applications requiring high current, pin drivers are used to switch MOSFETs in parallel to lower the current burden on each MOSFET. As shown in Figure 3.2, a single timed pin driver at 5 V drives two pin drivers at 12 V as a branching cascade to switch four MOSFETs each for the portable high power ultrasound driving system. Each pin driver/MOSFET unit is wired as shown in Figure 3.1. The output impedance of the driver was measured directly, and determined from manufacturer values of the MOSFETs, and eight 1 Ω parallel resistors to be almost entirely resistive and approximately 0.2-0.3 Ω.

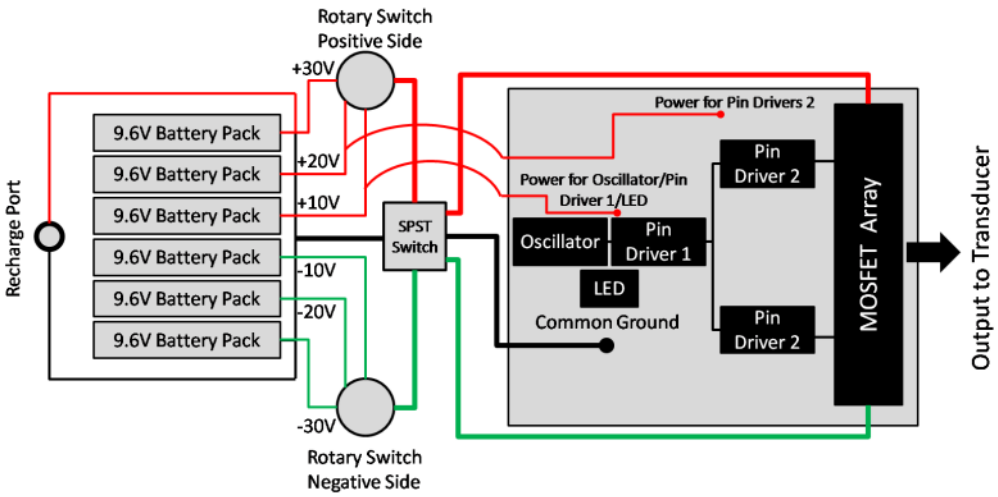

Figure 3.3. Wire layout for portable ultrasound system.

3.3.2 System Design

Figure 3.3 shows a schematic of the complete system, and Figure 3.4 is a photograph of the finished device. Figure 3 is divided into the battery supply and user control portion (left), TTL logic timing signal (middle yellow box), and parallel MOSFET ultrasound driving stage (right red box). The system is housed in a 4 x 6 x

2 in watertight plastic enclosure (#073, Serpac Inc.). The housing holds the circuit (1.5 x 2 x 1 in) and six 9.6 V, 1600 mAh NiCad rechargeable battery packs (#23-432, Radio Shack Inc.) tied together in series through two single draw rotary switches. The user can adjust power delivery to the transducer through the MOSFETs in 9.6 V increments over the range ±28.8 V.

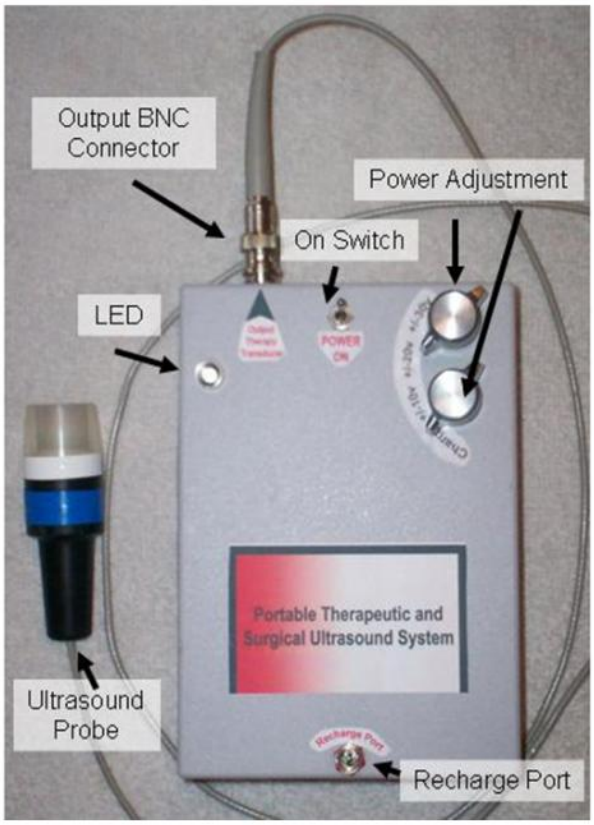

Figure 3.4. Portable therapeutic ultrasound system with 1.54 MHz ultrasonic probe. The unit is 4 x 6 x 2 in and weighs 5.5 lbs.

A blue "on" LED is tied into the on/off switch that supplies power to the crystal oscillator and pin driver through 5 V and 12 V 1 amp voltage regulators that also have bypass capacitors. The output of the device is terminated in a male BNC connector on the front panel. A battery recharge port at the back of the system is

wired to charge the six battery packs in series. To charge the system, the device is switched to the off position and the rotary switches are moved to a non-connected terminal as labeled on the devices panel. A parts list for the device is tabulated in appendix 3.1

3.3.3 Ultrasonic Probe

The ultrasound probe is constructed from lead zirconate titanate (PZT-4), 1.54 MHz, 0.75 in diameter piezoelectric ceramic with a radius of curvature of 1.5 in (EBL Products Inc.). The ceramic (air-backed) is housed in a PVC ergonomic plastic assembly that was built in-house on a micro lathe and milling system (Sherline Products Inc). The clear acrylic front of the transducer acts as a protective cover to the ceramic and an in-plane focal alignment standoff for the ultrasound energy. The probe is wired with 22 gauge coaxial cable terminated with a female BNC connector. The electrical impedance of the ultrasound probe was measured using commonly known methods (Figure 3.5), to determine the resonant frequency for high power driving efficiency [20].

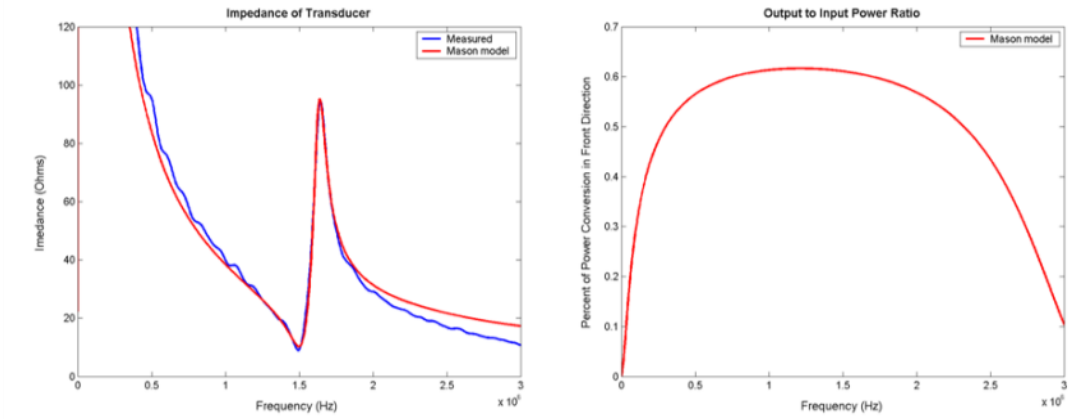

Figure 3.5. Left: Measured impedance and results from a Mason Model of transmission lines. Right: Calculated acoustic conversion efficiency from the Mason Model.

3.3.4 Measurements and Characterization

The output waveform and power spectrum of the device were collected using a Tektronics Model TDS2002B oscilloscope with the ultrasound probe attached and placed in an acoustically insulated water bath. The output impedance, resistance and reactance of the device were measured by attaching a 12Ω power resistor across the output of the device and measuring the phase and voltage changes across the component. The ultrasonic power output was determined with a force balance technique in which we measured the force that the ultrasound exerted on an acoustic absorbing object [21]. We compared these results to electrical measurements of power, using the electrical properties of the probe and a measured ultrasonic power conversion efficiency [22]. Battery life was determined for various output powers. The device was tested with other ultrasonic probes by interchanging the 1.54 MHz crystal oscillator with a function generator. The system was run with 1.7, 2.2 and 7.5 MHz transducers, and the output wave form was measured.

3.4 Results

The waveform of the device output and power spectrum at the 19.2 V_{pp}-V_{pp} battery setting are shown in Figures 3.6a and 3.6b. Figure 3.6c is the measured output waveform from the device while connected to a function generator driving a 7.5MHz probe under equivalent power application. Slight ringing at the corners of the 1.54MHz waveform is shown in Figure 3.6a; however, the driving signal is reasonably clean with no oscillations in the waveform and fast rise times between the push-pull cycles. The power spectrum, shown in Figure 3.6b, of the signal in Figure 3.6a is representative of a typical square-wave drive signal with corner signal spikes. Figure 3.6b shows the drive signals energy concentration is in the early megahertz frequencies. Figure 3.6c shows that the amplitude of the driver is attenuated for the

higher frequency of 7.5MHz. Furthermore, the waveform is asymmetric and exhibits small oscillations for positive and negative sides. When the TTL timing frequency is increased into the 10MHz range, the MOSFETS saturate and are unable to switch/operate at these speeds. The output resistance and reactance of the device was measured to be less than 0.3 Ω and almost entirely real with no measurable phase shift.

The electrical impedance for the ultrasound transducer probe of 12 Ω and an acoustic conversion efficiency of 63% at 1.54 MHz were obtained from the data shown in Figure 3.5, and used to determine power from the voltage measurement across the transducer. The ultrasonic power was measured at each power setting and results are shown in Table 3.1. The force balance approach gave slightly higher acoustic power values compared with the electrical power measurements. Acoustic output powers ranged from 5.77 to 51.4 W, with a maximum difference of 23% between the two power measurement methods.

The battery life at each power setting for sustained power output after full charge is also tabulated in Table 3.1. Maximum system life was for 1.7 hr at 5 to 6 W of acoustic energy. At the maximum acoustic energy setting, battery life decreased to 0.7 hr.

The portability of the system compares well with that of commercially available therapeutic systems. Clinical therapeutic systems such as the Therasound® medical instrumentation line from Rich Mar Inc. provide a maximum of 4 W of acoustical energy to the patient. These systems are comparable in size (7 x 7 x 6 in) and in weight (5 to 6 lb) to our system, but they require AC power. For applications at these low power levels, our system could be made considerably smaller, since most of the mass is the battery pack. For high power applications such as HIFU used in ultrasound surgery, our system is much smaller and lighter than typical RF amplifiers

(usually 12 x 24 x 7 in and 20 lb). Since ultrasound power levels for most surgical applications range from 40 to 60 W, the portable system satisfies current requirements. The system described here may not be able to deliver, at least on batteries, the higher power levels used in some research applications. However, according to the manufacturer's data, the circuitry in the device can provide 100 V peak to peak. At this voltage, our acoustic efficiency model estimates the device would produce an ultrasonic power of 130 W, which is similar to other proposed and bulkier systems.

Adapting the circuitry for other ultrasonic transducers was straightforward. The function generator that replaced the crystal oscillator drove 1.7, 2.2 and 7.5 MHz PZT-4 focused transducers at powers that produced cavitation and levitation when submerged in degassed water as shown if Figure 3.7. With the 7.5 MHz transducer, the MOSFETs began to heat to damage after 2 min at continuous full power. This was not surprising in view of the probe's low electrical impedance (4 Ω), a current draw of 7.5 A and greater MOSFET switching losses at the higher freqency. Thus, operating the 7.5 MHz probe continuously would require additional MOSFETs in parallel or the use of heat sinks to disipate thermal energy.

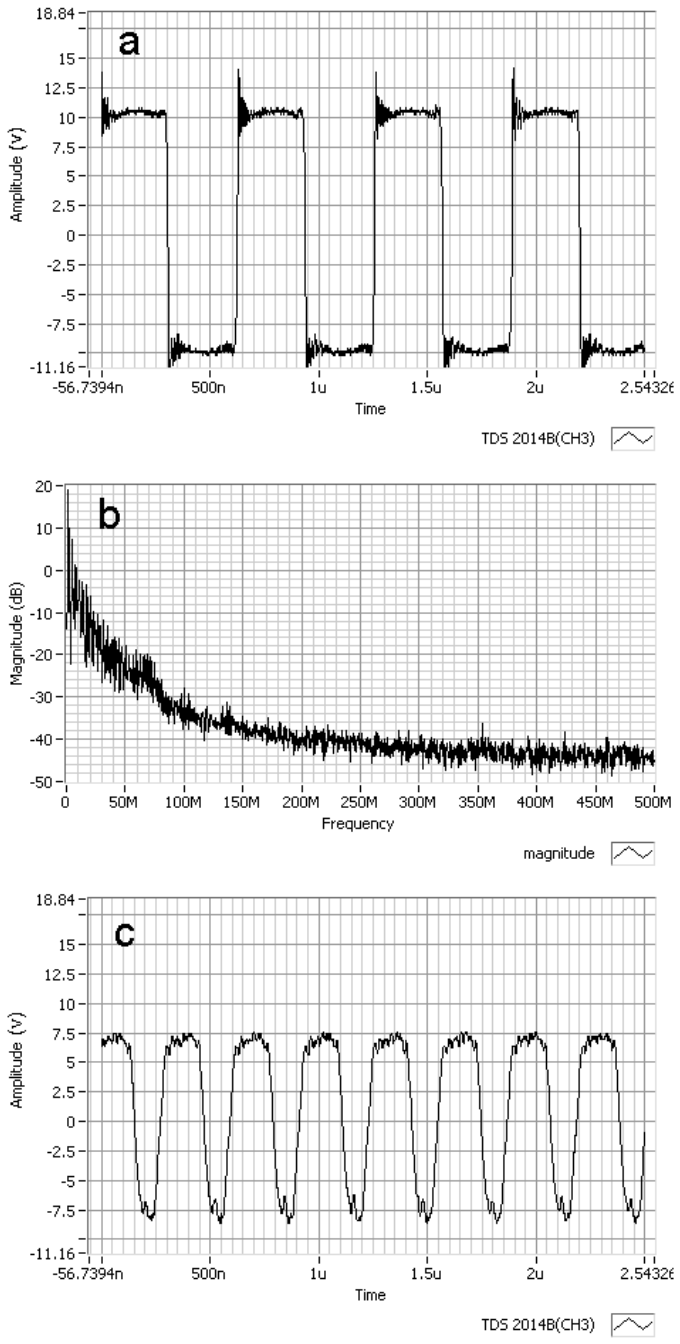

Figure 3.6. (a) Measured 1.54MHz output waveform from the device with slight ringing at the corners. The driving signal is mostly clean with no oscillations in the waveform and fast rise times between the push-pull cycles. (b) The power spectrum of the 1.54 MHz waveform. The drive signals energy concentration is in the early megahertz frequencies. (c) Measured while the timing signal came from a function generator, the higher frequency of 7.5MHz lead to attenuated drive voltage and asymmetry of the waveform with oscillations on both the positive and negative sides.

Table 3.1. Acoustic power measurements and battery life

Voltage Setting Vpp-Vpp (volts)	19.2	28.8	38.4	48.0	57.6
Force Balance (watts)	6.28	10.5	23.5	43.4	55.8
Electrical Measurement (watts)	5.25	11.8	21.0	32.8	47.3
Power Average (watts)	5.77	11.5	22.5	38.1	51.4
System Battery Life (hours)	1.7	1.2	1.0	0.8	0.7

Figure 3.7. 1.54 MHz ultrasound transducer levitating and cavitating water at full system power

3.5 Conclusions

The portable therapeutic ultrasound system drives an ultrasound transducer with a very low output impedance AC source, so that power from the supply is efficiently transferred to the device. The device can operate in the range of 1 to 10

MHz, which spans the relevant range for medical therapeutic ultrasound and HIFU systems.

The ultrasound driving circuit has an output impedance of 0.3 Ω and provides switching of ±28.8 V. The device can provide more than 50 W of acoustic energy from the 1.54 MHz transducer using no impedance tuning. Because the device consists of multiple battery packs, voltage regulators were wired to the nearest battery level to reduce energy waste. Combining the LED on-light, the heating of MOSFETs, voltage regulators and resistors, along with a back calculation of the acoustic output energy measured, we calculated an energy waste of less than 10% from thermal heating. The device is much smaller and lighter than commercially available systems, and costs only $150.00, of which 80% was battery costs.

REFERENCES

[1] Wu, J. & Nyborg, W. L. M. (2006). *Emerging Therapeutic Ultrasound.* Hackensack, New Jersey: World Scientific Publishing Co.

[2] Aus, G. (2006). Current status of HIFU and cryotherapy in prostate cancer: A review. *Eur. Urol., 50*(5), 927–934.

[3] Mitragotri, S. (2005). Healing sound: The use of ultrasound in drug delivery and other therapeutic applications. *Nat. Rev. Drug Discov., 4*, 255–260.

[4] Bailey, M. R., Khokhlova, V. A., Sapozhnikov, O. A., Kargl, S. G., & Crum, L. A. (2003). Physical mechanisms of the therapeutic effect of ultrasound (a review). *Acoust. Phys., 49*(4), 369-388.

[5] ter Haar, G. & Coussios, C.C. (2007). HIFU: Physical principles and devices. *Int. J. Hypertherm., 23*(2), 89-104.

[6] Vykhodtseva, N.I., Hynynen, K., & Damianou, C. (1995). Histologic effects of high intensity pulsed ultrasound exposure. *Ultrasound Med. Biol., 21*, 969–979.

[7] D. Cesario et al. (2008). *Contemporary cardiology, atrial fibrillation: From bench to bedside.* Natalie, M., & Jalife, J., (Eds.). Totowa, NJ: Humana Press.

[8] Park, E.J., Jung, K.I., & Yoon, S.W. (2005). Acoustic mechanisms as an enhancer for transdermal drug delivery. *J. Acoust. Soc. Am., 107,* 2788.

[9] Lewis Jr., G.K., Olbricht, W.L., & Lewis, G.K. (2008). Acoustic enhanced Evans blue dye in neurological tissues. *J. Acoust. Soc. Am. POMA.*

[10] Lewis Jr., G.K., Wang., P., Lewis, G.K., & Olbricht, W.L. (2008). Therapeutic ultrasound enhancement of drug delivery to soft tissues. *8th. Int. Sym. Ther. Ultrasound, AIP conf. Proc., 1113, 403-407.*

[11] Newman, C.M.H., & Bettinger, T. (2007). Gene therapy progress and prospects: Ultrasound for gene transfer. *Gene Therapy, 14,* 465–475.

[12] Lizzi, F. L., Coleman, D. J., Driller, J., Silverman, R., Lucas, B. and Rosado, A. (1986). A therapeutic ultrasound system incorporating real-time ultrasonic scanning. *Proc. 1986 IEEE Ultrasound. Symp.,* 981-984.

[13] Vaezy, S., Shi, X., Martin, R.W., Chi, E., Nelson, P.I., Bailey, M.R., & Crum, L.A. (2001). Real-time visualization of high-intensity focused ultrasound treatment using ultrasound imaging. *Ultrasound Med. Biol., 27,* 33–42.

[14] Crum, L.A. (2007). Smart therapeutic ultrasound device for mission-critical medical care. Project report. *NASA.*

[15] Owen, N.R., Bailey, M.R., Mortimer, B.J.P., Kolve, H., Hossack, J. & Crum, L.A. (2003). Development of power supplies for portable HIFU therapy systems. *Proc. 3rd Int. Symp. Ther. Ultrasound*, 399–404.

[16] Wood, R.W., & Loomis, A. (1927). The physical and biological effects of high frequency sound waves of great intensity. *Phil. Mag., 4*, 417-436.

[17] Lynn, J.G., Zwemer, R.L., Chick, A.J., & Miller, A.E. (1942). A new method for the generation and use of focused ultrasound in experimental biology. *J. Gen. Phys., 26*, 179-193.

[18] Fry, F. J., Sanghvi, N. T., Morris, R. F., Smithson, S., Atkinson, L., Dines, K., Franklin, T., & Hastings, J. (1986). A focused ultrasound system for tissue volume ablation in deep seated brain sites. *Proc. IEEE Ultrason. Symp.*,1001–1004.

[19] Lee, R. J., Buchanan, M., Kleine, L. J., & Hynynen, K. (1999). Arrays of multielement ultrasound applicators for interstitial hyperthermia. *IEEE Trans. Biomed. Eng., 46*(7), 880-890.

[20] Lewis Jr., G.K., Lewis Sr., G.K., Olbricht, W.L., (2008). Cost effective broad-band electrical impedance spectroscopy measurement circuit and signal analysis of piezo-matrials and ultrasound transducers. *Meas. Sci. Technol., 19*, 1-7.

[21] Maruvada, S., Harris, G. R., Herman, B. A., King, R.L. (2007). Acoustic power calibration of high-intensity focused ultrasound transducers using a radiation force technique. *J. Acoust. Soc. Am.*, *121*(3), 1434-1439.

[22] Redwood, M., & Lamb, J. (1956). On the measurement of attenuation in ultrasonic delay lines. *Proc. IEEE*, *103*(12), 773-780.

CHAPTER 4

DESIGN AND CHARACTERIZATION OF A HIGH-POWER ULTRASOUND DRIVER WITH ULTRALOW-OUTPUT IMPEDANCE[7,8]

4.1 Abstract

We describe a pocket-sized ultrasound driver with an ultralow output impedance amplifier circuit (less than 0.05 Ω) that can transfer more than 99% of the voltage from a power supply to the ultrasound transducer with minimal reflections. The device produces high-power acoustical energy waves while operating at lower voltages than conventional ultrasound driving systems because energy losses owing to mismatched impedance are minimized. The peak performance of the driver is measured experimentally with a PZT-4, 1.54 MHz, piezoelectric ceramic and modeled using an adjusted Mason model over a range of transducer resonant frequencies. The ultrasound driver can deliver a 100 V_{pp} (peak to peak) square-wave signal across 0-8 MHz ultrasound transducers in 5 ms bursts through continuous wave operation, producing acoustic powers exceeding 130 W. Effects of frequency, output impedance of the driver, and input impedance of the transducer on the maximum acoustic output power of piezoelectric transducers are examined. The small size, high-power and efficiency of the ultrasound driver makes this technology useful for research, medical and industrial ultrasonic applications.

[7]This work has been published as Lewis, G.K., Jr., Olbricht, W.L. (2009). Design and characterization of a high-power ultrasound driver with ultralow-output impedance. Rev. Sci. Instrum. 80, 114704

[8]This work has been published as Lewis, G.K., Jr., Olbricht, W.L. (2009). Ultrasound wave generating apparatus. United States PTC Patent Application. PCT/US2009/050297

4.2 Introduction

We present a new amplifier design and printed circuit board schematic for an efficient ultrasound driver that can be incorporated easily into acoustic applications in science and engineering. The principle underlying the driver design is based on earlier work that used a low output impedance driver in a portable high intensity focused ultrasound (HIFU) system [1] and in appendix 4.2. Here, we analyze an ultralow output impedance driver that delivers high current bursts, continuous wave and frequency sweep operation for single element, phased-array, and time-reversal acoustic applications.

Ultrasound has had decades of great success as a diagnostic imaging modality, but in recent years studies have shown that the application of ultrasound can be an effective therapy or enhance existing therapies in a variety of clinical applications [2-5]. For example, ultrasound has been used to lyse blood clots and to improve the action of thrombolytic agents [5]. It has been used to temporarily break down the blood-brain barrier, to enhance the delivery of anti-tumor agents and other drugs, to occlude blood vessels, to cauterize wounds, and to enhance wound healing [5-9]. Furthermore, high-intensity focused ultrasound potentially offers a new way to perform ablative surgery on a variety of organs including heart, liver, prostate, and brain [10-12]. The acoustic power that is required varies among applications. Some applications require relatively low power levels for acoustic streaming and agitation effects [2,4]. Other applications require high power levels, and in these cases tissue heating and acoustic cavitation are dominant effects [5, 13-15].

Despite the potential of ultrasound-based therapies, their translation and clinical implementation has been limited in part by the lack of cost-effective and convenient ways of generating ultrasound over a wide range of power levels [1]. The basic method of producing ultrasound power has not changed significantly in 50 years

[11, 16, 17]. Most ultrasound driving systems are based on high-voltage switching devices or RF amplifiers that are customarily built with a 50 Ω output impedance. The 50 Ω output impedance is a historical standard based on the development in the 1930s of coax cables for kilowatt radio transmitters [18]. The 50 Ω impedance was chosen as a compromise between power handling and low loss in air-dielectric coax transmission cable. The 50 Ω output impedance was subsequently used in laboratory electronic devices, and it is now an accepted standard for function generators, oscilloscopes, rf amplifiers, pulse generators and other electronic instruments.

A consequence of this standard is that the output impedance of conventional ultrasound drivers does not match the characteristic electrical impedance of typical ultrasound transducers. The maximum power-transfer theorem states: *to obtain maximum external power from a source with finite internal impedance, the impedance of the load must be made the same as that of the source.* Therefore, the output impedance of the ultrasound driver is matched to that of the transducer using special impedance-matching circuitry and automatic tuning devices [11, 16, 17]. Even then, only 50% of the amplifier's voltage is delivered across the transducer with the other 50% dissipated as heat.

Taking a different approach, we have developed a low voltage, high power 0-8 MHz ultrasound driver with an ultralow output impedance amplifier circuit (less than 0.05 Ω) that can transfer more than 99% of the voltage from the power supply to the transducer. It produces acoustical energy waves at lower voltages than those in conventional ultrasound drivers, since energy losses owing to mismatched impedance are eliminated. Since impedance matching circuitry is not required, the driver and printed circuit board (PCB) can be built for about $100. Acoustic energy production from the driver was measured experimentally and modeled mathematically using an adjusted Mason model over a range of transducer frequencies [19, 20]. The

performance of the driver with transducers connected directly to the driver's output was compared with its performance when traditional impedance matching was used. Results show that the ultrasound driver can deliver 100 V_{pp} square-wave signal across 0-8MHz ultrasound transducers with pulsed current draws in excess of 10 A. Modeling and experimental measurements show that maximum acoustic output power depends on the impedance of the ultrasound transducer and the output impedance of the ultrasound driver.

4.3 Methods

This section describes the ultrasound driver circuit, printed circuit board (PCB) design and construction, modeling and measurements of acoustic energy production, and an evaluation of driver performance with and without impedance matching to the transducer. Component specifications and part numbers are listed in appendix 4.2.

4.3.1 Circuit Schematic

The design of the ultralow-impedance, high-current, transistor-transistor logic (TTL) ultrasound driver builds on principles that were demonstrated in a simple prototype [1]. The prototype used 8 MOSFETs in parallel to deliver 50 W continuously without excessive heating of the MOSFETs. The present design uses additional MOSFETs to reduce the current through each MOSFET and to reduce the output impedance of the driver, which increases output power, provided there are no limitations from the power source.

Figure 4.1 is a schematic of the driver, which uses 14 MOSFETs in parallel to generate the driver output. A branched tree of pin drivers provides signals to the MOSFETs so that they switch synchronously. Each pin driver and MOSFET in Figure

4.1 is analogous to the pin driver and MOSFET used in the prototype, except that a single pin driver switches multiple MOSFETs in the present arrangement.

The first pin driver (EL71881SZ), shown at the left in Figure 4.1, is capable of driving high capacitive loads. A 5-10 V square wave from a crystal oscillator or function generator is supplied to pin 3 of the pin driver. Pins 1 and 8 are held at +5 V with 10 µF and 0.1 µF bypass capacitors to ground (not shown in Figure 4.1). Pin 2 is connected to pin 1 with a 10 kΩ resistor. Pins 4 through 6 are connected to earth ground. The output from pin 7 provides a 5 V square wave to drive the second generation of pin drivers. These pin drivers provide a 5 V square wave to the third generation of pin drivers, which regulate switching of the MOSFET's voltage drain. These four pin drivers are held at +12 V instead of +5 V because +12 V is the optimal voltage for MOSFET switching. The outputs of these pin drivers are split with two 0.1 µF coupling capacitors into the input pins 2 and 4 of the low on resistance N/P channel MOSFET (IRF7350, International Rectifier Inc.). Pins 1 and 3 of the MOSFET are held at a maximum of -50V and +50 V, respectively, with 820 Ω resistors across pins 1-2 and 3-4. A 10 µF bypass capacitor to ground is applied as well to pins 1 and 3 of the MOSFET (not shown in Figure 4.1). Pins 5-8 of the MOSFET are tied together and connected to the output drive signal through a standard BNC connector. The output impedance of ultrasound driver is determined from manufacturer's values of the MOSFETs. Measurements show it is almost entirely resistive and between 0.01 and 0.05 Ω. The input capacitance of the P- and N- Channel MOSFETs in parallel is 5.18 nF.

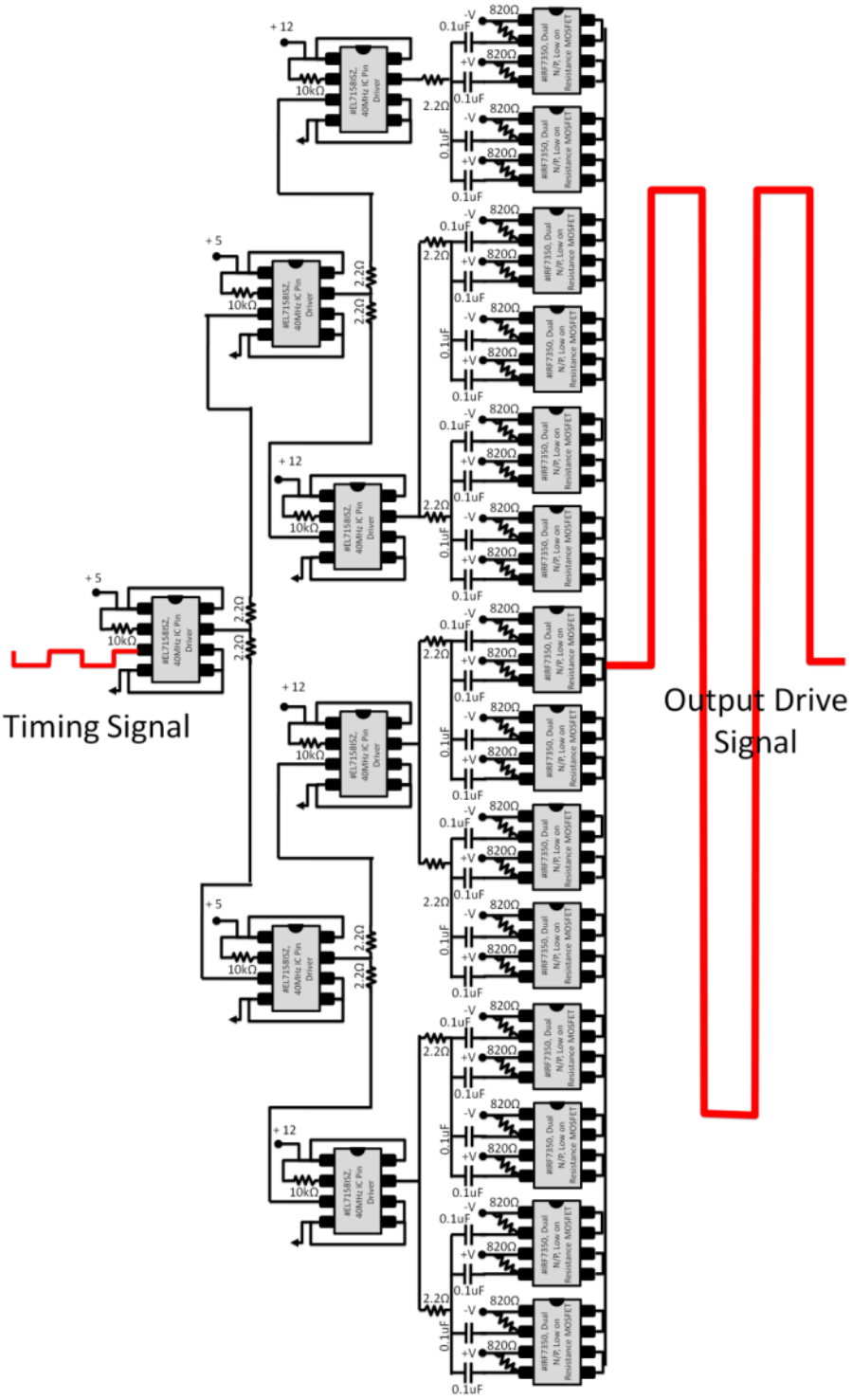

Figure 4.1. Schematic of the ultrasound driver. A TTL timed pin driver is used as a branching cascade to switch 14 low output impedance MOSFETs.

4.3.2 PCB Design and Construction

The PCB for the ultrasound driver is shown in Figure 4.2 where components are outlined in white and their respective values are given in black. The PCB design is created using PCB123® Layout V2 software from Sunstone Circuits Inc.

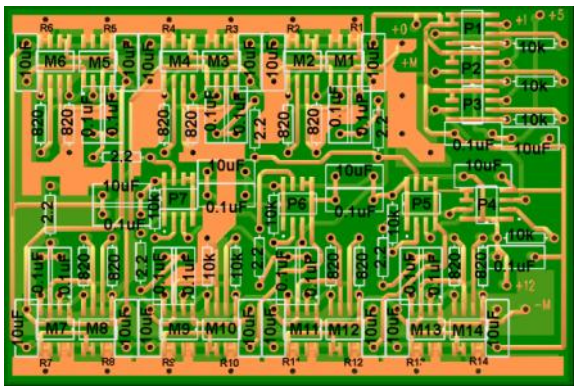

Figure 4.2. PCB layout for the ultralow output impedance ultrasound driver (2 x 3 in). Components are shown in white with corresponding values in black text. Extra copper visible on the output of components M1-M14 is used for thermal dissipation and balancing.

Pin-drivers P1 through P7 and MOSFETs M1 through M14 are soldered to the board using an iron at 700ºC. The remaining components, except for the 10µF bypass capacitors in-line with the MOSFETs, are added in the same way. If electrolytic capacitors are used, they must be installed with correct polarity. Heat sinks (3-050305U, Cool Innovations Inc.) with dimensions 4 x 7 x 5 mm are attached to pairs of adjacent MOSFETS with thermally conductive Locktight® expoxy (234476, Henkel) and activator (2301787387, Henkel). Thermal epoxy is applied to the bottom of the heat sinks, and activator is applied to the top surface of the MOSFETs. The heat sink and MOSFET are pressed together for 2 min. The in-line 10uF bypass capacitors are then soldered in place. MOSFETs M1 through M6 are in parallel on the PCB as are MOSFETs M7 through M14. To make the entire array parallel, three 22

gauge copper wires are attached between vias R6 and R7, R5 and R8, and R4 and R9. The positive output from the driver at R14 and a ground point on the PCB are connected with a BNC connector.

Pin-drivers P1 through P3 are powered at +5 V, and P4 through P7 are powered at +12 V. The input timing signal for the amplifier is supplied to the via marked +I in the top right of Figure 4.2. The timing signal may be supplied by a crystal oscillator or function generator. The MOSFET switching supply is marked as holes +M and –M in Figure 4.2. The voltages supplied to +M and –M determine the output voltage range of the MOSFETs. The digital PCB file may be obtained from the authors on request.

4.3.3 Driver Modeling

A Mason two T-port lossy transmission model adapted from Redwood [19] and shown in Figure 4.3 is used to characterize the electrical properties of the amplifier and piezoelectric transducers. The amplifier is a push-pull amplifier with output impedance R_{source}. The acoustic energy emitted by the transducer is conducted through a water path. The frequency responses of the transducer and the water path are represented as two T-port models. Each model is composed of transcendental periodic functions of frequency that are chosen to be consistent with reflections of acoustic energy at intervals corresponding to the time required for signals to travel back and forth along the length of the acoustic path.

Starting from the output of the amplifier at R_{source}, the model consists of a clamped capacitance of the piezoelectric material C_o.

$$C_o = \frac{\varepsilon_{33}^{\ s} \cdot A}{T_{pm}} \qquad (4.1)$$

where ε_{33}^{S} is the clamped dielectric constant for the material, T_{pm} is the thickness of the piezoelectric material (m), and A is the radiating area of the piezoelectric element (m^2). C_o is placed in parallel to the transformer Φ in the model that converts the voltage into a mechanical pressure:

$$\phi = k_t \cdot v_{pm} \cdot C_o \cdot \sqrt{\frac{\rho_{pm}}{\varepsilon_{33}^{s}}} \qquad (4.2)$$

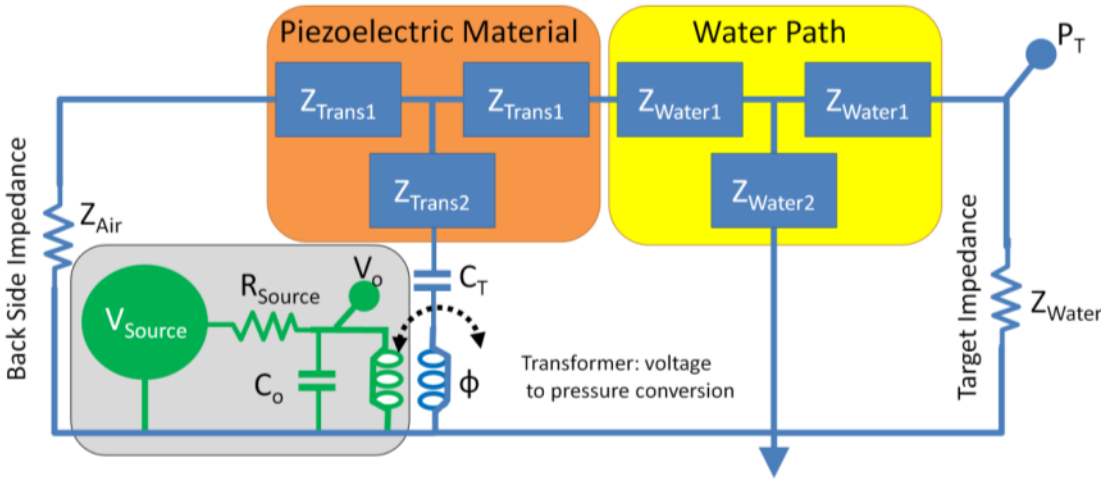

Figure 4.3. Mason model to study the effect of ultralow output impedance ultrasound driver in maximum power driving frequency. Amplifier output resistance R_s is varied in this model from 0.03-200 Ω, and the piezoelectric material is modeled as PZT-4 1.5 MHz and 8.0 MHz transducers. The piezoelectric material and water path are considered two port lossy transmission lines. The transformer converts electrical energy into pressure for the transducer conversion.

where k_t is the thickness coupling coefficient for the material, v_{pm} is the velocity of sound in the piezoelectric material (m/sec^2) and ρ_{pm} is the density of the piezoelectric material (kg/m^3).

The transformer Φ in series with negative capacitance C_T, represents the pressure output of the piezoelectric transducer, as in Redwood [19] where $C_T = -C_o / \phi^2$.

The piezoelectric material T-port model shown in Figure 4.3 is modeled as

$$Z_{Trans1} = Z_{pm} \cdot \tanh\left[\frac{\Gamma_{pm}(\omega) \cdot T_{pm}}{2}\right] \qquad (4.3),$$

$$Z_{Trans2} = Z_{pm} \cdot \operatorname{csch}\left[\Gamma_{pm}(\omega) \cdot T_{pm}\right] \qquad (4.4),$$

$$Z_{pm} = A \cdot \rho_{pm} \cdot v_{pm} \qquad (4.5),$$

$$\Gamma_{pm} = \alpha_{pm} + j\beta_{pm} \qquad (4.6),$$

$$\alpha_{pm} = \frac{\beta_{pm}}{2Q_m} \qquad (4.7)$$

And

$$\beta_{pm} = \frac{\omega}{v_{pm}} \qquad (4.8)$$

where Z_{pm} is the characteristic acoustic impedance of the piezoelectric material, Γ_{pm} is the material propagation vector, α_{pm} and β_{pm} are the attenuation coefficients in the material, ω is the radian frequency variable, and Q_m is the mechanical quality factor for the piezoelectric material. Values for the constants used in the model are provided in Table 4.1.

The water path T-port model in Figure 4.3 is modeled as

$$Z_{Water1} = Z_{wm} \cdot \tanh\left[\frac{\Gamma_{wm}(\omega) \cdot T_{wm}}{2}\right] \qquad (4.9)$$

and

$$Z_{Water2} = Z_{wm} \cdot \csc h\left[\Gamma_{wm}(\omega) \cdot T_{wm}\right] \qquad (4.10).$$

The terms for the water path model impedances Z_{Water1} and Z_{Water2} are similar to the transducer material (Equations 4.3-4.8) with similar meanings, however with different constant values as provided in Table 4.1.

Table 4.1. Compiled constant values and units used in the model presented.

	Symbol	**Value**	**Units**
Amplifier Properties			
Voltage Supply	V_{Source}	10	(v)
Output Impedance	R_{Source}	Variable	(Ohm)
Radian frequency variable	ω	Variable	(rads)
Piezoelectric Properties			
Clamped dielectric	ε_{33}^{S}	7.17×10^{-10}	na
Thickness of piezoelectric	T_{pm}	Variable	(m)
Radiating area	A	Variable	(m^2)
Thickness coupling coefficient	k_t	0.42	na
Velocity of sound in the piezoelectric material	v_{pm}	*4420*	(m/s)
Density of the piezoelectric material	ρ_{pm}	*7500*	(kg/m^3)
Mechanical quality factor for material	Q_m	128	na
Water Path Properties			
Velocity of sound in water	v_w	1540	(m/s)
Density of water	ρ_w	1000	(kg/m^3)

The transducer is air-backed, and is included in the model as a small backside impedance Z_{Air} *so* that mechanical energy is reflected in the forward direction toward the water target with its characteristic impedance Z_{water} .The value of Z_{Air} is chosen to match the models prediction of the actual electrical impedance properties of the ultrasound transducer used in this study. For the model Z_{Air} = 0.*38 x* Z_{Water}, where $Z_{Water} = A \cdot \rho_w \cdot v_w$.

From the circuit in Figure 4.3, two node voltages may be defined. By using conventional circuit theory and summing the currents at the two node points, two equations and two unknowns result. These can be related to the input drive voltage in matrix notation. The matrix equation can then be solved for the two unknown quantities, and the input and output power may be determined from an examination of the circuit model. Thus one can write for the output and input powers:

$$PowerOut = \frac{P_T(\omega)^2}{R_{Water}} \qquad (4.11),$$

where P_T is the voltage (or pressure) across R_{Water}, and

$$PowerIn = I_S(\omega) \cdot V_0(\omega) \cdot \cos(\theta) \quad (4.12)$$

where $I_S = (V_S - V_o(\omega))/R_S$ (4.13) and $\theta = angle(V_o) - angle(I_S)$ (4.14).

The efficiency of the amplifier is calculated by

$$Efficiency = \frac{PowerOut(\omega)}{PowerIn(\omega)} \quad (4.\ 15).$$

The Mason model often is used in ultrasonics to help develop transducer front and back matching layers, tune electrical networks, and estimate transducer transmit and receive impedances. Here, we use the model to predict the maximum power output and efficiency of the ultralow output impedance driver and to compare it with

50 Ω and impedance-matched amplifier sources when driving transducers. We varied the amplifier source impedance R_{Source} from 0.03 to 100 Ω and predicted the output power of four different PZT-4 transducers into a water target impedance R_{Water} . The characteristic frequency of the transducer was varied from 1.5 to 8.0 MHz, which simulates variations in the thickness of the piezoelectric transducers. The resonant electrical impedance of the transducer was varied between 0.37 and 10.6 Ω, which simulates variations in the transducer's cross-sectional area. The drive source V_s is taken as 10 V. Parameters for the model transient function constants including Z_{Trans1}, Z_{Trans2}, Z_{Water1}, and Z_{Water2} are compiled in Table 4.1, and were obtained from Redwood [19] and EBL Products Inc. for an air-backed PZT-4 transducer into a water bath target.

4.3.4 Measurements of Low Output Impedance Ultrasound Driver

The amplifier is tested by connecting the input (+I hole) to a function generator (Tektronix #ARG3102) and powering it with multiple adjustable power supplies (Agilent 6613C) for the +5, +12, and +/- MOSFETs power. MOSFET switching power is varied from 10 to 50 V_{pp}. Current drawn from the circuit is measured using the power supply current meter. The amplifier is tested in pulse and continuous wave mode by varying the TTL timing signal input. The output waveform and power spectrum of the driver are collected using an oscilloscope (Tektronics TDS2002B) with a 1.54 MHz lead zirconate titanate (PZT-4) piezoelectric ceramic (EBL Products Inc.). The ceramic is 0.75 in in diameter with a 1.5 in radius of curvature and the 12 Ω electrical impedance is measured by impulse impedance spectroscopy. The ultrasound probe is attached to the output and placed in an acoustically insulated water bath [1]. The drive waveform is also measured with 12 Ω and 50 Ω power resistors in series with the transducer probe to compare impedance matching techniques with the

ultralow output impedance driver. The output impedance, resistance and reactance of the amplifier are measured by attaching a 12Ω power resistor across the output of the amplifier and measuring the phase and voltage changes across the component at drive frequencies from 0 to 8 MHz. The ultrasonic power output from the 1.54 MHz transducer is determined in continuous wave operation by measuring the force that the ultrasound exerts on an acoustic absorbing object [21]. We compare results to electrical measurements of power, using measured electrical impedance properties of the 1.54 MHz probe [22] and the ultrasonic power conversion efficiency from the Mason model [1,19, 20].

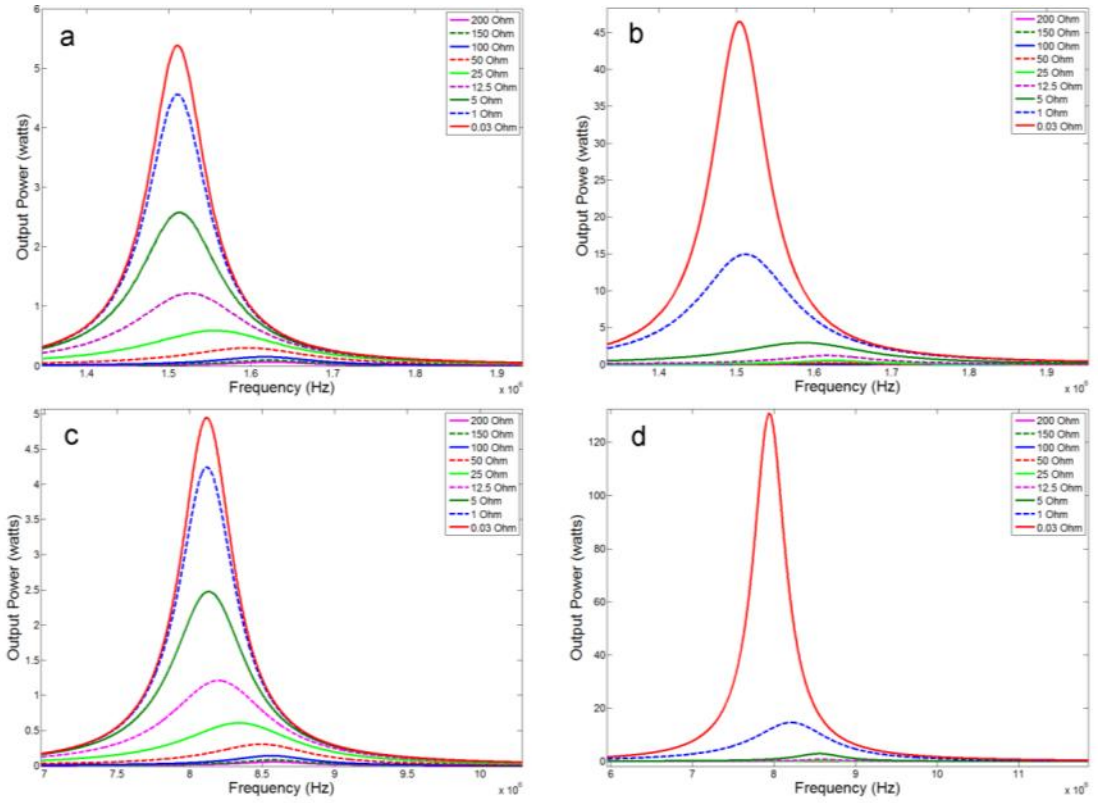

Figure 4.4. Predictions of the model shown in Figure 3. (4a) through (4d) show the maximum output power as a function of frequency for values of the amplifier source impedance R_s in the range 0.03 to 200 Ω . (4a) 1.5 MHz 10.3 Ω transducer. (4b) 1.5 MHz 1.2 Ω transducer. (4c) 8 MHz 10.6 Ω transducer. (4d) 8 MHz 0.37 Ω transducer

4.4 Results

4.4.1 Model Results

The predictions of the Mason model are shown in Figure 4.4. Figures 4.4a through 4d show the computed maximum output power from the transducer as a function of frequency for two transducers. Figure 4a and 4b pertain to a 1.5 MHz transducer with 10.3 Ω and 1.2 Ω resonant electrical impedance, respectively. Figure 4c and 4d pertain to an 8.0 MHz transducer with 10.6 Ω and 0.37 Ω resonant electrical impedance, respectively.

In every case the maximum power delivered to the transducer and, hence, the maximum acoustic energy generated by the device, are obtained for the smallest value of R_{Source}. The maximum acoustic power is determined by the piezoelectric transducer efficiency, which was estimated as 63% from input to output power ratios in the model. The electrical impedance of the piezoelectric also affects the maximum acoustic power according to:

$$PowerOut \approx \frac{V_o^{\,2}}{Z} \qquad (4.16)$$

where *PowerOut* is the acoustic power from the transducer, V_O is the voltage across the transducer and Z is the electrical impedance of the transducer. In this case, increasing the cross-sectional area of the transducer decreases the electrical impedance Z and increases acoustic power. Figure 4 shows that for small R_{Source}, the maximum acoustic power is obtained at the transducer's natural axial resonance frequency. For larger values of R_{Source}, maximum power occurs at frequencies slightly higher than the resonance frequency, especially for the 8.0 MHz transducer.

4.4.2 Ultrasound Diver Performance

The output waveform of the ultralow output impedance ultrasound driver at the 20 V_{pp} power setting is shown for 1.54 and 8 MHz TTL timing signals in Figure 4.5A and 4.5D respectively. Figure 4.5B is the measured output waveform from the driver while connected to a PZT-4, 1.54 MHz, and 0.75 in diameter piezoelectric ceramic used in this and prior studies [1, 7, 8]. Figure 4.5C is the power spectrum measurement from the waveform of Figure 4.5B. The waveform of the 1.54 MHz drive signal (Figure 4.5A and 4.5B) shows slight ringing at the corners without and with the ultrasound transducer attached to the output. Overall, the 1.54 MHz driving signal is reasonably clean with no oscillations in the waveform and fast rise times between the push-pull cycles. No measurable voltage drop or phase shift is noticeable between Figure 4.5A and 4.5B, showing the amplifier design has a very low output resistance and reactance. The power spectrum in Figure 4.5C is representative of a square-wave drive signal with slight corner signal spiking. Figure 4.5D shows that the amplitude of the driver is attenuated by approximately 20% for the higher frequency of 8 MHz.

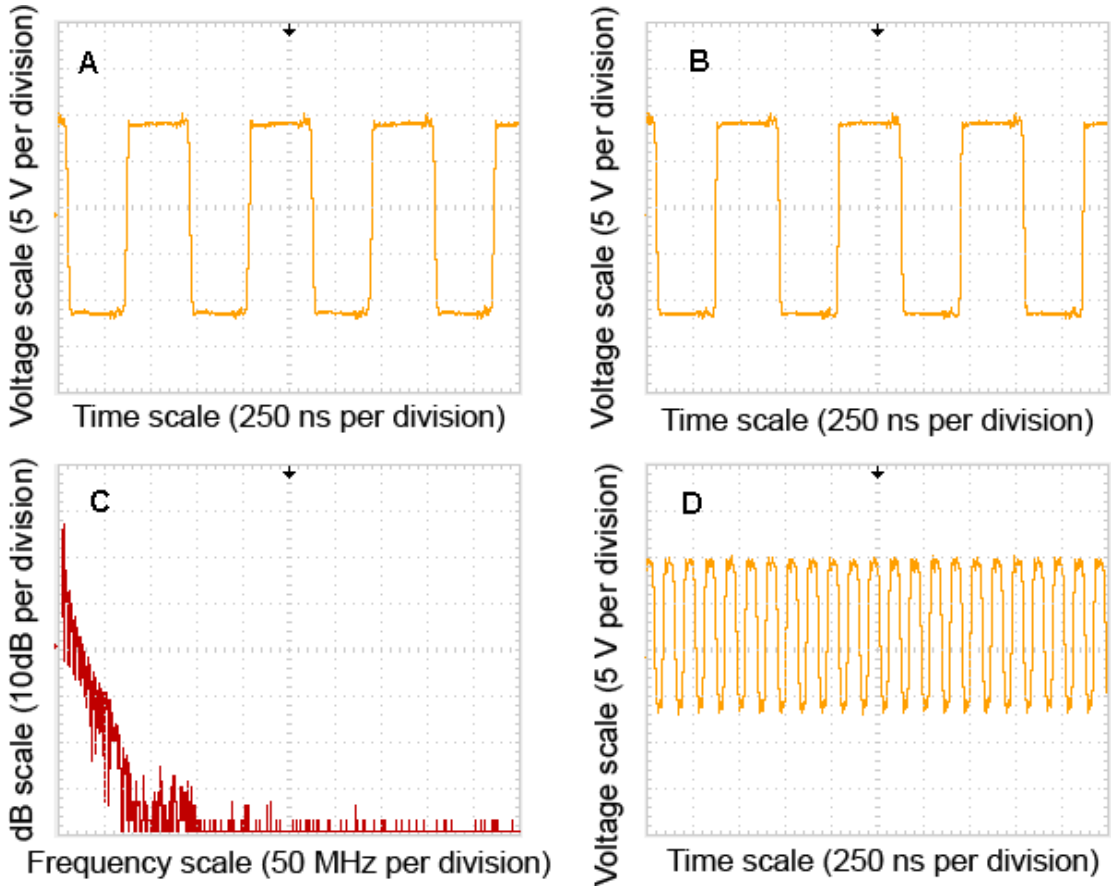

Figure 4.5. (A and B) Measured 1.54MHz output waveform from the ultrasound driver with slight ringing at the corners without and with the ultrasound transducer attached, respectively. (C) The power spectrum of the 1.54 MHz waveform. The drive signals energy concentration is in the early megahertz frequencies. (D) Measured 8.0 MHz signal shows attenuated drive voltage and asymmetry of the waveform with oscillations on both the positive and negative sides.

Furthermore, the waveform is asymmetric and exhibits small oscillations for positive and negative sides. When the TTL timing frequency is increased into the 10 MHz range, the MOSFETs saturate and are unable to switch at these speeds. The output resistance and reactance of the device was measured to be less than 0.05 Ω and almost entirely real with no measurable phase shift.

Figure 4.6 compares the performance of the driver when adjusting the output impedance of the driver to match the transducer. Clearly, this is reverse impedance

matching, since generally one matches the transducers impedance to the amplifiers output impedance. Figures 4.6A and 4.6B show the amplifier output without reverse impedance matching. Figure 4.6A gives the output without a transducer attached, and Figure 4.6B gives the output with the 1.54 MHz ultrasound transducer attached to the driver at 17 V_{pp} power setting. The output of the amplifier is effectively transmitted with a clean signal and 99% voltage transfer. Figures 4.6C and 4.6D show output waveforms from the driver when a 12 Ω power resistor is attached to the driver in series with the 12 Ω ultrasound transducer without and with the transducer attached, respectively. Signal distortion is present in Figure 4.6D with 62% voltage transfer from driver. Figures 4.6E and 4.6F show output waveforms from the driver when a 50 Ω power resistor is attached to the driver in series with the 12 Ω ultrasound transducer without and with the transducer attached, respectively. Signal distortion in Figure 4.6F is similar to that observed in Figure 4.6D for the 12 Ω resistor, but in this case voltage transfer to the transducer is reduced to 22%. These results show the ultralow output impedance driver performs best without matching the drivers' output impedance to the transducer. However, it could be advantageous to match the transducers input impedance to the ultralow output impedance of the driver by minimizing Z as predicted in Equation 4.16, thereby maximizing the output power from the driver.

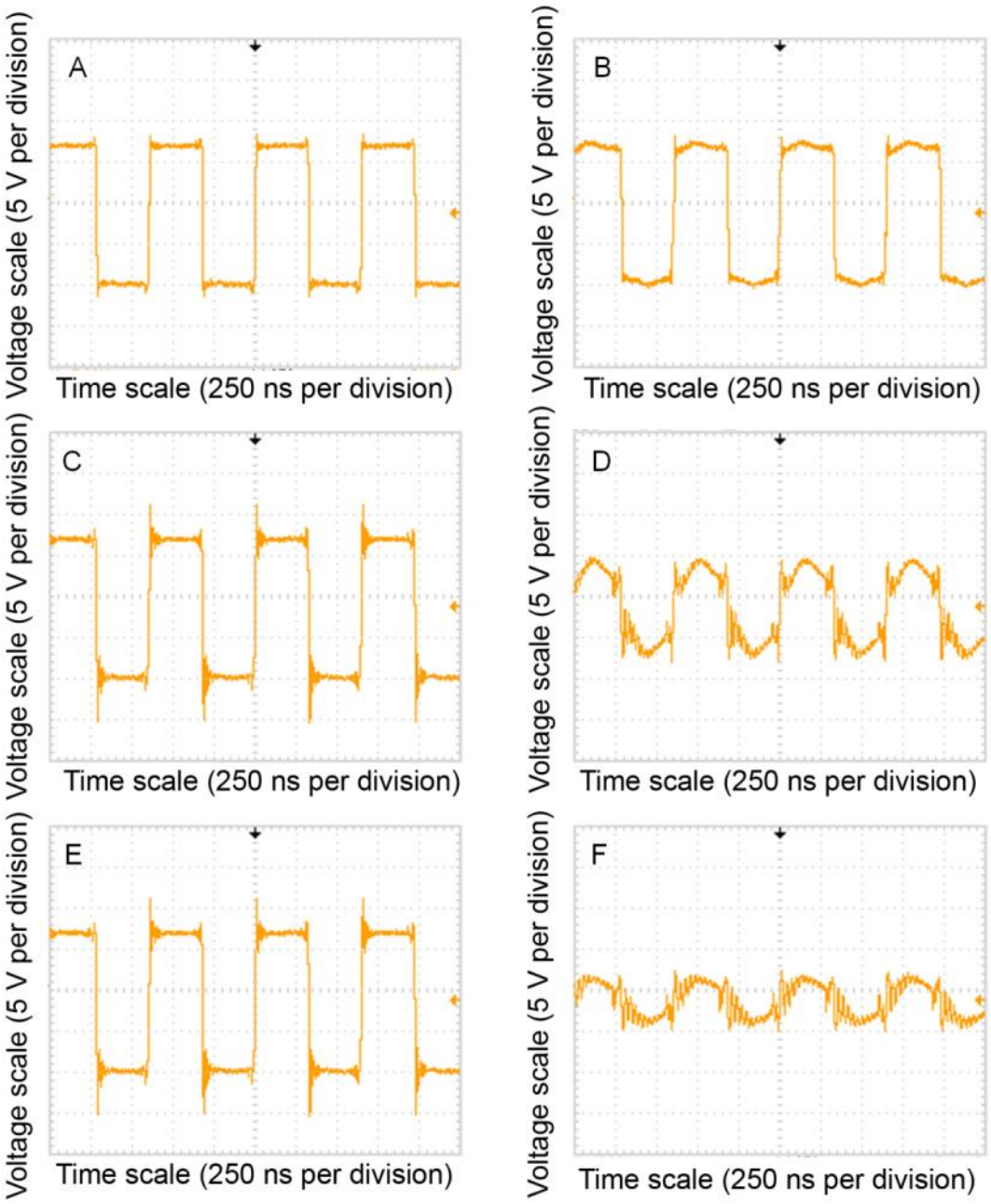

Figure 4.6. (A and B) Measured 1.54MHz output waveform from the ultrasound driver with slight ringing at the corners without and with the ultrasound transducer attached, respectively. (C and D) Output waveform from the ultrasound driver with 12 Ω impedance matching power resistor attached directly to driver in series to the 12 Ω ultrasound transducer without and with the transducer attached, respectively. (E and F) Output waveform measured with 50 Ω power resistor in series without and with transducer, respectively.

Minimizing *Z* would also result in energy waste across the amplifiers output impedance because of voltage division, and may not be appropriate for portable battery powered applications.

The temporal-average acoustic output power from the 1.54MHz ultrasound probe while driven at 50 V_{pp} is 48.0 W as determined from a force balance. Using electrical measurements of power and the electro-acoustic efficiency of 63% from the Mason model gives an output power of 33.0 W. The driver has a turn on delay of 10 ms due to capacitor coupling between pin-driver and MOSFETs. Once on, it is capable of providing short bursts of acoustic energy for less than 5 ms and for continuous-wave operation. The finished driver operating at 28 V_{pp} with the transducer used in this study is shown in Figures 4.7A and 4.7B. Figure 4.7A shows the driver powering the 1.54MHz transducer with a clean waveform and visually noticeable acoustic energy causing the water to vaporize. Figure 4.7B is a close up of the transducer in the water bath levitating and cavitating the water molecules into the air.

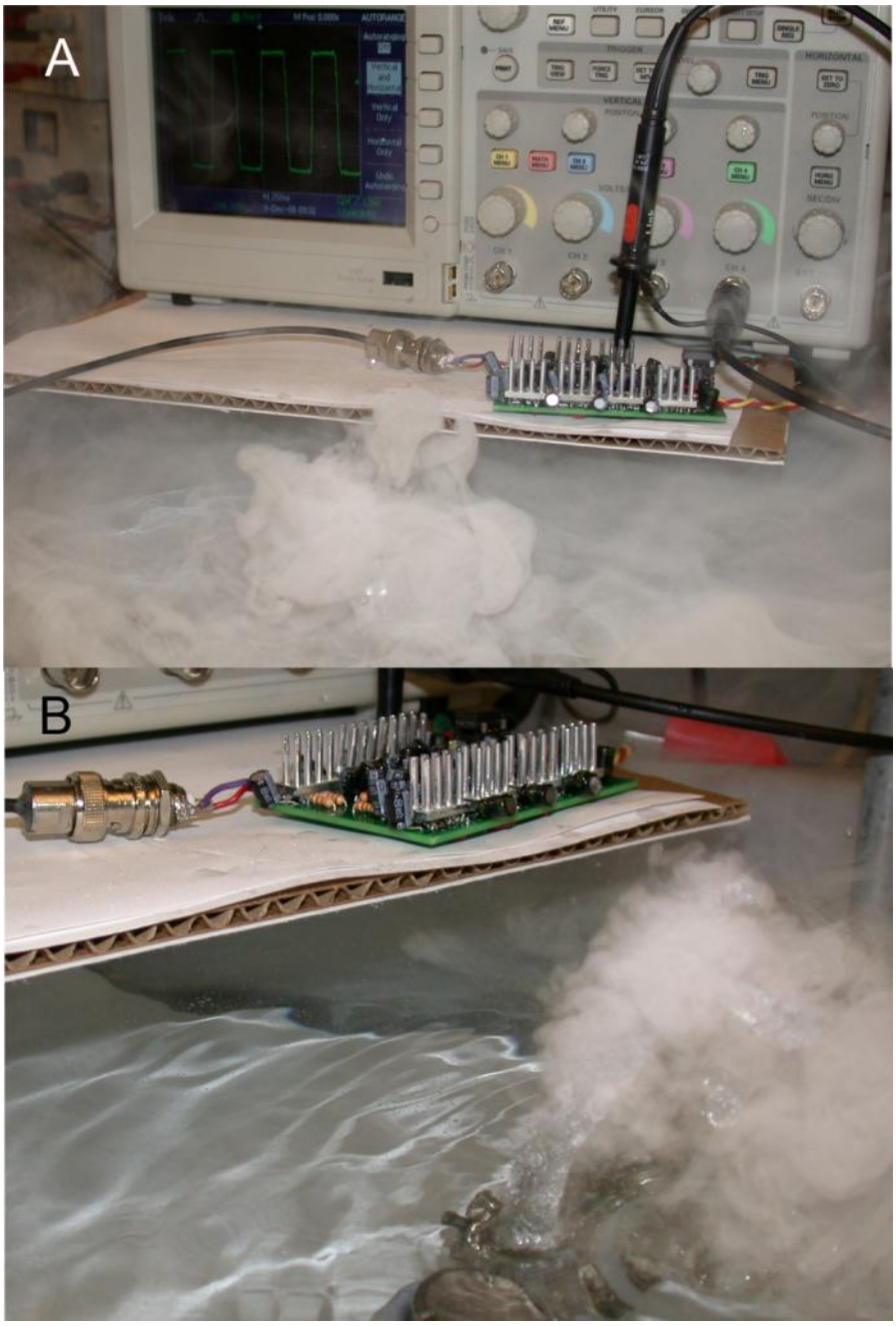

Figure 4.7. Complete high-power ultralow-output impedance ultrasound driver powering a 1.54 MHz ultrasound transducer. (A) Ultrasound driver operating at 28 V_{pp} with a clean waveform and high acoustic energy output causing the water to vaporize. (B) Close-up of the transducer in the water bath levitating and cavitating the water molecules into the air. Cavitation bubbles are visible in the water stream off the front face of the transducer.

4.5 Discussion

4.5.1 Amplifier Design

Managing the heat generated in the ultralow output impedance amplifier is essential for its sustained operation. The outputs of the 14 parallel MOSFETS are electrically and thermally connected with heat-sinking plains built directly into the PCB. The heat-sinking plains dissipate heat generated from switching losses in the MOSFETs and balance the temperature distribution between individual MOSFETs to prevent thermal runaway and damage to the ICs. Thermal management external heat-sinks that are attached to the top surface of the MOSFETs in groups of two are not necessary for low power applications in the range 0-10 W or for low driver frequency in the range 0-3 MHz. However, for high power applications in the range 20-60 W and for high driver frequency in the range 4-8 MHz, externally applied heat-sinks are necessary for continuous wave operation as shown in Figure 4.7.

4.5.2 Modeling Results of Acoustic Output Power

The Mason Model predicts that decreasing the output impedance of the driver source causes a shift in the drive frequency for maximum acoustic output power, as shown in Figure 4.4. The shift can be measured experimentally by using a 50 Ω output impedance function generator to drive the PZT-4, 1.54 MHz probe used in this study and comparing results with the ultralow impedance amplifier. The shift in maximum drive signal power from the actual electrical-resonance of the transducer is approximately 85 kHz for the 50 Ω driver. Although the magnitude of this shift seems modest, the results in Figure 4.4 suggest small shifts in the maximum power driver frequency can have significant effects on the output power achieved. For example, if a system is constructed to produce 1.5 MHz ultrasound with a 1.5MHz piezo-crystal and standard 50 Ω driving electronics to complement the frequency, over 50% of the input

energy may be lost, as seen in Figure 4.4A by comparing the peak value of the 50 Ω curve (approximately 0.5 W) to the power at 1.5 MHz (approximately 0.25 W) . With impedance matching circuitry corresponding to the 12.5 Ω curve in Figure 4.4A, the power loss in driving at the incorrect frequency is about 20%. With ultralow impedance drivers the maximum power drive is closely matched to the electrical-resonance of the transducer as shown is Figure 4.4a-d, and this problem is mitigated

4.5.3 Ultralow Impedance Ultrasound Driver

The ultrasound driver is useful in myriad applications that require both low and high power acoustic applications. Each amplifier can be constructed for under $100.00. Since the ultralow impedance driver delivers 99% of the voltage from the power supply to the transducer, batteries may be used to power the system in high and low power applications. The International Rectifier's low on-resistance MOSFET # IRF7350 can withstand 100 V_{pp} operation, according to the manufacturer, which could provide more than 10 Amps of current. At a 100 V_{pp}, our acoustic efficiency model estimates that the amplifier could produce an acoustic power of 130 W from the transducer used in this study.

The circuit drives existing transducers more efficiently than typical push-pull type amplifiers using impedance matching circuitry and rf amplifiers. If possible, however, it is beneficial to use ultralow impedance coax-cabling to connect the transducer to the ultralow impedance amplifier to maximize energy transfer and minimize waste in the form of heat. This will be important in implementing the ultralow impedance amplifier into efficient and portable therapeutic ultrasound applications [1, 17 and 23].

4.6 Conclusions

Modeling and experiments show that the ultralow impedance amplifier delivers maximum power close to the electrical-resonance of the ultrasound transducer. This is important in designing systems that are efficient at producing ultrasonic energy to limit energy waste and maximize energy transfer at low voltages.

The ultralow impedance ultrasound driver and PCB is considerably smaller (2 x 3 in) than typical rf amplifiers, is significantly less expensive, requires only DC power supplies and is 99% efficient at delivering the source voltage across the ultrasound transducer. The amplifier can operate in the range from 0 to 8 MHz, which spans the relevant range for medical therapeutic ultrasound and HIFU systems. The ultralow impedance driver has an output impedance of 0.01-0.05 Ω and provides switching of up to 100 V_{pp}. The amplifier can provide 48 W of acoustic energy from the 1.54 MHz transducer using no impedance tuning and has the potential to provide over 130 W of power using larger piezo-crystals and higher voltage power supplies. Further description and application of the driver in military, medical and research applications can be found in appendix 4.2.

REFERENCES

[1] Lewis Jr., G.K., Olbricht, W.L. (2008). Development of a portable therapeutic and high intensity ultrasound system of military, medical and research use. *Rev. Sci. Inst., 79*, 1-9.

[2] Wu, J., & Nyborg, W.L. (Eds.) (2006). Emerging Therapeutic Ultrasound. Hackensack, NJ: World Scientific Publishing.

[3] Aus, G. (2006). Current status of HIFU and cryotherapy in prostate cancer: A review. *Eur. Urol., 50*(5), 927–934.

[4] Mitragotri, S. (2005). Healing sound: The use of ultrasound in drug delivery and other therapeutic applications. *Nat. Rev. Drug Disc., 4*, 255-260.

[5] Bailey, M. R., Khokhlova, V. A., Sapozhnikov, O. A., Kargl, S. G., & Crum, L. A. (2003). Physical mechanisms of the therapeutic effect of ultrasound (a review). *Acoust. Phys., 49*(4), 369-388.

[6] Park, E.J., Jung, K.I., & Yoon, S.W. (2005). Acoustic mechanisms as an enhancer for transdermal drug delivery. *J. Acoust. Soc. Am., 107*, 2788.

[7] Lewis Jr., G.K., Olbricht, W.L., & Lewis, G.K. (2008). Acoustic enhanced Evans blue dye in neurological tissues. *J. Acoust. Soc. Am. POMA.*

[8] Lewis Jr., G.K., Wang., P., Lewis, G.K., & Olbricht, W.L. (2008). Therapeutic ultrasound enhancement of drug delivery to soft tissues. *8th. Int. Sym. Ther. Ultrasound, AIP conf. Proc., 1113, 403-407.*

[9] Newman, C.M.H., & Bettinger, T. (2007). Gene therapy progress and prospects: Ultrasound for gene transfer. *Gene Therapy, 14*, 465–475.

[10] ter Haar, G. & Coussios, C.C. (2007). HIFU: Physical principles and devices. *Int. J. Hypertherm., 23*(2), 89-104.

[11] Vykhodtseva, N.I., Hynynen, K., & Damianou, C. (1995). Histologic effects of high intensity pulsed ultrasound exposure. *Ultrasound Med. Biol., 21,* 969–979.

[12] Cesario, D. et al. (2008). *Contemporary cardiology, atrial fibrillation: From bench to bedside.* Natalie, M., & Jalife, J., (Eds.). Totowa, NJ: Humana Press.

[13] Guzman, H.R., Nguyen, D.X., McNamara, A.J., & Prausnitz, M.R. (2002). Equilibrium loading of cells with macromolecules by ultrasound: Effects of molecular size and acoustic energy. *J. Pharm. Sci., 91,* 1693–1701.

[14] Keyhani, K., Guzman, H.R., Parsons, A., Lewis, T.N., & Prausnitz, M.R. (2001). Intracellular drug delivery using low-frequency ultrasound: Quantification of molecular uptake and cell viability. *Pharm. Res., 18,* 1514–1520.

[15] Sundaram, J., Mellein, B.R., & Mitragotri, S. (2003). An experimental and theoretical analysis of ultrasound-induced permeabilization of cell membranes. *Biophys. J. 84*, 3087–3101.

[16] Vaezy, S., Shi, X., Martin, R.W., Chi, E., Nelson, P.I., Bailey, M.R., & Crum, L.A. (2001). Real-time visualization of high-intensity focused ultrasound treatment using ultrasound imaging. *Ultrasound Med. Biol., 27*, 33–42.

[17] Owen, N.R., Bailey, M.R., Mortimer, B.J.P., Kolve, H., Hossack, J. & Crum, L.A. (2003). Development of power supplies for portable HIFU therapy systems. *Proc. 3rd Int. Symp. Ther. Ultrasound*, 399–404.

[18] (2009). Why 50 Ω? *Microwave Encyclopedia.* Retrieved from the World Wide Web: www.microwaves101.com.

[19] Redwood, M., & Lamb, J. (1956). On the measurement of attenuation and ultrasonic delay lines, *Proc. IEEE*., *103*(12), 773-780.

[20] Morris, S. & Hutchens, C. (1986). Implementation of Mason's model on circuit analysis programs. *IEEE Trans. Ultrasonics, Ferroelect., Freq. Cont.*, *33*(3), 295-298.

[21] Maruvada, S., Harris, G. R., Herman, B. A., King, R.L. (2007). Acoustic power calibration of high-intensity focused ultrasound transducers using a radiation force technique. *J. Acoust. Soc. Am., 121*(3), 1434-1439.

[22] Lewis Jr., G.K., Lewis Sr., G.K., Olbricht, W.L., (2008). Cost effective broad-band electrical impedance spectroscopy measurement circuit and signal analysis of piezo-matrials and ultrasound transducers. *Meas. Sci. Technol., 19*, 1-7.

[23] Lewis Jr., G.K., Olbricht, W.L. (2008). Development of a portable therapeutic ultrasound system for military, medical and research use. *J. Acoust. Soc. Am., POMA 5*, 122.

CHAPTER 5

A PHANTOM FEASIBILITY STUDY OF ACOUSTIC ENHANCED DRUG PERFUSION IN NEUROLOGICAL TISSUE[9]

5.1 Abstract

To test the feasibility of using 1.1MHz focused ultrasound to increase the diffusion of drug through neurological tissue, tissue mimicking agar phantoms and a water soluble dye mimicking drug were exposed to 1.1MHz ultrasonic sound fields for 1 to 4 minutes in duration. Histology was then performed on the phantoms to assess the effect of ultrasound on the perfusion of dye. Mathematical analysis was used to quantify the extent of perfusion of dye and parametrically fit the experimental data to the theoretical diffusion equation. Results show a substantial increase in dye perfusion and not diffusion like behavior for the sonicated brain phantoms.

[9]This work has been published as Lewis, G.K., Jr., Olbricht, W.L. (2007). A phantom feasibility study of acoustic enhanced drug perfusion in neurological tissue. IEEE/NIH Life Science and Systems Workshop. © 2007 IEEE. Reprinted, with permission, from [IEEE, A phantom feasibility study of acoustic enhanced drug perfusion in neurological tissue, Lewis, G.K., Jr., Olbricht, W.L.]

5.2 Introduction

Designing effective therapies for brain cancer, including neuroblastoma, glioblastoma, and neurofibromatosis remains a significant challenge. Despite the development of drugs that are effective against these malignancies, the prognosis for patients remains poor. One reason for the poor outcome is that malignant cells can infiltrate healthy tissue surrounding the tumor, leading to poorly defined tumor boundaries. Migrating cells not only escape removal during tumor resection, but they may also avoid radiation and chemotherapy after resection. As a result, the tumor regrows, usually aggressively, and often at a location close to the site of the original tumor [1 and 2].

To address these issues new drug delivery methods have been developed to circumvent the blood-brain barrier and deliver drugs directly to brain parenchyma. Gliadel wafers impregnated with BCNU are implanted into the resection cavity to deliver high concentrations of drug to the surrounding tissue. However, the diffusivity of BCNU in tissue limits its penetration to a few millimeters from the wafer before it is eliminated by a variety of mechanisms [3]. This penetration distance is insufficient to reach more distant malignant cells. Similar considerations apply in convection enhanced delivery, a technique in which drugs are infused directly into the brain through a needle. Near the infusion site, transport is dominated by convection, but the strength of convection decays with distance from the infusion site and diffusion becomes important distant from the infusion needle [4 and 5]. Therefore, a method to increase the diffusion of compounds in tissue could enhance the therapeutic outcome of these drug delivery methods.

Acoustical techniques have been used in a variety of situations to enhance brain cancer treatments. For example, high intensity focused ultrasound (HIFU) has

been used to ablate and liquefy neurological tissues, and past and current studies are being conducted to assess the use of HIFU as a more complete surgical tool for minimally invasive therapy [6, 7 and 8]. Focused ultrasound is beginning to be assessed as a feasible way to deliver drugs to neurological tissues via selective disruption and permeablization of the blood brain barrier (BBB). Drugs that once could not cross the BBB because of molecular weight and hydrodynamic radius are now able to permeate into the neurological tissue with the application of ultrasound [8 and 9]. Ultrasound has also been used in other applications such as gene therapy and drug activation, and for further information on therapeutic ultrasound the authors cite [8].

In this study we explore the use of ultrasound to increase the perfusion of locally delivered tracer into an agarose gel that is used routinely as a mimic of brain tissue for drug delivery studies [10]. The ultimate goal is to increase the rate of transport of pharmaceutical agents relative to their elimination rate, and thereby extend the distance that drugs penetrate and maintain therapeutically useful concentrations.

5.3 Methods

Neurological tissue mimicking phantoms were prepared by filling standard 85 x 15 mm plastic Petri dishes with a solution of 0.6 wt% agar powder in warm distilled water. The dishes were then set aside to allow the solution to gel. Red food coloring, diluted in distilled water to 0.5 wt% was used to mimic water soluble drug and apply contrast to determine the extent of perfusion. Ultrasound (US) energy in the phantoms was generated by a lead zirconate titanate (PZT-4), 1 MHz, 20mm diameter piezoelectric ceramic with a radius of curvature corresponding to 40mm (EBL Products Inc., Connecticut, USA). The ceramic, housed in a PVC plastic assembly,

was driven at its center harmonic frequency, determined to be 1.1 MHz, by a +/- 200 volt, 55 Ohm, RF amplifying circuit. The circuit was constructed from Supertex Inc., TC6320 high speed switching MOSFET's. The RF driving circuit was supplied from a function generator (HP 8116A, HP USA) with a sinusoidal 1.1 MHz waveform. It was experimentally determined that the transducers input impendence was 65 Ohms at resonance, determined by measuring the voltage across the US transducer when attached to a 50 Ohm 10 V 1.1 MHz function generator source. A 95% acoustic conversion efficiency was estimated (as a high value) from supplied manufactures values. Measuring the amplifiers output voltage with and without the US device attached, knowing the US device impendence and using voltage division with the conversion efficiency of the ceramic a total acoustic output power was estimated to be 4.5 watts.

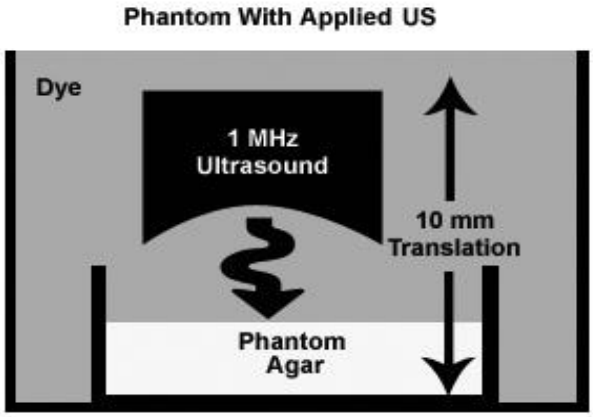

Figure 5.1. The experimental setup for the phantom study is shown. The sonicated phantom is immersed in 0.5 wt% diluted dye and pulse sonicated (15 seconds on and off) while simultaneously the transducer is oscillated up and down at 0.25Hz 10mm amplitude. The beginning position of the transducer was 40mm above the agar/dye interface, so that the US focus was placed on the surface. The control setup was the same without US.

The experimental setup shown in Figure 5.1, consisted of the control and the sonicated phantoms. Four phantoms for the control and experimental were conducted at each time point, for a total of 32 experimental measurements. The phantoms and dye where allowed to equilibrate to room temperature before the experiment. The phantoms were immersed in 500 ml of the dye and secured in position with clamps. Phantoms were sonicated on and off (15 seconds each) at their geometric center for durations of 1-4 minutes. The location of the focus of the transducer was positioned so that the focus at 40mm from the front surface of the US was placed on the agar/dye interface. The US was manually oscillated at 0.25 Hz over a 10mm translation to increase the sonicated volume (Figure 5.1). This was done for the duration of all experiments. For analysis purposes the location of the phantom/dye interface was taken to be zero. Histological readings were taken every minute for the control and sonicated phantoms. Histology on the phantoms was performed by taking a 1mm geometric center slice from the phantom and imaging it with a ccd camera/microscope system (Nikon Cool Pix 995, Nikon Inc. USA and Olympus BX51, Olympus Inc. USA). The digitally captured image was imported into MatLab® (Math Works Inc. USA) to determine the extent of the dye perfusion into the phantoms with and without applied US. By using Red-Green-Blue (RGB) color mapping and converting digital pixels into distance (mm) measurements, intensity vs. distance spectral curves of dye perfusion into the phantoms were produced.

We modeled the transport of the dye as one-dimensional diffusion from a source. Experimental data were compared with diffusion profiles for a constant source and a limited source as shown:

$$N(x,t) = N_0 erfc\left(\frac{x}{2\sqrt{Dt}}\right) \text{(constant source) (5.1)[11]}$$

$$N(x,t) = \left[\frac{Q}{\sqrt{\pi Dt}}\right]\exp\left[-\left(\frac{x}{2\sqrt{\pi Dt}}\right)^2\right] \quad \text{(limited source)} \qquad (5.2) \quad [11]$$

where: N_0 is the source concentration,

x is the diffusion distance,

Dt is the diffusion time product and

erfc is the complimentary error function.

Q is the total input concentration or integration of Eq. (1) from t=0 to infinity

Using a least squares approach, we parametrically fit the experimental data to the theoretical equations to compare differences in diffusion between the sonicated and control phantoms. The student T-test was used to determine statistical significance between control and US groups.

5.4 Results

Analysis of the experimental data shows that neurological tissue mimicking phantoms, that were sonicated, have a substantial increase in dye perfusion when compared to the control. Figure 4.2 shows experimental results at time points (TP) 1 and 4 minutes with a visual and quantifiable increase in dye perfusion into the sonicated phantoms (similar results for TP 2 and 3 were also quantified but not shown). At 1 and 4 minutes the surface intensity of dye uptake is 25% and 10% greater respectively then the corresponding controls, and the sonicated phantoms show an overall dye uptake increase of 84% and 25% respectively calculated by the difference in area under the color intensity curves at 1 and 4 minutes ($p<0.001$). Shown in the 4 minute intensity profile of Figure 5.2, we see that the control begins to follow the same shape of dye perfusion as the sonicated phantom at later TP's.

As expected and predicted by theory (Equation 5.1) we found that the perfusion of dye in the control phantom exhibited model diffusion behavior, TP 1 is shown in Figure 5.3. Also apparent in Figure 5.3 is that Equation 5.1 did not predict the experimental results of the spectral data from the sonicated phantoms at TP1. Figure 5.3 shows that sonication plays a role to increase the depth of dye perfusion and the method in which it moves into the phantom. Table 5.1 tabulates the diffusion coefficients of the sonicated and control phantoms for TP 1-4 and also gives the percent error of experimental data compared to the theoretical. We find that the diffusion coefficients for the sonicated phantoms are well above those of the control. At 1 minute the diffusion coefficient of the sonicated phantom is over 170% of its control and over the entirety of the experiment we find a 55% increase in diffusion coefficient when sonication is applied, ($p<0.001$) for all TP's.

Table 5.1. A tabulation of diffusion coefficients as determined from parametric fitting of experimental data. Note that the diffusion coefficients for No US were obtained using Eq. (1), while diffusion coefficients were calculated using Eq. (2) for US groups. The general trend is a noticeable increase in diffusion coefficient when US is applied to the sample.

Phantom Diffusion Coefficient And Percent Error	**With US** $(cm^2 \cdot sec^{-1})x10^{-4}$	**No US** $(cm^2 \cdot sec^{-1})x10^{-4}$
1 Minute	4.07, 4.69% error	2.35, 3.17% error
2 Minutes	5.40, 11.40% error	3.50, 6.80% error
3 Minutes	5.72, 4.92% error	3.68, 6.88% error
4 Minutes	4.83, 4.92% error	3.33, 3.00% error
Average Over Experiment	5.00, 6.48% error	3.22, 4.96% error

During the first time point TP1, Figure 5.2 shows that the surface intensity for the control is not equivalent to the US experiment. A further experiment was

conducted by the authors to address this surface anomaly; why the surface concentration of dye in gel for the control phantom did not equilibrate more rapidly. It was concluded that gelling surface properties, most plausibly different cross linking characteristics of the agar, lead to a mass-transport resistance at the surface of the agar phantom. The mass-transport resistance was not apparent when an inner section from the agar phantom was used as the surface for dye to diffuse into. Ultrasound therefore had an impact on breaking down the surface resistance of the phantom allowing rapid perfusion of dye Figure 5.2.

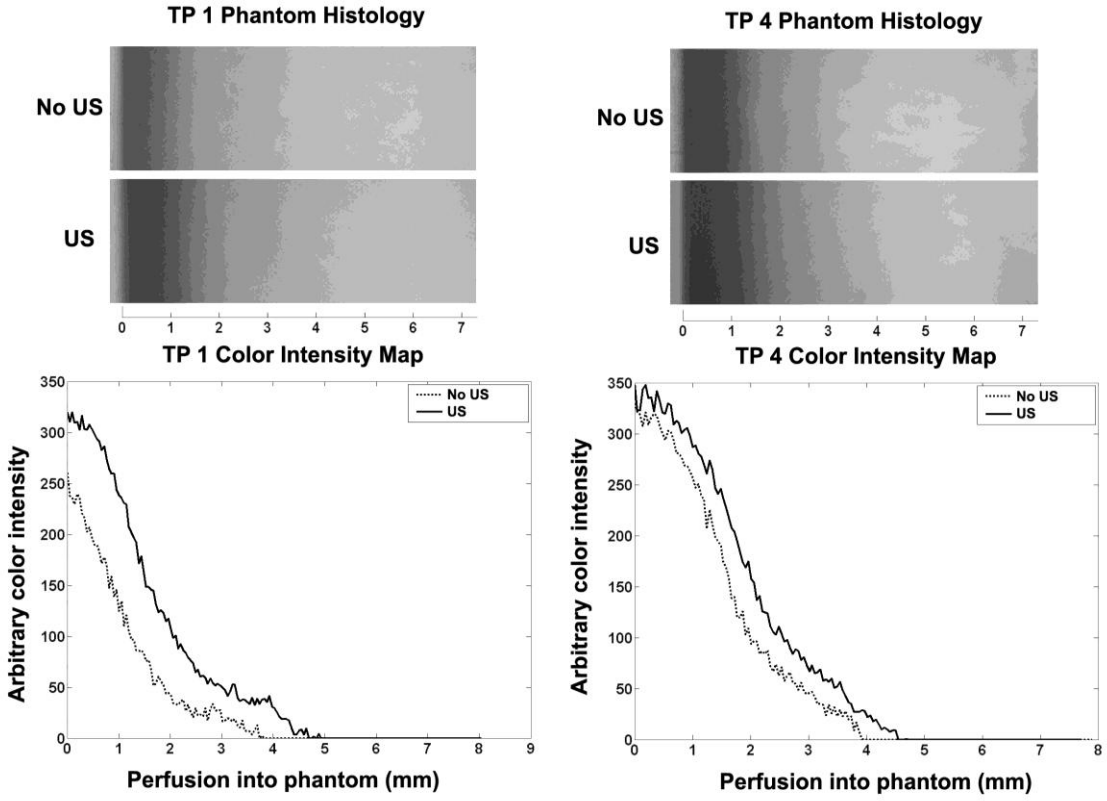

Figure 5.2. Top left and right are histology images taken from phantoms with and without applied US TP 1 and 4. Visible is the increase in dye penetration and intensity of the sonicated phantom. Bottom left and right are the corresponding RGB color intensity maps that correspond with the above images.

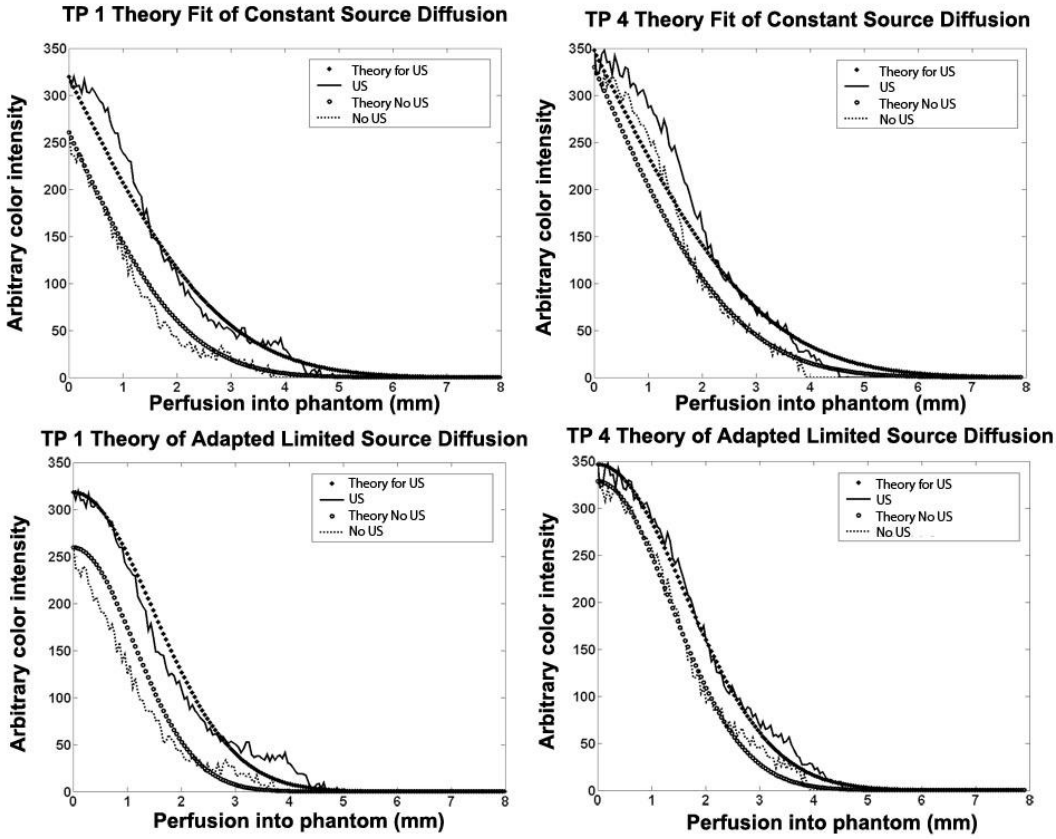

Figure 5.3. Plot of the theoretical fit to the experimental data for TP 1 and 4. Top left we see good agreement with control (No US) and constant source diffusion Eq. (5.1), note that US experimental data does not fit Eq. (5.1) well. Bottom left we find that Eq. (5.2) fits experimental data with US well but does not fit control. Top right graph shows that simple diffusion does not fit control or US phantom well for TP4. Bottom right graph shows that Eq. (5.2). fits both control and US phantom well. Overall Figure shows a noticeable increase in dye penetration when US is applied.

5.5 Conclusions

In this study we looked at the effect of 1.1 MHz ultrasound on the perfusion of dye into neurological tissue mimicking phantoms. We found a clear increase in dye

penetration and overall dye density in the sonicated verses control phantoms for all TP's ($p<0.001$). Most noticeably is the 170% initial increase of spectral intensity from dye uptake at the 1 minute TP as shown in Figure 5.2, where US was found to increase the surface mass-transfer of dye into agar gel by acoustic radiation pressures and agitation of the agar gel matrix. In the mathematical analysis and parametric fitting of the data we found good agreement of simple diffusion to the control experiments, however simple diffusion processes could not account for the enhanced transport of dye into the phantom with the application of US. All of the sonicated phantoms TP 1-4 data showed excellent agreement with the limited source diffusion equation. Overall the control experimental error averaged 4.96% while sonicated phantom groups averaged 6.48% error for the entire study.

From the results presented we find that 1.1 MHz ultrasound is a promising new method to increase the penetration of hydrophilic drug into brain tissue. The overall goal being the ability to use ultrasound to drive locally delivered chemotherapy agents past current diffusion limitations to reach migratory cancer cells. Further research is planed to study how changes in ultrasound parameters will affect the rate and level of dye perfusion in animal models. Different frequencies, powers, and pulse sequences appropriately below the brain tissue damage threshold will be analyzed to create a therapeutically useful regimen.

REFERENCES

[1] Giese, A., Bjerkvig, R., Berens, M.E., & Westphal, M. (2003). Cost of migration: Invasion of malignant gliomas and implications for treatment. *Am. Cancer Soc. J. Clin Oncol., 21*(8): 1624-1636.

[2] Lefranc, F., Brotchi, J., & Kiss, R. (2005). Possible future issues in the treatment of glioblastomas: Special emphasis on cell migration and the resistance of migrating cells to apoptosis. *J. Clin. Oncol., 23*(10), 2411-2422.

[3] Westphal, M., Hilt, D., Bortey, E., Delavault, P., Olivares, R., Warnke, P., Whittle, I., Jääskeläinen, J., & Ram, Z. (2003). A phase 3 trial of local chemotherapy with biodegradable carmustine (BCNU) wafers (Gliadel wafers) in patients with primary malignant glioma. *Neuro-Oncol. 5*(2), 79-88.

[4] Bobo, R.H., Laske, D.W., Akbasak, A., Morrison, P.F., Dedrick, R.L and Oldfield, E.H. (1994). Convection-enhanced delivery of macromolecules in the brain. *Proc. Natl. Acad. Sci., 91*, 2076-2080.

[5] Vogelbaum, M.A. (2007). Convection enhanced delivery for treating brain tumors and selected neurological disorders: Symposium review. *J. Neuro-Oncol., 83*, 97-109.

[6] Hill, C.R. & Haar, G.R. (1995). Review article: High intensity focused ultrasound--potential for cancer treatment. *Brit. J. Rad., 68*(816), 1296-1303.

[7] Vykhodtseva, N., Sorrentino, V., Jolesz, F.A., Bronson, R.T., & Hynynen, K. (2000). MRI detection of thermal effects of focused ultrasound on the brain. *Ultrasound Med. Biol., 26*(5), 871-880

[8] Mitragotri, S. (2005). Healing sound: The use of ultrasound in drug delivery and other therapeutic applications. *Nat. Rev. Drug Discov., 4*, 255-260.

[9] Mesiwala, A.H., Farrell, L., Wenzel, H.J., Silbergeld, D.L., Crum, L.A., Winn, H.R., & Mourad, P.D. (2002). High-intensity focused ultrasound selectively disrupts the blood-brain barrier in vivo. *Ultrasound Med. Biol. 28*(3), 389-400.

[10] Chen, Z., Gillies, G., Broaddus, W., Prabhu, S. et al. (2004). A realist realistic tissue phantom for intraparenchymal infusion studies. *J. Neurosurg. 101*(2), 314-322.

[11] Crank J. (1975). *The Mathematics of Diffusion.* Oxford: Oxford University Press.

CHAPTER 6

ACOUSTIC ENHANCED EVANS BLUE DYE PERFUSION IN NEUROLOGICAL TISSUES[10,11]

6.1 Abstract

The success of treating brain cancer such as neuroblastomas neurofibromatosis has not been very effective, and is in fact the leading of cancer-related death in patients younger than age 35. In the last recent developments in drug delivery methods have allowed doctors implant/inject time-release drugs into the tumor cavity that allows continuous release of chemotherapy; however results from these have not been as successful as anticipated. It is believed that non treated cancerous cells are able to migrate from the original tumor and relocate beyond the diffusion range for effective drug treatment. this study we utilize high frequency focused ultrasound to increase perfusion into phantoms that mimic brain tissue as a method to the rate of drug permeation into the tissue before vascular clearance cell migration reduce its effectiveness. Using various acoustic sequences we show a substantial increase in tracer perfusion into brain mimicking tissue then can be achieved by diffusion alone. We could therefore be able to reduce the time of delivery, the amount of drug delivered and drugs local impact range. This could significantly increase the success of local treatments and reduce systemic effects of chemotherapy.

In this study 1.58MHz therapeutic ultrasound was used to increase the perfusion of Evans blue dye (EBD) through neurological tissue-mimicking phantoms,

[10]This work has been published as Lewis, G.K., Jr., Lewis, G.K., Sr., Olbricht, W.L. (2007). Acoustic targeted drug delivery in neurological tissue. J. Acoust. Soc. Am. 122 3007

[11]This work has been published as Lewis, G.K., Jr., Lewis, G.K., Sr., Olbricht, W.L. (2007). Acoustic enhanced Evans blue dye perfusion in neurological tissues. J. Acoust. Soc. Am. POMA 2 020001

equine brain and avian muscle tissues. We show a substantial increase in EBD perfusion into the sonicated tissue then can be achieved by diffusion alone. We are therefore able to reduce the time of delivery, the amount of EBD delivered and the local impact range. This could significantly increase the success of delivering actual therapeutic treatments and reduce systemic effects of chemotherapy.

6.2 Introduction

The success of treating brain cancer such as neuroblastomas and neurofibromatosis has not been very effective, and is in fact the leading cause of cancer-related death in patients younger than age 35. Despite the development of drugs that combat these malignancies, the prognosis for patients remains poor. One reason for the poor outcome is that migrating cells escape removal during tumor resection, and in many cases avoid radiation and chemotherapy after resection. This allows the tumor to regrow, usually aggressively, and often at a location close to the site of the original tumor [1, 2]. In the last 10 years recent developments in drug delivery methods have allowed doctors to implant/inject time-release drugs into the tumor cavity that allows for continuous release of chemotherapy; however results from these studies have not been as successful as anticipated. Gliadel wafers impregnated with BCNU (also called carmustine) are implanted into the resection cavity to deliver high concentrations of drug to the surrounding tissue. However, the diffusivity of BCNU in tissue limits its penetration to a few millimeters from the wafer before it is eliminated by a variety of mechanisms [3].

Convection-enhanced drug delivery has been used to bypasses the blood-brain barrier by infusing drugs directly into the brain through a needle or microcatheter. The infusion establishes a pressure gradient that induces a flow in the brain away from the needle. Small molecules can be delivered over relatively large distances in the

brain, but larger molecules, including certain proteins with proven efficacy against malignant cells, are hindered in their transport [4, 5]. As a result, they cannot travel sufficiently far to reach migratory malignant cells. Drugs can be packaged inside nanoparticles such as polymeric spheres or liposomes, which protects the drug from elimination, but transport of these nanoparticles in the interstitium is even more hindered than that of proteins [6, 7].

The transport of proteins and nanoparticles can be improved by increasing the porosity or the effective "pore size" of the brain interstitium. For example, transport is enhanced when the proteins or nanoparticles are infused in a hyperosmolar solution that induces tissue swelling locally by drawing fluid into the interstitium from surrounding blood vessels and cells. Infusing an enzyme that temporarily degrades the extracellular matrix, which increases the permeability of the interstitium to proteins and nanoparticles, also enhances transport [8]. Although these methods work to some extent, additional transport enhancement is required to realize the potential of convection enhanced drug delivery.

In this study we utilize 1.58 MHz focused ultrasound to increase the perfusion of locally delivered Evans blue dye that is widely used in tissue diffusion experiments [9-11] into an agar gel that is used routinely as a mimic of brain tissue for drug delivery studies [12], equine brain and avian muscle tissue. The ultimate goal is to increase the rate of transport of pharmaceutical agents relative to their elimination rate, and thereby extend the distance that drugs penetrate and maintain therapeutically useful concentrations.

6.3 Methods

6.3.1 Specimen Setup and EBD Application

Neurological tissue mimicking phantoms were prepared by filling off-the-shelf 12 oz Solo Cups (Tops Super Market Brand, Ithaca, NY) with a solution of 0.6 wt% agar powder (Product #19461580, MP Biomedicals, Solon, OH). The powder was dissolved in 100 degree Celsius distilled water for 5 minutes and poured into the cups to a height of 2.5cm. The cups were then covered, set aside, and allowed to cool and gel (approximately 20 minutes). *Equine horse brain* was harvested from the Cornell Vet School two minutes post-mortem and prepared into 3x3x3 cm slices (the cortex surface was used for the ultrasound enhanced EBD perfusion). The equine brain experiments were conducted within 30 minutes of brain harvesting. *Avian muscle tissue* was purchased fresh from a local supermarket and cut into 3x3x3 cm squares for the study. Well characterized Evans blue dye (Product #203163, MP Biomedicals, Solon, OH) diluted in distilled water to 0.25 wt% was used to mimic water soluble drug and apply contrast to determine the extent of perfusion. During ultrasound application, the fresh tissues were placed in 12 oz cups, and all samples were covered by 200 ml of EBD and secured in position.

6.3.2 Ultrasound Setup, Dosing and Analysis

Ultrasound energy in the samples was generated by a lead zirconate titanate (PZT-4), 1.58 MHz, 25.4mm diameter piezoelectric ceramic with a radius of curvature corresponding to 40mm. The ceramic, air-backed and housed in a PVC plastic assembly, was driven at 1.58 MHz, by a +/- 200 volt amplifying circuit (TC6320 high speed ultrasound driver, Supertex Inc., San Jose, CA.). The acoustic source power was modeled mathematically using Mason's model [13-15], and measured directly with a calibrated hydrophone (Model #S158, Transducer Engineering Inc., Andover, MA).

All samples were sonicated 100% duty cycle at the average intensity of 3.00 watts/cm^2 (peak-focus-intensity 15 watts/cm^2) in the samples geometric center for durations of 1-4 minutes. The location of the focus of the transducer was positioned so that the focus at 40mm from the front surface of the US was placed on the sample/dye interface as shown in Figure 6.1. The US was oscillated at 0.25 Hz over a 10mm translation perpendicular to the samples surface to increase the sonicated volume for the duration of all experiments.

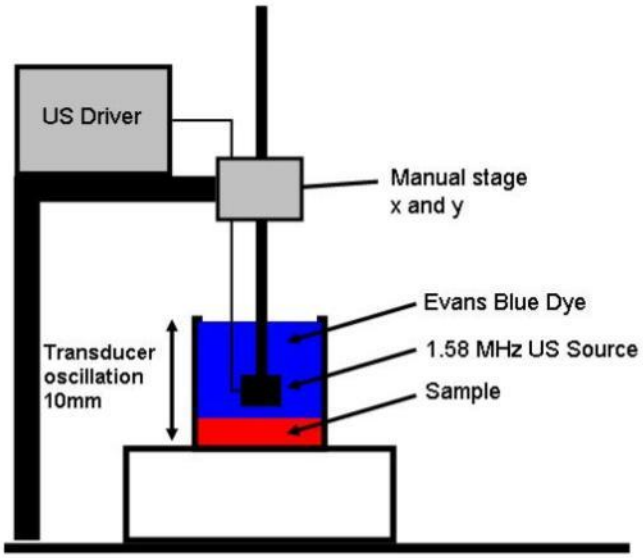

Figure 6.1. The experimental setup for the sample study is shown to the left. The sonicated phantom is covered in 0.25 wt% diluted Evans blue dye and sonicated at 100% duty while simultaneously the transducer is oscillated up and down at 0.25Hz 10mm amplitude. The beginning position of the transducer was 40mm above the sample/dye interface.

For analysis purposes the location of the sample/dye interface was taken to be zero. Sectional readings of EBD perfusion were taken every minute for the control and sonicated samples (four at each time point totaling 12 for each material). The section of the sample was performed by taking a 2mm geometric center slice from the sample and imaging the location of the US focused energy with a CCD camera/microscope

system (Nikon Cool Pix 995, Nikon Inc. USA and Olympus BX51, Olympus Inc. USA). The digitally captured images were imported into MatLab® 6.5 (Math Works Inc. USA) to determine the extent of the Evans blue dye perfusion into the samples with and without applied US. By using Red-Green-Blue (RGB) color mapping and converting digital pixels into distance (mm) measurements, intensity vs. distance concentration curves of EBD perfusion into the samples were produced. The four spectral intensity curves corresponding to each sectional measurement for each time point were averaged, and the area under the concentration curves for the sonicated and control were evaluated to quantify the density of EBD uptake. The areas for control and experimental groups was compared using a student T-test for statistical significance.

6.4 Results

Analysis of the experimental data shows the sample tissues have a substantial increase in EBD perfusion when compared to the control. Shown in Figure 6.2 are the sectional images of the EBD concentration gradient for three samples studied at two minutes (1, 3 and 4 minutes not shown). The red curves (peak uptake aprox. 600 for all) represents the EBD perfusion into the samples with US applied. The blue curves are the controls representing simple diffusion into the sample. Application of US enhanced EBD density of 61.5% (phantom), 93.2% (brain) and 52.8% (muscle) compared to the control ($p<0.001$).

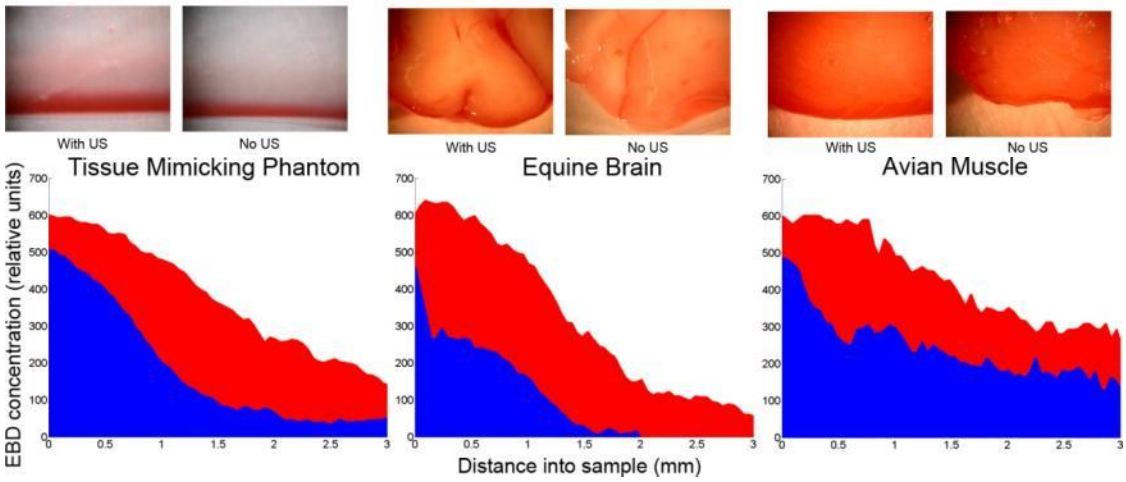

Figure 6.2. The above Figure shows the sectional images and the results of enhanced EBD delivery into a tissue mimicking phantom, equine horse brain and avian muscle tissues with the application of Therapeutic Ultrasound for two minutes in red, compared with the control in blue. The Figure shows concentration curves of the EBD uptake into the samples and that local delivery of EBD in conjunction with the application of Therapeutic Ultrasound may significantly enhanced the amount of EBD delivery into tissue. Application of US enhanced EBD density of 61.5% (phantom), 93.2% (brain) and 52.8% (muscle) compared to the control.

During all time points 1-4 minutes and shown in Figure 6.2 the surface intensity (x axis=0) for the control is not equivalent to the experimental with sonication, this was also noticed in our prior study [16]. We now believe that this edge effect and mismatch of concentration in the control and experimental groups is a surface mass transport resistance, and the limited diffusion of the dye into the samples for the short time points resulting in poor pixel intensity image mapping. Experimentally with the phantom, we found that if we removed the phantoms gelling surface with a razor, the mass-transport resistance was not apparent and EBD more readily perfused the phantom. The focused ultrasound had a sonoporation type effect as in transdermal drug delivery, and has an impact on breaking down the surface resistance of all samples allowing for quicker perfusion of dye and overall dye density uptake in the sonicated phantoms.

6.5 Supporting Analysis and Discussion of Results

To find the concentration profile of a chemotherapeutic diffusing through a tissue, the tissue can be modeled as a medium comprising three phases: extracellular space (ECS), intracellular space (ICS) and cell membrane (CM) [17-19]. The local chemotherapeutic concentration depends on its rate of transport through the tissue, its rate of elimination by degradation, metabolism, and permeation into blood capillaries, and its rate of binding and internalization. Under these conditions, the chemotherapeutic concentration diffusing through tissue is given by

$$\frac{\partial C}{\partial t} = -\nabla \cdot \left(-\alpha D_{ECS} \nabla C^{O}_{ECS} + \alpha \boldsymbol{v} C^{O}_{ECS}\right) - \left(\alpha k_{ECS} C^{O}_{ECS} + \beta k_{ICS} C^{O}_{ICS} + (1-\alpha-\beta) k_{M} C^{O}_{CM}\right) - \frac{\partial B}{\partial t} \quad (6.1)$$

where C and B are total concentrations of free and bound chemotherapeutic, respectively; $C^{O}_{ECS}, C^{O}_{ICS}, \text{and } C^{O}_{CM}$ are volume-averaged concentrations in the ECS, ICS and CM phases, respectively; t is the time following the beginning of diffusion from the source; α and β are volume fractions of ECS and ICS phases; D_{ECS} is the diffusion coefficient of the drug in ECS; $\boldsymbol{v}$ is the apparent velocity vector of interstitial fluid in ECS; and k_{ECS}, k_{ICS}, and k_{CM} are first-order elimination constants in ECS, ICS and CM phases, respectively [17].

This equation was applied to predict concentrations of BCNU and other chemotherapeutics released from polymeric wafers in the rat [18] and monkey brain [17]. Comparisons of the predictions with data showed that several assumptions can be made in the equation without introducing significant error, including that coefficients are independent of position, that free drug is in equilibrium locally with bound drug, and that convection is negligible compared with diffusion. Under these assumptions, the steady-state profile for total concentration C satisfies the one-dimensional equation $D\frac{\partial^2 C}{\partial x^2} - kC = 0$ (6.2), where x is distance from the BCNU wafer/tissue interface, D is

an apparent diffusion coefficient of drug in the brain, and k is a first-order elimination constant that combines the elimination mechanisms mentioned above. The solution of this equation with boundary conditions appropriate for release of drug from an implanted BCNU wafer is

$$\frac{C(x)}{C_i} = \frac{\exp\left(-\frac{H-x}{L}\phi\right) + \exp\left(\frac{H-x}{L}\phi\right)}{\exp\left(-\frac{H}{L}\phi\right) + \exp\left(\frac{H}{L}\phi\right)}, \text{ where } \phi = L\sqrt{\frac{k}{D}}. \quad (6.3)$$

Here, L is the half-thickness of the wafer, H is the perpendicular distance from the wafer/tissue interface to the edge of the brain, and C_i is the chemotherapeutic concentration at the wafer/tissue interface. The dimensionless concentration profile $C(x)/C_i$ is determined completely by the value of the modulus ϕ, which gives a quantitative estimate of the relative rates of elimination and diffusion of the drug in brain tissue. Using the results for monkey brain [17], the estimated values of the coefficients are D = 14.3 x 10^{-6} cm^2s^{-1}, L = 0.5 mm, k = 0.0028 s^{-1}, and H = 5 cm. The red curve in Figure 6.3 shows the dimensionless BCNU concentration C/C_i as a function of distance x into tissue. The Figure shows that C/C_i decreases significantly just a few millimeters away from the wafer. We found similar results for Evans blue dye in the experiments presented.

Results presented in section 6.3 and in Chapters 6, 8 and 9 shows that exposing tissue to ultrasound enhances diffusion in tissue. The effect of enhanced diffusion and its effect on drug penetration into tissue can be anticipated by plotting concentration profiles given by the solution above with an apparent diffusion constant D^* replacing the molecular diffusion constant D. This is shown in the blue curves in Figure 6.3 for $D^* = 5D$ to $300D$. If we define a penetration distance as the distance where C/C_i drops to 0.1, then the Figure shows that the penetration distance more than doubles for a tenfold increase in the apparent diffusion constant due to ultrasound exposure. For a

100-fold increase, the penetration distance would increase by nearly an order of magnitude.

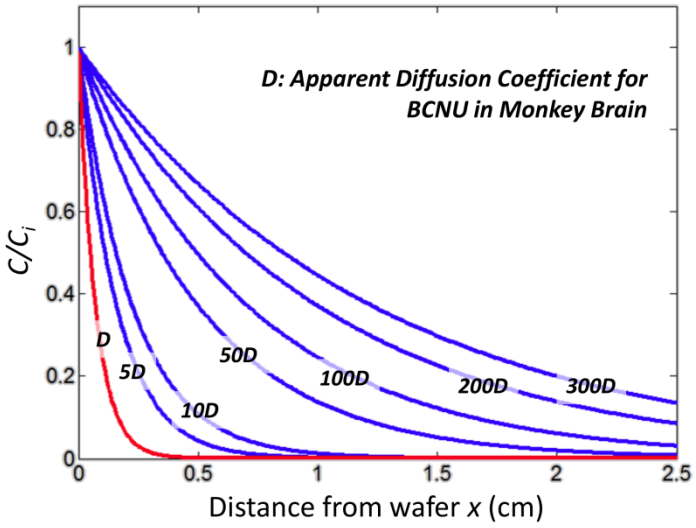

Figure 6.3 Dimensionless BCNU concentration profiles in tissue following its release from a wafer in monkey brain

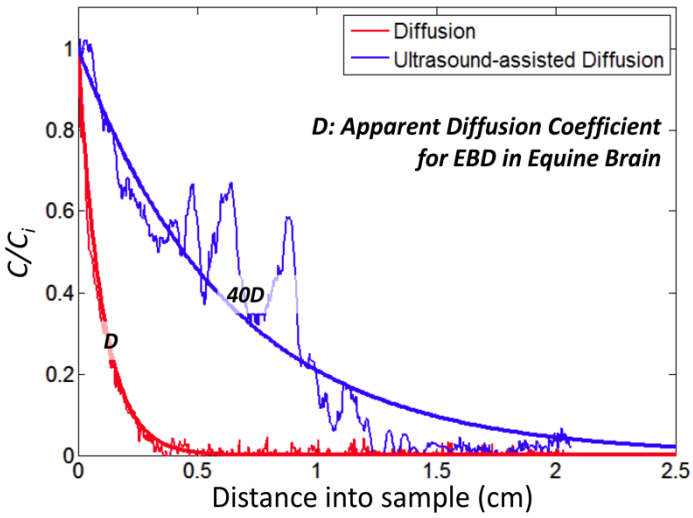

Figure 6.4 EBD concentration profiles after 2 min in equine brain tissue without ultrasound (red) and with 1W/cm^2 ultrasound (blue) for 2 min. Ultrasound increases the apparent diffusion coefficient by about 40x.

Figure 6.4 show example profile with and without exposure of the tissue to ultrasound at an intensity of 1 W/cm^2 for 2 min. The red curve shows the concentration profile of EBD in the sample without ultrasound (pure diffusion). The blue curve shows the concentration profile for tissue exposed to ultrasound.

Using the concentration profile, we can estimate that ultrasound exposure increases the *apparent* EBD diffusion coefficient by about a factor of 40 in this case. The fluctuations in concentration for the ultrasound case are outside error limits of the experiment and are probably due to heterogeneities in tissue structure such as transitions between white and gray matter. Structural variations in tissue influence the interaction between ultrasound and tissue, which could affect local EBD transport through the tissue. These fluctuations are not observed for experiments involving agarose gel brain phantoms. The effectiveness of diffusion based brain cancer therapies depends strongly on the penetration of the chemotherapeutic into the peri-tumoral space. If a 40x increase in the apparent diffusion constant could be realized clinically by using ultrasound to assist diffusion based strategies, the penetration of chemotherapeutic would be significantly enhanced, which could significantly improve outcomes of the therapy for glioblastoma patients.

6.6 Conclusions

In this study we looked at the effect of 1.58 MHz ultrasound on the perfusion of Evans blue dye into neurological tissue mimicking phantoms, equine brain and avian muscle tissue. We found a clear increase in EBD penetration and overall dye density in the sonicated verses control samples for all times ($p<0.001$). Experimentally, this was noticeable in Figure 6.2 at 2 minutes with enhanced dye uptake of 61.5% (phantom), 93.2% (brain) and 52.8% (muscle) compared to the controls. Applied therapeutic ultrasound to the sample-dye interface, was found to

increase the surface mass-transfer of EBD into the sample and increase the apparent diffusion coefficient of EBD in the tissue samples. We hypothesize that the acoustic pressures from the peak focal intensity of 15.2 watts/cm^2 and oscillation of the transducer field Figure 6.1, imparted radiation pressures of EBD into the sample, while also warming and agitating the porous matrix. These combined effects enhanced the perfusion of dye with sonication.

From the results presented we find that 1.58 MHz ultrasound is a promising new method to increase the penetration of hydrophilic drugs into brain tissue. The overall goal being the ability to use ultrasound to drive locally delivered chemotherapy agents past current diffusion limitations to reach migratory cancer cells. Continued research to study how changes in ultrasound parameters will affect the rate and level of dye perfusion in animal brain tissues will be our continuing focus. Different frequencies, powers, and pulse sequences appropriately below the brain tissue damage threshold will be analyzed to create a therapeutically useful regime.

REFERENCES

[1] Giese, A., Bjerkvig, R., Berens, M., & Westphal, M. (2003). Cost of migration: Invasion of malignant gliomas and implications for treatment. *Am. Cancer Soc. J. Clin. Oncol., 21*(8), 1624-1636.

[2] Lefranc, F., Brotchi, J., & Kiss, R. (2005). Possible future issues in the treatment of glioblastomas: Special emphasis on cell migration and the resistance of migrating cells to apoptosis. *J. Clin. Oncol., 23*(10), 2411-2422.

[3] Westphal, M., Hilt, D., Bortey, E., Delavault, P., Olivares, R., Warnke, P., Whittle, I., Jääskeläinen, J., & Ram, Z. (2003). A phase 3 trial of local chemotherapy with biodegradable carmustine (BCNU) wafers (Gliadel wafers) in patients with primary malignant glioma. *Neuro-Oncol., 5*(2), 79-88.

[4] Bobo, R.H., Laske, D.W., Akbasak, A., Morrison, P.F., Dedrick, R.L and Oldfield, E.H. (1994). Convection-enhanced delivery of macromolecules in the brain. *Proc. Natl. Acad. Sci., 91*, 2076-2080.

[5] Vogelbaum, M.A. (2007). Convection enhanced delivery for treating brain tumors and selected neurological disorders: Symposium review. *J. Neuro-Oncol., 83*: 97-109.

[6] Muller, R.H., Mader, K., & Gohla, S. (2000). Solid lipid nanoparticles (SLN) for controlled drug delivery–a review of the state of the art. *Eur. J. Pharm. Biopharm., 50*(1), 161-177.

[7] Panyam, J., & Labhasetwar , V. (2003). Biodegradable nanoparticles for drug and gene delivery to cells and tissue. *Adv. Drug Deliv. Rev.*, *55*(3), 329-347.

[8] Neeves, K.B., Sawyer, A.J., Foley, C.P. Saltzman, W.M., & Olbricht, W.L. (2007). Dilation and degradation of the brain extracellular matrix enhances penetration of infused polymer. *Brain Res., 1180,* 121-132.

[9] Woitzik, J., & Schilling, L. (2007). A new method for superselective middle cerebral artery infusion in the rat. *J. Neurosurg., 106(*5), 872-878.

[10] Aoki, T., Sumii, T., Mori, T., Wang, X., & Lo, EH. (2002). Blood-brain barrier disruption and matrix metalloproteinase-9 expression during reperfusion injury. *J. Stroke. 33*, 2711.

[11] Chan, P., Fishman, R., Caronna, J., Schmidley, J.W., Prioleau, G., & Lee, J. (2006). Induction of brain edema following intracerebral injection of arachidonic acid. *Ann. Neurol., 13*(6):625-632.

[12] Chen, Z., Gillies, G., Broaddus, W., Prabhu, S. et al. (2004). A realist realistic tissue phantom for intraparenchymal infusion studies. *J. Neurosurg., 101*(2), 314-322.

[13] Redwood, M. (1961). Transient performance of a piezoelectric transducer. *J. Acoust. Soc. Am., 33*(4), 537-536.

[14] Morris, S. & Hutchens, C. (1986). Implementation of Mason's model on circuit analysis programs. *IEEE Trans. Ultrasonics, Ferroelect., Freq. Cont.*, *33*(3), 295-298.

[15] Mason, W.P. (1958). *Physical acoustics and the properties of solids.* Toronto, Canada: D. Van Nostrand Company.

[16] Lewis, G.K., & Olbricht, W.L. (2007). A phantom feasibility study of acoustic enhanced drug perfusion in neurological tissue. *Proc. IEEE, LISA,* 67-70..

[17] Fung, L.K., Ewend, M.G., Sills, A., Sipos, E., *et al.* (1998). Pharmacokinetics of interstitial delivery of carmustine, 4 hydroperoxycyclophosphamide, and paclitaxel from a biodegradable polymer implant in the monkey brain. *Cancer Res., 58,* 672–684.

[18] Fung, L.K., Shin, M., Tyler, B., Brem, H. *et al.* (1996). Chemotherapeutic drugs released from polymers: Distrobution of 1,3-bis(2-chloroethyl)-1-nitrosourea in the rat brain. *Pharma. Res., 13*, 671-682.

[19] Saltzman, W.M. (2001). Drug delivery: Engineering principles for drug therapy. Oxford: Oxford University Press.

CHAPTER 7

THERAPEUTIC ULTRASOUND ENHANCEMENT OF DRUG DELIVERY TO SOFT TISSUES[12]

7.1 Abstract

Effects of exposure to 1.58MHz focused ultrasound on transport of Evans Blue Dye (EBD) and bovine serum albumin conjugated EBD in soft tissues are investigated when an external pressure gradient is applied to induce convective flow through the tissue. The magnitude of the external pressure gradient is chosen to simulate conditions in brain parenchyma during convection-enhanced drug delivery (CED) to the brain. EBD uptake and transport are measured in equine brain, avian muscle and agarose brain-mimicking phantoms. Results show that ultrasound enhances EBD uptake and transport, and the greatest enhancement occurs when the external pressure gradient is applied. The results suggest that exposure of the brain parenchyma to ultrasound could enhance penetration of material infused into the brain during CED therapy.

[12]This work has been published as Lewis, G.K., Jr., Wang, P., Lewis, G.K., Sr., Olbricht, W.L. (2009). Therapeutic ultrasound enhancement of drug delivery to soft tissues. 8th Int. Symp. Theras. Ultras. AIP Conf. Proc. 1113, pp. 403-407

7.2 Introduction

Over the last decade, a driving factor in pharmaceutical development and drug delivery has been the ability to target disease at the cellular and tissue levels. Local delivery of therapeutics often allows higher doses to be delivered without side effects that restrict dose levels in systemic delivery. Local delivery can be combined with controlled release to provide sustained high concentrations of drug in the immediate vicinity of affected tissue [1-3]. Local delivery is especially important in treating brain disorders, because most therapeutics administered intravenously do not cross the blood-brain barrier. Recent developments in treating brain gliomas, which are infiltrative tumors that present poor prognosis for patients, rely on local delivery methods. After resection of the tumor, malignant cells that have migrated from the tumor remain behind, surrounded otherwise by healthy tissue. These cells continue to grow, leading to the recurrence of the disease. CED is a local delivery technique in which therapeutics are infused directly into the brain interstitium through an implanted needle microcatheter [4, 5]. The infusion induces a convective flow of infusate through the interstitium. The infused drugs are subject to elimination via a variety of mechanisms. Therefore, the challenge in CED is to enhance penetration of infused therapeutics so that they reach migrating malignant cells before they are eliminated. Some of the most promising drugs for treating gliomas are large proteins and drugs packaged in nanoparticles, which, owing to their size, are especially difficult to move through brain interstitium under the convective force of the infusion. Therefore, any method to enhance transport of infused drugs could benefit the outcome of the therapy.

The use of ultrasound to enhance drug delivery has evolved over several decades. Perhaps the most extensively studied example is the use of ultrasound to enhance transdermal drug delivery [6, 7]. Exposure of skin to ultrasound can increase

the permeability of the stratum corneum, allowing transport across skin of some therapeutic compounds that would otherwise be excluded and enhancing transport rates of others. Although a variety of thermal and non-thermal mechanisms could be responsible for transport enhancement, acoustic cavitation and microstreaming [8, 9] may be the most important. At lower acoustic power, oscillations of endogenous microbubbles or microbubbles added to an infusate may induce similar microstreaming, even in the absence of cavitation.

We present results on the enhancement of Evans blue dye (EBD) and bovine serum albumin conjugated EBD transport into soft animal tissues using 1.58 MHz ultrasonic powers of 1.3 and 5.25 W in combination with an applied convective flow under conditions that simulate convection-enhanced drug delivery [10, 11].

7.3 Methods

7.3.1 Sample Preparation

Neurological-tissue-mimicking phantoms were prepared by filling 12 oz Solo Cups with a solution of 0.6 wt% agarose powder (MP Biomedicals, Solon, OH) [12]. The powder was dissolved in distilled water at 100º C for 5 min and then poured into the cups to a height of 1.5 cm. The cups were covered and allowed to cool and gel (about 20 min). Equine horse brain was harvested from the Cornell School of Veterinary Medicine immediately post-mortem and cut into 3 x 3 x 1.5 cm cortical slices. Experiments were conducted within 30 min of brain harvesting. Avian muscle tissue was purchased from a local supermarket and cut into 3 x 3 x 1.5 cm slices. A 0.25 wt% aqueous solution of Evans blue dye (MP Biomedicals, Solon, OH) was used to mimic a water-soluble drug. The EBD solution provided sufficient contrast to measure its extent of penetration into the phantom and tissue samples [10, 11, 13, 14].

Bovine serum albumin conjugated EBD was prepared by mixing albumin from bovine serum (molecular biology, powder, Sigma-Aldrich, OH) with Evans Blue dye (Product #203163, MP Biomedicals, Solon, OH)) in the ratio of 1:0.4 (Albumin:Evans Blue) by weight. The 5 mg/mL concentration solution was prepared in 0.9% NaCl (wt/vl) and sterile filtered through a 0.2 micron syringe filter (Supor® Sterile Syringe Filter, 0.2 Micron, 25Mm, Health Care Logistics). The filtrate was then dialyzed against 0.9% saline to remove excess Evans Blue with a 10 kDa MWCO Slide-A-Lyzer (Slide-A-Lyzer Dialysis Cassettes, 10,000 MWCO, 12-30 ml, Thermo Fisher Scientific Inc.). The dialysis was carried three times for one hour each at room temperature with dialysate 300 times the sample volume. The conjugate dye was stored in a cooler prior use. The solution is diluted to 2.5 mg/mL for the experimental procedures.

7.3.2 Convection background and setup

In CED, an infusion into the brain establishes a radial flow outward from the needle tip. The average velocity of infusate in the tissue V_c decays as $1/r^2$, where r is the distance from the needle tip. For a volumetric infusion rate of 1 μL·min^{-1}, a typical value in rodent experiments, V_c ranges from 670 to 3.0x10^{-7} m·s^{-1}, from the needle tip to r = 1.5 cm [16, 17]. The pressure gradient associated with this flow can be calculated from Darcy's law, provided that the porosity Φ and hydraulic permeability κ of the tissue can be estimated. For brain tissue, avian muscle, and agarose brain phantom estimates are κ_{brain}=5.63 x 10^{-12}, κ_{muscle}=5.00 x 10^{-14}, $\kappa_{agarose}$=2.05 x 10^{-12} and Φ_{brain}=20%, Φ_{muscle}=1.6%, $\Phi_{agarose}$=90% [16-19]. To achieve values of V_c that are similar to those in CED, pressure gradients were applied across the equine brain, avian muscle and brain phantom samples in conjunction with topical application of EBD.

A convection chamber was constructed and used to apply pressure gradients of 1330 $kPa \cdot m^{-1}$ for the brain and phantom samples, and 6650 $kPa \cdot m^{-1}$ for the avian muscle samples shown in Figure 7.1. In this system, the average velocity flow due to the applied pressure gradient is unidirectional and constant throughout the sample. The sample was held in place at the bottom of a cylindrical chamber, which was filled with EBD solution to a height of 5 cm. The bottom of the chamber contained a hole that opened into a collection chamber. The tissue sample was placed on a screen that covered the hole.

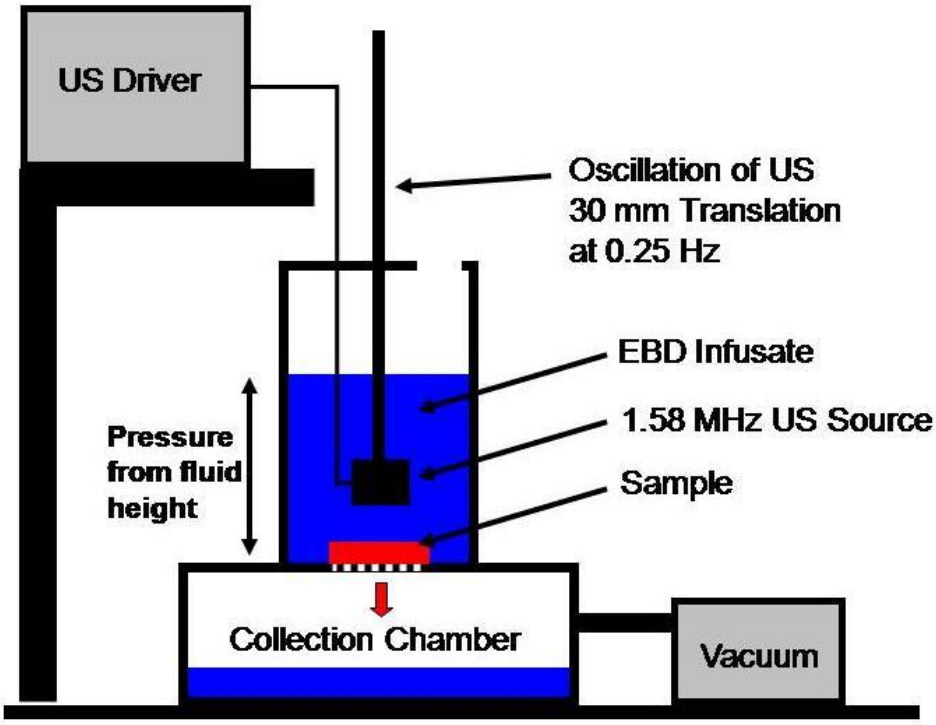

Figure 7.1. Experimental setup for ultrasound-enhanced convection. A 1.58MHz transducer sonicated the sample for 1-30 min. The pressure gradient across the sample was primarily provided by a vacuum pump, which induced convective flow through the sample.

The pressure in the collection chamber was reduced to the appropriate value for each sample by drawing a vacuum (Model 2534B-01, Welch Inc., Niles, IL). The resulting values of V_c were estimated from the applied pressure difference across the sample,

including the hydrostatic pressure from the liquid above the sample. For the specimens in this study we estimated V_c as 3.75 x 10^{-5}, 2.02 x 10^{-5} and 2.98 x 10^{-6} $m \cdot s^{-1}$ for the brain, muscle and phantom samples respectively.

7.3.3 Ultrasound setup and dosing

Ultrasound (US) energy was generated by a lead zirconate titanate (PZT-4), 1.58 MHz, 25.4 mm diameter piezoelectric ceramic with radius of curvature corresponding to 40 mm (EBL Products Inc., Hartford, CT). The transducer was driven at 1.58 MHz. US was applied at 100% duty cycle at the power of 1.30 and 5.25 W corresponding to a maximum acoustic intensity at the focal zone of 10.3 and 41.8 W/cm^2 in the sample's geometric center for durations of 1 to 30 min. The transducer was positioned with its focus at the sample-tracer interface. To increase the sonicated volume of tissue, the transducer was translated periodically over a distance of 30 mm perpendicular to the sample's surface at 0.25 Hz. The transducer was driven by a custom-built portable system and calibrated using a force balance technique in which we measured the force that the ultrasound exerted on an acoustic absorbing object [20]. The temperatures of the sonicated samples were recorded with a calibrated thermocouple placed 1.5 cm from the focus (Model 52II, Fluke Inc. Everett, WA).

7.3.4 **Data analysis**

The experiment was run for the three tissue samples and EBD tracer for 1, 2, 3 and 4 min with and without the applied pressure gradient and with and without exposure to ultrasound. For the phantom samples we collected additional data sets with EBD and AcEBD at 1, 2, 4, 6, 8, 10, 15 and 30 min with and without the applied pressure gradient and with and without exposure to ultrasound. For data analysis a 3 mm slice was taken from the geometric center of each sample. The intensity profile

was measured as in our previous studies [10, 11]. Area under the curve was calculated to quantify the amount of EBD uptake in each case. Phantom samples were further analyzed by plotting the dimensionless color intensity concentration profile $C(x)/C_i$ where C_i was the optically measured color intensity of the tracer at the sample interface and $C(x)$ was the color intensity as a function of distance into the sample as discussed in chapter 7. For EBD and AcEBD 1-30 min data sets, background noise is reduced to improve data interpretation by fitting the diffusion tail to equation 6.3 as in Chapter 6, Figure 6.4.

7.4 Results

In this section we present results for EBD and bovine serum albumin conjugated EBD (AcEBD) distribution in the tissue samples under the experimental conditions described in the methods section.

The distance of tracer penetration into all samples increased in the following order:

No applied pressure gradient and no ultrasound

Applied pressure gradient and no ultrasound

No applied pressure gradient and 1.3 W ultrasound

No applied pressure gradient and 5.25 W ultrasound

Applied pressure gradient and 1.3 W ultrasound

Applied pressure gradient and 5.25 W ultrasound

For the two tracers, EBD penetrated further into the samples under test at the various time points as compared to AcEBD. Ultrasound exposure led to increases in the sample temperature tabulated in Table 7.1. For equine brain and brain phantom, temperature changes were similar among the samples. Temperature increases for avian

muscle tissue were slightly larger. No tissue damage or changes in tissue morphology were observed in any sample.

Figures 7.2 and 7.3 show the EBD intensity as a function of distance into the sample for avian tissue after 4 min, brain tissue after 2 min and brain phantom after 1 min. The red curve shows the profile with no applied pressure gradient and no ultrasound; in this case EBD transport is purely diffusive. The green curve shows the profile with an applied pressure gradient but no ultrasound, which simulates CED. The blue curve shows the profile for tissue exposed to ultrasound with no applied pressure gradient. The yellow curve shows the profile for tissue exposed to ultrasound with an applied pressure gradient, which simulates an ultrasound-enhanced CED. For both power levels the combined effect of ultrasound and an applied pressure gradient gave greatest EBD uptake in all tissues.

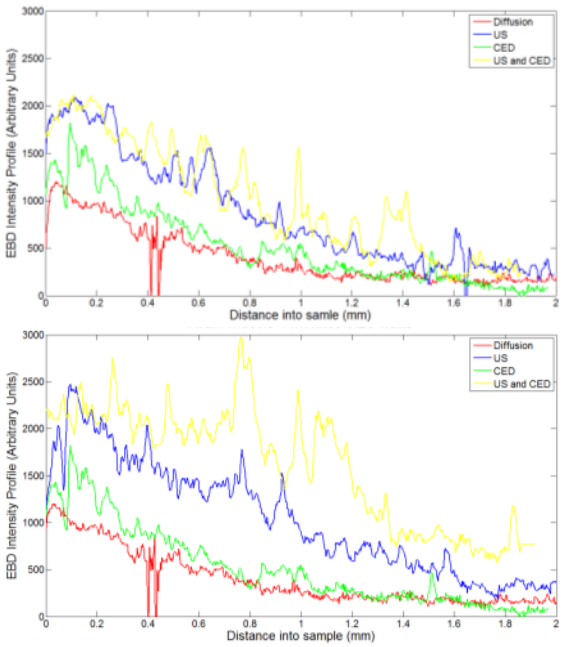

Figure 7.2. EBD profile of avian muscle tissue after sonication at 1.3 W (top) and 5.25 W (bottom) for 4 min. US combined with CED provided greatest EBD uptake enhancement of 240% (left) and 390% (right) as compared with diffusion alone.

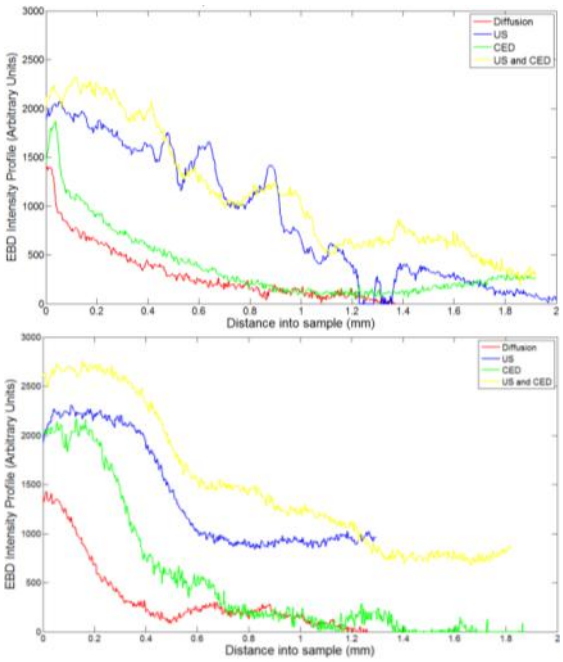

Figure 7.3. EBD profile of equine brain tissue (top) and brain-mimicking phantom (bottom) after 5.25 W sonication for 2 and 1 min, respectively. US combined with CED provided greatest EBD uptake enhancement of 560% (left) and 880% (right) compared with diffusion alone.

Figure 7.4 is a compilation of sectional EBD profile images used to produce Figures 7.2 and 7.3. Moving from left to right across the columns in the image shows the enhancement of EBD penetration into the three samples.

As in our previous studies [10, 11], the EBD intensities at the tissue/dye interface (x=0 mm) are not identical in the four cases in each Figure. This suggests the presence of a mass transfer resistance at the surface of the samples. Apparently, the application of ultrasound at 1.3 and 5.25 W decreases this mass transfer resistance at the interface and increases uptake into the sample.

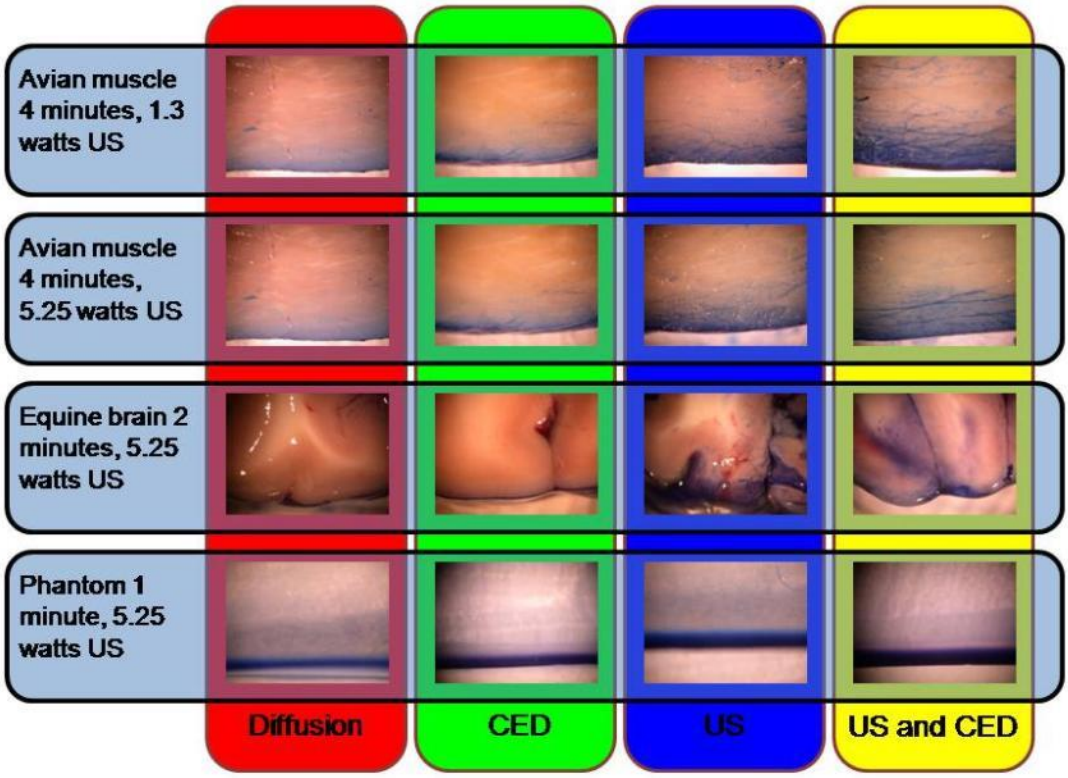

Figure 7.4. Compilation of sectional profile images to produce EBD profile curves in Figures 1 and 2

Table 7.1. Percent enhancement of EBD uptake into tissue samples as compared with diffusion alone. The corresponding temperature changes in the samples during US application is also shown.

Sample and US Power	CED	US	CED and US	Temperature Change
Avian Muscle 1.3 W	130%	220%	240%	4 ºC
Avian Muscle 5.25 W	130%	260%	390%	7 ºC
Equine Brain 5.25 W	185%	450%	560%	1 ºC
Brain Phantom 5.25 W	310%	590%	880%	2 ºC

The profile curves of Figure 7.5 show the dimensionless EBD and AcEBD concentration C/C_i as a function of distance into brain phantoms. The Figure shows that C/C_i decrease significantly for diffusion just a few millimeters away from the dye/sample interface. The effect of exposing the tissue to convection and ultrasound while the compound diffuses through the sample improves tracer penetration over all

time points studied and for the two different size molecules. Ultrasound combined with convection improved the perfusion of EBD by 277% and AcEBD by 327% as compared to diffusion of the two molecules into the phantom over 30 minutes.

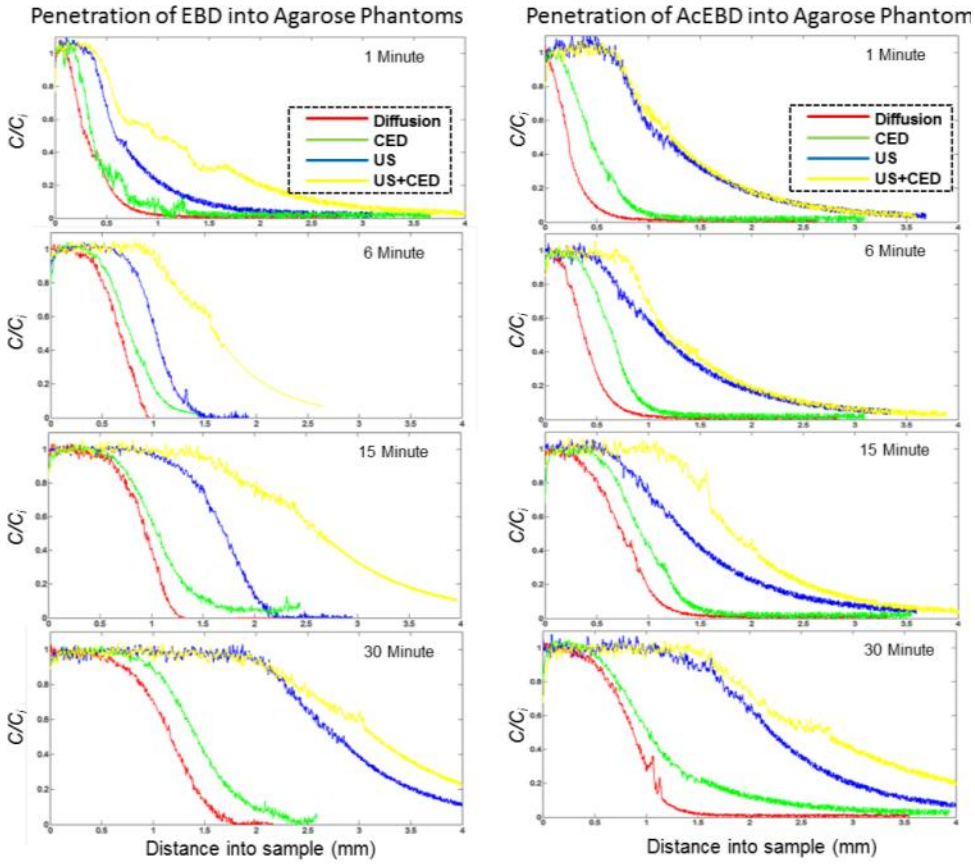

Figure 7.5. Dimensionless concentration profiles of EBD (left) and AcEBD (right) for brain-mimicking phantom after 5.25 W sonication for 1-30 min. US combined with CED provided greatest EBD and AcEBD uptake enhancement of 277% (left) and 327% (right) compared with diffusion alone at 30 minutes.

The shapes of the concentration profiles in Figures 7.2, 7.3 and 7.5 for cases with ultrasound suggest that ultrasound provides a mass transfer mechanism in addition to diffusion. The nearly flat profiles the EBD/sample interface (x=0) suggest a convection-dominated regime in this region. Further into the samples, the steeper

concentration gradients that are found are consistent with mass transfer dominated by diffusion.

Temperature rise in the tissue samples from the absorption of ultrasound is a possible source of diffusion enhancement. According to the Stokes-Einstein relation, the diffusivity is directly proportional to temperature and inversely proportional to solvent viscosity. For a 4 and 7 ºC increase in temperature, the diffusivity would increase by 11% and 16%, respectively, which is insufficient to explain the observed increases in EBD and AcEBD uptake, suggesting that enhanced diffusion due to tissue heating is not the dominant mechanism for enhanced EBD and AcEBD uptake.

7.5 Conclusion

We studied effects of therapeutic 1.58 MHz focused ultrasound at 1.3 and 5.25 W spatial-average power levels in combination with convective flow on the uptake of Evans blue dye into avian muscle, equine brain and neurological-tissue-mimicking phantoms. Furthermore, we evaluated the penetration of Albumin conjugated Evans blue dye into phantoms over longer experimental exposure times. Ultrasonic power levels were applied below tissue damage thresholds for short sonication times. Convection velocities were in the range of typical CED infusions in rodent brain. The study showed enhanced penetration effects when ultrasound was combined with CED in all samples at both power levels. The results suggest that CED in combination with ultrasound may enhance the penetration of therapeutics in the brain and increase the concentration of infused drugs over the penetration distance, which may improve the outcome of CED therapy. These promising results support further evaluation and examination of ultrasound-assisted CED *in vivo.*

REFERENCES

[1] Guerin, C., Olivi, A., Weingart, J., Lawson, C., & Brem, H. (2004). Recent advances in brain tumor therapy: local intracerebral drug delivery by polymers. *Inv. New drugs*, 22, 27-37.

[2] Panyam, J. & Labhasetwar, V. (2003). Biodegradable nanoparticles for drug and gene delivery to cells and tissue. *Adv. Drug Del. Rev., 55*(3), 329-347.

[3] Westphal, M., Hilt, D., Bortey, E., Delavault, P., Olivares, R., Warnke, P., Whittle, I., Jääskeläinen, J., & Ram, Z. (2003). A phase 3 trial of local chemotherapy with biodegradable carmustine (BCNU) wafers (Gliadel wafers) in patients with primary malignant glioma. *Neuro-Oncol. 5*(2), 79-88.

[4] Bobo, R.H., Laske, D.W., Akbasak, A., Morrison, P.F., Dedrick, R.L., Oldfield, E.H. (1994). Convection-enhanced delivery of macromolecules in the brain. *Proc. Natl. Acad. Sci. USA, 91*, 2076–2080.

[5] Vogelbaum, M.A. (2007). Convection enhanced delivery for treating brain tumors and selected neurological disorders: Symposium review. *J. Neuro-Oncol., 83*: 97-109.

[6] S. Mitragotri (2004). Sonophoresis: a 50-year journey. *Drug Discov. Today, 9*(17), 735-736.

[7] Lavon, I., & Kost, J. (2004). Ultrasound and transdermal drug delivery. *Drug Discov. Today*, *9*(15), 670-676.

[8] Guzman, H.R., Nguyen, D.X., McNamara, A.J., & Prausnitz, M.R. (2002). Equilibrium loading of cells with macromolecules by ultrasound: Effects of molecular size and acoustic energy. *J. Pharm. Sci., 91*, 1693–1701.

[9] Keyhani, K., Guzman, H.R., Parsons, A., Lewis, T.N., & Prausnitz, M.R. (2001). Intracellular drug delivery using low-frequency ultrasound: Quantification of molecular uptake and cell viability. *Pharm. Res., 18,* 1514–1520.

[10] Lewis, G.K., & Olbricht, W.L. (2007). A phantom feasibility study of acoustic enhanced drug perfusion in neurological tissue. *Proc. IEEE, LISA 2007,* 67-70..

[11] Lewis, Jr. G.K., Olbricht, W.L., & Lewis Sr.,G.K (2007). Acoustic targeted chemotherapy in neurological tissue. *J. Acoust. Soc. Am.,* 122, 3007.

[12] Chen, Z., Gillies, G., Broaddus, W., Prabhu, S. et al. (2004). A realist realistic tissue phantom for intraparenchymal infusion studies. *J. Neurosurg. 101*(2), 314-322.

[13] Woitzik, J., & Schilling, L. (2007). A new method for superselective middle cerebral artery infusion in the rat. *J. Neurosurg., 106(*5), 872-878.

[14] Aoki, T., Sumii, T., Mori, T., Wang, X., & Lo, EH. (2002). Blood-brain barrier disruption and matrix metalloproteinase-9 expression during reperfusion injury. *J. Stroke. 33*, 2711.

[15] Chan, P., Fishman, R., Caronna, J., Schmidley, J.W., Prioleau, G., & Lee, J. (2006). Induction of brain edema following intracerebral injection of arachidonic acid. *Ann. Neurol., 13*(6):625-632.

[16] Neeves, K.B., Lob, C.T., Foley, C.P., Saltzman, W.M., & Olbricht, W.L. (2006). Fabrication and characterization of microfluidic probes for convection enhanced drug delivery. *J. Cont. Release,111*(3), 252–262.

[17] Neeves, K.B., Sawyer, A.J., Foley, C.P. Saltzman, W.M., & Olbricht, W.L. (2007). Dilation and degradation of the brain extracellular matrix enhances penetration of infused polymer. *Brain Res., 1180,* 121-132.

[18] Datta, A.K. (2006). Hydraulic Permeability of Food Tissues. *Int. J. Food Prop., 9*(4), 767–780.

[19] Deumier, F., Trystram, G., Collignan, A., Guedider, L., & Bohuon, P. (2003). Pulsed vacuum brining of poultry meat: interpretation of mass transfer mechanisms. *J. Food Eng*., *58*(1), 85-93.

[20] Maruvada, S., Harris, G. R., Herman, B. A., King, R.L. (2007). Acoustic power calibration of high-intensity focused ultrasound transducers using a radiation force technique. *J. Acoust. Soc. Am., 121*(3), 1434-1439.

CHAPTER 8

ULTRASOUND ASSISTED CONVECTION ENHANCED DRUG DELIVERY TO THE BRAIN *IN VIVO* WITH A NOVEL TRANSDUCER CANNULA ASSEMBLY[13,14]

8.1 Abstract

In traditional convection enhanced delivery (CED), drugs are infused locally into tissue through a cannula inserted into brain parenchyma. Transport of the infused material is dominated by convection, which enhances drug penetration into tissue compared with diffusion mediated delivery. Ultrasound has been shown to assist and/or mediate the delivery of pharmaceuticals across membranes and through tissues. The purpose of this study was to demonstrate the feasibility of ultrasound-assisted convection enhanced delivery (UCED) to the brain *in vivo* using rats with a novel, low profile transducer cannula assembly (TCA), and portable and pocket-sized ultrasound system. A total of 40 Sprague–Dawley rats (350 to 450 g) were divided into two equal groups and further divided into four equal subgroups (n=5 in each). The rats were anesthetized, secured into ear bars on a sterotax, and a craniotomy was performed. The caudate of the rodent brain was infused with 0.25 wt% Evans blue dye (EBD) in Phosphate-Buffered Saline (PBS) at two different infusion rates of 0.25 µL/min for *group 1*, and 0.5 µL/min for *group 2*. Infusion flow rate was slowly increased over 10 minutes from 0.05 to 0.25 µl/min for *group 1* n=20 rodents and 0.1 to 0.5 µl/min for *group 2* n=20 rodents, and maintained at the final flow rate for 20 min thereafter, for a

[13]This work has been filed as Lewis, G.K. Jr., Olbricht, W.L. (2010). Ultrasound assisted brain drug delivery cannula United States Provisional Patent Application. 61311064

[14]This work is in preparation for being published as Lewis, G.K., Jr., Schulz, Z., Pannullo, S., Southard, T., Olbricht. W.L. (2011). Ultrasound assisted convection enhanced delivery in vivo with a novel transducer cannula assembly.

total experiment duration of 30 min in both groups. Using the TCA without ultrasound, the four control subgroups were infused without and with microbubbles (CED and CED+MB). The four UCED subgroups (UCED and UCED+MB) followed the same protocol with the addition of simultaneous continuous wave 1.34 MHz ultrasound operating at a total acoustic power of 0.11 +/- 0.005 W and peak spatial intensity at the cannula tip of I= 49.7 mW/cm^2. Frozen section and histology was performed on the brains, and infusion distribution was three-dimensionally reconstructed using MatLab® analysis. Hematoxylin and Eosin (H&E) staining was used to assess tissue damage and morphological changes to the brain. The application of UCED and UCED+MB improved EBD total volumetric distribution by 2.24 to 3.25 and 1.16 to 1.70 times, respectively ($p<0.001$). On gross and histological examination, no ultrasound or microbubble related damage to the brain tissue was found. The TCA and battery-powered ultrasound device show promise to improve the distribution of infusate during CED in clinical practice.

8.2 Introduction

Convection enhanced delivery (CED) uses a cannula and syringe pump for direct infusion of therapeutics into the brain to bypass the blood-brain barrier [1]. The infusion takes place through a cannula that is inserted directly into brain parenchyma. The infusion establishes a pressure gradient in the tissue that causes material to flow outward from the needle tip. Small molecules such as sucrose can be transported effectively by convection. However, larger molecules such as proteins may interact with components of the extracellular matrix (ECM) and with cell membranes, which can inhibit their transport. Furthermore, many therapeutics of clinical interest are subject to elimination by several mechanisms, including clearance into capillaries, binding to cell membranes, internalization into cells, and enzymatic metabolism. The

distance that a therapeutic penetrates into the brain and its concentration profile in the interstitium depend on relative rates of convection and elimination. In principle, increasing the infusion rate can increase the rate of convection and thereby increase the distance that infused molecules penetrate at therapeutically useful concentrations. However, brain tissue is poroelastic, and it deforms in response to the local pressure associated with the infusion. For sufficiently high infusion rates, the tissue separates from the outer surface of the infusion needle, which opens a gap allowing infused material to escape the parenchyma [2,3]. Although judicious catheter designs can reduce this effect, backflow along the outside of the needle sets an upper limit on the infusion rate, which, in turn, sets an upper bounds on the convection rate and penetration distance in the parenchyma.

Extending the penetration distance in CED is essential for the treatment of glioblastoma multiforme (GBM), a high-grade glioma that is usually treated with tumor resection, external beam irradiation and chemotherapy. However, GBM characteristically has diffuse boundaries, and invariably malignant cells have migrated away from the main tumor prior to resection, thus limiting the impact of surgery. Traditional chemotherapy and radiation therapy administered post-resection are unable to eliminate all of the remaining malignant cells. As a result, the malignancy recurs, usually within 1 cm of the original tumor. Median survival is approximately one year after the diagnosis of GBM [4].

In both small and large animal models, convection enhanced delivery (CED) has been used to infuse a variety of compounds including small molecules [1,5,6], larger molecules [1,7-9], therapeutics encapsulated in liposomes [10] and nanoparticles [11]. In human clinical trials, CED has been used with both single and multiple cannula placements to deliver a variety of agents directly into the brain [12-14]. The results of these studies are highly variable, but some have shown that infused

therapeutics can penetrate deep into the brains of small animals with tumor xenografts [10], and these studies often show corresponding decreases in mortality. In larger animals and human trials, however, delivery of the drug to malignant cells remains a major challenge for CED [15,16], as described in recent reviews [17-19].

New applications of ultrasound for drug delivery have been evolving over the last two decades. Transdermal drug delivery via sonophoresis or cavitation-based delivery has been extensively studied in both animals and humans [20-23]. Ultrasound exposure of skin to a wide range of frequencies increases the permeability of the stratum corneum, increasing and the transport rates of therapeutics through the epidermal layers . Although a variety of thermal and non-thermal mechanisms could be important, a consensus among investigators who have studied the effect of ultrasound parameters on transport enhancement is that the underlying mechanism is acoustic cavitation [24, 25]. Large implosion forces and micro jets generated during the collapse of cavitation bubbles at the skin surface disrupt the cellular layers, opening paths to underlying tissue and capillaries. At lower power levels, ultrasound can generate acoustic streaming, which is a local convective motion of liquid due to oscillating bubbles. If the liquid contains a concentration gradient of a solute, acoustic streaming can enhance mass transfer of the solute without inducing a significant bulk motion of the liquid. Recently, high intensity focused ultrasound (HIFU) has been shown to be an effective tool to target systemic drug treatments [26, 27]. Where ultrasound mediated disruption of the blood brain barrier is being studied to help drugs escape the blood stream and enter the brain [27]. Ultrasound has also been shown to enhance the convective transport of molecules in agarose, muscle and brain tissue *in vitro* [28-30].

In this study we demonstrate that ultrasound may be applied in conjunction with CED to enhance the penetration of small molecules in the caudate of the rat

brain. Additionally, we show that this may be done with a novel 0.64 cm diameter 1.34 MHz transducer cannula assembly (TCA) developed in our laboratory, powered by an ultralow-output impedance hand-held ultrasound generating device that costs under $200.00 in parts [32,33,36]. Although we constructed a special TCA for this experiment, the results imply that ultrasound may also improve the distribution volume for other catheter designs that have been introduced. The ability of ultrasound to improve CED, and the portability and low-cost of the ultrasound generating technology, suggests great promise in progressing CED in medical applications.

8.3 Methods

8.3.1 Ultrasound Transducer and Cannula Assembly

The ultrasound transducer cannula assembly (TCA) consists of three main parts: 1. A cylindrical lead zirconate-titanate (PZT-4) ceramic, 2. A 30 gauge infusion needle and 3. A sterotaxic guide arm for precision alignment. The TCA is a novel axial resonating device that provides a cylindrical therapeutic acoustic field around the infusion needle during stereotaxic guided CED treatment.

As shown in Figure 8.1, a 3x3 cm sheet of polarized 1.34 MHz PZT-4 (EBL-4, EBL Products Inc) with gold electrodes was machined into a cylinder with diameter of 0.64 cm using a CNC milling machine (5400, Sherline Products Inc.) and general diamond tipped bore. The center of the cylindrical ceramic was found, and a precision diamond grinding point (4376A11, McMaster-Carr Inc.) was used to grind a 0.08 cm diameter hole through the center. All of the ceramic machining was conducted under a water bath to prevent toxic dust particles and remove heat generated from tooling process. The grinding point was also used to remove gold conductor from the top (inside) surface around the hole in the ceramic to electrically isolate the brass tube from the top surface.

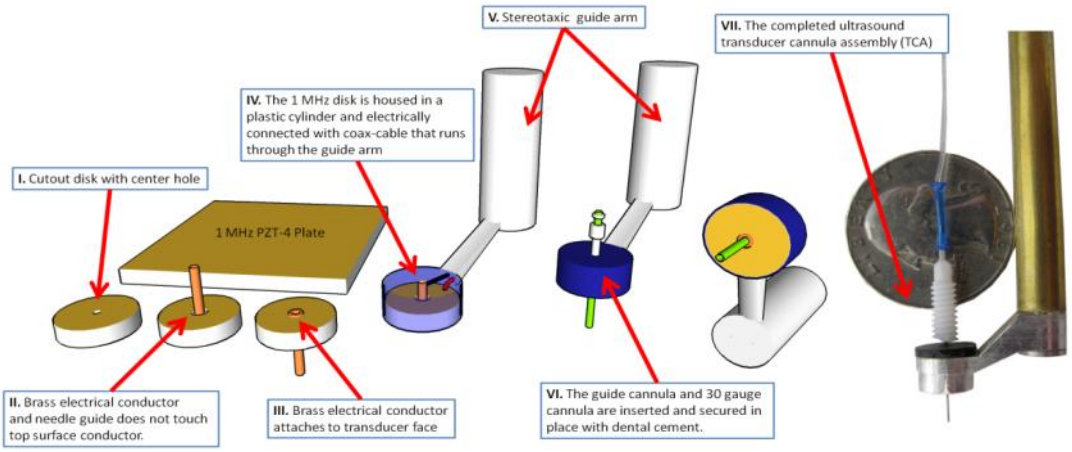

Figure 8.1. Construction of the transducer cannula assembly. I. Machine the PZT-4 into a disk with center hole. II. Connect a brass tube to front face of ceramic using solder. III. Place the ceramic in a watertight PVC/aluminum housing with sterotaxic guide arm, and connect ground and hot leads to the transducer through the guide arm. V-VI. Attach the guide-cannula and infusion cannula to the transducer and secure to the popper height with epoxy. VII. Actual finished device.

The brass tube was flanged and inserted through the hole in the ceramic, and connected to the front face (bottom surface) with solder. The ceramic with brass tube was then placed in a low-profile PVC/aluminum assembly (Air-backed) with a sterotaxic guide arm as shown. The brass tube (electrical-ground) and top surface (electrical-hot) of the ceramic were wired through the stereotaxic guide arm with 5 Ω coax-cable (NMEF 1/22-15044 SJ, Cooner Wire Inc.). A 30 gauge cannula-guide and 11 mm infusion cannula (8IC317I and 8IC317G, Plastics One Inc.) were mounted onto the assembly and affixed to the housing with 5-minute epoxy. The infusion cannula was positioned through the center of the assembly and perpendicular to the face of the transducer, to allow 5 mm of length from the face of the transducer to the cannula's tip. The electrical impedance of the transducer cannula assembly (TCA) was

measured using commonly known methods, to determine the resonant frequency for efficient ultrasound generation [31].

8.3.2 Pocket-sized Ultrasound System

The principles underlying the technology and construction of battery powered, pocket-sized ultrasound systems have been described elsewhere [32-36]. Here we briefly present a new ultralow output impedance ultrasound driver, based off of a 16-MOSFET, surface mount component, printed circuit board (PCB) design, and its application in ultrasound-assisted convection enhanced delivery to the brain.

The ultralow output impedance ultrasound driver was constructed on a double-sided PCB, which was designed and created using PCB123® Layout V2 software from Sunstone Circuits Inc. The 3.8 x 7.62 cm PCB has 16 N/P channel parallel MOSFETs in a transistor-transistor logic (TTL) timing configuration to provide efficient voltage transfer from the driver to the ultrasound transducer. The ultrasound driver, 1.34 MHz crystal clock oscillator (ECS-100A-010, ECS Inc.) to time the driver at the resonance of the TCA, and three 7.4 V 2400 mAh rechargeable lithium ion battery packs (18650, Portable Power Inc.) wired in series are all enclosed in an ergonomic 12.2 x 7.9 x 3.3 cm plastic enclosure (PPLX, PacTec Inc). Power from the system may be made adjustable by switching between system battery packs to provide control of the clamped push-pull square wave drive signal between +/-7.4 or +/- 11.1 V. For the purpose of this experiment the system was used at +/- 11.1 V setting because of the high electrical impedance of the TCA. The ultrasound technology is available through contacting the authors.

8.3.3 Ultrasound Exposimetry

The peak ultrasonic intensity of the acoustic field was measured with an omnidirectional reference hydrophone (HNR 1000, calibrated July 12th 2010, Onda Inc.) in parallel planes 0.25 mm from the TCA's face and at the cannula tip (5 mm from the TCA face). The TCA was submerged in a distilled and degassed (2 ppm) water tank (30 x 30 x 85 cm in size) that was made almost completely anechoic by placing a 1.27 cm thick wall of sound absorbing rubber around its wall (8456K417, McMaster-Carr Inc).

Precise, micromanipulator-controlled positioning of the hydrophone was performed by hand using micro milling machine (5400, Sherline Products Inc.). Ultrasonic waves detected by the hydrophone were recorded by measured voltages using a digitizing oscilloscope (TDS2002B, Techtronix Inc.) and converted into intensity measurements using a calibration table provided by Onda Inc. The scanning step size for each plane was 1 mm and the scanning area was 10 x 10 mm. Spatial peak-temporal peak-intensity were determined for each plane by scanning with the hydrophone in 1 mm increments and averaging over 3 measurements [37,38]. The total acoustic power was measured with a radiation force balance system (RFB 2000, Onda Inc.) using a rubber disk absorbing target (RFB CTK, Onda Inc.) in distilled and degassed water. We compared these results with electrical measurements of intensity and power using the electrical properties of the TCA and measured ultrasonic power conversion efficiency from the Mason transmission line model [32, 33, 36].

8.3.4 Animal Experiments

Rats were anesthetized and euthanized by procedures approved by the Institutional Animal Care and Use Committee (IACUC) at Cornell University. A total of 40 Sprague–Dawley rats (350 to 450 g) were divided into two groups with four

subgroups (5 rats in each subgroup). Animals were anesthetized by inhalation of isoflurane gas and secured in a stereotaxic frame. The head was shaved, 0.5 ml of bupivicaine was applied under the skin as a local anesthetic and an incision was made in the skin along the dorsal midline of the skull. A small craniotomy (6-7 mm diameter) was made over the left side of the exposed skull using a dental drill. The TCA was guided using a micromanipulator to +0 mm anterior, +3 mm lateral and -5.5 mm ventral from bregma, lowered at 0.25mm per second into the caudate of the rat brain and allowed to equilibrate for two minutes. 1-2 ml of artificial cerebral spinal fluid (aCSF) and a gel-foam dam was used to couple acoustic energy from the face of the TCA into the rodent brain. The TCA was powered on with the pocket-sized ultrasound system at the +/-11.1 V setting and infusion began.

For each rat, the entire experiment lasted a total of 30 min. The control subgroups of CED and CED+MB (n=5 in each) were infused using the TCA with no ultrasound therapy for 30 min. For the experimental subgroups of UCED and UCED+MB (n=5 in each), infusion and ultrasound exposure at an acoustic power of 0.11 +/- 0.005 W, and TCA face intensity of 0.095 W/cm^2 which corresponded to a cannula tip intensity of 0.0497 W/cm^2 for 30 min was applied simultaneously. Filtered Evan's blue dye (EBD) 0.25 wt% in phosphate buffered saline (PBS) without or with 5 x 10^5 stabilized microbubbles per μL with median diameter of 2.5 μm (Targestar^{TM}-P, Targeson Inc.) was infused using a microinfusion pump (Worker Bee^{TM}, Bioanalytical Systems, Inc.).

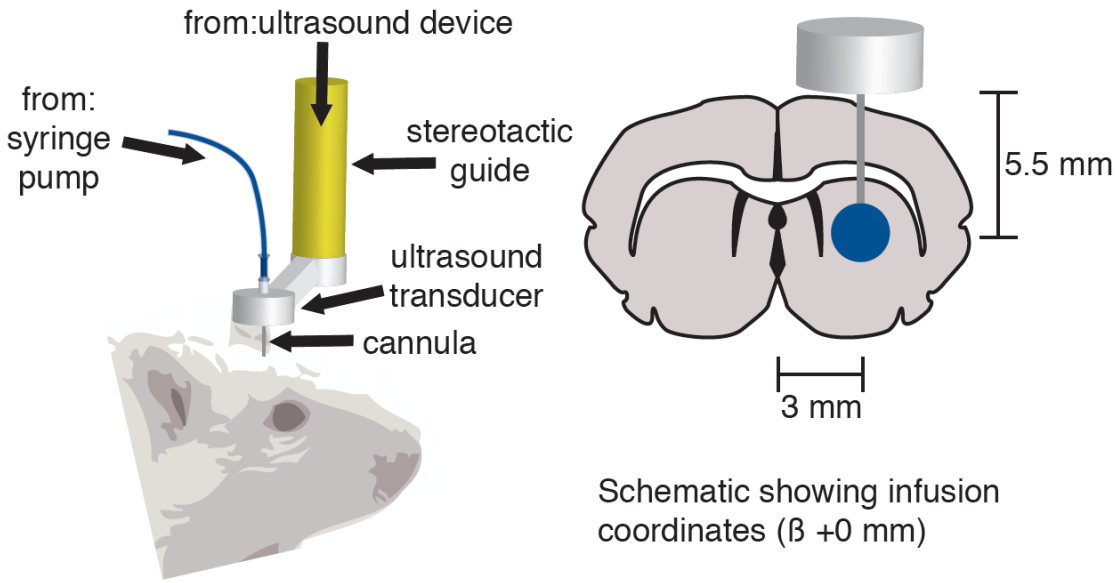

Figure 8.2. Animal experimental setup for using TCA in rat brain. The rat is secured with ear bars in a stereotaxic frame and a small craniotomy is performed on the left hemisphere. The TCA is guided 5.5 mm deep into the caudate of the rat brain.

The starting infusion flow rate for the experiments of *group 1* was 0.05 µL/min for 5 min, the infusion flow rate was then increased to 0.1 µL/min for an additional 5 min, to the final flow rate of 0.25 µL/min for 20 min. For *group 2* the starting infusion flow rate was 0.1 µL/min for 5 min, the infusion flow rate was then increased to 0.25 µL/min for an additional 5 min, to the final flow rate of 0.5 µL/min for 20 min. After 30 min of simultaneous infusion and ultrasound therapy the experiment was stopped. The TCA was left in the tissue for 1-2 min before being removed while euthanasia via cardiac urethane injection was performed. The animal was removed from the stereotaxic frame and immediately perfused with 200 mL of PBS followed by 200 mL 4% paraformaldehyde fix. The brain was then promptly removed from the skull using bone cutters and prepared for frozen section in 30% sucrose and 4% paraformaldehyde solution for one day, and moved to 60% sucrose and 4% paraformaldehyde solution

for another day, before being frozen on dry ice in optimal cutting temperature (OCT) embedding.

8.3.5 Image, Statistical and Histological Analysis

Tissue slices were imaged using a CCD camera (Cannon Power Shot G10, Cannon Inc.) arranged on a cryostat (Microm HM 550, Thermo Scientific®) during frozen section through the brain in the coronal plane. The high resolution 14 Mpix Joint Photographic Experts Group (JPEG) image files were captured at the first visualization of EBD in the brain tissue and after every fith 50 μm brain slice until EBD was no longer distinguishable. The digital image files were cropped to include the rodent brain with a white ring of OCT embedding around its outside and resized to 100 x 70 pixels with a locked aspect ratio using Adobe® Photoshop® for further analysis in MatLab® (Mathworks Inc.).

Each coronal brain section was loaded into MatLab® using the *imread()* function and the pixel to physical length ratio was determined using a calibration ruler measure taken in the picture frame windows. The *imread()* function returned a 100 x 70 x 3 unit8 matrix of Red Green Blue (RGB) 24-bit color intensity data for each pixel in each frame. RGB pixel values making up the white ring of OCT imbedding around the brain tissue section were used to adjust for slight lighting variations between image frames and samples studied. The white OCT RGB pixel values were measured in the top, bottom, left and right quadrants of the image frames, averaged, and used to determine a weighting factor. Across samples on average, the standard white OCT pixels of the data sets had RGB values of Red=171, Green=175 and Blue=177, respectively. These standard OCT values were used to determine each channel's color intensity waiting factor per image frame. Each RGB waiting factor was then applied across the 100 x 70 x 3 unit8 matrix of RGB data frames. For volume distribution

analysis of EBD in the brain section the Red, Green and Blue intensity values that composed each pixel were added algebraically with additional weight placed on the Blue channel (Red channel + Green channel + 2x Blue channel) to generate a 100 x 70 x 1 summed color intensity matrix. A threshold value of 260 intensity counts was experimentally determined to best include all of the EBD pigment image data and was applied across the summed color intensity matrix where any matrix component over 260 was set to 0. The final intensity matrix for each picture frame consisted of 100 x 70 matrix values ranging from 0-260, with 1 being the darkest pigment, 260 being the lightest pigment and 0 acting as an empty matrix space holding component. EBD distribution area in each picture frame was measured by whether or not each pixel in the 100 x 70 matrix picture frame held a value greater than 0. The EBD volume distribution represented by each brain section was calculated by multiplying each frames distribution area by 5 x 50 μm, for a total slice width of 250 μm (to account for all sections each individual slice represented). Each analyzed image section was then placed into a 3D-stack and summed as a whole to obtain the total brain distribution volume of EBD. The 3D stack was additionally compiled using the *contourslice()* and *isosurface()* functions in MatLab® to generate a 3D visualization of each data set and to display the total infusion distribution volume in the rodent brain. The left hemisphere and the left caudate of each rat brain were analyzed separately to compare EBD distribution in the two regions. In analysis of the left caudate, the 100 x 70 pixel image frames of each data set were cropped in Adobe® Photoshop® to include only the gray matter track of the caudate region, and then reanalyzed as before.

Statistical analysis was performed using MatLab®. An ANOVA was used to analyze the statistical significance of the total infusion distribution volumes in the four control and four experiential subgroups. The statistical tests compared if the means from the groups were equal, against the alternative that the means were not equal. The

p-value was used to determine if the difference between groups was significantly greater then chance.

Histological examination was used to determine any acute and morphological changes due to ultrasound-assisted CED. Fixed brain tissue samples from rodents undergoing CED, CED+MB, UCED and UCED+MB infusions were delivered to the Cornell University Veterinary Pathology Department and 10 μm coronal sections at the cannula insertion plane and were collected using the paraffin method, and saved on microscope slides for histology. Histological analysis was conducted by hematoxylin and eosin (H&E) staining of 10 μm sections by the Cornell University Veterinary Pathology Department, and obtaining an independent review from the Pathology Department at Cornell University to determine if any difference between subgroups was found.

8.4 Results

8.4.1 Transducer Cannula Assembly and Ultrasound System

The construction of the TCA required multiple iterations and careful machining because of the fragility of the ceramic. Soldering and final wire connections were completed under stereoscope. The electrical impedance magnitude of the TCA is shown in Figure 8.3. The TCA resonates at 1.18 MHz with a 380 Ω electrical impedance and anti-resonance at 3.1 MHz. The phase angle (not shown) was approximately 0 degrees at resonance. In practice, the TCA was found to operate best when driven at 1.34 MHz with the portable ultrasound generator that was used in this study. Estimates of the acoustic output power and intensity from the Mason transmission line model at 1.34 MHz and the power and intensity measured with the hydrophone were within +/- 10% of each other.

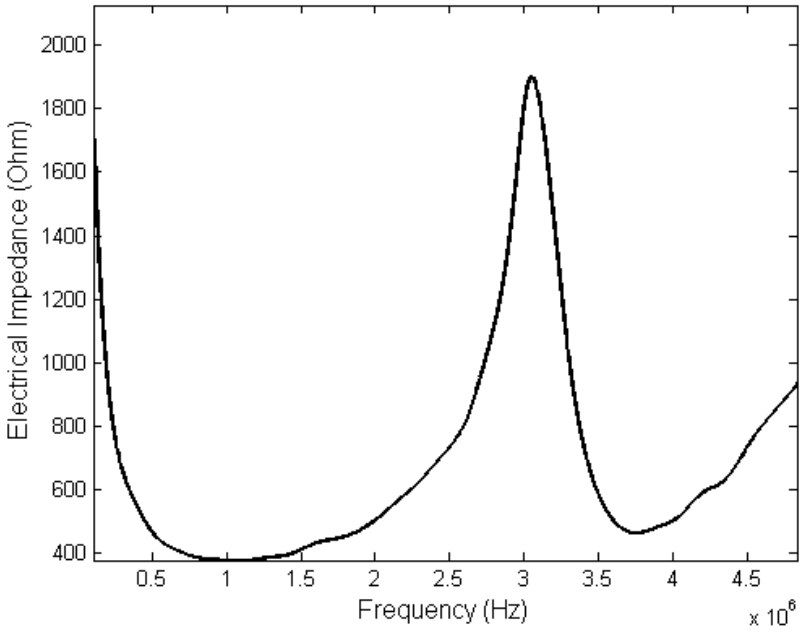

Figure 8.3. Electrical impedance of TCA. Resonance occurs at 1.18 MHz with 380 Ω impedance. The phase angle (not shown) is approximately 0 degrees at resonance. Parallel resonance occurs at 3.1MHz.

The stereotaxic guided TCA allowed for accurate insertion of the infusion cannula into the rat caudate and the portable ultrasound system freed up considerable bench-top space as compared to traditional bench-top RF amplifiers that require wall power. This allowed the experiment to be conducted in a straight forward and repeatable manner.

8.4.2 Ultrasound Dosimetry

The mechanical index (MI) is a standard measure of the acoustic output in ultrasound systems defined as the peak rarefactional pressure of an ultrasound longitudinal wave propagating in a uniform medium, divided by the square root of the center frequency of the transmitted ultrasound wave. According to the FDA for

diagnostic obstetrics application, the MI should not exceed 1.9, and for ophthalmic applications the MI should not exceed 0.2 [39-41]. In order to calculate the maximum MI achieved by the TCA using S.I. units (f=1.34 MHz, I=950 W/m^2), we used the intensity (I) and acoustic impedance of soft tissue (Z~1.6e6 kg/m^{2}s) [42] in order to calculate the pressure (P) and derived the following formula for the TCA to calculate a MI of 0.034 according to:

$$MI = \frac{P}{\sqrt{f}} = \frac{\sqrt{I \cdot Z}}{\sqrt{f}} = \frac{\sqrt{950 \cdot 1.6e6}}{\sqrt{1.34}} \times 10^{-6} = 0.034 \qquad (8.1)$$

Another standard measure is the thermal Index (TI). TI is defined as the ratio of the emitted acoustic power to the power required to raise the temperature of tissue by 1^{o}C. The TI is intended to indicate the likely temperature rise that might be produced after long exposure. A larger TI value represents a higher risk of damage due to temperature increases. For therapeutic applications, the FDA requires that TI's over 6 require further explanation and safety analysis. The calculated soft-tissue thermal index (T_s) using the ultrasound power (P) for the TCA was 0.638 as calculated by:

$$T_s = \frac{P \cdot f}{210} = \frac{(0.11)(1.34e3)}{210} = 0.638 \qquad (8.2)$$

The calculated MI was less than 0.2 and the T_s value achieved was less than 6 for the TCA. The TCA is considered safe according to established FDA guidelines and standards developed from the American Institute of Ultrasound in Medicine.

8.4.3 In Vivo Ultrasound-assisted Convection Enhanced Delivery

Typical raw data sets are presented in Figure 8.4 from the CED (4A), CED+MB (4B), UCED (4C) and UCED+MB (4D) subgroups of *group 2* receiving 0.5μL per min infusions. A red border is shown around the brain section of the cannula insertion point in each of the four subgroups. Image slices in each subgroup are 250 μm apart from one another in both anterior and posterior directions. The results illustrate EBD distribution volume in the rodent brain for 30 min of treatment. Optically quantifiable, EBD pigment is more diffuse and extends over a broader per slice area and total number of slices during UCED and UCED+MB as compared to CED and CED+MB. Backflow of EBD along the needle track into the corpus callosum during 0.5μL per min infusions is also more pronounced in the CED and CED+MB subgroups as compared to the UCED and UCED+MB subgroups. In the slower 0.25μL per min infusions (not shown) backflow as well as convection of EBD into the caudate region was reduced.

Figures 8.5 shows the three-dimensional reconstructions of EBD distribution volumes in the presented brain slices of Figure 4 for the left hemisphere and left caudate of the rodent brain, respectively. Figure 8.5 A-D shows the volume distribution of *group 2* 0.5μL per min EBD infusions during CED, CED+MB, UCED and UCED+MB, respectively. In the CED and CED+MB controls (5A and B) the EBD dye stays in an 810 x 675 x 2500 μm volume around the infusion cannula in the gray matter of the caudate and the highly permeable white matter track of the corpus callosum. In UCED and UCED+MB treatment (5C and D), the EBD penetrates out of the control volume distribution by 2.24 to 3.25 and 1.16 to 1.70 times, respectively ($p<0.001$), and though the entire left caudate in the case of UCED radiating into the ventricles and corpus callosum of the rat brain.

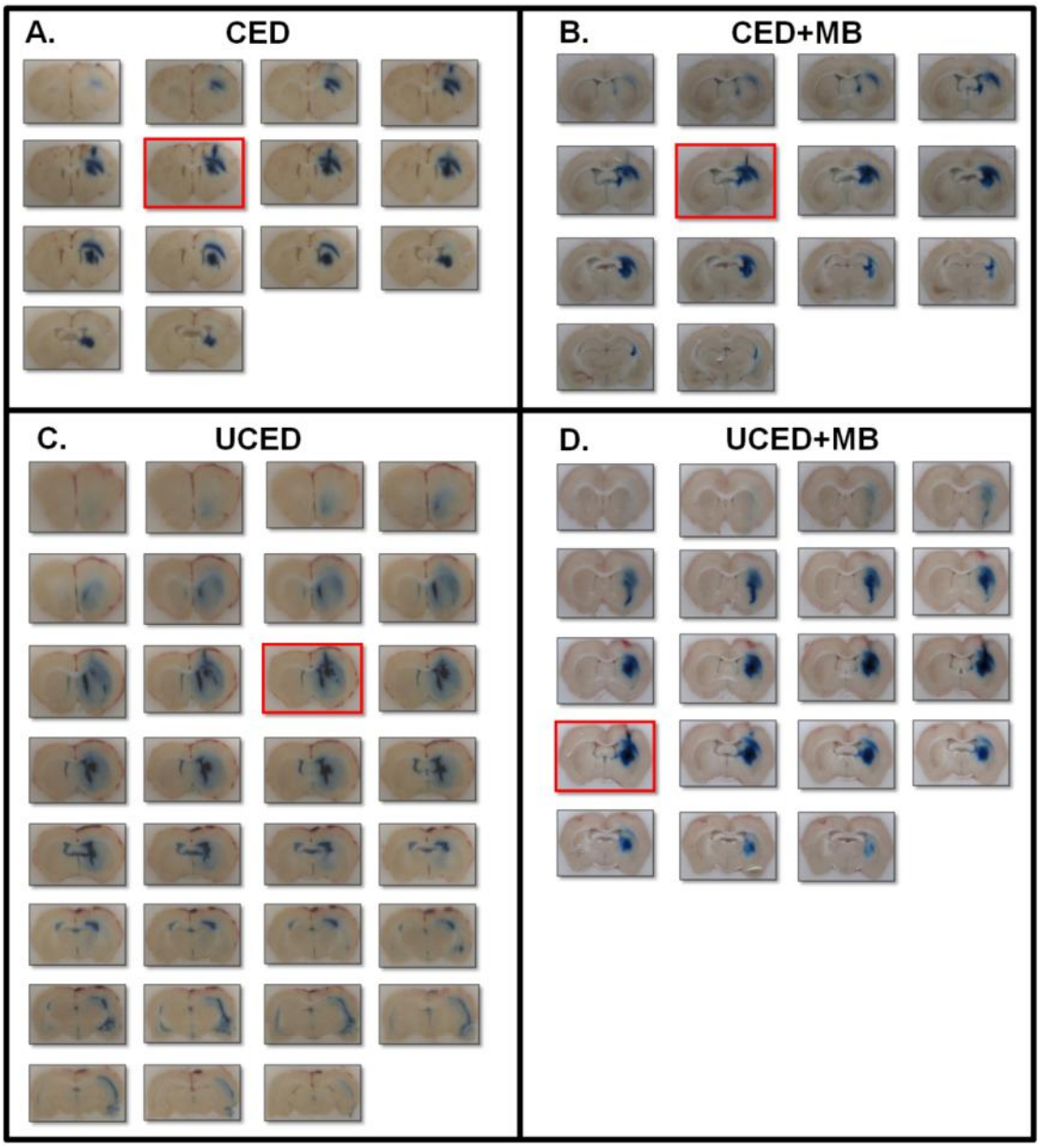

Figure 8.4. Brain sections from the four subgroups of group 2 studied after 30 minutes of Evans blue infusions at 0.5 μL per minute with a 30 gauge cannula. A. Convection enhanced delivery (CED) and B. Convection enhanced delivery with microbubbles (CED+MB) provide similar infusion profiles for the rodents in each group. C. Ultrasound-assisted convection enhanced delivery (UCED) delivers EBD further into the brain and more diffusely spread across the caudate. D. Ultrasound-assisted convection enhanced delivery with microbubbles (UCED+MB) shows further EBD penetration over CED and CED+MB, but is more localized in the rodent caudate versus UCED which spreads EBD out of the caudate region. Backflow of EBD along the needle track into the white matter track of the corpus callosum is reduced with UCED and UCED+MB as compared to controls.

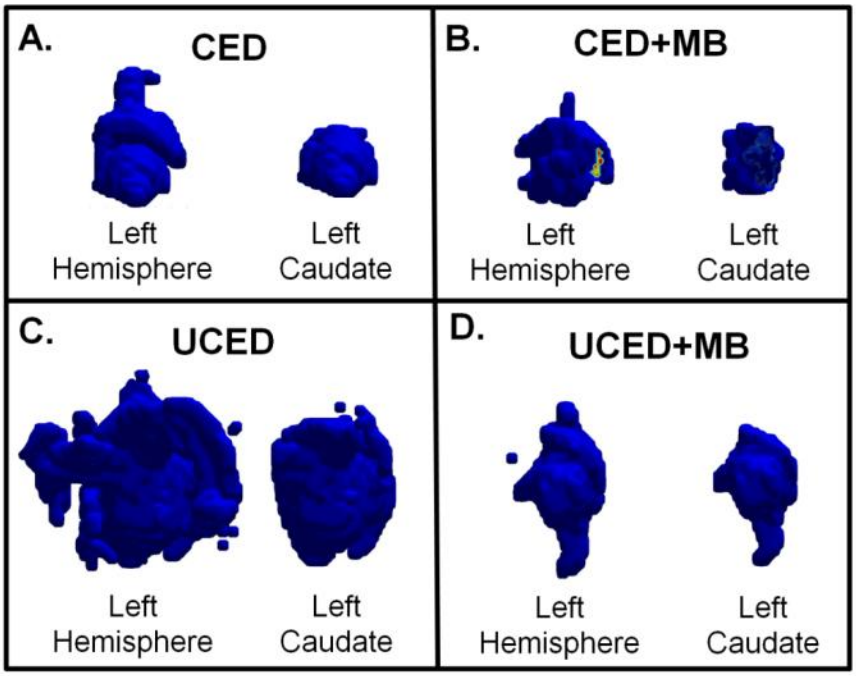

Figure 8.5. 3D Infusion reconstruction of the four subgroups of group 2 brain sections from Figure 4. The cannula is in the plane of the Figure and the transducer cannula assembly (TCA) is positioned at the top of each Figure. A. Convection enhanced delivery (CED). B. Convection enhanced delivery with microbubbles (CED+MB). C. Ultrasound-assisted CED (UCED). D. Ultrasound-assisted CED with microbubbles (UCED+MB)

MatLab® analysis comparing the total distribution volume of EBD in the rodents' left hemisphere and left caudate for the two 0.25 and 0.5µL per min infusion groups and respective subgroups is shown in Figure 8.6. ANOVA analysis between the subgroup means was statistically significant $p<0.05$ and $p<0.001$ with standard deviations of the CED, CED+MB, UCED and UCED+MB groups of 0.29, 1.50, 0.67 and 1.68, respectively in the left brain, 0.41, 1.95, 0.71 and 0.65, respectively in the left caudate for 0.25µL per min infusion of *group 1*, and 1.90, 5.31, 0.56, 1.25, respectively in the left brain, 0.62, 1.99, 0.36, 0.40, respectively in the left caudate for 0.5µL per min infusion of *group* 2. UCED and UCED+MB increased the distribution volume of EBD by 2.24x and 1.37x (46.3 mm^3 and 26.9 mm^3) as compared to CED

and CED+MB (20.6 mm^3 and 19.7 mm^3) in the left hemisphere of the rodent brain in *group 1*, respectively. Within the left caudate of *group 1*, UCED and UCED+MB increase the distribution volume of EBD by 2.44x (33.1 mm^3) and 1.7x (27.0 mm^3) as compared with CED (13.6 mm^3) and CED+MB (15.9 mm^3), respectively. For the higher infusion rate of *group 2*, UCED and UCED+MB increase the distribution volume of EBD by 2.96x (111 mm^3) and 1.16x (37.1 mm^3) as compared to CED (37.4 mm^3) and CED+MB (31.9 mm^3) in the left hemisphere, and 3.25x (70.2 mm^3) and 1.54x (30.2 mm^3) in the left caudate, respectively.

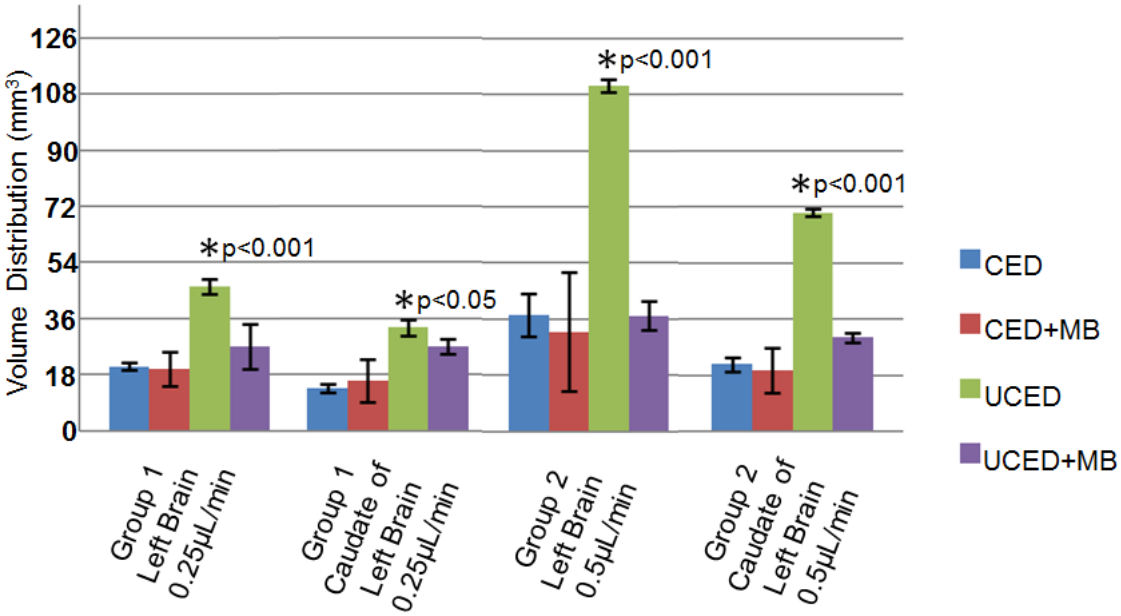

Figure 8.6. Analysis of total EBD volume distribution in the rodent brain with subgroup standard error bars. UCED and UCED+MB increases EBD volume distribution by 2.24x and 1.37x in the left hemisphere and 2.44x and 1.70x in the left caudate, respectively, as compared with CED and CED+MB receiving 0.25µL per min infusions. For 0.5µL per min infusions of group 2,UCED and UCED+MB increases EBD volume distribution by 2.96x and 1.16x in the left hemisphere and 3.25x and 1.54x in the left caudate, respectively. The left hemisphere and left caudate subgroups of groups 1 and 2 are statistically significant with independent means p<0.05 and p<0.001*.*

Figures 8.7 and 8.8 represent the EBD distribution profile in the rodent caudate for subgroups of *group 1* and *group 2*. The Figures show the area of EBD in the caudate of the rodent brain for each slice as a function of the anterior–posterior (AP) distance, defined here as the distance between the slice and the slice containing the infusion point. The black lines represent the area of slices averaged over all animals in each subgroup. The shaded regions represent the standard deviations of the data within each subgroup (n=5). Area measurements below 0.3 mm^3 in Figures 8.7 and 8.9 are subject to artifact from poor signal to noise ratio. Additionally, the TCA provided an acoustic field perpendicularly circumferential to the cannula, approximately 3.2 mm in radius at the infusion site. Across all groups and subgroups, the maximum area of penetration occurs in slices near the infusion point, and the penetration area decreases as the distance from the infusion sites increase in both directions. Ultrasound-assisted subgroups (UCED and UCED+MB) show greater distribution of EBD in the rodent caudate with a larger per slice area of EBD. Ultrasound-assisted subgroups also show higher standard deviations of EBD area in each slice as compared to CED alone. The area under each curve corresponds to the total volume distribution as presented in the bar graph of Figure 8.6.

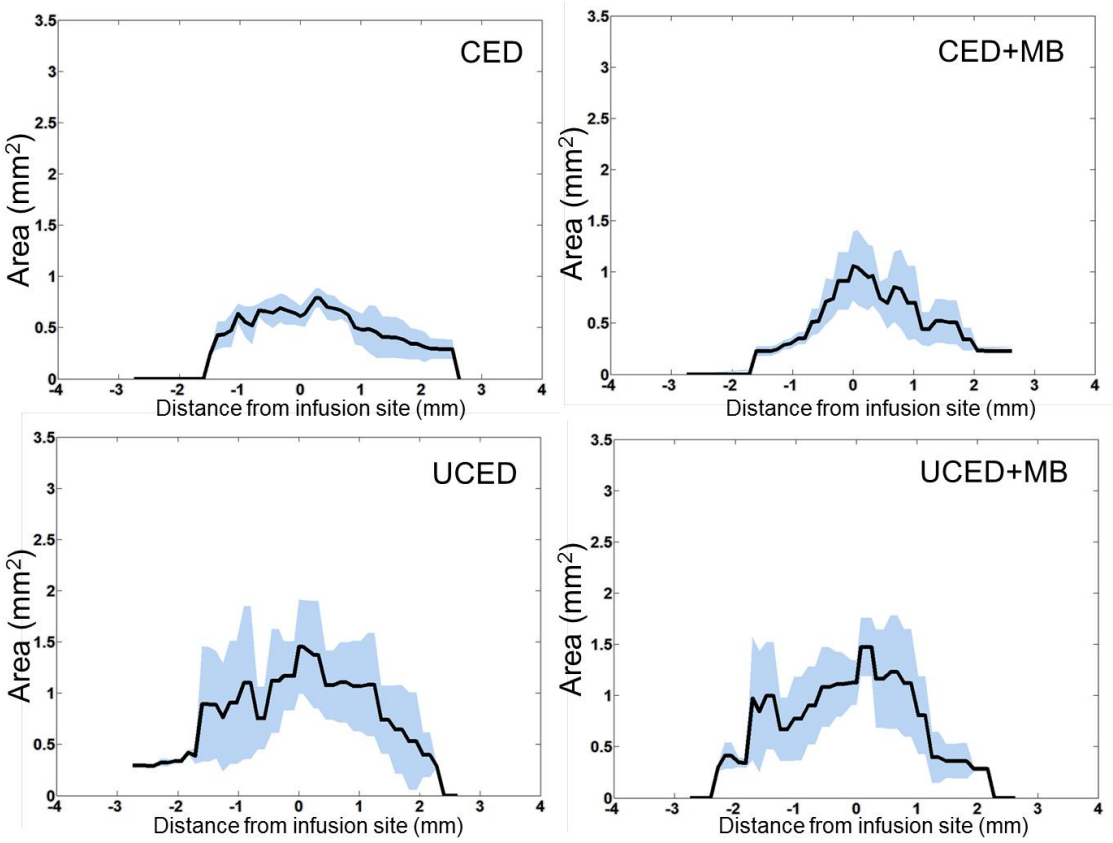

Figure 8.7. Group 1 0.25 µL per min infusion analysis of EBD distribution profile in the rodent caudate as a function of the AP distance in the region ±4 mm from the infusion site. The black line represents the average area of EBD at the given position. The shaded region represents the standard deviation of EBD area (n=5)

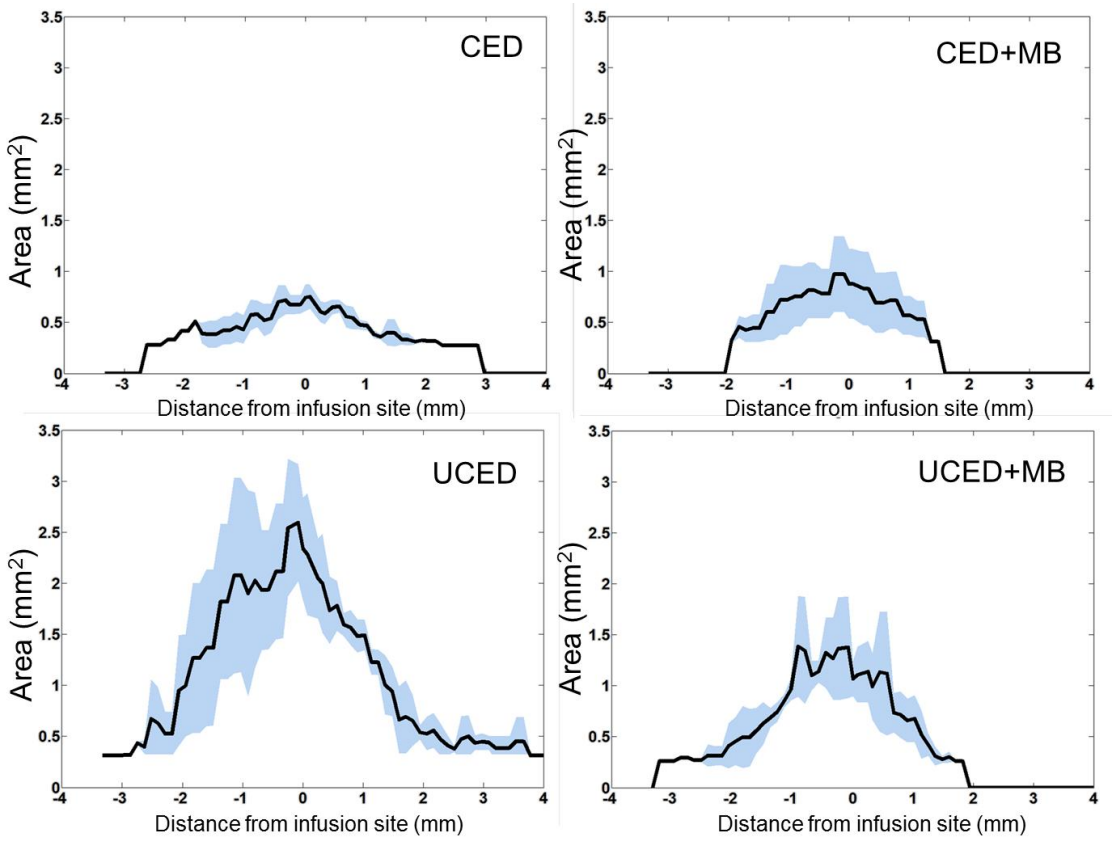

Figure 8.8. Group 2 0.5 µL per min infusion Analysis of EBD distribution profile in the rodent caudate as a function of the AP distance in the region ±4 mm from the infusion site. The black line represents the average area of EBD at the given position. The shaded region represents the standard deviation of EBD area (n=5)

To obtain additional information about the shape of the distribution volume for the infusion protocols of *group 1* and *group 2*, the data in Figures 8.7 and 8.8 was redrawn in Figure 8.9 as a function of the square of the AP distance, i.e. the distance between the slice and slice containing the infusion point. If the infusion of EBD into the rodent caudate were isotropic and the shape of the EBD infusion volume was spherically symmetrical around the AP direction, then the control subgroups (CED and CED+MB) in Figure 8.9 should fall on a straight line with slope of magnitude π [11], and the ultrasound-assisted subgroups (UCED and UCED+MB) could have a different distribution profile. The data for the CED, UCED, CED+MB and UCED+MB treatments in Figures 8.7 and 8.8 approximate straight lines with slopes close to π, but only in the vicinity of the infusion point. This suggests that the distribution volume is spherical for these groups close to the infusion point, but that it deviates from sphericity away from the infusion point. For UCED and UCED+MB subgroups, the magnitude of the slope deceases slower than it does for CED and CED+MB. The spherical part of the distribution is smallest for *group 2* CED, which has a spherical distribution only for the first five or six slices adjacent to the infusion point. For all of the data groups, the magnitude of the slope diminishes with increasing distance from the infusion point. This indicates preferential transport of EBD in the AP direction, i.e. orthogonal to the slices. Of all subgroups studied, ultrasound-assisted infusions maintain the largest distribution, particularly in the case of the higher infusion rate of *group 2*. One might expect the UCED and UCED+MB distribution patterns to vary beyond the ultrasound field (circularly +/- 3.2 mm perpendicular to cannula tip), however due to size limitations of the rodent brain and experimental setup this ultrasound field boundary effect is unnoticeable. Additionally, area measurements of EBD falling below (0.3 mm^2) may have image artifact and not enough contrast to

obtain accurate signal to noise ratios. For reference, dotted line segments with slope of magnitude π are drawn in Figure 8.9.

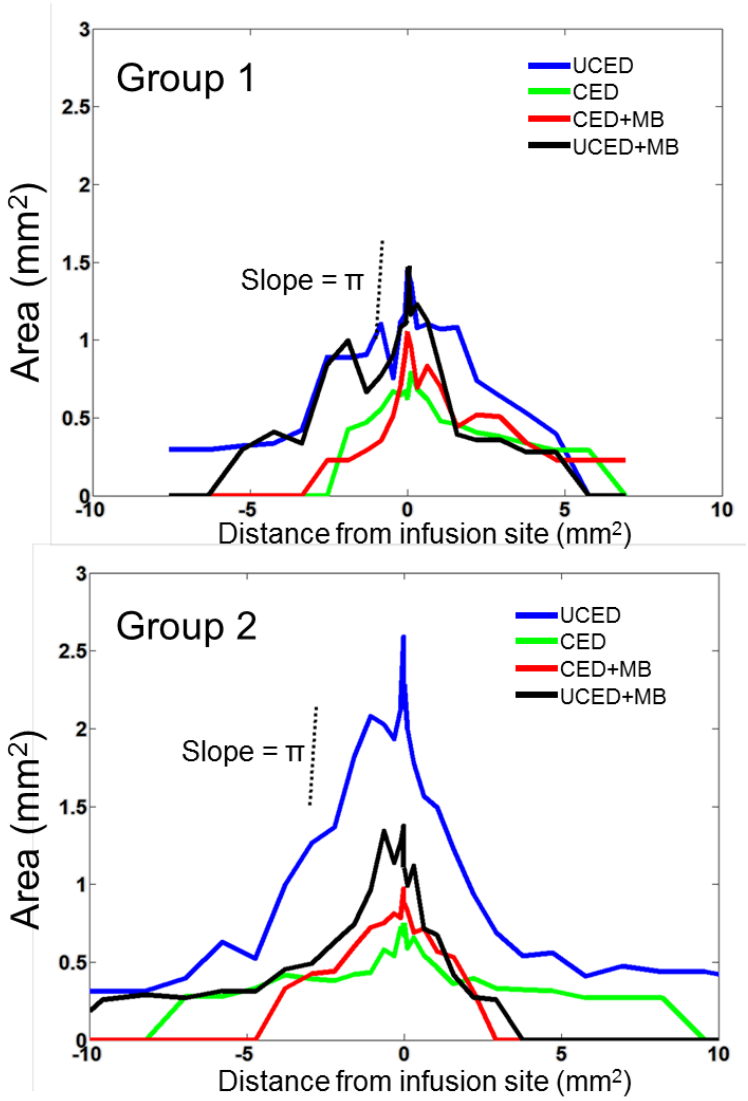

Figure 8.9. The area of EBD in rodent caudate for each slice plotted as a function of the square of the AP for group 1 and group 2. Each solid colored line is the average area for each treatment at the given position. A dotted line segment with a slope magnitude of π is drawn for reference. Data that fall on a line with slope of π or −π indicate regions where the infusion of EBD is locally isotropic. Deviations from the slope indicate an anisotropic volume distribution.

Gross examination of the brain was performed after ultrasound exposure to detect visible lesions on the brain surface. Visual examination of the post-UCED treated brains did not indicate any noticeable damage or significant change to the brain structure as compared with CED. The histological examination for the four groups is shown in Figure 8.10. The histology shows CED, CED+MB, UCED and UCED+MB subgroups of *group 2* after H&E staining in the coronal plane. The arrow with box on the slides denotes the area of magnification and position of needle track. Histologic changes are similar across all groups and include mild parenchymal disruption, edema and hemorrhage around the needle track and injection site. In some cases, hemorrhage extends a short distance within the leptomeninges or along white matter tracts. Rare neurons directly associated with the needle tracks have pyknotic nuclei (necrosis). Also, in all groups, cortical neurons are multifocally basophilic and angular (dark neurons) and there are occasionally well-circumscribed foci of edema in the superficial cerebral cortex. These changes are not restricted to the injection site and are interpreted as artifacts of surgery and/or handling. Overall, histology for all groups show only minor acute damage since cells are distributed evenly and proper anatomical structure is maintained for the four groups.

8.5 Discussion

The goal of this research was to determine if a novel 1.34 MHz ultrasound transducer cannula device powered by a portable, light-weight ultrasound system could be used for ultrasound-assisted convection enhanced delivery to the brain *in vivo*. Sonicators of various forms have been shown to enhance transport transdermally *in vitro* and *in vivo* through the skin using low intensities [20-23], as well as various other tissues such as muscle and brain [28-30].

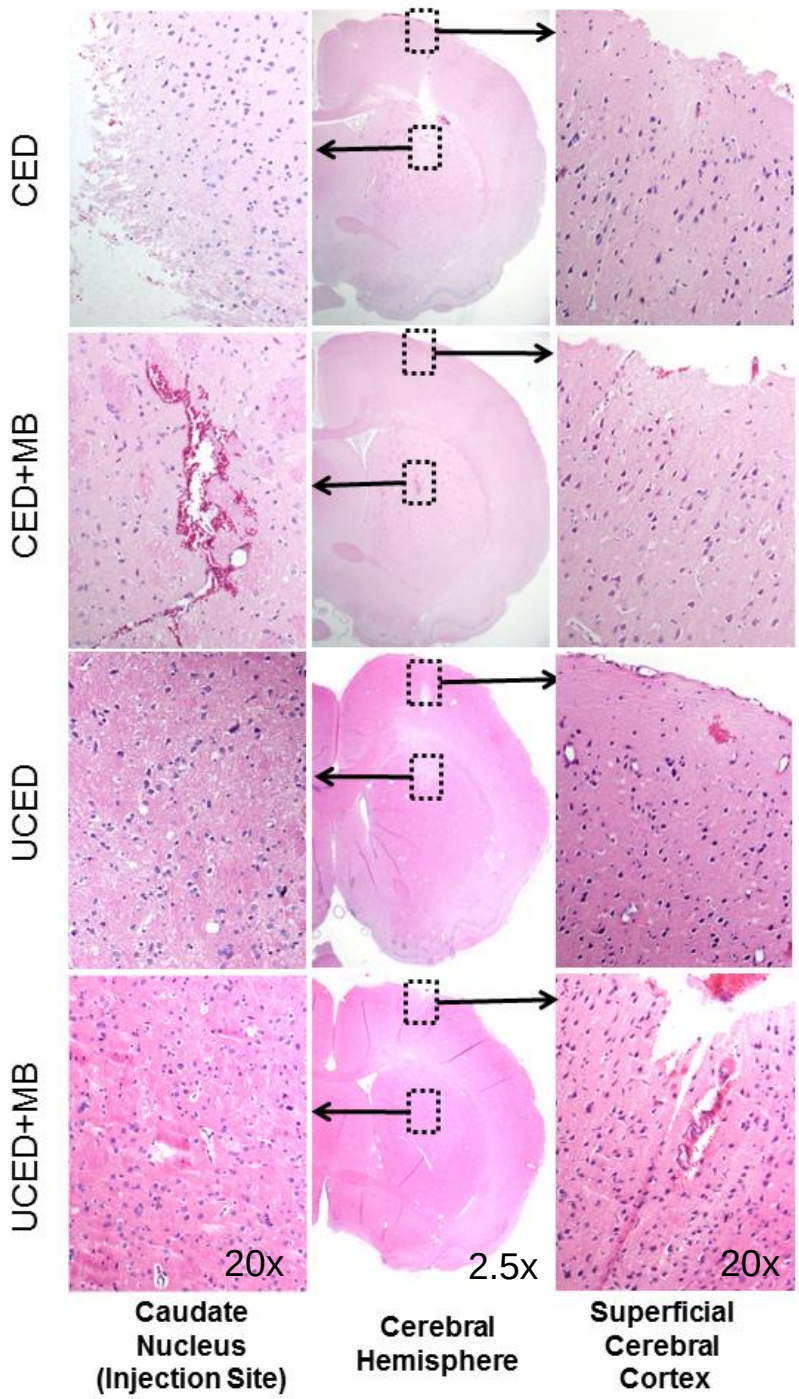

Figure 8.10. Hematoxylin and eosin stain of rodent brains (10 um coronal slices) in the cannula insertion path. CED, CED+MB, UCED and UCED+MB show similar histological results in both the cortex and caudate of the rodent brains. Mild parenchymal disruption, edema and hemorrhage around the needle track and injection site are equivalent for the group.

Considerable amounts of research have been conducted in using pulsed high intensity focused ultrasound (HIFU) to open the blood brain barrier and allow systemically administered therapy to enter the brain, and HIFU shows great promise as a new technique to deliver targeted therapy [26, 27]. Convection enhanced delivery (CED) techniques for drug delivery to the brain have also made major strides over the last 10 years, however the maximum flow rate and therapeutic penetration of drug that can be achieved in CED often is determined by the onset of backflow along the outside of the infusion cannula [1-19]. Backflow along the tissue cannula interface is directly proportional to the volumetric flow rate imposed, the radius of the infusion cannula and the permeability/tissue-resistance to convective transport.

The transducer cannula assembly (TCA) and portable ultrasound system used in this study was utilized to simultaneously sonicate and inject Evan's blue dye (EBD) into the caudate of the rat brain. The application of 1.34 MHz at a total acoustic power of 0.11 +/- 0.005 W and peak spatial intensity at the cannula tip of I= 0.0497 W/cm^2 was shown to enhance the volume distribution of EBD into the caudate of the rat by 2.44x and 3.25x at 0.25 µL/min and 0.5 µL/min infusion rates, respectively as compared to the controls ($p<0.001$). Gross and histological examination showed no significant cellular damage to the rat brain due to ultrasound exposure.

As shown in Figure 8.6, where the volume distribution was calculated for the eight subgroups, ultrasound had an overall effect of increasing EBD distribution in the brain tissue by approximately 2.24 to 3.25x for UCED, and 1.16 to 1.70x for UCED+MB subgroups as compared with controls. This is visualized in Figure 8.4C and D and reconstructed in Figure 8.5C and D, where UCED provided extended EBD distribution. Figures 8.7, 8.8 and 8.9 also show that ultrasound-assisted infusions increase the per slice area of EBD penetration. Ultrasound may provide a mechanism

here to mitigate EBD vascular clearance and elimination from the brain, which presents one of the challenges for CED as discussed in the introduction.

The effect of increased volumetric distribution in the caudate with stabilized microbubbles measured in the UCED+MB infusions of *groups 1 and 2* as compared with CED+MB controls may have resulted from increased streaming [43, 44] and micro-mixing [44, 45] of the microbubbles and EBD at the needle/tissue interface. However, an overall reduction of volumetric distribution of EBD was found with the addition of microbubbles into the infusate when compared with UCED alone. The microbubbles possibly acted as acoustic absorbers and reflectors in the brain parenchyma, thereby limiting the ultrasound effect to a smaller region of the brain by attenuating ultrasound beyond the infusion volume. The mixing and oscillation of the microbubbles in the acoustic field may have had an effect of improving EBD delivery into the caudate brain tissue over CED+MB subgroups. The propagation of the microbubbles in the direction of the acoustic radiation generated characteristic elliptical infusion profiles in the UCED+MB subgroups with the long access of the ellipse being parallel to the infusion cannula. Interestingly, CED and CED+MB infusions have approximately the same total distribution volume in the caudate as shown in Figure 8.6 but have different caudate infusion profiles as shown in Figures 8.7 and 8.8. CED+MB infusions have higher EBD distribution close to the infusion point versus CED infusions.

Ultrasound-assisted convection enhanced delivery (UCED) shows advantages over traditional CED in the rat brain and warrants further investigation into the mechanisms of augmentation. The interaction of the ultrasound field on brain tissue permeability during UCED treatment should be assessed and probed real-time under parametric sonication intensities. During CED infusions, the pressure at the outlet of the needle is sufficiently large to deform the tissue radially, forming a fluid-filled

cavity around the needle tip. The interaction of ultrasound with this cavity/tissue interface could enhance mass transfer from the cavity into the tissue. Frenkel et al. showed that non-destructive low intensity ultrasound widened intercellular spaces between epithelial cells at fluid-tissue interfaces [46]. Investigations into the phenomenon indicated that the effects were due to transverse waves generated at the fluid/tissue interface. These waves increased the penetration and mass transport of nanoparticles from the fluid medium into adjacent epithelium, and increased the rate of effective diffusion through the tissues [47].

Acoustic streaming has been shown to increase the mass transport of nanoparticles for improved transdermal delivery [47-49]. The imposed radiation force on infusate shows promise to mitigate and prevent backflow along the tissue/cannula interface thereby allowing greater infusion rates in CED. At the higher infusion rate of *group 2,* CED subgroups showed backflow and reduction of EBD delivery to the caudate whereas UCED subgroups were able to successfully deliver at higher infusion rates into the rodents caudate. However due to the small size of the rodent caudate, during UCED protocols EBD radiated into the ventricles of the rodent brain. Additionally, acoustic cavitation is currently considered to be one of the most dominant and vital mechanism for ultrasound mediated drug delivery [26, 27, 49]. Numerous *in vivo* studies have shown that stabilized microbubbles, used as cavitational nucleation agents, make ultrasound mediated delivery more efficient, useful, and able to be conducted under low acoustic intensities. In some applications, microbubbles are shown to enable ultrasound mediated delivery where low-intensity ultrasound alone was ineffective [48-49]. Here, we find that microbubbles at the concentration and acoustic intensity applied hindered improving the distribution volume of EBD, however microbubbles may be particularly useful in improving

UCED at different acoustic intensities and pulse sequences, and at lower microbubble infusate concentrations.

In addition to microbubbles, larger molecular weight infusate molecules and nanoparticles that present a greater challenge to CED in clinical practice should be studied with UCED administration *in vivo*. Finally, judicious CED catheter designs that have been developed in the past should be tested with ultrasound assistance.

8.6 Conclusion

Ultrasound continues to evolve with new uses in a range of medical applications from drug delivery to non-invasive surgical techniques. With the price of portable and powerful ultrasound therapy equipment decreasing and the uses of ultrasound in medicine increasing, many more ultrasound assisted modalities are in the pipeline for treatment of human diseases. In particular, treatment of malignant brain tumors, which pose particular challenges due to the obstacles known to limit drug delivery in the brain. This study builds upon our *in vitro* work in using ultrasound with CED to increase the penetration of molecules in equine horse brain [28-30]. Here, we show that ultrasound is capable of safely enhancing the permeation and distribution of small molecules through the rat caudate *in vivo*. These early *in vivo* findings suggest that ultrasound energy interactions with tissues and fluids may have a broad impact to improve CED treatments; not only with our specially designed infusion system, but potentially with any CED cannula design.

REFERENCES

[1] Bobo, R.H., Laske, D.W., Akbasak, A., Morrison, P.F., Dedrick, R.L., Oldfield, E.H. (1994). Convection-enhanced delivery of macromolecules in the brain. *Proc. Natl. Acad. Sci. USA, 91*, 2076–2080.

[2] Chen, M.Y., Lonser, R.R., Morrison, P.F., Governale, L.S., Oldfield, E.H. (1999). Variables affecting convectionenhanced delivery to the striatum: a systematic examination of rate of infusion, cannula size, infusate concentration, and tissue–cannula sealing time, *J. Neurosurg. 90*, 315–320.

[3] Morrison, P.F., Chen, M.Y., Chadwick, R.S., Lonser, R.R., Oldfield, E.H. (1999). Focal delivery during direct infusion to brain: role of flow rate, catheter diameter, and tissue mechanics. *Am. J. Physiol. Regul. Integr. Comp. Physiol. 277*, R1218–R1229, 1580–1596.

[4] Rainov, N.G., Soling, A., Heidecke, V. (2006). Novel therapies for malignant gliomas: a local affair? *Neurosurg. Focus, 20, E9.*

[5] Groothuis, D.R., Benalcazar, H., Allen, C.V., Wise, R.M., Dills, C., Dobrescu, C., Rothholtz,V. & Levy, R.M. (2000) Comparison of cytosine arabinoside delivery to rat brain by intravenous, intrathecal, intraventricular and intraparenchymal routes of administration. *Brain Res.* 856, 281–290, 2000.

[6] Groothuis, D.R., Ward, S., Itskovich, A.C., Dobrescu, C., Allen, C.V., Dills, C., & Levy, R.M. (1999). Comparison of c-14- sucrose delivery to the brain by

intravenous, intraventricular, and convection-enhanced intracerebral infusion. *J. Neurosurg., 90*, 321–331.

[7] Lieberman, D.M., Laske, D.W., Morrison, P.F., Bankiewicz, K.S., & Oldfield, E.H. (1995). Convection-enhanced distribution of large molecules in gray matter during interstitial drug infusion. *J. Neurosurg., 82*, 1021–1029.

[8] Bankiewicz, K.S., Eberling, J.L., Kohutnicka, M., Jagust, W., Pivirotto, P., Bringas, J., Cunningham, J., Budinger, T.F. & Harvey-White, J. (2000). Convection-enhanced delivery of AAV vector in Parkinsonian monkeys; in vivo detection of gene expression and restoration of dopaminergic function using pro-drug approach. *Exp. Neurol.* 164, 2–14.

[9] Broaddus, W.C., Prabhu, S.S., Gillies, G.T., Neal, J., Conrad, W.S., Chen, Z., Fillmore, H., & Young, H.F. (1998). Distribution and stability of antisense phosphorothioate oligonucleosides in rodent brain following direct intraparenchymal controlled-rate infusion. *J. Neurosurg. 88*, 734–742.

[10] Mamot, C., Nguyen, J.B., Pourdehnad, M., Hadaczek, P., Saito, R., Bringas, J.R., Drummond, D.C., Hong, K., Kirpotin, D.B., & McKnight, T. (2004). Extensive distribution of liposomes in rodent brains and brain tumors following convection-enhanced delivery. *Neuro-oncol*., *68*, 1-9.

[11] Neeves, K.B., Sawyer, A.J., Foley, C.P. Saltzman, W.M., & Olbricht, W.L. (2007). Dilation and degradation of the brain extracellular matrix enhances penetration of infused polymer. *Brain Res., 1180*, 121-132.

[12] Laske, D.W., Youle, R.J. & Oldfield, E.H. (1997). Tumor regression with regional distribution of the targeted toxin TFCRM107 in patients with malignant brain tumors. *Nat. Med.*3, 1362–1368.

[13] Ren, H., Boulikas, T., Söling, A., Warnke, P.C., Rainov, N.G. (2003). Immunogene therapy of recurrent glioblastoma multiforme with a liposomally encapsulated replication-incompetent semliki forest virus vector carrying the human interleukin-12 gene a phase i/ii clinical protocol. *J. Neuro-Oncol. 64*, 147–154.

[14] Rand, R.W., Kreitman, R.J., Patronas, N., Varricchio, F., Pastan, I. & Puri, R.K. (2000) Intratumoral administration of recombinant circularly permuted interleukin-4-Pseudomonas exotoxin in patients with high-grade glioma. *Clin. Cancer Res.* 6, 2157–2165.

[15] Weber, F., Asher, A., Bucholz, R., Berger, M., Prados, M., Chang, S., … Puri, R.K. (2003). Safety, tolerability, and tumor response of il4-Pseudomonas exotoxin (nbi-3001) in patients with recurrent malignant glioma. *J. Neuro-Oncol., 64,* 125–137.

[16] Kunwar, S., Prados, M.D., Chang, S.M., Berger, M.S., Laff, F.F. (2007). Direct intracerebral delivery of cintredekin besudotox (IL13-PE38QQR) in recurrent malignant glioma: a report by the Cintredekin Besudotox Intraparenchymal Study Group. *J. Clin. Oncol., 25,* 837-844.

[17] Vogelbaum, M.A. (2007). Convection enhanced delivery for treating brain tumors and selected neurological disorders: symposium review. *J. Neuro-Oncol., 83*, 97-109.

[18] Lopez, K.A., Waziri, A.E., Canoll, P.D., Bruce, J.N. (2006). Convection-enhanced delivery in the treatment of malignant glioma. *Neurol. Res., 28*, 542-548.

[19] Huynh, G.H., Deen, D.F., Szoka, F.C.J. (2006). Barriers to carrier mediated drug and gene delivery to brain tumors. *J. Control Release., 110*, 236-259.

[20] Mitragotri, S., Blankschtein, D., Langer, R. (1995). Ultrasound-mediated transdermal protein delivery. *Science, 269*, 850-853.

[21] Boucaud, A., Garrigue, M.A., Machet, L., Vallant, L., Patat, F. (2002). Effect of sonication parameters on transdermal delivery of insulin to hairless rats. *J. Pharm., Sci. 91*, 113-119.

[22] Machet, L., Boucaud, A. (2002). Phonophoresis: efficiency, mechanisms and skin tolerance. *Int. J. Pharm., 243, 1-15*.

[23] Smith, N.B., Lee, S., Shung, K. (2003). Ultrasound–mediated transdermal *in vivo* transport of insulin with low-profile cymbal arrays. *J. Ultrasound Med. Bio., 29*, 1205-1210.

[24] Guzman, H.R., Nguyen, D.X., McNamara, A.J., & Prausnitz, M.R. (2002). Equilibrium loading of cells with macromolecules by ultrasound: Effects of molecular size and acoustic energy. *J. Pharm. Sci., 91,* 1693–1701.

[25] Keyhani, K., Guzman, H.R., Parsons, A., Lewis, T.N., & Prausnitz, M.R. (2001). Intracellular drug delivery using low-frequency ultrasound: Quantification of molecular uptake and cell viability. *Pharm. Res., 18,* 1514–1520.

[26] Patrick, J.T., Nolting, M.N., Goss, S.A., Dines, K.A., Clendenon, J.L., Rea, M.A., Heimburger, R.F. (1990). Ultrasound and the blood brain barrier. *Adv. Exp. Med. Biol., 267,* 369-381.

[27] Hynynen, K., Clement, G. (2007). Clinical applications of focused ultrasound - The brain. *Int. J. Hyperth., 23,* 193-202.

[28] Lewis, G.K., & Olbricht, W.L. (2007). A phantom feasibility study of acoustic enhanced drug perfusion in neurological tissue. *Proc. IEEE, LISA,* 67-70.

[29] Lewis, Jr. G.K., Olbricht, W.L., & Lewis Sr.,G.K (2007). Acoustic targeted chemotherapy in neurological tissue. *J. Acoust. Soc. Am., 122,* 3007.

[30] Lewis Jr., G.K., Wang., P., Lewis, G.K., & Olbricht, W.L. (2008). Therapeutic ultrasound enhancement of drug delivery to soft tissues. *8th. Int. Sym. Ther. Ultrasound, AIP conf. Proc., 1113, 403-407.*

[31] Lewis Jr., G.K., Lewis Sr., G.K., Olbricht, W.L., (2008). Cost effective broad-band electrical impedance spectroscopy measurement circuit and signal analysis of piezo-matrials and ultrasound transducers. *Meas. Sci. Technol., 19,* 1-7.

[32] Lewis Jr., G.K., Olbricht, W.L. (2008). Development of a portable therapeutic and high intensity ultrasound system of military, medical and research use. *Rev. Sci. Inst., 79,* 1-9.

[33] Lewis Jr., G.K., Olbricht, W.L. (2008). Development of a portable therapeutic ultrasound system for military, medical and research use. *J. Acoust. Soc. Am., POMA 5,* 122.

[34] Lewis Jr., G.K., & Olbricht, W.L. (2009). Wave Generating Apparatus, UPCT Patent Application No. PCT/US2009/50297.

[35] Henderson P., Lewis Jr., G.K., Olbricht, W.L., Spector, J. (2010). A portable high intensity focused ultrasound device for the non invasive treatment of varicose veins. *J. Vas. Surg., 51*(3), 707-711.

[36] Lewis Jr. GK, Olbricht WL. (2010). Design and characterization of a high-power ultrasound driver with ultralow-output impedance. *Rev. Sci. Inst., 80*(11), 1-8.

[37] IEEE. (1990). *Guide for medical ultrasound field parameter measurements.* New York: Institute of Electrical and Electronics Engineers, Inc.

[38] AIUM. (1998). *Acoustic output labeling standard for diagnostic ultrasound equipment.* Laurel, MD: American Institute of Ultrasound in Medicine.

[39] AIUM. (1988). Bioeffects considerations for the safety of diagnostic ultrasound. *J Ultrasound Med.,* 7(9 Suppl), S1–S38.

[40] AIUM. (1993). *Bioeffects and safety of diagnostic ultrasound.* Laurel, MD: American Institute of Ultrasound in Medicine.

[41] AIUM. (2000). *Mechanical bioeffects from diagnostic ultrasound: AIUM consusus statements, 19,* 67–170.

[42] Schroeder, A., Kost, J., & Barenholz, Y. (2009). Ultrasound, liposomes, and drug delivery: Principles for using ultrasound to control release of drugs from liposomes. *Chem. Phys. Lipids. 162,* 1-16.

[43] Sakamoto, S., & Watanabe, Y. (1999). Effects of existence of microbubbles for increase of acoustic streaming. *Jpn. J. Appl. Phys., 38,* 3050-3052.

[44] Collis, J., Manasseh, R., Liovic, P., Tho, P., Ooi, A,, Petkovic-Duran, K., & Zhu, Y. (2010). Cavitation microstreaming and stress fields created by microbubbles. *Ultrasonics, 50,* 273-279.

[45] Farrara, K., Pollard, R., & Borden, M. (2007). Ultrasound microbubble contrast agents: Fundamentals and application to gene and drug delivery. *Annual. Rev. Biomed. Eng. 9,* 415-447.

[46] Frenkel, V., Oberoi, J., Park, M., Deng, C., Stone, M.J., Neeman, Z., Wood, B.J., Horne M.K. 3rd, & Li K.C.P. (2006). Pulsed-high intensity ultrasound (HIFU) enhances thrombolysis in an in vitro model. *Radiol., 239*, 86–93.

[47] Frenkel, V., Kimmel, E., & Iger, Y. (2000). Ultrasound-facilitated transport of silver chloride (AgCl) particles in fish skin. *J Cont. Release, 68*, 251–261.

[48] Ohl, C.D., Arora, M., Ikink, R. (2006). Sonoporation from jetting cavitation bubbles. *Biophys J., 91*, 4285–4295.

[49] van Wamel, A., Kooiman, K., & Harteveld, M. (2006). Vibrating microbubbles poking individual cells: drug transfer into cells via sonoporation. *J. Cont. Release, 112,* 149–155.

CHAPTER 9

IN VIVO ULTRASOUND ASSISTED CONVECTION ENHANCED DELIVERY: POWER RANGING ANALYSIS AND STANDING WAVE PHENOMENA[15,16]

9.1 Abstract

Therapeutic ultrasound has been used to enhance and/or mediate drug delivery in various applications including convection-enhanced delivery (CED) of tracers to the rodent brain. While ultrasound has been shown to increase the delivery volume of tracers in neurological tissue safely, the exposure range of *safe* ultrasound energy levels is not well documented and/or explored. This is especially true in the case of continuous low-intensity ultrasound therapy to the brain as discussed in Chapter 9, since most research has focused on using ultrasound to disrupt the blood-brain barrier at much higher acoustic intensities but for much shorter ultrasonic application times. To explore the acute effects of ultrasound to the live rodent brain, we applied ultrasound using the Transducer Cannula Assembly (TCA) through a small craniotomy *in vivo* under four different acoustic intensities ranging from 0.062 to 0.155 W/cm^2 in a total of 4 Sprague–Dawley rats for 30 minutes. After which histological analysis was conducted on the brain tissue specimens to asses for neuronal damage.

Additionally, because ultrasound is being used in continuous wave mode for ultrasound-assisted CED (UCED), it should be possible to induce standing waves in

[15]This work is in preparation for being published as Lewis, G.K., Jr., Schulz, Z., Pannullo, S., Southard, T., Olbricht. W.L. (2011). Levels of safe ultrasound therapy to improve convection enhanced delivery to the brain.

[16]This work is in preparation for being published as Lewis, G.K., Jr., Guarino, S. Ghandi, G., Olbricht. W.L., Sarvazyan, A. (2011). Time-reversal techniques in ultrasound-assisted convection-enhanced drug delivery to the brain: Technology development and in vivo evaluation.

the brain tissue and generate banding patters of tracers. We show possible results of this observed "standing wave phenomena" in the rodent brain *in vivo* during UCED, which suggests low-intensity ultrasound may provide a tool for additional drug delivery applications beyond improving the distribution of pharmaceuticals in the brain.

9.2 Introduction to Standing Waves

Standing waves are well documented phenomena formed by the constructive interference of two mechanical waves traveling in opposite directions, including ultrasound waves propagating in a media. The constructive interference of two equal and opposite waves, and the formation of a standing wave results in an interference pattern with nodes and anti-nodes that do not move in space temporally. The anti-nodes represent the maximum displacement and amplitude of the ultrasound wave, whereas the nodes represent areas of minimum displacement which experience very little acoustic pressure from the ultrasound wave. Standing waves are commonly formed when an ultrasound source of consistent frequency and position, continuously generates an incident wave which then interferes with its own reflection off a boundary.

Standing waves have been exploited in a number of applications, both biomedical and otherwise. Some examples include using ultrasonic standing waves to immobilize cells in a gel matrix at areas of minimal acoustic pressure (nodes) in the standing wave field as well as creating a physical force field filter within microfluidic devices [1,2]. However, it is generally believed that standing waves in brain tissue are undesirable since localized high energy sites at the anti-nodes could cause damage to neuronal tissue. At the 1-2 MHz frequencies in particular, the wavelength resembles

the dimension of an artery in the brain, which could prove problematic if high energy spots were formed on this scale [3].

9.3 Methods

9.3.1 Ultrasound Generator and Ultrasound Exposimetry

The ultrasound generator discussed in Chapters 3-5 was powered with two adjustable 0-20 V standard lab power supplies to drive the Transducer Cannula Assembly (TCA) discussed in Chapter 9, up to the maximum +/- 20 V power setting. The acoustic power and intensity was measured using a calibrated hydrophone and power meter as in Chapter 9. The four acoustic intensities at the cannula tip and total acoustic powers applied to the rodent brains during UCED were 0.062 W/cm^2 and 0.12 W +/- 0.005 W, 0.087 W/cm^2 and 0.16 W +/- 0.005 W, 0.112 W/cm^2 and 0.23W +/- 0.005 W, and 0.155 W/cm^2 and 0.31W +/- 0.005 W.

9.3.2 Power Ranging Animal Experiments

Rats were anesthetized and euthanized by procedures approved by the Institutional Animal Care and Use Committee (IACUC) at Cornell University. A total of 4 Sprague–Dawley rats (350 to 450 g) received UCED at 4 different ultrasound intensities ranging from 0.062 to 0.155 W/cm^2 for 30 min. A small craniotomy was made as in Chapter 9 to expose the brain. The TCA was guided using a micromanipulator to +0 mm anterior, +3 mm lateral and -5.5 mm ventral from bregma, lowered at 0.25 mm per second into the caudate of the rat brain and allowed to equilibrate for two minutes. 1-2 ml of artificial cerebral spinal fluid (aCSF) and a gel-foam dam was used to couple acoustic energy from the face of the TCA into the rodent brain. The TCA was powered on with the ultrasound generator.

Filtered Evan's blue dye (EBD) 0.25 wt% in phosphate buffered saline (PBS) was infused using a microinfusion pump with a starting infusion flow rate of 0.1

μL/min for 5 min, the infusion flow rate was then increased to 0.25 μL/min for an additional 5 min, to the final flow rate of 0.5 μL/min for 20 min. After 30 min of simultaneous infusion and ultrasound therapy the experiment was stopped. The TCA was left in the tissue for 1-2 min before being removed while euthanasia via cardiac urethane injection was performed. The rodent brains were prepared for histological analysis and reviewed by the Veterinary Pathology Department at Cornell University as in Chapter 9.

9.4 Histological Results and Conclusions from Power Ranging

Gross examination of the brain was performed after ultrasound exposure to detect visible lesions on the brain surface. Visual examination of the post-UCED treated brains did not indicate any noticeable damage or significant change to the brain structure. The histological examination for the four groups is shown in Figure 9.1. The arrow with box on the slides denotes the area of magnification and position of needle track. Histologic changes are similar across all groups as well as rodents receiving lower acoustic UCED intensities as discussed in Chapter 9. Histology showed mild parenchymal disruption, edema and hemorrhage around the needle track and injection site. In some cases, hemorrhage extended a short distance within the leptomeninges or along white matter tracts. Rare neurons directly associated with the needle tracks show pyknotic nuclei (necrosis). Also, in all groups presented, cortical neurons are multifocally basophilic and angular (dark neurons) and there are occasionally well-circumscribed foci of edema in the superficial cerebral cortex. These changes were not restricted to the injection site and are interpreted as artifacts of surgery and/or handling.

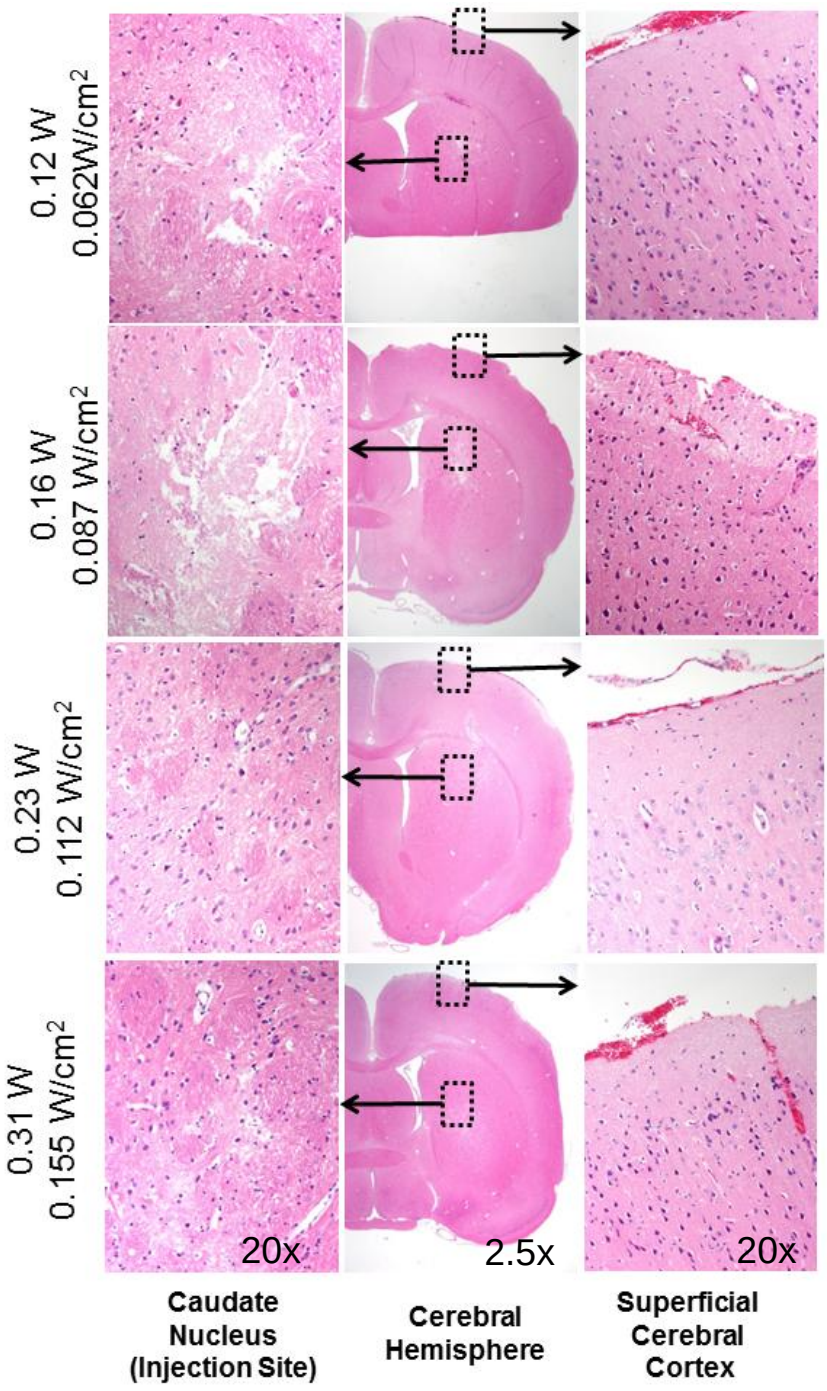

Figure 9.1. Hematoxylin and eosin stain of rodent brains (10 um coronal slices) in the cannula insertion path. Acoustic intensities of 0.062, 0.087, 0.112 and 0.155 W/cm^2 show similar histological results in both the cortex and caudate of the rodent brains. Mild parenchymal disruption, edema and hemorrhage around the needle track and injection site are equivalent for the group.

The results presented here suggest that ultrasound applied below 0.155 W/cm^2 to the brain for 30 min produces no noticeable neuronal damage to the caudate or cortex. Greater acoustic intensity control from the TCA as well as further experimentation will be required in order to determine the level of ultrasound exposure to the brain that causes acute neuronal damage. Furthermore, the limited literature on the continuous application of ultrasound to the brain for drug delivery will require parametric analysis to understand the safe operating window for UCED. Finally, acute exposure and histology may not be adequate to asses for neurological damage from ultrasound exposure since neuronal degeneration may take up to 3-5 days before detectable by cresyl violet staining [4]. Future UCED research will inevitable require survival surgeries to understand post procedural effects to ultrasound exposure.

9.5 Standing Wave Findings and Discussion

The current work of *in vivo* brain drug delivery utilizes 1.34 MHz ultrasound in conjunction with CED to infuse Evans blue dye directly into the rat brain caudate. The results are generally a distribution volume of dye with a spherical or ellipsoid shape as shown in Figure 9.2A. However, in two rodents during the vast UCED experimentation, distinct, non-continuous bands of dye were observed in brain sections close to the needle track and directly above the TCA as shown in Figure 9.2B. This phenomenon could be attributed to the formation of a standing ultrasound wave within the rat brain during the UCED infusion. This formation is likely the result of the incident ultrasound waves interfering with reflections from the rodent skull generating a steady spatial field of nodes and anti-nodes.

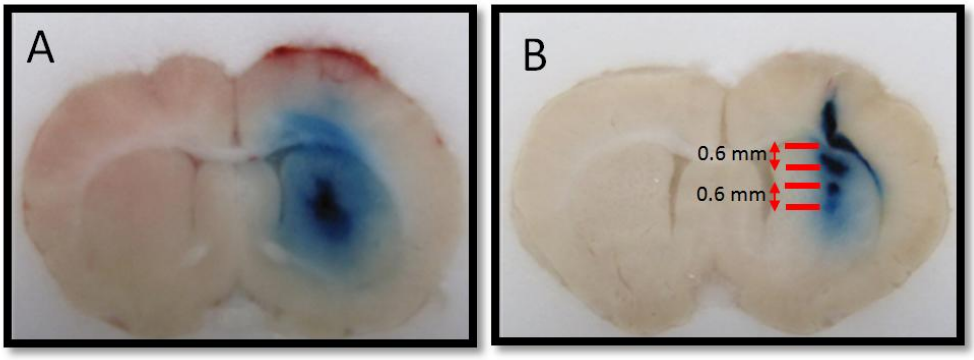

Figure 9.2 UCED Infusion Profiles. The rat brain in (A) shows a relatively uniform distribution, while the brain in (B) shows clear banding of the infused dye approximately 0.6mm apart.

The observed banding is analagous to other processes whereby material accumulates in a standing wave field. However, the exact mechanism in brain tissue has not yet been identified. One possibility is that the tracer accumulates in the nodes, or the areas of least acoustic pressure. The other possibility is that the tracer accumulates at the anti-nodes where the ultrasound waves have the greatest amplitude. This increased energy could cause increased tissue permeability, causing tracer to preferentially accumulate at the anti-nodes.

To better understand whether tracer is accumulating at the nodes or anti-nodes, we calculated the wavelength of ultrasound in brain tissue and compared the result to the distance between the bands,

$$f = \frac{c}{\lambda} \qquad (9.1)$$

where f is the frequency, c is the speed of sound in brain tissue (1460 m/s, [5]), and λ is the wavelength. We calculated the wavelength to be 1.09 mm, resulting in a node to node distance of 0.545 mm. The distance between the bands in the two experiments

experiencing this phenomena are approximately 0.6 mm, which supports the conclusion that dye is accumulating at the nodes.

Though this result runs counter to the objective of maximizing volume distribution of an infusate as discussed in Chapter 9, it may have other applications. For instance, if various standing wave patterns could be induced during an infusion, greater spatial and temporal control over the infusion could be achieved; this control could prove especially valuable with highly toxic treatments. Difficulty arises in reproducing this *in vivo* result. Inducing a standing wave depends on correct alignment in the desired geometry as well as the correct ultrasound frequency. Inducing such a standing wave field *in vivo* would likely require real-time imaging and precise positioning of the ultrasound source. However, if standing waves prove harmful to the brain, measures can be taken to prevent their formation, such as randomizing frequency or moving the source [6].

Perhaps the most important implication of this observation of standing waves is that it lends supporting evidence showing that ultrasound is not only having an effect on brain tissue, but that ultrasound also directly affects the distribution profile of the infusate during CED. Advancing the knowledge of how ultrasound can affect the infusion profile will allow for the parameters governing UCED to be optimized as it evolves into a clinically relevant therapy for neurological disorders.

REFERENCES

[1] Gherardini, L., et al. (2005). A new immobilization method to arrange particles in a gel matrix by ultrasound standing waves. *Ultrasound in Med. & Biol.* 31 261-272.

[2] Hawkes, J.J., Coakley, W.T. (2001). Force field particle filter, combining ultrasound standing waves and laminar flow. *Sensors and Actuators* B 75 213-222.

[3] Culp, W.C, McCowan, T.C. (2005). Ultrasound augmented thrombolysis. *Current Medical Imaging Reviews* 1 5-12.

[4] Bancroft, J.D., Gamble, M. (2008). Theory and practice of histological techniques, Sixth Edition. Elsevier, *Philadelphia Pa.* pp. 366-388.

[5] Goss SA, Johnston RL, Dunn F. (1980). Compilation of empirical ultrasonic properties of mammalian tissues. *J Acoust. Soc Am.* 68 (1980) 93-108.

[6] Tang, S.C., Clement, G.T. (2010) Standing wave suppression for transracial ultrasound by random modulation. *IEEE Trans Biomed Eng.* 57 203-5.

CHAPTER 10

A LOOK INTO THE FUTURE OF BIOMEDICAL ULTRASOUND APPLICATIONS AND ULTRALOW IMPEDANCE DESIGN PRINCIPLES

10.1 Abstract

Translational research is the hallmark of biomedical engineering with a positioned outcome of improving the quality and duration of life for mankind. Our team of engineers and clinicians seeks to solve problems that touch close to home and affect millions of people every year. Our drive is to quickly innovate and prototype ultrasound-based solutions, and place them into clinical hands for evaluation, preliminary testing and clinical-feedback as quickly as possible. This rapid, iterative approach to our research is possible because we have built the facility and possess the talent to develop every piece of an ultrasound based system in our biomedical acoustics laboratory. From the onset of every project our team tackles, clinically inspired motivation drives engineering design innovation, while our collaborations drive technology translation.

Our team of ultrasound engineers from the Department of Biomedical Engineering at Cornell University developed a platform ultrasound technology in 2007 discussed in chapters 3 and 4 of this dissertation, which reduces the cost and size of ultrasound devices by orders of magnitude. The principles behind the technology are to reduce the output impedance of the ultrasound generator and the input impedance of the ultrasound transducer to zero (ideally), to create zero resistance to energy flow and optimize electrical power transfer for battery powered ultrasound devices. This pioneering approach of zero output and input impedance pushes the efficiency of

ultrasound systems, and provides ultrasound power in a smaller form. Since our technology's inception, motivations from physicians have driven ultrasonic innovations to improve drug delivery in glioblastoma brain cancer therapy (Chapters 5, 6, 7, 8 and 9), develop non-invasive varicose vein treatment systems, and improve fetal heart rate monitoring to allow easy and consistent measurements during labor.

Figure 10.1 Ultralow output impedance ultrasound power generation technology. A 10-channel high power ultrasound driver is shown on the lab bench.

10.2 Ultrasound-assisted Brain Cancer Therapy (In Vivo Preclinical Studies)

Our laboratory has developed and commenced testing of a new ultrasound-based drug delivery system for pre and post-resection treatment of high-grade malignant gliomas. Surgery and adjuvant radiation are standard treatments for these malignancies. However, invasive malignant cells migrate into surrounding healthy tissue and, as a consequence, are not all removed in surgery, leading to tumor recurrence, usually close to the site of the original tumor. Convection enhanced

delivery (CED) has emerged as a leading investigational delivery technique for the treatment of several disorders, including glioblastoma which presents an especially poor prognosis for patients. CED bypasses the blood-brain barrier by infusing compounds through a needle or microcatheter directly into the brain parenchyma or brain tumor. The clinical trials of CED show mixed results and suggest that the outcome of therapy depends strongly on the extent of penetration of drug into the brain, which is determined by infusion velocity, and the relative rates of convection and elimination during CED. In collaboration with Drs. Susan Pannullo, Mark Souweidane and George Lewis Sr. of the Department of Neurosurgery at Weill Cornell Medical College (WCMC) and Transducer Engineering Inc., respectively, we have developed ultrasound-assisted convection enhanced drug delivery technology (UCED) to improve the penetration and spatial control of pharmaceuticals in the brain shown in Figure 10.2

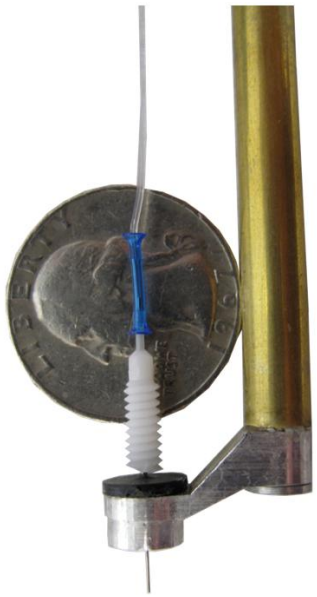

Figure 10.2 Ultrasound-assisted CED cannula for improved drug delivery in brain cancer therapy.

We have developed *in vitro* and *in vivo* models of UCED brain tumor treatments, and have shown that combining ultrasound with traditional CED improves the penetration and distribution of tracer molecules by 2-3 times *in vivo*. This work involves both the basic science of transport mechanisms as well as the translational science of scaling the UCED brain cancer therapy into a large animal model at Cornell Weill Cornell Medical Hospital. If successful, we will transition the technology to human treatment in the next few years.

Furthermore, we have enlisted new collaborators from Artann Laboratories Inc. to combine time-reversal acoustics (TRA) with convection-enhanced delivery (CED) to improve the delivery of therapeutics to the interstitium of the brain. Together we have developed a novel TRA system that is used to infuse tracers into the brain parenchyma while simultaneously exposing the tissue to safe levels of 1-MHz, low intensity, ultrasound energy. The system includes a combined infusion needle-hydrophone, a 10-channel ultralow-output impedance amplifier (Figure 10.1), a broad-band ultrasound resonator, and MatLab®-based TRA control and user-interface. TRA allows easy coupling of ultrasound therapy through the skull without complex phase-correction and array design. The smart targeting TRA based UCED system has been tested *in vitro* and *in vivo* and results show it provides 1-mm spatial resolution for UCED and improves tracer distribution in the brain over CED alone.

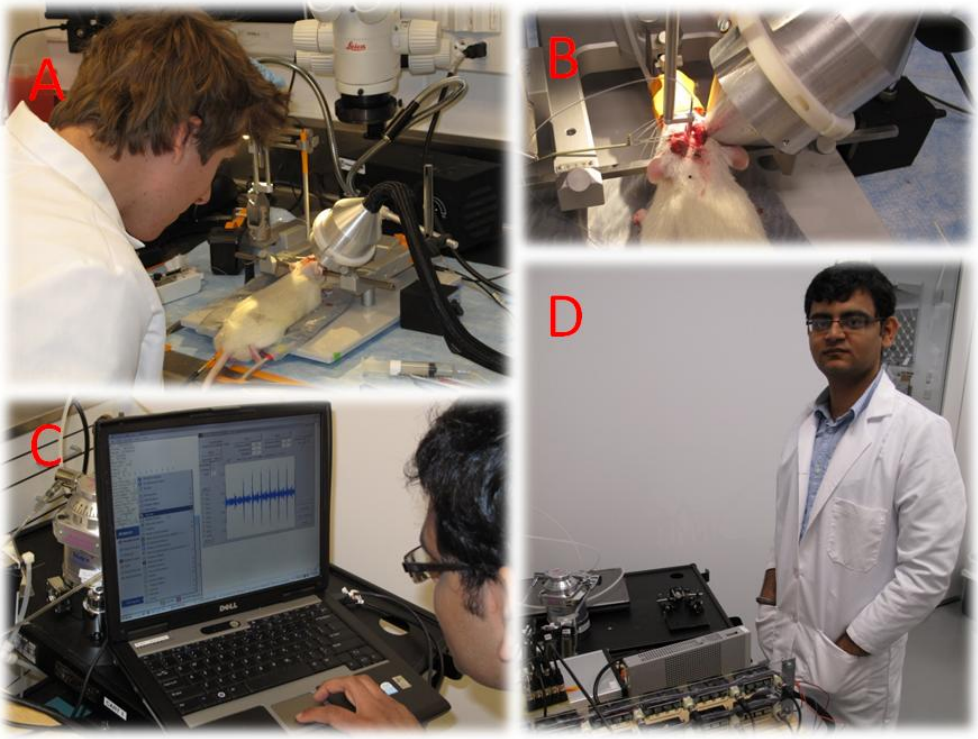

Figure 10.3. Delivery and setup of TRA-CED system at Cornell University Biomedical Engineering Laboratories. A) Surgical setup of rodent positioned in stereotax device and TRA-CED system arranged for preliminary in vivo testing. B) Close up of surgical prep, smart ultrasound needle cannula and ultrasound therapy transducer resonator. C) First successful TRA-CED focusing in the rodent brain in vivo. D) Artann researcher standing next to TRA-CED system in animal surgery suite.

10.3 Non-invasive High Intensity Focused Ultrasound Varicose Vein Treatment (In Vivo Preclinical Studies)

Varicose veins affect more than 30 million people in the United States each year. They cause emotional distress and discomfort for patients and, if left untreated, can progress to deep venous thrombosis, skin ulceration, limb loss or death. Clinicians perform more than 150,000 varicose vein treatments in the U.S. each year, using methods such as vein stripping, sclerotherapy, and endovenous laser and RF treatment, which together comprise a $450MM market. Because these methods are invasive, they incur added costs in training, equipment, facilities, and staff. In collaboration with Drs. Jason Spector and Peter Henderson from the Department of Surgery at WCMC, we

have developed and tested the first battery-powered handheld HIFU system to non-invasively cauterize and occlude varicose veins shown in Figures 10.4 and 10.6.

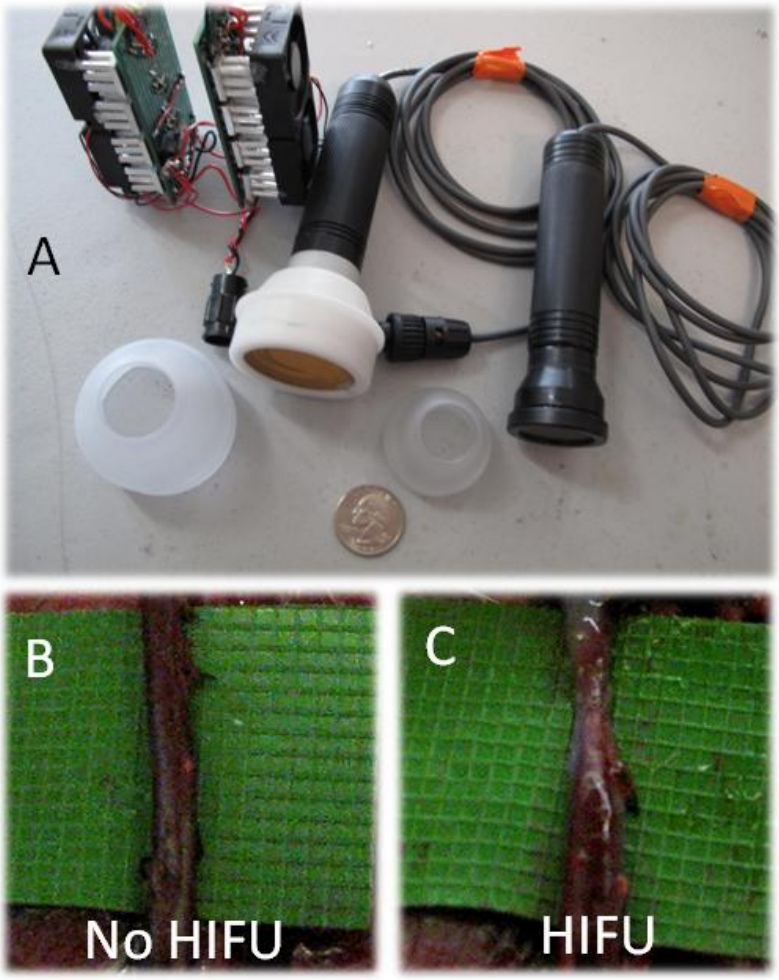

Figure 10.4. Hand held HIFU and its use to non-invasively cauterize and occlude veins in vivo. A) Shows the electronic heart of the system and ultrasound transducer probes, B and C) Show results from in vivo ablation of rodent inferior vena cava.

Figure 10.5. Dr. Peter Henderson, M.D. performing surgical cauterization using portable ultrasound device.

By focusing ultrasound energy to a sharp point with the handheld HIFU system, we are able to successfully ablate and occlude veins without damaging surrounding tissue. The handheld device has gone through multiple design iterations with our team, and we have tested the device in both *ex vivo* and *in vivo* platforms. We will soon be incorporating low-cost ultrasound image guidance into the system and begin testing on large animal porcine models. The technology has potential to be utilized similar to a Bovie Pen for tissue cauterization in a range of clinical applications.

10.4 Improved Fetal Heart Rate Monitoring for Mothers and Doctors (Clinical Studies)

Doppler ultrasound has been used for over 20 years in measuring the fetal heart rate (FHR) during labor and delivery of neonates. However, aside from switching the signal processing from continuous-wave Doppler to pulse-wave Doppler FHR monitoring in the late 1980's, few ultrasound advances have improved the field. Our collaborator from Cayuga Medical Center, Dr. Steven Gelber, found this frustrating and with our Cornell and Transducer Engineering Inc. research team decided to improve FHR monitoring as well as uterine contraction monitoring—using ultrasound.

During labor there is movement from the fetus inside the womb as well as from the mother. Due to a very limited detection range, traditional ultrasound transducers, which are strapped to the mother's belly, lose the heart rate signal. The transducer must then be repositioned by the nurse to redetect the FHR. Wireless telemetry devices for FHR monitoring exist, but FHR detection only works well if the mother and fetus do not move. We have designed a custom transducer that improves fetal tracking and spatial heart rate detection yet works with existing FHR commercially available devices from GE and Philips Healthcare shown in Figure 10.6 and depicted in Figure 10.7.

Our team has designed and tested the FHR monitoring transducer in the lab, and on 25 patients at Cayuga Medical Center under IRB approval, with an improved area detection capability of 2 times across a range of body mass indexes.

Figure 10.6. Wide-beam ultrasound transducer developed in comparison to traditional commercially available transducer for FHM

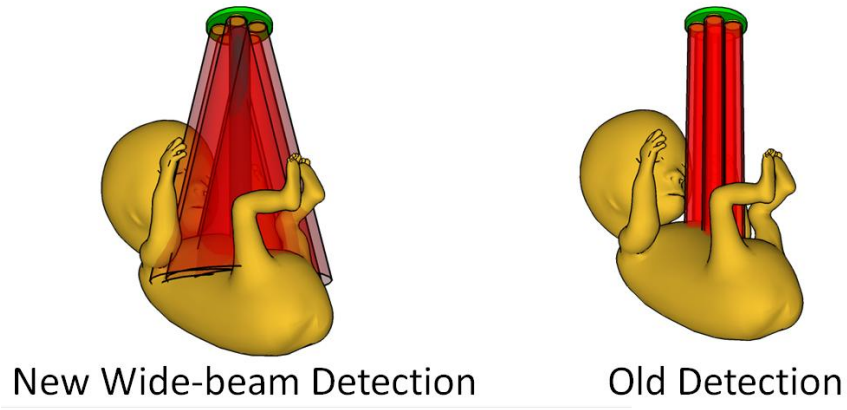

Figure 10.7. Schematic of improved detection of fetal heart rate by broadening the acoustic beam.

Additionally, we have begun development of an ultrasound based solution to measure the uterine contraction strength and duration with a signal processing approach using the same ultrasound transducer used for FHR monitoring. The overall

goal is to provide the doctor a single ultrasound device to perform all heart rate and contraction measurements throughout the labor and delivery, and not require repositioning or wires tethering the mother.

10.5 The Future Not All Ready In Progress

The future of ultrasound is truly amazing with unbounded possibilities, and it will possibly cover the largest spectrum of medical related applications of any other non-ionizing energy source. The potential of low impedance design and the development of battery powered ultrasound devices open a new door to possibilities in both diagnostic and therapeutic applications. By successfully integrating power, electronics and transducer into a single device ultrasound may be geared to medical implants, injectable devices and primary healthcare applications. Furthermore, the reduction of the cost of these systems affords the translation of ultrasound technology to populations where healthcare is not accessible or cost prohibited.

Over the course of this desertion the ground work has been laid to improve a number of healthcare related problems with an ultrasonic twist. Significant focus was spent on the development of the core ultrasound generation technology and its application to improve transport in brain drug delivery. The ability of ultrasound to enhance transport rates in other tissues and across membranes is also well documented; however, its applications are not yet in broad clinical practice. This dissertation contributes to shifting into a new paradigm in ultrasound engineering “low impedance design”, as well as opening new doors to the use of ultrasound in ultrasound-assisted convection enhanced delivery, and portable applications.

Our collaborative team of engineers and clinicians will continue to extend and improve ultrasound into new medical tools while also developing a better understanding of the multiplicity of acoustic, drug and tissue interactions. The

biomedical engineering answers of the future will not be black on white, but through complex and thoughtful analysis, curiosity and creativity, solutions will be found.

CHAPTER 11

CROSS-CUTTING THEMES IN BIOMEDICAL ACOUSTICS AND LESSONS LEARNED DURING DOCTORAL STUDIES

11.1 Introduction

The American Doctorate of Philosophy (Ph.D.) comes from the Latin term *philosophiae doctor* translating in the English language to "the love of wisdom and pursuit of in depth knowledge". The Ph.D. is one of the most advanced degrees awarded to an individual by an academic university after the completion of novel independent research and in depth analysis under supervision from a dissertation committee. The process of receiving a Ph.D., some may say, is a long and daunting task involving research, data analysis, and practical experience. My doctoral training has been a combination of all of this, and has been dependent upon the input of numerous advisors, collaborators and students who have helped me reach this substantial milestone. The scope of doctoral training received from advisory committees, departments and universities is an invaluable resource for future endeavors. I have found that the value of the degree is not the diploma, but the knowledge and lessons learned, and the breadth of experiences obtained opening up new doors in creativity, critical thinking and exploration which I bring with me to the next phase in my career.

My dissertation, *Medical Ultrasound for Brain Drug Delivery and Rehabilitation Medicine* was both a unique educational experience covering a spectrum of academic and social complexities, as well as a scientific contribution

developing new engineering approaches, techniques and ultrasonic applications to improve human health. The lessons learned along this educational pathway continually prove useful in the conduct of research and the sharing of knowledge. The cross-cutting themes evolved from an array of biomedical engineering collaborations I have forged. This has set the foundation for new applications and better understanding of bioacoustics effects of ultrasound.

My training in acoustics began well over sixteen years ago, starting with my early childhood apprenticeship in ultrasound transducer design and electrical/mechanical engineering. This experience gave me the foundational knowledge I needed to pursue innovations in ultrasound. Over the course of my hands on training, I have been afforded the benefit of developing a unique practical understanding, insight and instinct into engineering. Combined with my bachelors and doctoral studies of human physiology, neurobiology and biomedical acoustics for tissue engineering, brain drug delivery and rehabilitation medicine, I have acquired a distinctive ability for innovating ultrasound technology, studying and optimizing bioacoustics effects and solving challenging medical problems. Furthermore, having incredibly supportive advisors, knowledgeable collaborators and enthusiastic students has thrust my research quickly forward.

11.2 Cross-Cutting Themes

After over 60 years of medical ultrasound applications spanning the diagnostic and therapeutic medical realm, ultrasound is still the widely accepted “go-to” tool for immediate non-invasive imaging and healing in physiotherapy and rehabilitation. Due to the multiplicity and complexity of the interactions ultrasound waves have with biological tissues and media in therapeutic applications, it is not surprising that the significance of each mechanism of interaction is not clearly understood. In fact, much

of the research to date has focused on using therapeutic ultrasound for clinical outcomes in randomized placebo controlled trial. Only recently, within the last decade, has cellular and small animal research begun to elucidate the mechanisms behind therapeutic ultrasound.

As discussed in Chapter 1, the interactions of acoustic waves with biological media provide a number of effects/mechanisms that can be utilized when various ultrasonic energy forms are delivered, and thereby stimulate the media and surrounding area. A significant focus of this dissertation included the use of ultrasound to improve transport rates in media; this includes drugs in brain and muscle, nutrients in tissues, and the washout of pain mediators and inflammatory cytokines at joint targets. The therapeutic results obtained are generated from a combination of cavitation, micro mixing, thermal, streaming, mechanical oscillation, dispersion and other interactions that are highly dependent on acoustic power and mode/repetition of delivery. The overall effect in many biological scenarios is that the ultrasound field and path of propagation creates a dynamic environment, increasing the kinetics and transport rates locally. At a low acoustic intensity regime, micro mixing from stable cavitation, acoustic streaming and mechanical oscillation of the media may provide the strongest forces for improving transport rates. Evidence from the work presented throughout the dissertation in tracer transport with ultrasound, research from other groups, as well as future research that is now underway, support this hypothesis. One observation at the low acoustic intensity is that cells are not oblivious to the acoustic pressure field, and interact and release cytokines in response to mechanical stimulation.

Recent research conducted by our lab has shown that stimulating osteoarthritis synovial fibroblasts in 2D and 3D culture systems with low intensity therapeutic ultrasound (LITUS) has a down regulation effect on the level of pro-inflammatory

cytokine secretions of Interleukin (IL)-6, IL-8, and Vascular endothelial growth factor. Other work conducted in the field has shown that LITUS stimulates neuronal cells, bone cells and a number of other cell types under various exposure parameters. The role that ultrasound plays in changing the *in situ* environment as well as the cell-signaling cascade is still a confounding issue that should be addressed to optimize clinically useful LITUS therapies.

At higher acoustic intensities the onset of transient cavitation and thermal coagulation are the acoustic-tissue interaction mechanisms that clearly dominate in this regime. High intensity acoustic fields provide clouds of cavitation activity that release tremendous amounts of mechanical energy. Transient cavitation has found medical application in transdermal drug delivery and blood brain barrier disruption to mediate the delivery of pharmaceuticals across the stratum corneum and brain vasculature, respectively. The energy released during cavitation "sonoporates" the tissue, thereby disrupting the tissue structure and membranes and allows drug to diffuse more readily through the medium. Most ultrasound assisted transient cavitation based drug delivery regimes only use cavitation energy for short durations since extended treatments would produce significant amounts of heat and cause thermal coagulation. On the other hand, high intensity focused ultrasound (HIFU) is used for noninvasive thermal ablation of tissues by slowly heating a region of interest and raising the focal volume of the acoustic field to a temperature for cell death and tissue necrosis.

The future of ultrasound applications will utilize the full range of frequencies, intensities and treatment durations. Combination devices that sonoporate tissues using short cavitation treatments, and then utilize continuous ultrasound to provide acoustic streaming and stable cavitation to enhance drug transport could lead to a variety of new controlled release systems. Furthermore, the combined drug delivery, cell

stimulatory and healing use of ultrasound is a unique field to study requiring a multidisciplinary approach with biology, physics, and engineering disciplines.

11.3 Lessons Learned

I have found that the gravity of every learning experience may never truly be appreciated until a letdown becomes a success, or a mishap is bypassed by wisdom. I am a leaper, an instinctual persevere who learns from mistakes. This personality has driven me since I was a child from disassembling my parents' prized Bavarian cuckoo clock, to running for class president, designing clinical and reach tools, and building and leading my own lab. Nothing always goes as planned, the cuckoo clock never made it fully back together, it took me over a year to finally be class president, the doctor broke my ultrasound device on the first day of use, and the beautiful lab provided to me as only a Ph.D. candidate did not have any equipment. Learning is an exciting process and the points I share from my doctoral studies will prove useful for any individual wishing to educate and innovate. I share this wisdom to guide achievement in academic research.

Simplicity and the elegance found in simple proofs and engineering concepts has a very important place in science and teaching. Being able to present ideas, convey messages and deliver technology in general terms is an invaluable asset for an academic career. During my doctoral studies, I learned that presenting clear ideas and breaking down concepts into the building block stages is important to understand the overall purpose of a project, engineering concept or learning objective. An example of this was in developing miniaturized ultrasound systems by starting with the most simplistic requirements of power source, amplifier and transducer. By breaking down a well-established technology into simplistic terms, new ideas were generated resulting in substantial improvements and technological breakthroughs. In ultrasound

systems, impedance to energy transfer was one of these barriers. However, by minimizing the electrical and mechanical impedance of ultrasound systems, Ultralow Impedance Ultrasound Design (UIUD) reduced the opposition to energy transfer from power source to ultrasonic vibration. By applying UIUD, lower voltages (less than 4 V) could be used to generate abundant ultrasonic power. In UIUD, energy transfers efficiently because electrical to mechanical conversion losses are reduced; this allowed us to design protabl therapeutic ultrasound devices as well as high power multichannel arrays for biomedical acoustic research.

Beyond engineering and research I have learned that teaching new ideas and concepts is more effective when the abstract and complex ideas are introduced in simple terms. I found this with my students I trained and mentored during my doctoral studies. In teaching a new concept, I would first introduce the overarching idea that might be out of the comfort area of the student, but shortly thereafter return to presenting the idea in basic concepts already grasped by the students. This approach is useful since students appreciate the significance of the knowledge/skill to be acquired while also building confidence in their ability and hastening the learning process. More importantly, teaching in this fashion allows the students to attack new problems on their own using the fundamental tools they acquired after mentorship. From teaching to research I look to present ideas and develop experiments that are as simple and elegant while still conveying the appropriate knowledge and answering the scientific question.

Questioning ambiguity and *critical thinking* are essential elements to conducting good research. Clearly presented ideas allow the audience to understand the conveyed message as discussed above. Over the last 4 years I have attended many scientific presentations, read and skimmed hundreds of journal articles, and reviewed and written research proposals for funding. By participating in this process, I quickly

learned that ambiguity in presentations and written language invariably results in miscommunication of the experiments and results of them. From the research prospective, explicit descriptions and critical presentation of the experimental outcomes is respected from the scientific community and is a metric of good research. Additionally, the format in which results are presented and conveyed to the audience can make or break your research in the eyes of the scientific community. It is therefore extremely important to present your research in a coherent fashion in an appropriate forum for the target audience. A lay audience may only be interested in the big-impact on their lives, while the scientific community would be interested in critical assessment of the results, knowledge gained and their impact in designing the next round of experiments.

In developing research experiments and fundable proposals critical thinking about the experiments is a must. In most cases, the experiments are generally still in the process of design and have not yet been carried out successfully. In designing a research proposal and a successful research career, significant time must be spent on brainstorming and thinking critically on the experimental protocol and success criteria. A poorly thought out proposal will inevitably be ambiguous to the reviewer, and will reflect negatively on the aptitude of the investigator, ultimately reducing chances for success. Grantsmanship and the ability to clearly convey a research proposal is truly an art that matures as different experience shape your background, and in order to be successful at it having mentorship in the process is very helpful. Crafting proposals in multidisciplinary research in many cases requires collaborators that provide supportive insight and are very important to translational research projects.

Collaborations are ties to knowledge and in order to be a successful teacher and investigator it is important to have collaborators who can add breadth to your scientific impact and reach. Immersing myself with senior investigators had a

tremendous impact on my learning and grantsmanship during my doctoral studies. It was important to work with clinicians who were on the front lines with patients, particularly for my interest in clinical research and improving healthcare from an engineer's perspective. These collaborators not only brought credentials to my research team, but also provided clinical practicality and translational acceptance to the research goal. Collaborators of numerous disciplines have brought new ideas and tools that proved useful in developing a better understanding of my own research objectives. Cross pollination of labs and research agendas in many cases inspired new ideas and discoveries. This was the case for my dissertation work that flourished with multidisciplinary collaborates from biology and chemistry to neurosurgeons and gastroenterologists.

Leadership, being thoughtful and mindful of others is an important attribute to a leader, particularly one that is trying to educate and inspire. I have been a leader my whole life, from hockey captain to student government president. Additionally, I have operated small businesses with employees and consulted on a number of occasions, yet it was not until my graduate work that I learned how important it was to be understanding of my students' social dynamic and educational goals. In building a small student army to help me during my doctoral studies, I found that there was a delicate balance between pushing students to reach for their goals as well as my labs research agenda, while also supporting my students' other obligations. At first this was somewhat difficult for me because of the university dynamic with the constant turn over and limited retention time of students. It was frustrating and difficult to train each student over and over again, and this was disheartening when trying to move my experimental goals forward. However, I found that being a good leader required me to able to position students into roles that they could flourish in while simultaneously reducing my required retraining efforts on individuals in the group.

In my last 2 years of doctoral work I found that was able to balance the passing of knowledge from group member to group member, while keeping students motivated and self-resilient on their projects. A key to the smooth transitions were to appoint research leaders who had the duty of passing on key knowledge to the new student members who entered the lab. This allowed the more senior members to have a supervisory role in training the new students. Each student, whether senior or new, still had their own individual project that they designed and carried out under the core research themes of my research. I found that this approach gave the students a sense of project ownership and for most of the students this resulted in successful research and students who enjoyed working on the project: A win-win scenario.

Finally, leadership roles require the building of camaraderie between the team and confidence of the individual members. I learned that student teams seem to work the best to carry out the research goals, especially in projects requiring significant patience and focus. In some cases, the individual students on the team may have independent projects, but still work together on additional, supplementary projects that would be difficult for any one person to carry out alone. The idea of team research and shared responsibility is important for group camaraderie and synergy, and invaluable in the students' future careers.

11.4 Concluding Remarks

My doctoral study at Cornell University under the mentorship of Dr. William Olbricht, Dr. Ronald Booker and Dr. Lawrence Bonassar was a remarkable experience. I developed an in-depth understanding of biomedical acoustic applications and bioacoustics tissue interactions. I gained invaluable mentoring, laboratory management and collegiate teaching skills. Additionally, I formed a vast array of

relationships with clinicians and scientific investigators who have interest in similar biomedical research applications.

Now I am starting my independent research career and taking all the lessons learned and applying them to new biomedical problems and developing a deeper understanding of the mechanisms of ultrasonic interactions with biological media. By applying critical thinking and looking for the underlying building blocks to unravel the complexity of problems, I will be able to overcome unmet needs to better human health. Furthermore, providing strong leadership and mentorship to my students and lab, and tying in collaborators across disciplines will make for an exciting, innovative and multifaceted research agenda. From cell to tissue to human, I will conduct cross cutting research that applies basic mechanisms and state-of-the-art design concepts to treat and prevent disease for a happier, healthier life.

APPENDIX

3.1 Appendix

Parts list for amplifier components

1. Low output impedance MOSFET, quantity 8 (#IRF7350, International Rectifier Inc. or #FDS4559, Fairchild Semiconductor Inc.)
2. Pin driver, quantity 3 (#EL7158ISZ, Intersil Inc.)
3. 1.54 MHz TTL Crystal Oscillator, quantity 1 (#SE1216- ND, Epson Toyocom Inc.)
4. 10kΩ,+/-5%, ¼ watt resistor, quantity 3 (General)
5. 820Ω, +/-5%, ¼ watt resistor, quantity 16 (General)
6. 2.2Ω, +/-5%, ¼ watt resistor, quantity 8 (General)
7. 1Ω, +/-5%, 5 watt resistor, quantity 8 (General)
8. 47uF, +/-20%, 50 volt electrolytic capacitor, quantity 12 (General)
9. 0.1uF, +/-20%, 50 volt electrolytic capacitor, quantity 12 (General)

Parts list for housing and miscellaneous parts

1. Plastic enclosure, quantity 1 (#073, Serpac Inc.)
2. Rotary switch, quantity 2 (#275-1386, Radio Shack Inc.)
3. SPST 3-way switch, quantity 1 (#275-612, Radio Shack Inc.)
4. LED, quantity 1 (#276-316, Radio Shack Inc.)
5. Voltage regulator 5 volts, quantity 1 (#276-1770, Radio Shack Inc.)
6. Voltage regulator 12 volts, quantity 2 (#276-1771, Radio Shack Inc.)
7. Prototyping board, quantity 1 (#276-150, Radio Shack Inc.)

8. DC power connector, quantity 1 (#274-1563, Radio Shack Inc.)
9. NiCad 9.6 volt battery with charger, quantity 6 (#23-432, Radio Shack Inc.)

4.1 Appendix

Parts list for amplifier components

1. PCB Circuit Board, quantity 1 (Sunstone Circuits Inc.)
2. Low output impedance MOSFET, quantity 14 (#FDS4559, Fairchild Semiconductor Inc of #IRF7350, International Rectifier Inc..)
3. Pin driver, quantity 7 (#EL7158ISZ, Intersil Inc.)
4. 10kΩ,+/-5%, ¼ watt resistor, quantity 7 (General)
5. 820Ω, +/-5%, ¼ watt resistor, quantity 14 (General)
6. 2.2Ω, +/-5%, ¼ watt resistor, quantity 8 (General)
7. 10uF, +/-20%, 50 volt electrolytic capacitor, quantity 19 (General)
8. 0.1uF, +/-20%, 50 volt electrolytic capacitor, quantity 19 (General)
9. BNC connector, quantity 2 (General)
10. Heat-sinks, quantity 7 (#3-050305U Cool Innovations Inc)
11. Thermal conductive epoxy, quantity 25ml (Locktight® idh#234476 3873 Henkel Inc.)
12. Activator, quantity 13ml (Locktight® idh#230178 7387 Henkel Inc.)

4.2 Appendix

ULTRASOUND WAVE GENERATING APPARATUS[17]

4.2.1 Abstract

In one embodiment, there is provided in an ultrasound wave generating apparatus a low output impedance transistor based driver circuit that has the ability to apply a drive signal at a frequency corresponding to an ultrasound transducer's resonant frequency. The low output impedance of the driver circuit allows for a substantial portion of the energy to be delivered to the ultrasound transducer and converted to ultrasound energy. The power transfer efficiency of the presented circuit allows ultrasound drivers to be powered by portable battery packs, while still delivering high ultrasound acoustic power. The ultrasound driver can provide energy in sufficient amounts making it suitable for a range of ultrasound driving applications including but not limited to therapeutic low and high power clinical systems, high intensity focused ultrasound HIFU, acoustical welding, industrial inspection, and other various forms of low-to-high power acoustic devices. Other embodiments of ultrasound transducer drivers and of other components of portable ultrasound generator apparatus in various embodiments are set forth herein.

4.2.2 Field of the Invention

This invention relates to transducer provisioned apparatuses in general and in particular to ultrasound wave generating apparatuses for use in a wide variety of applications.

[17]This work has been published as Lewis, G.K., Jr., Olbricht, W.L. (2009). Ultrasound wave generating apparatus. United States PTC Patent Application. PCT/US2009/050297

4.2.3 Background of the Invention

In the last two decades therapeutic ultrasound has received attention from the medical community as a tool to relieve arthritis, to improve rehabilitation, and to enhance wound healing processes. Ultrasound at higher energies plays a role in surgical applications such as prostate therapy, and brain tumor and cardiac tissue ablation. Therapeutic ultrasound and its effects on tissue properties are currently being studied in research. For example, researchers are assessing the ability of ultrasound for large molecule transdermal drug delivery, in targeted chemotherapy delivery to brain cancer, and in cellular gene transfer applications. The potential of a combined portable ultrasound imaging and therapeutic system is currently being studied to great lengths for military, industrial, and medical applications. Despite the widespread use of ultrasound, the basic hardware has not changed significantly in the past 50 years.

The ability to drive ultrasound transducers for therapeutic, surgical, mechanical, military, and other applications is of importance to medical doctors and acoustical engineers and professionals in numerous additional fields.

4.2.4 Summary of the Invention

In one embodiment, there is provided an ultrasound wave generating apparatus having a low output impedance transistor based driver circuit that has the ability to apply a drive signal at a frequency corresponding to an ultrasound transducer's resonant frequency. The low output impedance of the driver circuit allows for a substantial portion of the energy to be delivered to the ultrasound transducer and converted to ultrasound energy. The power transfer efficiency of the presented circuit allows ultrasound drivers to be powered by portable battery packs, while still delivering high ultrasound acoustic power. The ultrasound driver can provide energy in sufficient amounts making it suitable for a range of ultrasound driving applications

including but not limited to therapeutic low and high power clinical systems, high intensity focused ultrasound HIFU, acoustical welding, industrial inspection, and other various forms of low-to-high power acoustic devices. Other embodiments of ultrasound transducer drivers and of other components of portable ultrasound generator apparatus in various embodiments are set forth herein.

In another embodiment, a low output impedance power supply can be incorporated in a portable ultrasound sensing apparatus. Various embodiments of an ultrasound sensing apparatus are set forth herein.

4.2.5 Brief Description of the Drawings

The features described herein can be better understood with reference to the drawings described below. The drawings are not necessarily to scale, emphasis instead generally being placed upon illustrating the principles of the invention. In the drawings, like numerals are used to indicate like parts throughout the various views.

Figure 4.2.1 is a schematic block diagram of an ultrasound wave generating apparatus;

Figure 4.2.2 is a schematic diagram of a driver circuit in combination with a timing circuit;

Figure 4.2.3 is a block diagram of a driver circuit in combination with a timing circuit, wherein the driver circuit includes a plurality of transistor pairs arranged in parallel pairs;

Figure 4.2.4 is a schematic diagram of a power supply having a driver circuit with a plurality of transistor pairs arranged in parallel;

Figure 4.2.5 is a schematic diagram of a power supply having a plurality of series connected power supply stages;

Figure 4.2.6 is a plot of resonant frequency (expressed as a point value) versus driver circuit output impedance for illustrating an effect of driver circuit output impedance on resonant frequency;

Figure 4.2.7 is a depiction of an exemplary user interface component of an ultrasound wave generating apparatus, wherein actuator virtual control buttons are displayed on a display of an ultrasound wave generating apparatus;

Figure 4.2.8 is a Mason model power output chart for an ultrasound transducer in one embodiment; where the ultrasound transducer is provided by a 10.3 Ohm ultrasound transducer having a nominal frequency of resonance of 1.5 MHz;

Figure 4.2.9 is a Mason model power output chart for an ultrasound transducer in one embodiment; where the ultrasound transducer is provided by a 1.2 Ohm ultrasound transducer having a nominal frequency of resonance of 1.5 MHz;

Figure 4.2.10 is a Mason model power output chart for an ultrasound transducer in one embodiment; where the ultrasound transducer is provided by a 10.6 Ohm ultrasound transducer having a nominal frequency of resonance of 8 MHz;

Figure 4.2.11 is a Mason model power output chart for an ultrasound transducer in one embodiment; where the ultrasound transducer is provided by a 0.37 Ohm ultrasound transducer having a nominal frequency of resonance of 8 MHz;

Figure 4.2.12 is an impedance versus frequency plot for a selected ultrasound transducer in one embodiment;

Figures 4.2.13-4.2.18 are signal plots illustrating specific output drive signals, each being associated with a particular candidate transducer assembly of a set of candidate transducer assemblies;

Figure 4.2.19 is a diagram showing a single transducer element ultrasound transducer;

Figure 4.2.20 is a diagram showing a plural transducer element ultrasound transducer;

Figure 4.2.21 is a physical form view of an ultrasound wave generating apparatus in one embodiment;

Figure 4.2.22 is a front view of probe for an ultrasound wave generating apparatus;

Figure 4.2.23 is a photograph of probe for an ultrasound wave generating apparatus;

Figure 4.2.24 is a top view of a printed circuit board carrying components of a power supply in one embodiment;

Figure 4.2.25 is a bottom view of the printed circuit board as shown in Figure 5.24;

Figure 4.2.26 is a photograph of a transmission line for an ultrasound wave generating apparatus having a braided coaxial cable transmission line;

Figure 4.2.27 is a diagram of a transmission line for an ultrasound wave generating apparatus having a twisted coaxial cable transmission line;

4.2.6 Detailed Description of the Invention

A high level schematic diagram of an ultrasound wave generating apparatus is shown and described with reference to Figure 4.2.1. Ultrasound wave generating apparatus 1000 can include a power supply 10, and an ultrasound probe 80 having a transducer 90 operative for emission of ultrasound waves. Ultrasound probe 80 can emit waves at a frequency within the ultrasound frequency range of from about 20 kHz to about 200 MHz. In some embodiments, ultrasound wave generating apparatus 1000 can also include a transmission line 70.

Referring to power supply 10, power supply 10 can include driver circuit 20, timing circuit 30, power distribution and control circuit 40, and power source 50. Driver circuit 20 can be operative to have low output impedance, *e.g.* of under 0.5 Ohms. Power supply 10 can be housed in a housing 12 as is represented by dashed in border 12. Power supply 10 and its associated housing 12 in one embodiment can be portable and in one embodiment power supply 10 and housing 12 can be hand held. Probe 80 can include an ultrasound transducer 90 which emits ultrasound waves in response to electrical signals received thereby. Transducer 90 can be housed in a probe housing 82 as is represented by dashed in border 82.

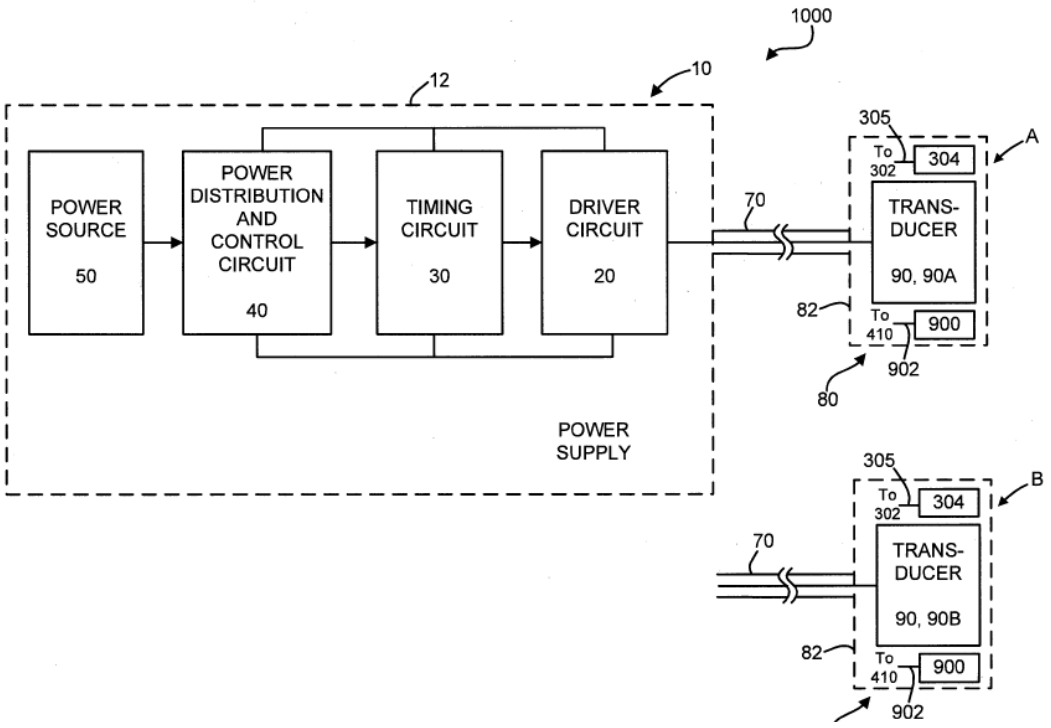

Figure 4.2.1 is a schematic block diagram of an ultrasound wave generating apparatus

Probe 80 and its associated housing 82 in one embodiment can be portable and in one embodiment probe 80 and associated housing 82 can be hand held.

In one embodiment, transmission line 70 can be deleted and ultrasound wave generating apparatus 1000 can include a single housing. For example, transducer 90 can be housed in housing 12, or power supply 10 can be housed in housing 82 of probe 80.

Ultrasound wave generating apparatus 1000 can be conFigured to be operative in a single, or alternatively in multiple operating modes. A drive signal output by power supply 10 can have a different set of characteristics for each operating mode. Further, ultrasound wave generating apparatus 1000 can be operative so that an operating mode of apparatus 1000 and therefore output drive signal changes in response to control inputs that are input into apparatus 1000 by an operator. In some

possible operating modes, power supply 10 outputs a continuous drive signal at a steady state frequency. A mode of operation where power supply 10 outputs a continuous drive signal is useful, in a wide range of applications *e.g.*, in ultrasound therapy medical applications, imaging applications, industrial applications, automobile applications, fuel cell applications, water purification applications, filtering applications, food industry applications, industrial applications, ultrasound therapy medical applications, commercial cutting applications, small particle removal applications, industrial and/or commercial mixing applications, and liquid vaporization applications. In another mode of operation, power supply 10 is operative to output a short burst drive signal. Such mode is useful in a wide range of applications, *e.g.*, in ultrasound therapy medical applications, imaging applications, and industrial applications. The emission of ultrasound waves by apparatus 1000 either in a continuous mode or a burst mode can also be useful, *e.g.*, for cooling of electric motors by recycling bubbles in a coolant, aiding in cooling of batteries, preparation of substrates for fermentation, assisting in distillation of mixed bio-fuels and waste, assisting the converting of plant oils to biodiesel by cavitation, desalinating and purifying water, and preparing of crude oils.

Driver circuit 20 in one embodiment can include a transistor pair having associated first and second clamping voltage terminals, where the clamping voltage terminals have voltages that are alternatingly passed to an output of the driver circuit. The transistor pair can be controlled with an oscillating timing signal for controlling timing of the switching of the transistors of the transistor pair so that the transistors of the transistor pair alternate between conducting and non-conducting states. With the transistors of the transistor pair alternating between conducting and non-conducting states, the voltages of the first and second clamping voltage terminals can be alternatingly applied to the output of the driver circuit. The driver circuit can be

provisioned to include a low output impedance that is mismatched with respect to the impedance of the transducer. The provisioning of the driver circuit to include a low output impedance provides numerous advantages as will be set forth further herein.

In one embodiment, a plurality of the described transistor pairs can be connected in parallel for reduction of an output impedance of the driver circuit, and for increasing an output current capacity of the driver circuit. The driver circuit can be conFigured to have an output current capacity of more than 50 Amperes while being capable of outputting an output drive signal of relatively low voltage. Outputting an output signal of low voltage, *e.g.*, $50V$ or lower is advantageous in a variety of applications where a higher output voltage can pose a risk to humans.

In another aspect, the output drive signal output by the driver circuit for driving the ultrasound transducer can be a bipolar signal having alternatingly positive and negative polarities. Configuring a driver circuit to output a bipolar drive signal provides variation in the forces imparted to transducer 90 for causing vibration thereof, thus increasing an expected lifetime and performance of transducer 90. In another aspect, an applied bipolar drive signal can be an imbalanced bipolar signal so that compression forces are imparted to transducer in greater magnitudes than expansion forces.

In one embodiment, ultrasound wave generating apparatus 1000 is conFigured to be a single mode apparatus so that at all times, when operative to output a drive signal, the ultrasound wave generating apparatus 1000 outputs a drive signal having the same set of characteristics. However, in one embodiment, the ultrasound wave generating apparatus 1000 can include enhanced control features configuring the ultrasound wave generating apparatus so that an operator, *e.g.*, via actuation of control actuator of a user interface of the apparatus, can adjust one or more characteristics of an output drive signal to change a mode of operation of the apparatus. Drive signal

characteristics that can be subject to adjustment can include such characteristics as amplitude, frequency, maximum positive voltage, minimum negative voltage, and the pattern (*e.g.*, "continuous pattern," "burst pattern") of the apparatus's output drive signal. Apparatus 1000 can be operative so that an operator can adjust one or more characteristics of a drive signal via actuation of a user interface actuator. Apparatus 1000 can also be operative so that an operator can adjust one or more characteristics of a drive signal via replacement of a transducer assembly, as is set forth herein.

In one embodiment, ultrasound wave generating apparatus 1000 can be provisioned so that a transducer assembly of apparatus 1000 is replaceable and further so that differently conFigured candidate transducer assemblies can be associated to power supply 10. In one example, each of plurality of candidate transducer assemblies can include a probe 80 and a transmission line 70 terminating in a detachable connector 72 that can be detachably coupled with a connector 220 (see Figure 4.2..21) of power supply 10. The ultrasound wave generating apparatus 1000 can be conFigured so that each candidate transducer assembly that can be associated to power supply 10 has an associated output drive signal having a predetermined set of characteristics well suited for driving the transducer of the particular associated transducer assembly. The ultrasound wave generating apparatus 1000 can be conFigured so that the specific output drive signal output by driver circuit 20 is responsive to which of a plurality of transducer assemblies is presently attached to the power supply 10. In one embodiment, apparatus 1000 can be conFigured so that an output drive signal that is specific to a particular transducer assembly can be subject to adjustment via control inputs that are input to apparatus 1000 by an operator using a user interface of apparatus 1000.

Referring now to Figure 4.2.2, a schematic diagram of driver circuit 20 in combination with timing circuit 30 in a particular embodiment is shown and described.

In general, in one embodiment, an output of driver circuit 20 can be responsive to a timing signal output by timing circuit 30 which controls a timing of an output drive signal. As shown in Figure 4.2.2, driver circuit 20 can include at least one transistor pair 204 and 206 having associated first and second clamping voltage terminals. A timing signal output by timing circuit 30 can be operative to cause switching between transistors of the transistor pair for output of a signal that varies between output of the voltage at the first clamping voltage terminal and the voltage at the second clamping voltage terminal. In the embodiment of Figure 4.2.2, driver circuit 20 is provided by a transistor push pull pair having first and second clamping terminal voltages. In the embodiment described, the first clamping voltage terminal 220 can be clamped to +50*V* and the second clamping voltage terminal 222 can be clamped to -50*V*. Referring to timing circuit 30, an oscillating timing signal can be output by timing circuit 30 for causing alternating switching of transistor 204 and transistor 206. In the embodiment of Figure 4.2.2, transistor 204 and 206 are provided by metal oxide semiconductors field effect transducers (MOSFETs). First transistor 204 clamped to the first clamping voltage terminal (+50*V*) is provided by a PMOS transistor, while the second clamping voltage terminal (-50*V*) is provided by an NMOS transistor. Timing circuit 30 in the particular embodiment of Figure 4.2.2 includes a pin driver integrated circuit 302 that outputs at pin 7 thereof a unipolar 0*V*-12*V* timing signal. In another embodiment, transistors 204 and 206 can be provided by bipolar junction transistors (BJTs). Driver circuit 20 in the embodiments set forth herein can have inactive and active states. An active state of driver circuit 20 is defined when there is a time varying voltage present at the output of the driver circuit 20.

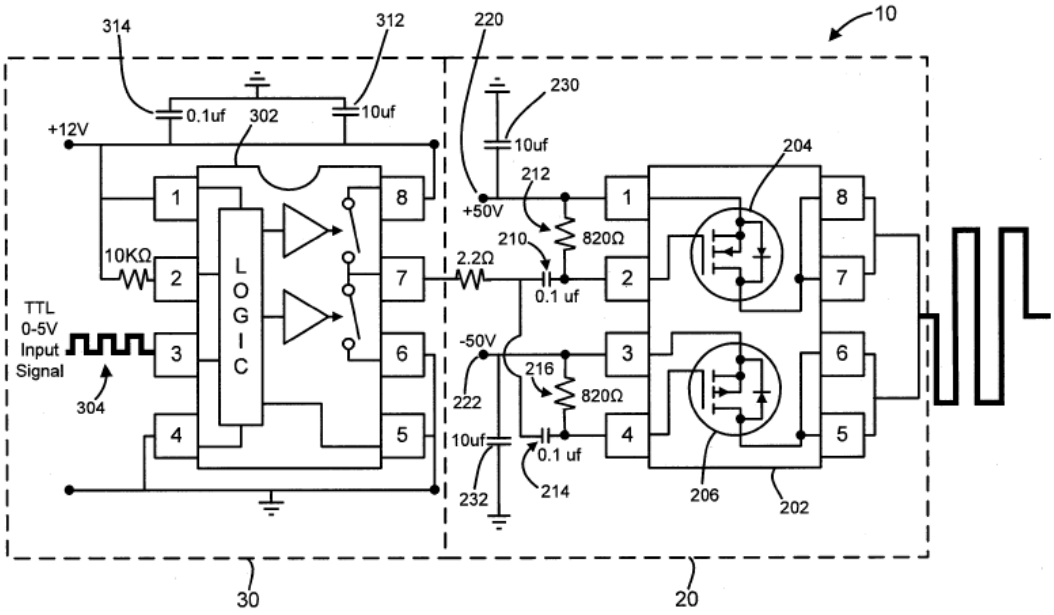

Figure 4.2.2 is a schematic diagram of a driver circuit in combination with a timing circuit

In the particular embodiment as shown in Figure 4.2.2, a transistor pair 204, 206 of driver circuit 20 can include a plurality of Metal Oxide Semiconductor Field Effect Transistors (MOSFETs) arranged in a particular configuration. In the embodiment of Figure 4.2.2, a pair of MOSFETs namely, PMOS transistor 204 and NMOS transistor 206 are provided on a common integrated circuit 202 and are arranged in a push pull configuration. In the particular embodiment, a timing signal output of timing circuit 30 is commonly applied as a gate drive signal to the gates of transistors 204 and 206 through a capacitive coupling circuit. Further regarding MOSFET push pull pair 204 and 206, an oscillating timing signal having a timing controlled by the output of the timing circuit 30 can be commonly applied to gates of the respective push pull pair and respective sources of the pair can be clamped to first and second respective terminal voltages. With the noted oscillating timing signal applied to the MOSFET pair, (PMOS and NMOS) the pair can oscillate between a first

state in which PMOS transistor 204 conducts and NMOS transistor 206 is cut off and a second state in which NMOS transistor 206 conducts and PMOS transistor 204 is cut off.

With further reference to features of timing circuit 30 as shown in the embodiment of Figure 4.2.2, pin 7 of the pin driver integrated circuit 302 in the embodiment of Figure 4.2.2 is the output that provides a 0 to 12V square wave to regulate the switching of the MOSFET's voltage drain. As is detailed in Figure 4.2.2, the unipolar square wave output of pin driver integrated circuit 302 can be converted into a bipolar square wave with use of capacitive coupling circuit. In the embodiment of Figure 4.2.2, a capacitive coupling circuit is provided by coupling capacitors 210 and 214 in combination with resistors 212 and 216. From pin 7 of the pin driver 302 in the embodiment of Figure 4.2..2, a 2.2 Ohm resistor splits off with two 0.1mF coupling capacitors 210 and 214 into the input pins 2 and 4 of the low on resistance N/P channel MOSFET integrated circuit 202. MOSFET integrated circuit 202 can be provided by an IRF7350 MOSFET integrated circuit of the type available from International Rectifier Corporation. Further, resistor 212 is connected between pin 2 and the positive terminal voltage and resistor 216 is connected between the negative terminal voltage and pin 4 of MOSFET integrated circuit 202. Resistors 212 and 216 function to allow for a voltage differential from gate to source. MOSFET integrated circuit 202 in one embodiment can be provided by an IRF7350 MOSFET integrated circuit of the type available from International Rectifier Corporation. In another embodiment, MOSFET integrated circuit 202 can be provided by an FDS4559 integrated circuit of the type available from Fairchild Semiconductor Corporation. Pins 1 and 3 of MOSFET integrated circuit 202 are held at a maximum of - 50V and + 50V , respectively, with 820 Ohm resistors across pins 1−2 and 3−4. Bypass capacitors 230 and 232 are applied as well to pins 1 and 3 of the MOSFET. Capacitor 230 and

capacitor 232, which are tied to ground function to remove noise from the gate drive signal. Pins 5−6 and 7−8 of MOSFET integrated circuit 202 are tied together and coupled. The output drive signal can be applied to the ultrasound transducer through a standard BNC connector 220 as shown in Figure 4.2.10. In one embodiment, (not shown) the pins 5-6 and 7-8 of MOSFET integrated circuit 202 can be tied together and coupled through 1 Ohm 5W power resistors.

The use of a unipolar timing signal in combination with the capacitive coupling circuit (in the described embodiment of Figure 4.2.2 including capacitors 210 and 214, and resistors 212 and 216), for converting the unipolar timing signal into a bipolar output for input to transistors 204 and 206 provides significant advantages. Pin driver integrated circuits of the type of pin driver integrated circuit 302 having unipolar outputs are mass produced and are available at low cost as off-the-shelf component parts. Thus, use of a unipolar timing signal allows use of a low cost component part. Further, as a unipolar output component pin driver integrated circuit 302 can be powered using a single terminal voltage, the use of a unipolar output timing circuit reduces overall power supply complexity and cost.

Referring to MOSFET integrated circuit 202, MOSFET integrated circuit 202 can include PMOS transistor 204 and NMOS transistor 206 forming a transistor pair for driver circuit 10. In the example shown, the transistors are connected in a push pull pair. An output from pin driver integrated circuit 302 as described in the embodiment of Figure 4.2.2 can be capacitively coupled with use of a capacitive coupling circuit and input into gates of PMOS transistor 204 and NMOS transistor 206. When a square input wave 0 -12V signal is capacitively coupled for output of a bipolar input signal, and where the bipolar input signal is applied to the gates of PMOS transistor 204 and NMOS transistor 206 with the source of PMOS transistor 204 clamped at a suitable clamping voltage, *e.g.,* at + 50V , and the source of NMOS transistor 206 clamped at -

50*V* , the MOSFET pair will alternate between conditions of (a) NMOS cut off, with PMOS conducting and (b) PMOS cut off and NMOS conducting. Operating as described, a transducer driving output signal of the MOSFET pair will be a ± 50*V* square wave. ConFigured as described, it will be seen that the amplitude of the output drive signal output by driver circuit 20 will be dependent essentially only on the voltages at clamping voltage terminal 220 and at clamping voltage terminal 222 but will not be dependent on an amplitude of a timing signal output by timing circuit 30. In the particular embodiment of Figure 4.2.2, an output of timing circuit 20 can control a timing of switching of driver circuit 20; however, an amplitude of the output timing signal can have essentially no effect on an output drive signal output by driver circuit 20.

Referring to further aspects of timing circuit 30, timing circuit 30 in the embodiment of Figure 4.2.2, pin driver integrated circuit 302 can be selected to be capable of driving high capacitive loads. Pin driver integrated circuit 302 can be provided by an EL71581SZ pin driver available from Intersil Corporation. Pin driver integrated circuit 302 can be supplied with a 5*V* square wave transistor-transistor logic (TTL) at pin 3. In one embodiment, the input timing signal 304 can be provided by a crystal oscillator (not shown) having an output frequency that is selected to correspond to the ultrasound probe's resonant frequency (the resonant frequency of transducer 90) for maximum power transfer. Selecting a crystal oscillator of timing circuit 30 to have an output frequency corresponding to the resonant frequency of transducer 90 provides certain advantages. An oscillator (not shown in Figure 4.2.2) can be included by an SE1216-ND crystal oscillator integrated circuit of the type available from EPSON Toyocom Corporation. Pins 1 and 8 are held at +12*V* with 10m*F* and bypass capacitor 312 (*e.g.*, 10m*F*,47*uF*) and bypass capacitor 314 (*e.g.*, 0.1m*F*) to ground. Pin 2 is connected to Pin 1 with a 10*k* Ohm resistor. Pins 4 through 6 are connected to earth

ground. Driver circuit 20 as shown in Figure 4.2.2 has a measured low output impedance of about 0.5 Ohms when integrated circuit 202 is provided by an IRF750 integrated circuit available from International Rectifier Corporation (1.5 Ohms if 1 Ohm series power resistor is included). Where the driver circuit 20 as shown in Figure 4.2.2 is devoid of an output series power resistor, driver circuit 20 has a current output capacity of about 10 Amperes. Schemes for decreasing an output impedance of and increasing a maximum current output capacity of driver circuit 20 are set forth herein.

Referring to the embodiment with reference to the block diagram of Figures 4.2.3 and 4.2.4 and the circuit diagram of Figure 4.2.4, the embodiment of Figure 4.2.3 is a scaled up version of the circuit of Figure 4.2.2, scaled up by providing a plurality of transistor pairs as set forth in the embodiment of Figure 4.2.2 in parallel. As shown in the embodiment of Figures 4.2.3 and 4.2.4, driver circuit 20 can include a plurality of such push pull transistor pairs arranged in a parallel configuration. In the embodiment of Figures 4.2..3 and 4.2.4, driver circuit 20 includes eight (8) transistor pairs. However, it will be understood that driver circuit 20 can include 1 to N transistor pairs in parallel, substantially as conFigured in Figure 4.4.2. Providing a plurality of MOSFET push pull pairs reduces an output impedance of driver circuit 20 and increases the power delivery efficiency of driver circuit 20. With driver circuit 20 provisioned to have an output impedance of less than about 0.5 Ohms, and with transducer 90 having an appropriate impedance 95%-100% of the energy from the power supply 10 can be delivered to transducer 90.

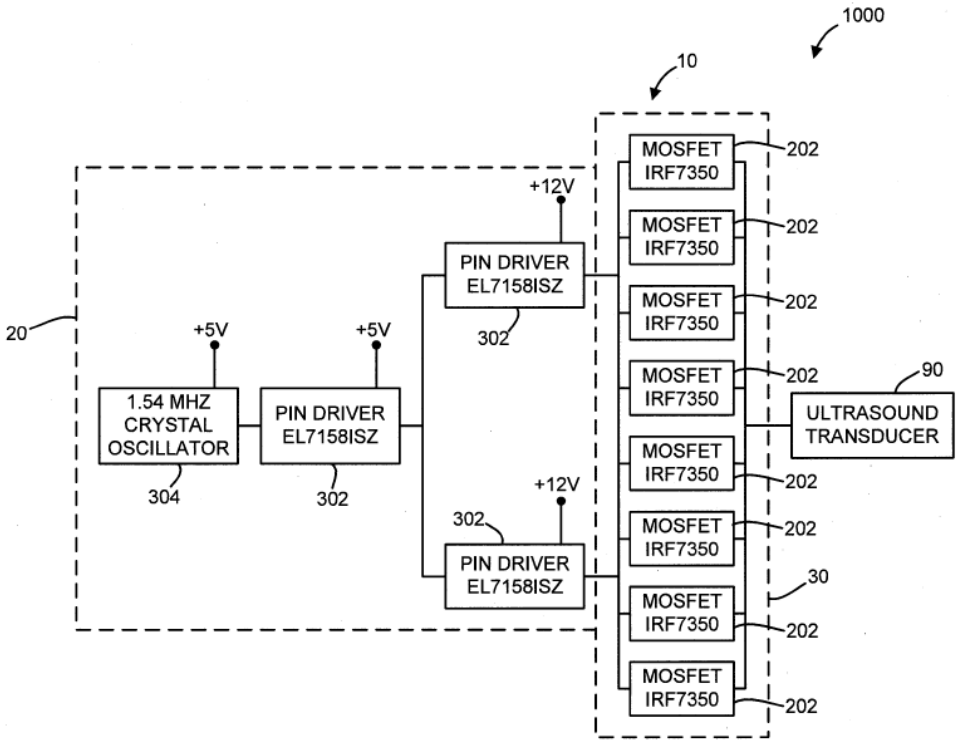

Figure 4.2.3 is a block diagram of a driver circuit in combination with a timing circuit, wherein the driver circuit includes a plurality of transistor pairs arranged in parallel pairs;

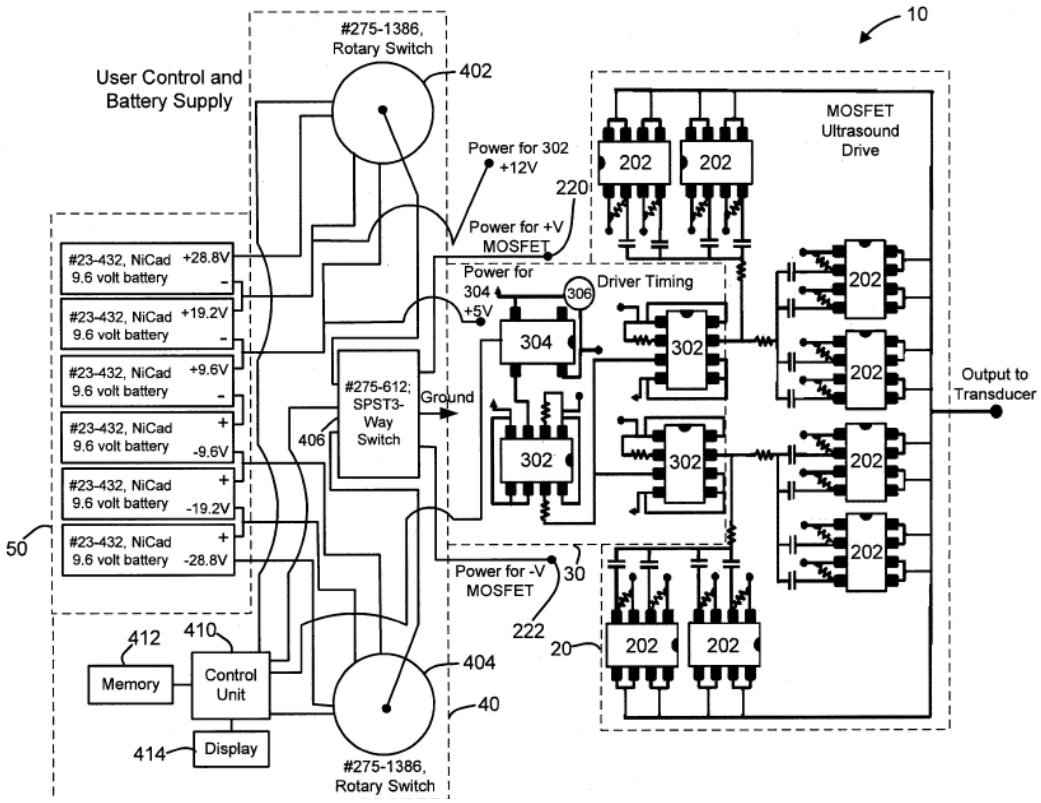

Figure 4.2.4 is a schematic diagram of a power supply having a driver circuit with a plurality of transistor pairs arranged in parallel

Referring to the embodiment of Figures 3 and 4, the Intersil Corporation EL7158ISZ pin driver integrated circuit 302 including a pin driver acts as the logic switch for the MOSFETs that supply the power oscillation drive to the ultrasound transducer. For high power continuous wave applications requiring high current, pin drivers are used to switch MOSFETs in parallel to lower the current burden on each MOSFET. As shown in Figures 4.2.3 and 4.2.4, a single timed pin driver at 5*V* drives two pin drivers at 12*V* as a branching cascade to switch four MOSFETs each for the portable high power ultrasound driving system. Each pin driver/MOSFET unit is wired as shown with respect to the single transistor pair embodiment of Figure 4.2.2. Referring to the circuit of Figure 4.2.2, 1 Ohm power output series resistors (not

shown) can optionally be included at the output of each transistor pair. With the series resistors, the output impedance of the driver circuit 20 was measured directly, and determined from manufacturer values of the MOSFETs, and the eight 1 Ohm parallel power output series resistors (which can optionally be deleted) to be almost entirely resistive and approximately 0.2 – 0.3 Ohms. The output impedance can be reduced by removing the power output series resistors. Where driver circuit 20 includes a plurality of transistor pairs, the effective output impedance of the driver circuit 20 can be given by the formula

$$R_D = \frac{R_P}{N}$$

where RP is the output impedance of an individual transistor pair. Thus, where each transistor pair has an output impedance of about 0.5 Ohms, and there are eight (8) pairs, the total output impedance can be expected to be about 0.06 Ohms. Where the output impedance associated with each pair is about 1.5 Ohms, and there are eight (8) pairs, the output impedance of driver circuit 20 would be expected to be about 0.19 Ohms. By scaling up driver circuit 20, via arranging additional transistor pairs in parallel, an output impedance of driver circuit 20 can be reduced to continually lower levels. For example, where an output resistance of an individual transistor pair is 0.5 Ohms, an output impedance resulting by including 16 pairs to parallel would be about $\frac{0.5}{16} = 0.03$ Ohms. Referring to the circuit of Figures 4.2.3 and 4.2.4 in an additional aspect, a timing of a first set of four transistor pairs is provided by first pin driver integrated circuit and a timing for a second set of four transistor pairs is provided by a second pin driver integrated circuit. Providing such a balanced configuration, where each pin driver integrated circuit that outputs a timing signal that is coupled to a transistor pair, is coupled to an equal number of transistor pairs reduces noise relative to an imbalanced configuration (*e.g.* one in which a first pin driver integrated circuit

provides timing for four transistor pairs, and a second pin driver integrated circuit provides timing for two transistor pairs. Referring to the circuit of Figures 4.2.3 and 4.2.4, while a particular chip layout is described embodying a particular degree of integration, it is understood that alternative scales of integration are possible. For example, the dual MOSFET integrated circuits described can be replaced with four MOSFET integrated circuits. In one embodiment the entirety of circuit components of the driver circuit 20, timing circuit 30, and power distribution and control circuit 40 can be provided on a common integrated circuit.

In the development of apparatus 1000, it was determined that including additional transistor pairs can increase an input capacity of driver circuit 20, thereby decreasing the frequency bandwidth of driver circuit 20. For expanding a frequency bandwidth of power supply 10, power supply 10 can be provisioned as shown in Figure 4.2.5.

In the embodiment of Figure 4.2.5, power supply 10 can include a plurality of power supply stages 11-1, 11-2, 11-3. Each stage, 11-1, 11-2, 11-3 can include a driver circuit 20, a timing circuit 30, power distribution circuit 40, an associated power source 50, *e.g.*, a battery power source or AC to DC converter and an associated stage ground 5. Providing each stage to have an associated power source that can be isolated from the power sources of remaining stages can be advantageous for a variety of reasons. For example, such arrangement mitigates ground coupling and looping, provides isolated power supply stages for multiple channel transducer drive, and provides power supply backup protection. In the embodiment of Figure 4.2.5, there are three (3) power supply stages. However, power supply 10 could also have 1, 2, or N power supply stages. For connecting the stages, an output of a driver circuit 20 of a first stage, *e.g.*, 11-1 is input into the stage ground 5 of the succeeding stage. That is, an output of stage 11-1 is input into ground 5 of stage 11-2, and the output of driver

circuit 20 of stage 11-2 is input into the stage ground 5 of stage 11-3. The stage ground 5 of a first stage 11-1 in the described example can be connected to earth ground.

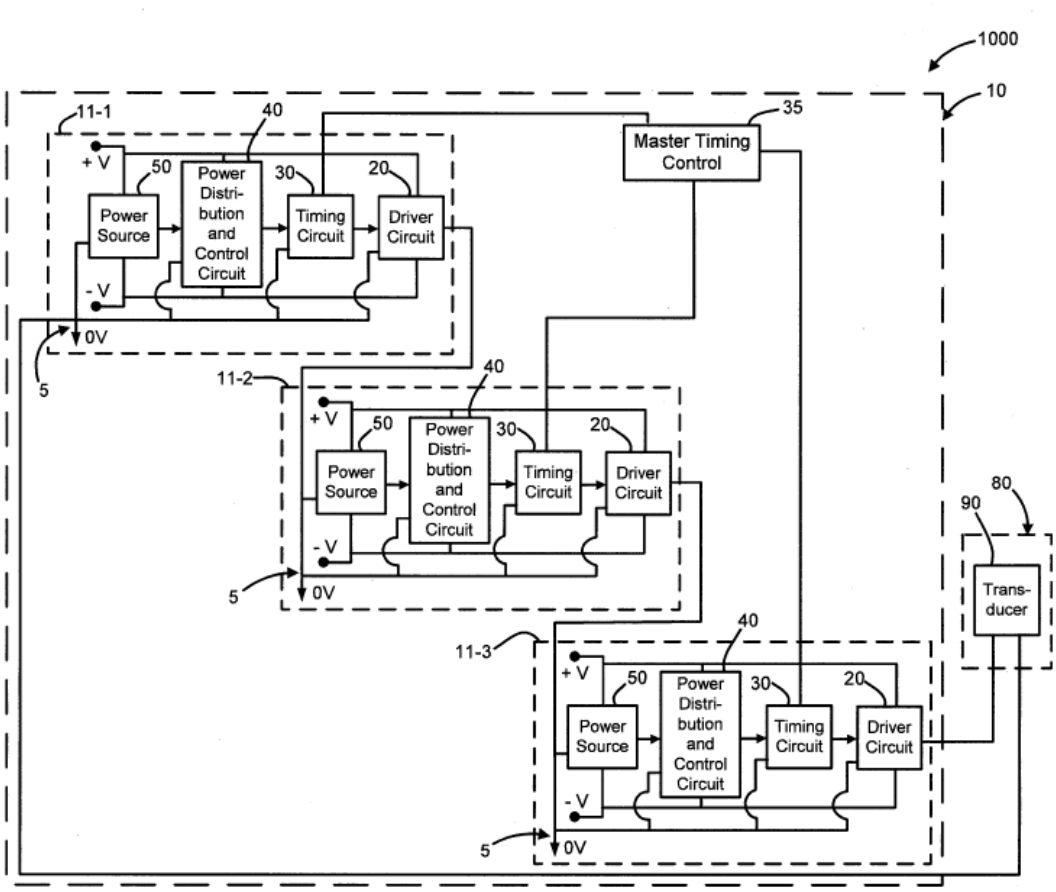

Figure 4.2.5 is a schematic diagram of a power supply having a plurality of series connected power supply stages

Providing a plurality of series connected power supply stages as shown in Figure 4.2.5 operates to sum the voltages of the various stages. For example, if each stage is similarly conFigured and the first stage has an output voltage of ± M*V*, the output of power supply would be ± NM*V* where N is the number of stages, and M is the voltage output of each stage. Accordingly, the multiple stage power supply set

forth herein is operative to provide the function of a voltage transformer without design complexities and manufacturing obstacles sometimes posed by transformers. In some applications, the incorporation of a transformer is advantageous.

The providing of multiple power supply stages increases a frequency bandwidth of power supply 10 and allows a bandwidth restriction problem associated with disposing transistor pairs in parallel to be overcome. An input capacitance of power supply 10 is reduced as stages are added. For example, if each stage is similarly conFigured and the first stage has an input capacitance C1, the input capacitance of multiple series power supplies would be N/C where N is the number of stages and C is the input capacitive of each stage.

An effective output impedance of driver circuit 20 of the third stage 11-3 will be the sum of the output impedance of each driver circuit 20 of power supply 10. However, it will be seen that the value of the effective in output impedance can be maintained at a low impedance level by configuring each stage's driver circuit 20 to have a low output impendence. It is seen that where each stage has an output impedance of 0.03 Ohms, (*e.g.*, as in the 16 transistor pair example set forth herein) an effective output impedance of the last stage driver circuit will be under 0.1 Ohms, still providing excellent voltage transfer to the load, even in cases where a transducer has low impedance (*e.g.*, even where the load has an impedance of 1.0 Ohms, a voltage ratio between load and source would be above 90% (90.9%)).

In another aspect, power supply 10 including multiple stages 11-1, 11-2, 11-3 in series can include a master timing control unit 35. Master timing control unit 35 can be isolated from each stage. Master timing control unit 35 can operate to control a frequency at which each power supply stage 11-1, 11-2, 11-3 switches. Master timing control unit 35 can be operative to switch each stage at a certain frequency or at different frequencies. It has been mentioned that each stage 11-2, 11-2, 11-3 can be

similarly conFigured. For example, each stage 11-1, 11-2, 11-3 can have the same number of transistor pairs arranged in parallel. In another example, each stage 11-1, 11-2, 11-3 can have a different number of transistor pairs, each stage having a number of transistor pairs ranging from 1 to N.

The power supply drive circuits set forth in Figures 4.2.2-4.2.4 generally feature low output impedance, a relatively low voltage output signal, and high output current capacity. It has been described that an output impedance of driver circuit 20 can be decreased by providing a plurality of transistor pairs in parallel as shown in the embodiment of Figures 4.2.3-4.2.4. Also, an output current capacity of drive circuit 20 can be increased by providing transistor pairs as shown in the circuit of Figure 4.2.2 in parallel. The output current capacity of driver circuit 20 is approximately the sum total of the output MOSFET output current capacity for each individual transistor pair. For example, in the driver circuit of Figure 4.2.2, the single transistor pair driver circuit, having a transistor pair formed on integrated circuit 302 has an output current capacity of about 10 Amperes. In the embodiment of Figures 4.2.2-4.2.3 having eight (8) transistor pairs arranged in parallel where the pairs are formed on a smaller conFigured MOSFET integrated circuit, the output current capacity is about 80 Amperes. The output current capacity of driver circuit 20 can be increased or decreased by increasing or decreasing the number or transistor pairs that are arranged in parallel in driver circuit 20. Similarly, an output impedance of driver circuit 20 decreases as additional transistor pairs are added driver circuit 20. In the embodiment of Figure 4.2.2 where driver circuit 20 shows a single transistor pair driver circuit, driver circuit 20 has an output impedance of 0.5 Ohms. In the embodiment of Figures 4.2.2-4.2.3, where driver circuit 20 has eight (8) transistor pairs arranged in parallel and the integrated circuits that are set forth herein, driver circuit 20 has an output impedance of about

$$R_D = \frac{R_P}{N} = 0.6 \text{ Ohms}$$

The output impedance of driver circuit 20 can be adjusted to a desired output impedance by increasing or decreasing a number of parallel arranged transistor pairs in driver circuit 20.

According to the maximum power theorem, maximum power is delivered to a load where an impedance of a load is matched to an output impedance of a source. In some embodiments, apparatus 1000 can be conFigured so that an impedance of a load is matched to an impedance of driver circuit 20. In other embodiments however, load impedance can be mismatched with respect to an impedance of driver circuit 20, which can be provisioned to have a low output impendence (*e.g.,* less than 0.5 Ohms), and apparatus 1000 can be provisioned so that a ratio of an output impedance of driver circuit 20 to a load impedance is less than 1/10. Provisioning an output impedance to be low (*e.g.,* less than 0.5 Ohms) and further so that an output impedance to load impedance ratio is less than 1/10 provides a number of advantages. For example, configuring driver circuit 20 to have a low output impedance and low (*e.g.,* 1/10 or less impedance ratio) results in high energy conversion efficiency. A substantial majority of energy is delivered to the load, (*i.e.*, the transducer 90). As such, very little energy is lost as heat in the driver circuit 20. Such result is particularly advantageous in, *e.g.*, medical applications where heat generated by apparatus 1000 can pose danger to a patient. For any application where power source 50 is provided by one or more batteries, high energy conversion efficiency embodiments set forth herein yield significant advantages in terms of battery life. Maintaining a low driver circuit output impedance and impedance ratio also assures that a source voltage closely corresponds to a load voltage, thus improving the controllability and ease of use of the apparatus. A

voltage delivered to a transducer 90 can substantially be set by establishing a source voltage.

Driver circuit 20 as set forth herein can include an associated source voltage when driver circuit 20 is in an active state and when driver circuit 20 outputs a drive signal having a frequency, *e.g.*, to a resonant frequency of transducer 90. A driver circuit source voltage can be measured directly by measuring voltage across output terminal of a driver circuit in an open circuit condition (without current flow there is no voltage drop across the driver circuit's impedance contributing components). Further, with a load attached across the output terminals of a driver circuit, and with the driver circuit driving the load, *e.g.*, at a frequency corresponding to the resonant frequency, the voltage at the load can be expressed as

$$V_{Load} = \frac{V_{Source}\, R_{Load}}{R_{Source} + R_{Load}} \qquad (4.2.1)$$

where R_{Source} is the output impedance of driver circuit 20. Accordingly, the ratio of a voltage across a load (the transducer), to a source voltage can be expressed as

$$\frac{V_{Load}}{V_{Source}} = \frac{R_{Load}}{R_{Load} + R_{Source}} \qquad (4.2.2)$$

Thus, it is seen that as the output impedance of the driver circuit 30 tends to zero, the load voltage more closely approximates the source voltage. Further, it is seen that by configuring apparatus 1000 so that the ratio of the source output impedance to the load impedance is maintained at or below 1/9, the amplitude of voltage across the load relative to the amplitude of the source voltage at the driver circuit will remain at or above 90 percent. Various embodiments of apparatus 1000 having such ratio are set forth herein. In other embodiments set forth herein, a voltage ratio of load to source is

at or above 95% and in other embodiments is at or above 99%. Prospective examples with expected associated data are set forth in Table 4.2.1 below.

Table 4.2.*1 Impedance of driver and transducer load to source voltage ratio*

Embodiment	Driver Circuit Output Impedance	Transducer Impedance	Load To Source Voltage Ratio
1	0.5 Ohms	8 Ohms	94.1%
2	0.03 Ohms	1 Ohm	97.1%
3	0.5 Ohms	5 Ohms	90.9%
4	0.09 Ohms	3 Ohms	97.1%
5	0.03 Ohms	10 Ohms	99.7%

Another advantage of configuring driver circuit 20 to include a low output impedance and low impedance ratio is that such configuration reduces an amount of shift in a resonant frequency of transducer 90. Referring to Figure 4.2.6, there is shown a plot of the resonant frequency of transducer 90 (the frequency of a drive signal output by driver circuit 20 at which maximum power is output by ultrasound transducer 90) versus source output impedance of driver circuit 20. As the source output impedance increases, the resonant frequency shifts significantly (from about 1.51 MHz to about 1.63 MHz in the described example). Reducing the amount of resonant frequency shift by reducing the source output impedance improves controllability and ease of use of apparatus 1000 for the reason that a resonant frequency that is observed for a particular transducer is more proximate a nominal frequency of resonance for the particular transducer (normally provided by a manufacturer of the transducer and determined based on material properties of transducer 90).

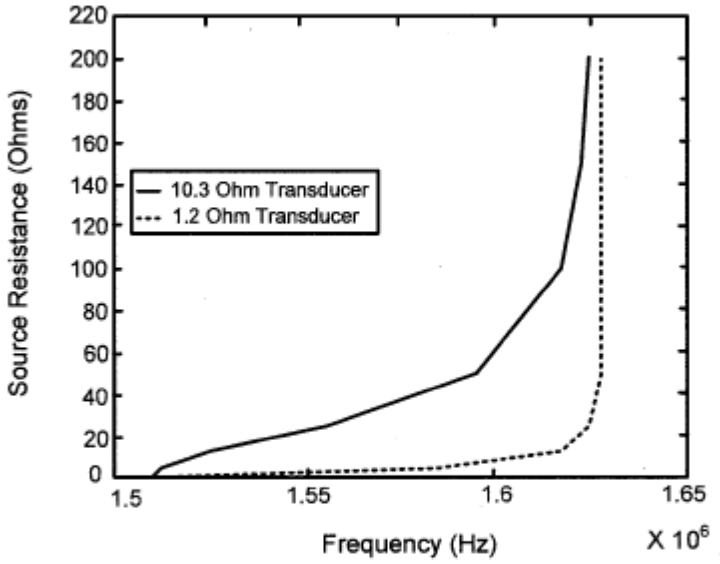

Figure 4.2.*6 is a plot of resonant frequency (expressed as a point value) versus driver circuit output impedance for illustrating an effect of driver circuit output impedance on resonant frequency*

Referring to additional advantages of the low output impedance high output current configuring driver circuit 20, a high output current capacity at driver circuit 20, about 50 Amperes or more in some embodiments (while low current output capacity embodiments are advantages in certain applications) allows high energy output at transducer 90 (about 50 Watts or more in some embodiments) with modest voltages of less than 100*V*, and in several embodiments, about 50*V* or lower or 25*V* or lower. Such functionality (high energy output with only modest voltages) is advantageous in numerous applications, including in medical applications where risk of harm to a patient or caregiver in proximity to transducer 90 is posed by exposure to high voltages, *e.g.* of 100*V* or more. In some applications, however, an output of over 100*V* is advantageous.

In one embodiment, ultrasound wave generating apparatus 1000 can be a single mode apparatus, which has a fixed (non-interchangeable) transducer 90 and which outputs a drive signal of the same characteristic each time it is activated for output of a drive signal. In another embodiment, ultrasound wave generating apparatus 1000 can be a multiple mode apparatus capable of output of drive signals of different characteristics at different times. Apparatus 1000 can be operative so that apparatus 1000 outputs a drive signal having a different set of characteristics in response to an operator input control that is input into a user interface of apparatus 1000. Apparatus 1000, where provisioned so that a transducer assembly thereof is one of a plurality of replaceable candidate transducer assemblies, can be operative so that apparatus 1000 outputs a different output drive signal having a different set of characteristics responsively which of the candidate transducer assemblies is presently associated to power supply 10.

Power distribution and control circuit 40 in the embodiment of Figure 4.2.4 can include a three-way switch integrated circuit 404. Switch integrated circuit 404 can be manually moved by an operator to switch the switch integrated circuit 404 between an OFF position and an ON position. In the ON position, power from power source 50 is coupled to the clamping voltage terminals of driver circuit 20. Power supply ground can be used to isolate +5*V* and +12*V* supplies, thus reducing a wiring burden. In another aspect, power distribution and control circuit 40 can include a control unit 410. Control unit 410 can be provided by a microcontroller or a microprocessor. Control unit 410 can be associated with memory 412, which can store various data, program data, and setup data for determining characteristics of an output signal output by driver circuit 20. Control unit 414 can be in communication with display 414, which can be conFigured to have user interface capability.

For illustrating additional features including control features of apparatus 1000, Figure 4.2.4 shows a further detailed schematic of a power supply shown in the block view of Figure 4.2.3. In Figure 4.2.4, there is shown driver circuit 20, timing circuit 30, power distribution and control circuit 40, and power source 50. Power source 50 in one embodiment can include a plurality of 9.6*V*, 1600 mA h NiCad rechargeable battery packs. Power source 50 in another embodiment can include an AC to DC converter for coupling to an AC wall outlet power source. The battery packs can be, *e.g.* No. 23-432 battery packs available from RadioShack Corporation. Power supply 10 can also include rotary switches 402 and three-way switch 404 forming power distribution and control circuit 40. The user can adjust power delivery to the transducer through the MOSFETs in 9.6*V* increments over the range ± 28.8*V*. Additional batteries can be included for increasing the voltage range of power source. A blue "on" LED 306 in the embodiment of Figure 4.2.4 is tied into the on/off switch that supplies power to the crystal oscillator integrated circuit 304 and pin driver integrated circuits 302 through 5*V* and12*V* 1*A* voltage regulators that also have bypass capacitors. The output of the device is terminated in a male Bayonet Neill Concelman (BNC) connector on the front panel. A battery recharge port at the back of the system (not shown) is wired to charge the six battery packs in series. To charge the system, the device is switched to the off position and the rotary switches are moved to a non-connected terminal as labeled on the devices panel.

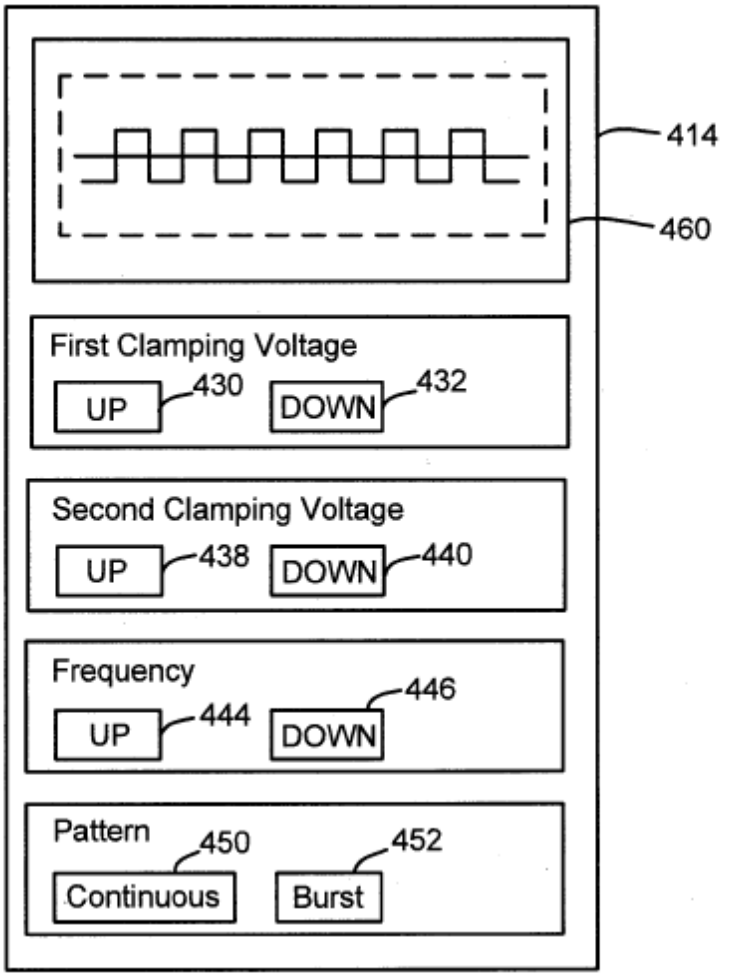

Figure 4.2.*7 is a depiction of an exemplary user interface component of an ultrasound wave generating apparatus, wherein actuator virtual control buttons are displayed on a display of an ultrasound wave generating apparatus*

A user interface of ultrasound wave generating apparatus 1000 can be partially provided by switch 402 and switch 404 which can be used by an operator to control voltages at clamping voltage terminals 220, 222 and can be partially provided by switch 406. A user interface of ultrasound wave generating apparatus 1000 can also include additional control actuators. For example, apparatus 1000 can be conFigured so that display 414 displays various virtual control buttons which can be actuated by

an operator. One example of apparatus 1000 where display 414 is conFigured to include an interface control button is shown in Figure 4.2.7.

In the example at Figure 4.2.7, apparatus 1000 can be operative so that buttons 430, 432 can be used to adjust a voltage at first clamping voltage terminal 220, buttons 438, 440 can be used to control a voltage at second clamping voltage terminal 222, buttons 444, 446 can be used to control a frequency of a drive signal output by driver circuit 20, and buttons 450, 452 can be used to control a pattern of low output drive signal, *e.g.*, to select between a "continuous pattern" or a "burst pattern." In the embodiment set forth herein, control unit 410 can be in communication with switches 402 and 404 so that a voltage at clamping voltage terminals 220, 222 can be adjusted either with use of voltage switches 402, 404 or buttons 430, 432, 438, 440. In preview area 460, there can be displayed a representation of the output drive signal expected to be output when the present set of control parameters is applied. For control of output drive signal frequencies with use of a user interface, control unit 410 can be communicatively coupled to timing device 304 as is indicated in the schematic drawing of Figure 4.2.4. Timing devices such as the crystal oscillator integrated circuit specifically set forth can be selected to be programmable, so that a frequency within a range of frequencies can be selected via input of a control to the device. For expansion of the range of selectable frequencies, a plurality of timing devices having overlapping frequency of ranges can be included in timing circuit 30. Appropriate multiplexing circuitry (not shown) can be provided for allowing selection of an appropriate timing device based on a selected frequency.

In some embodiments of apparatus 1000 where transducer 90 is one of a plurality of candidate replaceable transducers incorporated in one of a plurality of respective transducer assemblies, an output drive signal of apparatus 1000 can be responsive to which transducer assembly (*e.g.* with reference to Figure 4.2.1,

transducer assembly A or transducer assembly B), is presently associated to power supply 10. In the specific embodiment described replaceable transducer assemblies A and B incorporate transmission line 70 and probe 80. However, in another embodiment, replaceable parts of apparatus 1000 that incorporate a transducer (*i.e.*, the transducer assembly) can incorporate probe 80 only with transmission line 70 being a fixed component part. In another embodiment, a transducer assembly incorporating transducer 90 can comprise essentially only transducer 90. A transducer assembly that consists essentially only of transducer 90 can be provided as a plug in component of a circuit board. To the end that apparatus 1000 can adjust characteristics of an output drive signal responsively to which of a plurality of candidate transducer assemblies is presently associated to power supply 10, each candidate transducer assembly can have an associated memory 900 (see Figure 4.2.1) storing an identifier for the transducer, *e.g.*, in the form of a text based alpha numeric identification number. As shown in Figure 4.2.1 memory 900 can be housed within housing 82 of probe 80.

Apparatus 1000 can be operative so that when a new transducer assembly (*e.g.*, A, B and another assembly, C, etc.) is associated to power supply 10, the transducer assembly identifier information stored in memory 900 is communicated to control unit 410, via appropriate communication apparatus 902. For example, control unit 40 and memory 900 can be in communication via a communication apparatus 902 provided by a two wire interface, *e.g.*, a Phillips I2C bus. Control unit 410 can be operative so that responsively to identification data being communicated between memory 900 and control unit 410, control unit 410 establishes appropriate settings for output of a drive signal having a specific set of characteristics for driving the ultrasound transducer of the specific transducer assembly presently associated to power supply 10.

Hereinabove, it has been described that output drive signal characteristics of an output drive signal can be made responsive to an associated transducer assembly by way of communicating of data respecting an identity of a transducer assembly. In another embodiment, apparatus 1000 can be operative so that output drive signal characteristics output by driver circuit 20 are responsive to an associated transducer by way of being controlled with use of specific timing circuitry associated to the transducer assembly of a set of candidate transducer assemblies.

In one example, as explained with reference to Figure 4.2.1, each transducer assembly of a set of candidate transducer assemblies (which may or may not be the full set of candidate transducer assemblies) can be provided with an associated timing device. As shown in Figure 4.2.1, a crystal oscillator integrated circuit 304 can be associated to transducer assembly A, and crystal oscillator integrated circuit 304 can be associated to transducer assembly B. Each crystal oscillator integrated circuit 304 can have associating communication apparatus 305 for communicating with remaining components of timing circuit 30. Communication apparatus 305 can comprise a copper wire. Apparatus 1000 can be operative so that when a new transducer assembly is associated to power supply 10, a timing device associated to the new transducer assembly is made active to control one or more output characteristics of the output drive signal. Referring to the example in Figure 4.2.1, apparatus 1000 can be operative so that when transducer assembly A is associated to a power supply 10, timing device 304 of transducer assembly A controls a timing of the output drive signal. Apparatus 1000 can also be operative so that when the transducer assembly B is associated to power supply 10, timing device 304 disposed with transducer assembly B controls a timing of the output drive signal output by drive circuit 20.

Reference will now be made to ultrasound transducer 90 of probe 80. Ultrasound transducer 90 of probe 80 can be provided by a PZT-4, 1.54 MHz, and

0.75 in. diameter piezoelectric ceramic with a radius of curvature of 1.5 of the type available from EBL Products, Inc. Such transducer by EBL Products, Inc. is given a nominal frequency of resonance of 1.5 MHz by the manufacturer. Housing 82 can be provided by a polyvinyl chloride (PVC) ergonomic plastic assembly. Such assembly can be custom built using a micro-lathe and milling system of the type available from Sherline Products, Inc. The clear acrylic front of the housing 82 acts as a protective cover to the ceramic transducer 90 and also functions as an in-plane focal alignment standoff for the ultrasound energy emitted by transducer 90. Regarding referenced elements herein, a reference to element "90" herein will be regarded as a reference to any of specific transducers referenced herein, *e.g.*, transducer 90, 90A, 90 90B, and so forth.

Transducer 90 can be wired with use of a transmission line 70 provided by a 22 gauge coaxial cable terminated with a connector 72 (Figure 4.2.21) which can be provided by female BNC connector. Transducer 90 can have power output characteristic as shown in Figures 4.2.8, 4.2.9, 4.2.10, and 4.2.11, and impedance characteristics as shown in Figure 4.2.12. In Figures 4.2.8, 4.2.9, 4.2.10, and 4.2.11, there is shown a maximum power output curve, for various transducers calculated using the Mason Model, while being driven by differently conFigured driver circuits having different output impedances over a range of frequencies. Figure 4.2.8 is a power output plot for a transducer having a nominal frequency of resonance of 1.5 MHz and an impedance of 10.3 Ohms. Figure 4.2.9 is a power output plot for a transducer having a nominal frequency of resonance of 1.5 MHz and an impedance of 1.2 Ohms. Figure 4.2.10 is a power output plot for a transducer having a nominal frequency of resonance of 8 MHz and an impedance of 10.6 Ohms. Figure 4.2.11 is a power output plot for a transducer having a nominal frequency of resonance of 8 MHz and an impedance of 0.37 Ohms. A resonant frequency of ultrasound transducer 90

can be regarded as the frequency at which the ultrasound transducer emits maximum power when driven by the output drive signal output by driver circuit 20 that is to drive the transducer.

Referring to Figure 4.2.6, and again with reference to power output plots of Figures 4.2.8, 4.2.9, 4.2.10, and 4.2.11, it is seen that a resonant frequency will shift slightly as an output Impedance of driver circuit 20 is increased. Regarding "resonant frequency" as referred to herein, it is understood that a number of factors can contribute to a transducer's resonant frequency, *e.g.*, the output impedance of the driver circuit 20, the impedance of transmission line 70. Nevertheless, as the primary determinants of the frequency at which transducer 90 resonates are the material properties of transducer, the reference to "resonant frequency of the transducer" is appropriate. Also, if an output impedance of driver circuit 20 and transmission line 70 are maintained at approximately low levels, the contribution of the driver circuit output impedance, and the impedance of transmission line impedance will be negligible.

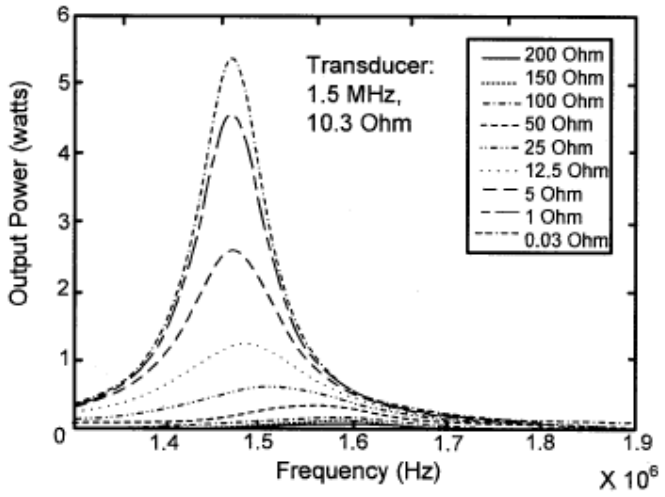

Figure 4.2.8 is a Mason model power output chart for an ultrasound transducer in one embodiment; where the ultrasound transducer is provided by a 10.3 Ohm ultrasound transducer having a nominal frequency of resonance of 1.5 MHz

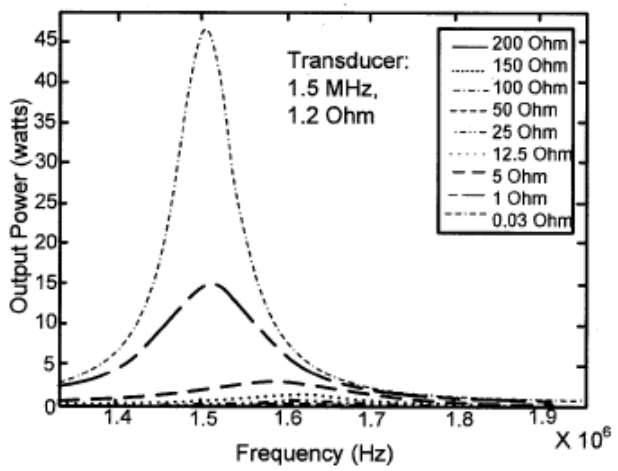

Figure 4.2.9 is a Mason model power output chart for an ultrasound transducer in one embodiment; where the ultrasound transducer is provided by a 1.2 Ohm ultrasound transducer having a nominal frequency of resonance of 1.5 MHz

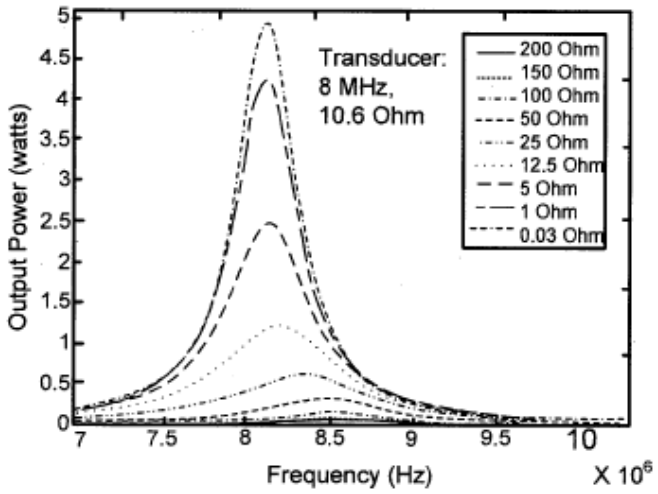

Figure 4.2.10 is a Mason model power output chart for an ultrasound transducer in one embodiment; where the ultrasound transducer is provided by a 10.6 Ohm ultrasound transducer having a nominal frequency of resonance of 8 MHz

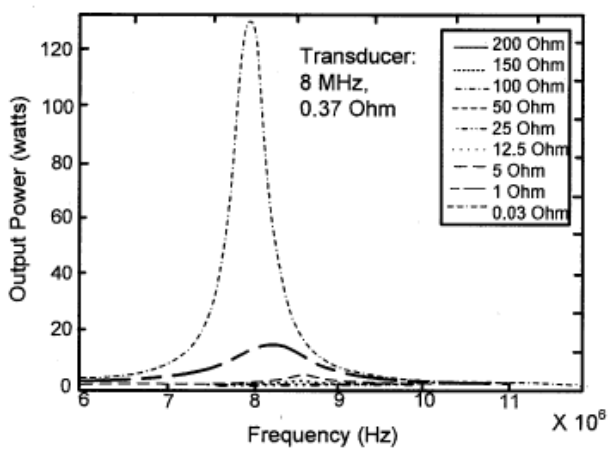

Figure 4.2.11 is a Mason model power output chart for an ultrasound transducer in one embodiment; where the ultrasound transducer is provided by a 0.37 Ohm ultrasound transducer having a nominal frequency of resonance of 8 MHz;

In Figure 4.2.12, there is shown an impedance versus frequency curve for the noted PZT-4, 1.5 MHz (nominal frequency of resonance), 8 Ohm transducer. Impedance characteristics of a ceramic transducer can be measured, *e.g.,* with use of a standardly known meter method for measuring impedance. In the described example for transducer 90, an impedance of transducer 90 is at its lowest value of about 8.0 Ohms at an impedance measurement equipment frequency of about 1.5 MHz. The impedance measuring equipment frequency at which an impedance of transducer 90 is at its lowest value with reference to Figure 4.2.12 can be regarded as a measurement of the resonant frequency of transducer 90.

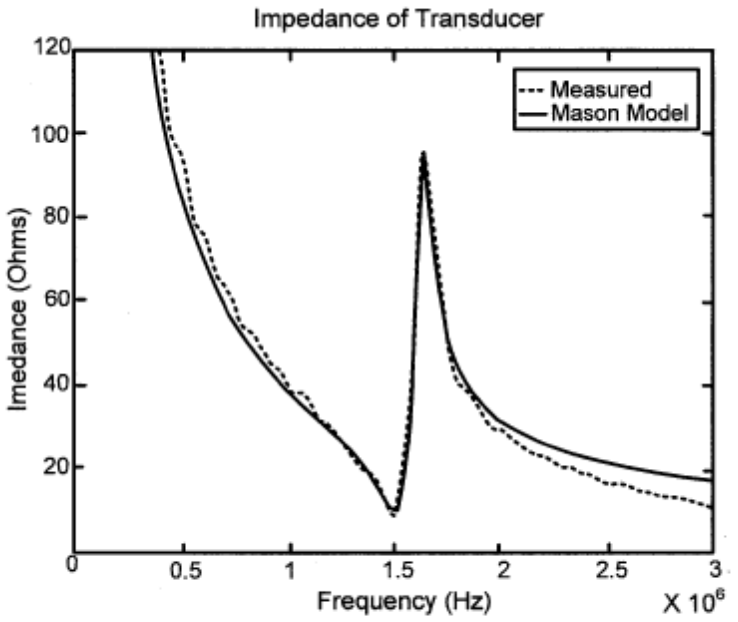

Figure 4.2.12 is an impedance versus frequency plot for a selected ultrasound transducer in one embodiment;

However, as noted, the resonant frequency of transducer 90 when driven by driver circuit 20 can be expected to be dependant, in part, on characteristics of driver circuit 20. By definition, when driven at the resonant frequency power output of transducer 90 is at its highest level. A resonant frequency can be expressed as a point value (*e.g.*, 1.54 MHz) or as a range of frequencies at which power output is above a predetermined percentage (*e.g.*, 90%) of a maximum power output value. A drive frequency corresponding to the resonant frequency can be regarded as a frequency of about the resonant frequency as expressed at a point value. A drive frequency corresponding to the resonant frequency can also be regarded as a frequency within a resonant frequency range, where a resonant frequency is expressed as a frequency range.

It has been noted that power supply 10 can be operative so that an output drive signal for driving transducer 90 can have a frequency corresponding to the resonant frequency of transducer 90. In another aspect, power supply 10 can be conFigured so that an output drive signal output by power supply 10 for driving transducer 90 can oscillate between a positive and negative voltage.

Provisioning power supply 10 to output a drive signal for driving transducer 90 that includes both positive and negative polarity provides significant advantages. Referring to transducer 90, transducer 90 in general will compress when a voltage of a first polarity is applied thereto and will expand when a voltage of a second polarity is applied thereto. Accordingly, applying a drive signal with positive and negative polarity provides variation in the stresses that are applied to transducer 90 for causing emissions of ultrasound waves, thereby increasing the life of transducer 90. In another aspect, providing a driver signal with oscillating positive and negative polarity results in any standing voltages of transducer 90 cancelling and thereby reducing a magnitude of standing voltages. Still, further use of a bipolar output drive signal allows use of both positive and negative channels of a transistor pair (*e.g.*, transistor 204, transistor 206 as shown in Figure 4.2.2) reducing thermal fatigue of the transistor pair and increasing the current output capacity of the transistor pair, thereby allowing higher power output with reduced voltage below hazardous levels. (It will be seen that a ± 50*V* signal applied to a load produces the same output power as a ± 0 - 100*V* drive signal, but with substantially safer voltage levels).

In another aspect, power supply 10 can be operative to output an imbalanced bipolar signal for driving transducer 90. An "imbalanced" bipolar signal herein can have, in one embodiment, an amplitude difference between first and second polarities of 1*V* or greater (*e.g.*, a +10*V* to -9*V* imbalanced bipolar signal); in another embodiment, 5*V* or greater (*e.g.*, a +5*V* to -10*V* imbalanced bipolar signal); in another

embodiment, 20*V* or greater (*e.g.*, a +100*V* to -80*V* imbalanced bipolar signal); and in another embodiment, 40*V* or greater (*e.g.*, a +30*V* to -70*V* imbalanced bipolar signal). In the development of apparatus 1000, it was determined that the capacity of transducer 90 to withstand forces imparted thereto is increased with reference to compression forces relative to expansion forces. Transducer 90 will be compressed when a negative voltage drive signal is applied thereto and expanded when a positive voltage drive signal is applied thereto (or alternatively, depending on the setup, compressed when a positive voltage drive is applied and expanded when a negative voltage drive signal is applied). Nevertheless, driving transducer 90 with both positive and negative voltage drive signals advantageously produces variations of the range of motion of transducer 90. By provisioning power supply 10 to output an imbalanced bipolar drive signal, both compression and expansion forces can be imparted to transducer 90, and yet compression forces can be imparted to transducer 90 in greater magnitude than expansion forces.

Referring again to Figure 4.2.4, the provisioning of apparatus 1000 so that both positive clamping terminal voltage and a negative clamping terminal voltage can be independently adjusted via operator input controls input using a user interface of apparatus 1000, allows the output drive signal output by drive circuit 20 to be precisely tuned to the limits imposed by the physical properties of transducer 90 without exceeding such levels.

Referring to Table 4.2.2, various prospective examples of transducer assemblies are summarized in connection with exemplary drive signals associated with each transducer assembly.

Table 4.2.2 Examples of transducers with various drive signals

Transducer Assembly	Transducer	Resonant Frequency (Expressed As Point Value)	Resonant Frequency (Expressed As Range At Which Power Conversion Efficiency Is 90% Of Maximum)	Nominal Frequency of Resonance (Normally Provided By Manufacturer)	Impedance of Transducer (As Measured Utilizing Impedance Measuring Equipment)	Exemplary Drive Signal
A	90A	1.54 MHz	1.47-1.58 MHz	1.5 MHz	8 Ohms	Continuous Imbalanced Bipolar Square Wave at about 1.54 MHz
B	90B	1.01 MHz	0.95-1.09 MHz	1 MHz	14 Ohms	Continuous Balanced Square Wave at 1.01 MHz
C	90C	2.60 MHz	2.45-2.68 MHz	2.5 MHz	5 Ohms	Continuous Unipolar Sinusoidal Wave at 2.60 MHz
D	90D	3.11 MHz	3.01-3.22 MHz	3 MHz	7 Ohms	Continuous Imbalanced Bipolar Sinusoidal at 3.11 MHz
E	90E	7.55 MHz	2.51-11.56 MHz	7.5 MHz	15 Ohms	Burst Balanced Bipolar Square Wave at 7.55 MHz
F	90F	1.52/4.15/6.51	1.45-1.59/3.85-4.35/6.37-6.62 MHz	1.5/4/6.5	3 Ohms	Continuous frequency sweeping signal at 1.52 MHz (bipolar imbalanced), 4.15 MHz (bipolar imbalanced), 6.51 MHz (bipolar imbalanced)

Characteristics of a suitable output drive signal associated with the transducer assemblies A, B, C, D, E, and F are summarized in Figures. 4.2.13, 4.2.14, 4.2.15, 4.2. 4.2.16, 4.2.17, and 4.2.18. In the illustrative Table B and in associated Figures. 4.2.13-4.2.18, the output drive signal is shown as being identical (to two decimal points) to the resonant frequency of transducer 90 It will be understood that due to tolerances, an actual drive signal can correspond to a resonant frequency without being identical to the resonant frequency.

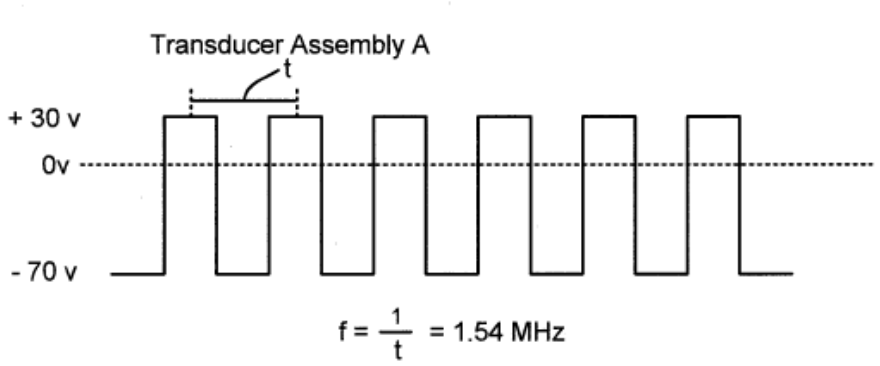

Figure 4.2.13 are signal plot illustrating specific output drive signals, being associated with a particular candidate transducer assembly A

Referring to Figure 4.2.13, imbalanced bipolar output drive signal is shown having a possible voltage peak of +30*V* and a negative voltage peak of -70*V*. The output drive signal of Figure 4.2.13 is operative to result in compression force being imparted to transducer 90 in greater magnitude than expansion forces. Apparatus 1000 can be provisioned so that the characteristics of the drive signal of Figure 4.2.13 can be set either responsively to operator control using a user interface of apparatus 1000 or responsively to a particular transducer assembly being associated to power supply 10. In the case where apparatus 1000 is operative to output a drive signal of particular characteristics responsively to association of a particular transducer assembly, *e.g.*, A, B, C, D, E, F, apparatus 1000 can further be operative so that characteristics of the drive signal can be further subject to change via control inputs that are input by an operator using a user interface of apparatus 1000 after the association is completed.

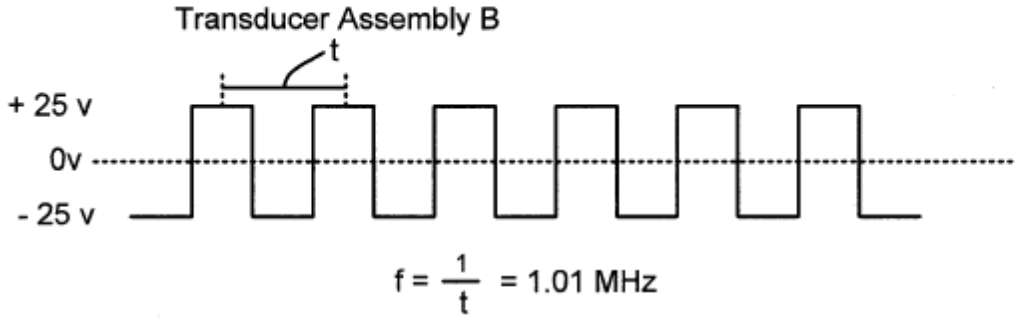

Figure 4.2.14 are signal plot illustrating specific output drive signals, being associated with a particular candidate transducer assembly B

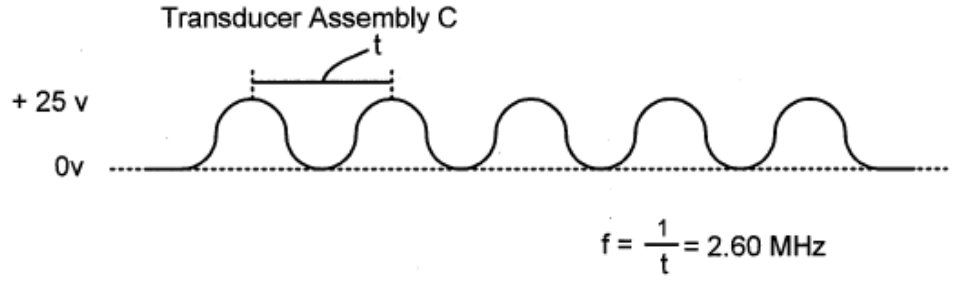

Figure 4.2.15 are signal plot illustrating specific output drive signals, being associated with a particular candidate transducer assembly C

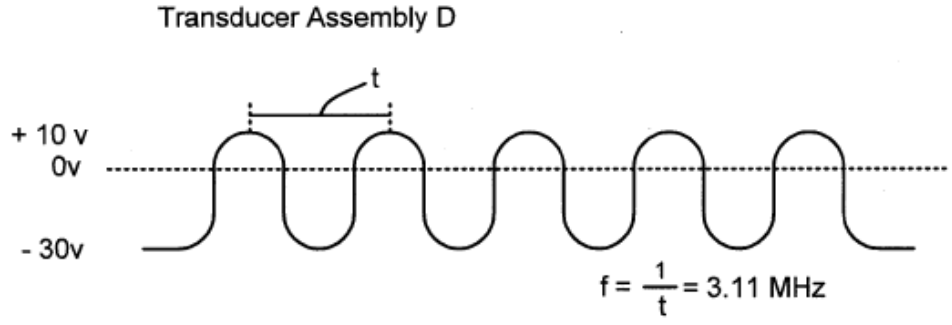

Figure 4.2.16 are signal plot illustrating specific output drive signals, being associated with a particular candidate transducer assembly D

Figures 4.2.13, 4.2.14, 4.2.15, 4.2.16, 4.2.17, and 4.2.18 illustrate drive signals that can be set responsively to control inputs that are input by an operator using a user interface of apparatus 1000 and/or responsively to a particular transducer assembly being associated to power supply 10. Characteristics of the drive signal of Figure 4.2.13 have been characterized herein above. Referring to the output drive signal of Figure 4.2.14, the output drive signal of Figure 4.2.14 is a balanced bipolar output drive signal suitable for driving transducer assembly B transducer assembly having transducer 90, 90b. Referring to Figure 4.2.15, the output drive signal of Figure 4.2.15 is a unipolar sinusidal output drive signal suitable for driving transducer assembly C having transducer 90, 90c. Referring to Figure 4.2.16, the output drive signal of Figure 4.216 is an imbalanced bipolar sinusoidal drive signal suitable for driving transducer assembly D having transducer 90, 90d. Referring to the output drive signals of Figures 4.2.13-4.2.16, the output drive signals of Figures. 4.2.13-4.2.16 can be regarded as "continuous" drive signals by virtue of their lack of repeated null periods between periods of oscillation. The drive signal of Figure 4.2.17 can be regarded as a burst signal by virtue of it having null periods, pn, intermediate of periods of oscillation. In some applications, *e.g.*, imaging, apparatus 1000 can be operative to output null periods, pn, intermediate of periods of oscillation for purposes of conserving power, where null periods, pn, will not negatively impact function of apparatus 1000. In some imaging apparatuses, for example, it is only necessary that periods of oscillation be timed with exposure periods.

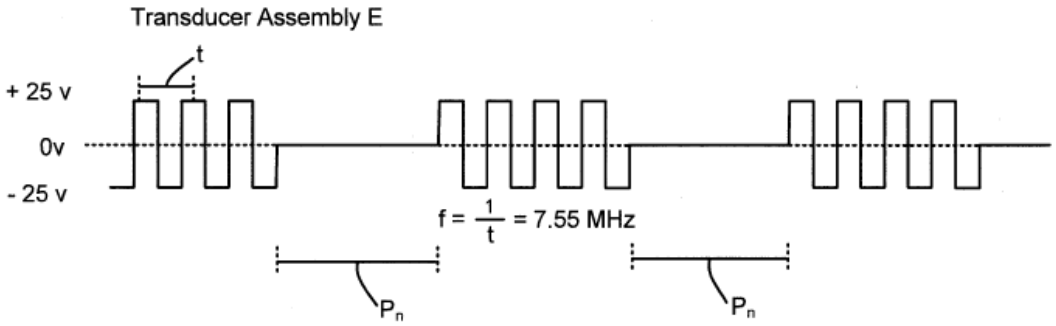

Figure 4.2.17 are signal plot illustrating specific output drive signals, being associated with a particular candidate transducer assembly D

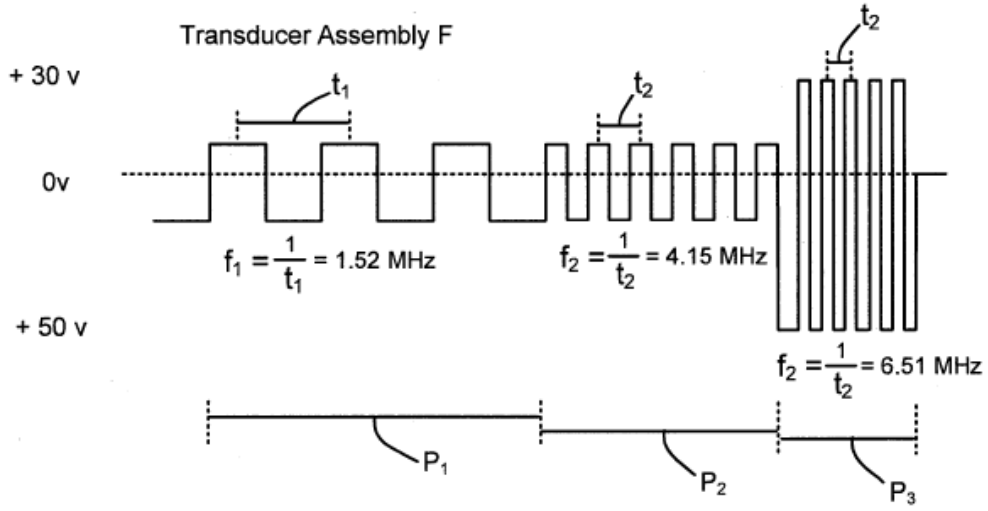

Figure 4.2.18 are signal plot illustrating specific output drive signals, being associated with a particular candidate transducer assembly D

It is seen that apparatus 1000 can be conFigured so that a switching between transducer assemblies of apparatus 1000 causes switching between modes of operation of apparatus 1000. For example, with transducer assembly A associated, apparatus 1000 can operate in a mode in which apparatus 1000 outputs an imbalanced bipolar drive signal. Apparatus 1000 can further be conFigured so that a mode of operation of apparatus 1000 changes responsively to a presently associated transducer assembly being switched, *e.g.*, to a mode of operation in which bipolar balanced drive signal (when transducer assembly B is associated), or to a mode of operation in which a unipolar drive signal is output (when transducer assembly C is associated).

In one embodiment, as shown in Figure 4.2.19, transducer 90 can be provided by a single transducer element, *e.g.*, a single transducer disk 91 having a certain impedance and nominal frequency of resonance. In one embodiment, as shown in Figure 4.2.20, transducer 90 can include plural transducer elements, *e.g.*, a plurality of transducer disks arranged in series. In a particular embodiment, each of transducer elements (*e.g.*, ceramic disks) can have a particular associated nominal frequency of resonance and a particular resonant frequency when driven by a driver circuit 20 of a certain configuration. In the example of Figure 4.2.20, transducer 90 includes three (3) transducer elements 91. However, transducer 90 could also include, *e.g.*, two (2) transducer elements, or N transducer element.

Figure 4.2.19 is a diagram showing a single transducer element ultrasound transducer;

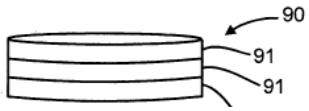

Figure 4.2.20 is a diagram showing a plural transducer element ultrasound transducer

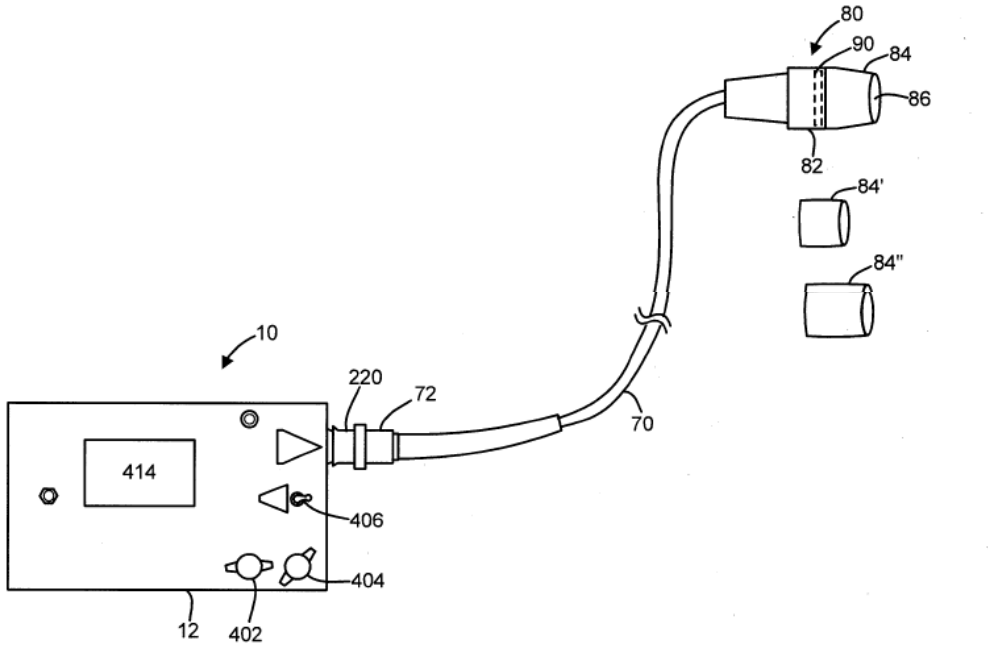

Figure 4.2.21 is a physical form view of an ultrasound wave generating apparatus in one embodiment

Referring to Table 4.2.2, transducer assembly F illustrates the use case where a transducer assembly includes a transducer comprising a plurality of transducer disks, each having a different nominal frequency resonance and resonant frequency. Each of the elements can comprise a transducer disk of the PZT series of transducer elements available from EBL Products. Such a transducer can be advantageously driven with a

drive signal as shown in Figure 4.2.18. The drive signal of Figure 4.2.18 is a frequency sweeping drive signal having a changing frequency. During period p1, the drive signal has a frequency of 1.52 MHz corresponding to the resonant frequency of the first transducer element. During period p2, the drive signal has a frequency of 4.15 MHz corresponding to the resonant frequency of the second transducer element. During period p3, the drive signal has a frequency of 6.51 MHz corresponding to the resonant frequency of the third transducer element of transducer 90F.

A physical form view of ultrasound generator 1000 is shown in Figure 4.2.21. Power supply 10 can be small and lightweight, *e.g.*, about 5 pounds. Housing 12 for power supply 10 can have dimensions of about $4 \times 6 \times 2in.3$. Housing 82 for probe 80 can be provided by a polyvinyl chloride (PVC) ergonomic plastic assembly. Referring to housing 82, ultrasound transducer 90 (shown dashed in) can be housed at a distal end of housing 82 as shown in Figure 4.2.21 and standoff component 84 can be disposed to extend from the distal end of housing 82. Standoff component 84 can define a cavity 86. Cavity 86 can be adapted to receive a coupling medium. A coupling medium such as ultrasound fluid or water can be disposed within cavity 86. A suitable ultrasound fluid coupling medium is No. NTNMAA001X ultrasound fluid available from The National Medical Association (NMA). In some applications, probe 80 of apparatus 1000 can be adapted so that standoff component 84 can be replaceably removed from housing 82. Further, standoff component 84 can be provided as one of a family of candidate standoff components which can include, *e.g.*, component 84' and 84". Standoff component 84 can include a light transmissive wall 85. As is best seen in the view of Figure 4.2.23, light transmissive wall 85 can be light transmissive to allow visual viewing into an interior of cavity 86. As shown in the front view of Figure 4.2.22, with transducer periphery 91 dashed in, a periphery of standoff component 84 can be substantially aligned with a periphery of standoff component 84 at the interface

between the transducer 90 and standoff component 84. Light transmissive wall 85, as best seen in Figure 4.2.23 permits an operator to view an interior of cavity 86 to determine, *e.g.*, the quality of a coupling medium disposal within cavity (*e.g.*, whether the coupling medium is substantially free of bubbles). Light transmissive wall 85 can be formed partially about the periphery of standoff component 84. In the embodiments of Figure 4.2.23, light transmissive wall 85 is formed entirely about the periphery of standoff component 84. Transmission line 70 can have a length of about 1m. In another embodiment, transmission line 70 can be deleted and power supply 10 and transducer 90 can be housed in a common housing.

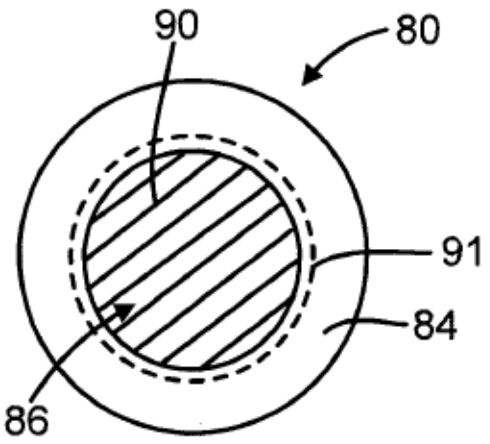

Figure 4.2.*22 is a front view of probe for an ultrasound wave generating apparatus;*

Figure 4.2.*23 is a photograph of probe for an ultrasound wave generating apparatus*

Additional housing and packaging features of apparatus 1000 in one embodiment are set forth with reference to Figures 4.2.24 and 4.2.25. Figures 4.2.24 and 4.2.25 show top and bottom views of a printed circuit board 15 carrying MOSFET integrated circuits 202 of driver circuit 20. In the views of Figures 4.2.24 and 4.2.25, the dashed in border 12 indicates a location of housing 12 when printed circuit board 15 is disposed in housing 12. In the embodiment of Figure 4.2.24, MOSFET integrated circuits 202 can be distributed at an outer periphery of circuit board 15 so that integrated circuits 202 are more proximate a periphery of printed circuit board 15 than a longitudinally extending imaginary center axis 17 of printed circuit board 15. In the embodiment of Figures 4.2.24 and 4.2.25, each MOSFET integrated circuit 202 of driver circuit 20 is so located. Distributed as described proximate housing boundary 12

heat generated by integrated circuits 202 is more likely to be conducted to an exterior of housing 12, thus removing heat from integrated circuits 202 and increasing the power output capacity of MOSFET integrated circuits 202 and of driver circuit 20.

Figure 4.2.*24 is a top view of a printed circuit board carrying components of a ultrasound power supply in one embodiment*

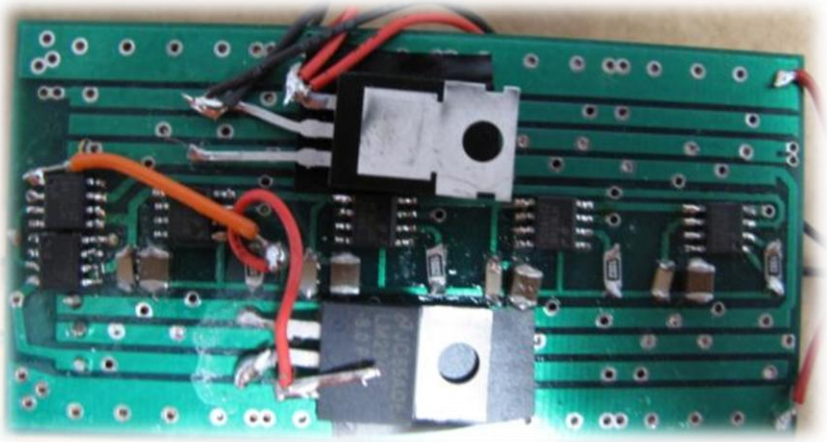

Figure 4.2.*25 is a bottom view of the printed circuit board as shown in Figure 5.24*

Referring to the circuit diagrams of Figures 4.2.24 and 4.2.25, an output of driver circuit 20 can include an output from each of a plurality of MOSFET integrated circuits co-located at a common node 250. As seen in the physical form view of Figures 4.2.24 and 4.2.25, common node 250 can be physically constituted by a planar conFigured output voltage plane. Common node 250 conFigured as an output voltage plane can be distributed over a two dimensional area of printed circuit board 15 to partially define one or more surfaces of printed circuit board 15. In the embodiment of Figures 4.2.24 and 4.2. 25, the output voltage plane is distributed to partially define each of a top surface and a bottom surface of printed circuit board 15. As shown, the common node 250 where provided by an output voltage plane can include a planar surface exposed to an exterior or printed circuit board 15. The common node 250 where provided by an output voltage plane as shown in Figures 4.2.24 and4.2. 25 can be formed from a printed circuit board copper surface laminate that is appropriately etched and provided to commonly connect the respective outputs of the various transistor pairs of driver circuit 20. With a common node 250 being constituted with a planar conductor defining a surface of printed circuit board 15 significant heat is removed from the circuit components of apparatus 1000 including from MOSFET integrated circuits 202 of driver circuit 20 thus increasing a power output capacity of MOSFET integrated circuits 20. Common node 250 where provided by an output voltage plane can be distributed such that the output voltage plane is in thermal contact or near thermal contact with an electrically insulative portion of a plurality of (and in one embodiment each) MOSFET integrated circuits 202. With such configuration, there is encouraged a distribution of thermal energy to the end that each of a plurality of MOSFET integrated circuits 202 and in one embodiment each MOSFET integrated circuit has approximately a common operating temperature. Configuring driver circuit 20 so that each MOSFET integrated circuit 200 has

approximately a common operating temperature reduces noise output by driver circuit 20. Specifically, configuring driver circuit 20 so that each
MOSFET integrated circuit 200 has approximately a common operating temperature can be expected to reduce differences in oscillating and switch timing operations that would create ripple and noise in an output of driver circuit 20.

The system in one embodiment is housed in a housing 12 provided by a 4´ 6´ 2*in*.3watertight plastic enclosure, No. 073 of the type provided by Serpac, Inc. The housing holds the circuit (1.5´ 2´1*in*.3) and six 9.6*V* , 1600 mA h NiCad rechargeable battery packs (No. 23−432 available from RadioShack Corporation) tied together in series through two single draw rotary switches.

Referring again to Figure 4.2.1, the various impedances of driver circuit 20, transmission line 70, and transducer 90 can be coordinated in a specific manner. In one embodiment, driver circuit 20 has an output impedance of about 0.5 Ohms. Provisioning driver circuit 20 to have an output impedance that is not matched with the impedance of transducer 90 improves energy transfer efficiency of apparatus 1000. By provisioning driver circuit 20 to have a low output impedance very little energy is dissipated as heat in driver circuit 20. Accordingly, driver circuit 20 will be maintained in a state that is safe to the touch throughout operation of driver circuit 20.

An impedance of transmission line 70 can also be coordinated with the output impedance of driver circuit 20 and an impedance of transducer 90. In one example, transmission line 70 can be provisioned to have an impedance of value that is about the output impedance of driver circuit 20 so that the impedance of transmission line 70 matches the output impedance of driver circuit 10, but, like driver circuit 20, is mismatched with respect to transducer 90.

In developing apparatus 1000 it was determined that advantages are exhibited by configuring the impedance of transmission line 70 to be low, *e.g.*, about 5 Ohms or

lower and in other embodiments, 1 Ohm or lower. In one example, transmission line 70 where provided by a coaxial cable is provided by a 5 Ohm coaxial cable, part number 1/22-15044 available from Cooner Wire, Inc. of Chatsworth, CA. The impedance of transmission line 70 can be reduced by providing a plurality of coaxial cables in parallel. Where a plurality of coaxial cables are provided in parallel in the formation of transmission line 70, an impedance of transmission line 70 can be expressed as

$$R_{EFF} = \frac{R_C}{N} \qquad (4.2.3)$$

where R_C is the impedance of each individual cable and N is the number of cables. Thus, a transmission line impedance where transmission line 70 includes six (6) of the referenced coaxial cables would be less than 1 Ohm. A plurality of cables can be arranged in a specific configuration. In the embodiment of Figure 4.2.25, transmission line 70 is provided by a plurality of braided coaxial cables arranged in parallel. In the embodiment of Figure 4.2.26, transmission line 70 is provided by a plurality of twisted coaxial cables arranged in parallel. The specific configurations as shown in Figure 4.2.25 and Figure 4.2.26 operate to reduce noise.

Figure 4.2.26 is a photograph of a transmission line for an ultrasound wave generating apparatus having a braided coaxial cable transmission line

Figure 4.2.27 is a diagram of a transmission line for an ultrasound wave generating apparatus having a twisted coaxial cable transmission line

A small sample of systems methods and apparatus that are described herein is as follows:

A1. An ultrasound wave generating apparatus comprising:

a power supply having a power source, a timing circuit, and a transistor based driver circuit for output of a drive signal, wherein the driver circuit includes a transistor pair including first and second transistors, and first and second clamping voltage terminals, the first and second transistors having respective first and second gates, wherein the timing circuit is operative to output a timing signal for controlling timing of the drive signal output by the driver circuit;

an ultrasound transducer conFigured to emit ultrasound energy, the ultrasound transducer being coupled to the driver circuit so that the drive signal output by the driver circuit drives the ultrasound transducer, wherein a frequency at which the ultrasound transducer emits maximum power when driven by the output drive signal defines a resonant frequency of the ultrasound transducer;

wherein the driver circuit is operative to output a drive signal having a frequency corresponding to the resonant frequency; and

wherein the apparatus is conFigured so that the transducer has an associated load voltage when the driver circuit outputs the drive signal to drive the transducer at a frequency corresponding to the resonant frequency, wherein the apparatus is further

conFigured so that the driver circuit has an associated source voltage when the driver circuit outputs the drive signal at a frequency corresponding to the resonant frequency, and wherein the apparatus is conFigured so that the amplitude of the load voltage is at least 90 percent of the amplitude of the source voltage when the driver circuit outputs a drive signal at a frequency corresponding to the resonant frequency.

A2. The ultrasound wave generating apparatus of claim A1, wherein the ultrasound transducer is operative so that compression force is imparted to the ultrasound transducer when the drive signal is of a first voltage polarity, and further so that an expansion force is imparted to the ultrasound transducer when the drive signal is of a second voltage polarity, and further so that the drive signal is a continuous bipolar drive signal so that both of compression forces and expansion forces are imparted to the ultrasound transducer.

A3. The ultrasound wave generating apparatus of claim A1, wherein the ultrasound transducer is operative so that compression force is imparted to the ultrasound transducer when the drive signal is of a first voltage polarity, and further so that an expansion force is imparted to the ultrasound transducer when the drive signal is of a second voltage polarity, and further so that the drive signal is an imbalanced continuous bipolar drive signal so that both of compression forces and expansion forces are imparted to the ultrasound transducer, and further so that the compression forces are of greater magnitude than the expansion forces.

A4. The ultrasound wave generating apparatus of claim A1, wherein the driver circuit is operative so that the drive signal has an output current capacity of greater than 50 amperes.

A5. The ultrasound wave generating apparatus of claim A1, wherein the power supply includes a capacitive coupling circuit coupling the timing signal to the first and second gates of the transistor pair, wherein the timing signal is a unipolar timing signal, and wherein the capacitive coupling circuit converts the unipolar timing signal into a bipolar input signal for input into the driver circuit.

A6. The ultrasound wave generating apparatus of claim A1, wherein the transistor based driver circuit includes a plurality of transistor pairs connected in parallel, each of the transistor pairs having first and second transistors, wherein each of the transistor pairs is coupled to the first and second clamping voltage terminals.

A7. The ultrasound wave generating apparatus of claim A1, wherein the ultrasound wave generating apparatus includes a user interface and is operative so that at least one characteristic of the drive signal can be changed in response to an operator control input that is input utilizing the user interface.

A8. The ultrasound wave generating apparatus of claim A1, wherein the ultrasound wave generating apparatus is adapted so that the ultrasound transducer is incorporated in a replaceable ultrasound transducer assembly that is one of a plurality of candidate ultrasound transducer assemblies that can be associated to the ultrasound wave generating apparatus, and wherein the ultrasound wave generating apparatus is operative so that the drive signal has at least one characteristic that is responsive to which of the plurality of candidate ultrasound transducer assemblies is presently associated to the ultrasound wave generating apparatus.

A9. The ultrasound wave generating apparatus of claim A1, wherein the ultrasound wave generating apparatus includes a user interface and is adapted so that the ultrasound transducer is incorporated in a replaceable ultrasound transducer assembly that is one of a plurality of candidate ultrasound transducer assemblies that can be associated to the ultrasound wave generating apparatus, wherein the ultrasound wave generating apparatus is operative so that the drive signal output by the driver circuit is responsive to each of (a) a switching of a candidate transducer assembly, and (b) a control input that is input by an operator utilizing the user interface.

A10. The ultrasound wave generating apparatus of claim A9, wherein each of the plurality of candidate transducer assemblies includes a timing device disposed therein for controlling a timing of the driver circuit.

A11. The ultrasound wave generating apparatus of claim A1, wherein the ultrasound wave generating apparatus is operative in a first mode of operation and in a second mode of operation, wherein the ultrasound wave generating apparatus in the first mode of operation outputs an imbalanced bipolar output drive signal, wherein the apparatus in the second mode of operation outputs an output drive signal that is selected from the group consisting of a unipolar output drive signal and a balanced output drive signal.

A12. The ultrasound wave generating apparatus of claim A11, wherein the ultrasound wave generating apparatus includes a replaceable transducer assembly incorporating the transducer, the transducer assembly being one of a plurality of candidate transducer assemblies, wherein the ultrasound wave generating apparatus is operative so that the ultrasound wave generating apparatus switches operation from the first mode of operation to the second mode of operation responsively to the transducer

assembly being replaced with another of the plurality of candidate transducer assemblies.

A13. The ultrasound wave generating apparatus of claim A1, wherein the apparatus further includes a housing for housing the ultrasound transducer, the housing having a distal end at which the ultrasound transducer is disposed, wherein there is further disposed at the distal end a standoff component defining a cavity for carrying ultrasound coupling medium, the standoff component having a light transmissive wall adapted to permit visual viewing of an interior of the cavity through the light transmissive wall.

A14. The ultrasound wave generating apparatus of claim A1, wherein the apparatus includes a transmission line coupling the driver circuit and the transducer, the transmission line including a plurality of coaxial cables arranged in parallel, and further being arranged in a braid configuration.

A15. The ultrasound wave generating apparatus of claim A1, wherein the apparatus includes a transmission line coupling the driver circuit and the transducer, the transmission line including a plurality of coaxial cables arranged in parallel, and further being arranged in a twisted configuration.

A16. The ultrasound wave generating apparatus of claim A1, wherein the transducer comprises a single transducer element having a first associated nominal frequency of resonance.

A17. The ultrasound wave generating apparatus of claim A1, wherein the transducer comprises a plurality of transducer elements.

A18. The ultrasound wave generating apparatus of claim A1, wherein the transducer comprises first and second transducer elements, the first transducer element having a first resonant frequency, the second transducer element having a second resonant frequency.

A19. The ultrasound wave generating apparatus of claim A1, wherein the ultrasound transducer comprises first and second transducer elements, the first transducer element having a first resonant frequency, the second transducer element having a second resonant frequency, and wherein the apparatus is conFigured so that the driver circuit is operative to output a frequency sweeping drive signal, the frequency sweeping drive signal having a frequency corresponding to the first resonant frequency during a first period, the frequency sweeping drive signal having a frequency corresponding to the second resonant frequency during a second period.

A20. The ultrasound wave generating apparatus of claim A1, wherein the power supply has a plurality of power supply stages, each power supply stage having an associated driver circuit and power source, wherein the plurality of the power supply stages include first and second power supply stages, the second power supply stage being successive in relation to the first power supply stage, and wherein an output of the first of the power supply stages is input into a stage ground of the second power supply stage.

A21. The ultrasound wave generating apparatus of claim A1, wherein the power supply includes a user interface conFigured to permit an operator to independently adjust the first terminal clamping voltage and the second terminal clamping voltage via input of control inputs utilizing the user interface.

A22. The ultrasound wave generating apparatus of claim A1, wherein the power source includes a battery power source.

A23. The ultrasound wave generating apparatus of claim A1, wherein the power source includes an AC/DC converter.

A24. The ultrasound wave generating apparatus of claim A1, wherein the driver circuit includes a MOSFET integrated circuit, and wherein the apparatus includes a housing and printed circuit board for carrying the MOSFET integrated circuit, the printed circuit having a peripheral edge that is proximate the housing when the printed circuit board is disposed in the housing, wherein the MOSFET integrated circuit is disposed on the printed circuit at a location that is more proximate the peripheral edge of the circuit board that a longitudinal centerline of the printed circuit board.

A25. The ultrasound wave generating apparatus of claim A1, wherein the driver circuit includes a plurality of transistor pairs and a plurality of pin drivers for providing switching of the plurality of transistor pairs, wherein the driver circuit is conFigured so that each of the plurality of pin drivers for providing switching drives a common number of transistor pairs.

A26. The ultrasound wave generating apparatus of claim A1, wherein the apparatus includes a printed circuit board carrying the first and second transistors of the driver

circuit and wherein an output of the driver circuit includes common node that combines outputs of the first and second transistors, wherein the common output node is constituted by an output voltage plane having a planar surface area partially defining a surface of the printed circuit board.

B1. An ultrasound wave generating apparatus comprising:

a power supply having a power source, a timing circuit, and a transistor based driver circuit for output of a drive signal, wherein the driver circuit includes a transistor pair including first and second transistors, and first and second clamping voltage terminals, the first and second transistors having respective first and second gates, wherein the timing circuit is operative to output a timing signal for controlling timing of the drive signal output by the driver circuit;

a hand held housing for housing the power supply;

an ultrasound transducer conFigured to emit ultrasound energy, the ultrasound transducer being coupled to the driver circuit so that the drive signal output by the driver circuit drives the ultrasound transducer, wherein a frequency at which the ultrasound transducer emits maximum power when driven by the output drive signal defines a resonant frequency of the ultrasound transducer;

wherein the driver circuit is operative to output a drive signal having a frequency corresponding to the resonant frequency; and

wherein the apparatus is conFigured so that the transducer has an associated load voltage when the driver circuit outputs the drive signal to drive the transducer at a frequency corresponding to the resonant frequency, wherein the apparatus is further conFigured so that driver circuit has an associated source voltage when the driver circuit outputs the drive signal at a frequency corresponding to the resonant frequency, and wherein the apparatus is conFigured so that the amplitude of the load voltage is at

least 90 percent of the amplitude of the source voltage when the driver circuit outputs a drive signal at a frequency corresponding to the resonant frequency;

wherein the ultrasound transducer is operative so that compression force is imparted to the ultrasound transducer when the drive signal is of a first voltage polarity, and further so that an expansion force is imparted to the ultrasound transducer when the drive signal is of a second voltage polarity, and further so that the drive signal is an imbalanced continuous bipolar drive signal so that both of compression forces and expansion forces are imparted to the ultrasound transducer, and further so that the compression forces are of greater magnitude than the expansion forces;

wherein the driver circuit is operative so that the drive signal has an output current capacity of greater than 50 amperes.

wherein the power supply includes a capacitive coupling circuit coupling the timing signal to the first and second gates of the transistor pair, wherein the timing signal is a unipolar timing signal, and wherein the capacitive coupling circuit converts the unipolar timing signal into a bipolar input signal for input into the driver circuit;

wherein the transistor based driver circuit includes a plurality of transistor pairs connected in parallel, each of the transistor pairs having first and second transistors, wherein each of the transistor pairs is coupled to the first and second clamping voltage terminals;

wherein the ultrasound wave generating apparatus includes a user interface and is adapted so that the ultrasound transducer is incorporated in a replaceable ultrasound transducer assembly that is one of a plurality of candidate ultrasound transducer assemblies that can be associated to the ultrasound wave generating apparatus, wherein the ultrasound wave generating apparatus is operative so that the drive signal output by the driver circuit is responsive to each of (a) a switching of a candidate

transducer assembly, and (b) a control input that is input by an operator utilizing the user interface;

wherein the apparatus further includes a housing for housing the ultrasound transducer, the housing having a distal end at which the ultrasound transducer is disposed, wherein there is further disposed at the distal end a standoff component defining a cavity for carrying ultrasound coupling medium, the standoff component having a light transmissive wall adapted to permit visual viewing of an interior of the cavity through the light transmissive wall;

wherein the apparatus includes a transmission line coupling the driver circuit and the transducer, the transmission line including a plurality of coaxial cables arranged in parallel, and further being arranged in one of a braid or twisted configuration;

wherein the power supply has a plurality of power supply stages, each power supply stage having an associated driver circuit and power source, wherein the plurality of the power supply stages include first and second power supply stages, the second power supply stage being successive in relation to the first power supply stage, and wherein an output of the first of the power supply stages is input into a stage ground of the second power supply stage.

wherein the user interface is conFigured to permit an operator to independently adjust the first terminal clamping voltage and the second terminal clamping voltage via input of control inputs utilizing the user interface;

wherein the power source includes a battery power source;

wherein the driver circuit includes a MOSFET integrated circuit, and wherein the apparatus includes a housing and printed circuit board for carrying the MOSFET integrated circuit, the printed circuit having a peripheral edge that is proximate the housing when the printed circuit board is disposed in the housing, wherein the

MOSFET integrated circuit is disposed on the printed circuit at a location that is more proximate the peripheral edge of the circuit board that a longitudinal centerline of the printed circuit board;

wherein the driver circuit includes a plurality of transistor pairs and a plurality of pin drivers for providing switching of the plurality of transistor pairs, wherein the driver circuit is conFigured so that each of the plurality of pin drivers for providing switching drives a common number of transistor pairs; and

wherein the apparatus includes a printed circuit board carrying the first and second transistors of the driver circuit and wherein an output of the driver circuit includes common node that combines outputs of the first and second transistors, wherein the common output node is constituted by an output voltage plane having a planar surface area partially defining a surface of the printed circuit board.

C1. An ultrasound wave generating apparatus comprising:

a power supply having a timing circuit for outputting a timing signal, and a transistor based driver circuit for output of a drive signal, wherein the driver circuit includes a transistor pair including first and second transistors, and first and second clamping voltage terminals, the first and second transistors having respective first and second gates, wherein the timing circuit is operative to output a timing signal for controlling timing of the drive signal output by the driver circuit;

an ultrasound transducer conFigured to emit ultrasound energy, the ultrasound transducer being coupled to the driver circuit so that the drive signal output by the driver circuit drives the ultrasound transducer, wherein the ultrasound transducer includes an impedance rating and a frequency rating and wherein the driver circuit is operative to output the drive signal at a frequency of about the frequency rating of the ultrasound transducer; and

wherein the driver circuit includes an output impedance and wherein the apparatus is conFigured so a value of the output impedance of the driver circuit is less than 10 percent of a value of the impedance rating of the ultrasound transducer.

C2. The ultrasound wave generating apparatus of claim C1, wherein the ultrasound wave generating apparatus is operative to output more than 50 Watts of ultrasound energy.

C3. The ultrasound wave generating apparatus of claim C1, wherein the power supply includes a capacitive coupling circuit coupling the timing signal to the first and second gates of the transistor pair, wherein the timing signal is a unipolar timing signal, and wherein the capacitive coupling circuit converts the unipolar timing signal into a bipolar input signal for input into the driver circuit.

C4. The ultrasound wave generating apparatus of claim C1, wherein the transistor based driver circuit includes a plurality of transistor pairs connected in parallel, each of the transistor pairs having first and second transistors, wherein each of the transistor pairs is coupled to the first and second clamping voltage terminals.

C5. The ultrasound wave generating apparatus of claim C1, wherein the apparatus includes a battery power source.

C6. The ultrasound wave generating apparatus of claim C1, wherein the power supply includes a user interface conFigured to permit an operator to independently adjust the first terminal clamping voltage and the second terminal clamping voltage via input of control inputs utilizing the user interface.

D1. An ultrasound wave generating apparatus comprising:

a power supply having a timing circuit for outputting a timing signal, and a transistor based driver circuit for output of a drive signal, wherein the driver circuit includes a transistor pair including first and second transistors, and first and second clamping voltage terminals, the first and second transistors having respective first and second gates, wherein the timing circuit is operative to output a timing signal for controlling timing of the drive signal output by the driver circuit;

an ultrasound transducer conFigured to emit ultrasound energy, the ultrasound transducer being coupled to the driver circuit so that the drive signal output by the driver circuit drives the ultrasound transducer, wherein the ultrasound transducer includes an impedance rating and a frequency rating and wherein the driver circuit is operative to output the drive signal at a frequency of about the frequency rating of the ultrasound transducer;

wherein the driver circuit includes an output impedance and wherein the apparatus is conFigured so a value of the output impedance of the driver circuit is less than 10 percent of a value of the impedance rating of the ultrasound transducer;

wherein the ultrasound wave generating apparatus is operative to output more than 50 Watts of ultrasound energy;

wherein the power supply includes a capacitive coupling circuit coupling the timing signal to the first and second gates of the transistor pair, wherein the timing signal is a unipolar timing signal, and wherein the capacitive coupling circuit converts the unipolar timing signal into a bipolar input signal for input into the driver circuit;

wherein the transistor based driver circuit includes a plurality of transistor pairs connected in parallel, each of the transistor pairs having first and second transistors,

wherein each of the transistor pairs is coupled to the first and second clamping voltage terminals;

wherein the apparatus includes a battery power source; and

wherein the power supply includes a user interface conFigured to permit an operator to independently adjust the first terminal clamping voltage and the second terminal clamping voltage via input of control inputs utilizing the user interface.

While the present invention has been described with reference to a number of specific embodiments, it will be understood that the true spirit and scope of the invention should be determined only with respect to claims that can be supported by the present specification. Further, while in numerous cases herein wherein systems and apparatuses and methods are described as having a certain number of elements it will be understood that such systems, apparatuses and methods can be practiced with fewer than the mentioned certain number of elements.

4.2.*7* *Claims*

1. An ultrasound wave generating apparatus comprising:

a power supply having a power source, a timing circuit, and a transistor based driver circuit for output of a drive signal, wherein the driver circuit includes a transistor pair including first and second transistors, and first and second clamping voltage terminals, the first and second transistors having respective first and second gates, wherein the timing circuit is operative to output a timing signal for controlling timing of the drive signal output by the driver circuit;

an ultrasound transducer conFigured to emit ultrasound energy, the ultrasound transducer being coupled to the driver circuit so that the drive signal output by the driver circuit drives the ultrasound transducer, wherein a frequency at which the

ultrasound transducer emits maximum power when driven by the output drive signal defines a resonant frequency of the ultrasound transducer;

wherein the driver circuit is operative to output a drive signal having a frequency corresponding to the resonant frequency; and

wherein the apparatus is conFigured so that the transducer has an associated load voltage when the driver circuit outputs the drive signal to drive the transducer at a frequency corresponding to the resonant frequency, wherein the apparatus is further conFigured so that the driver circuit has an associated source voltage when the driver circuit outputs the drive signal at a frequency corresponding to the resonant frequency, and wherein the apparatus is conFigured so that the amplitude of the load voltage is at least 90 percent of the amplitude of the source voltage when the driver circuit outputs a drive signal at a frequency corresponding to the resonant frequency.

2. The ultrasound wave generating apparatus of claim 1, wherein the ultrasound transducer is operative so that compression force is imparted to the ultrasound transducer when the drive signal is of a first voltage polarity, and further so that an expansion force is imparted to the ultrasound transducer when the drive signal is of a second voltage polarity, and further so that the drive signal is a continuous bipolar drive signal so that both of compression forces and expansion forces are imparted to the ultrasound transducer.

3. The ultrasound wave generating apparatus of claim 1, wherein the ultrasound transducer is operative so that compression force is imparted to the ultrasound transducer when the drive signal is of a first voltage polarity, and further so that an expansion force is imparted to the ultrasound transducer when the drive signal is of a second voltage polarity, and further so that the drive signal is an imbalanced

continuous bipolar drive signal so that both of compression forces and expansion forces are imparted to the ultrasound transducer, and further so that the compression forces are of greater magnitude than the expansion forces.

4. The ultrasound wave generating apparatus of claim 1, wherein the driver circuit is operative so that the drive signal has an output current capacity of greater than 50 amperes.

5. The ultrasound wave generating apparatus of claim 1, wherein the power supply includes a capacitive coupling circuit coupling the timing signal to the first and second gates of the transistor pair, wherein the timing signal is a unipolar timing signal, and wherein the capacitive coupling circuit converts the unipolar timing signal into a bipolar input signal for input into the driver circuit.

6. The ultrasound wave generating apparatus of claim 1, wherein the transistor based driver circuit includes a plurality of transistor pairs connected in parallel, each of the transistor pairs having first and second transistors, wherein each of the transistor pairs is coupled to the first and second clamping voltage terminals.

7. The ultrasound wave generating apparatus of claim 1, wherein the ultrasound wave generating apparatus includes a user interface and is operative so that at least one characteristic of the drive signal can be changed in response to an operator control input that is input utilizing the user interface.

8. The ultrasound wave generating apparatus of claim 1, wherein the ultrasound wave generating apparatus is adapted so that the ultrasound transducer is incorporated in a

replaceable ultrasound transducer assembly that is one of a plurality of candidate ultrasound transducer assemblies that can be associated to the ultrasound wave generating apparatus, and wherein the ultrasound wave generating apparatus is operative so that the drive signal has at least one characteristic that is responsive to which of the plurality of candidate ultrasound transducer assemblies is presently associated to the ultrasound wave generating apparatus.

9. The ultrasound wave generating apparatus of claim 1, wherein the ultrasound wave generating apparatus includes a user interface and is adapted so that the ultrasound transducer is incorporated in a replaceable ultrasound transducer assembly that is one of a plurality of candidate ultrasound transducer assemblies that can be associated to the ultrasound wave generating apparatus, wherein the ultrasound wave generating apparatus is operative so that the drive signal output by the driver circuit is responsive to each of (a) a switching of a candidate transducer assembly, and (b) a control input that is input by an operator utilizing the user interface.

10. The ultrasound wave generating apparatus of claim 9, wherein each of the plurality of candidate transducer assemblies includes a timing device disposed therein for controlling a timing of the driver circuit.

11. The ultrasound wave generating apparatus of claim 1, wherein the ultrasound wave generating apparatus is operative in a first mode of operation and in a second mode of operation, wherein the ultrasound wave generating apparatus in the first mode of operation outputs an imbalanced bipolar output drive signal, wherein the apparatus in the second mode of operation outputs an output drive signal that is selected from the group consisting of a unipolar output drive signal and a balanced output drive signal.

12. The ultrasound wave generating apparatus of claim 11, wherein the ultrasound wave generating apparatus includes a replaceable transducer assembly incorporating the transducer, the transducer assembly being one of a plurality of candidate transducer assemblies, wherein the ultrasound wave generating apparatus is operative so that the ultrasound wave generating apparatus switches operation from the first mode of operation to the second mode of operation responsively to the transducer assembly being replaced with another of the plurality of candidate transducer assemblies.

13. The ultrasound wave generating apparatus of claim 1, wherein the apparatus further includes a housing for housing the ultrasound transducer, the housing having a distal end at which the ultrasound transducer is disposed, wherein there is further disposed at the distal end a standoff component defining a cavity for carrying ultrasound coupling medium, the standoff component having a light transmissive wall adapted to permit visual viewing of an interior of the cavity through the light transmissive wall.

14. The ultrasound wave generating apparatus of claim 1, wherein the apparatus includes a transmission line coupling the driver circuit and the transducer, the transmission line including a plurality of coaxial cables arranged in parallel, and further being arranged in a braid configuration.

15. The ultrasound wave generating apparatus of claim 1, wherein the apparatus includes a transmission line coupling the driver circuit and the transducer, the

transmission line including a plurality of coaxial cables arranged in parallel, and further being arranged in a twisted configuration.

16. The ultrasound wave generating apparatus of claim 1, wherein the transducer comprises a single transducer element having a first associated nominal frequency of resonance.

17. The ultrasound wave generating apparatus of claim 1, wherein the transducer comprises a plurality of transducer elements.

18. The ultrasound wave generating apparatus of claim 1, wherein the transducer comprises first and second transducer elements, the first transducer element having a first resonant frequency, the second transducer element having a second resonant frequency.

19. The ultrasound wave generating apparatus of claim 1, wherein the ultrasound transducer comprises first and second transducer elements, the first transducer element having a first resonant frequency, the second transducer element having a second resonant frequency, and wherein the apparatus is conFigured so that the driver circuit is operative to output a frequency sweeping drive signal, the frequency sweeping drive signal having a frequency corresponding to the first resonant frequency during a first period, the frequency sweeping drive signal having a frequency corresponding to the second resonant frequency during a second period.

20. The ultrasound wave generating apparatus of claim 1, wherein the power supply has a plurality of power supply stages, each power supply stage having an associated

driver circuit and power source, wherein the plurality of the power supply stages include first and second power supply stages, the second power supply stage being successive in relation to the first power supply stage, and wherein an output of the first of the power supply stages is input into a stage ground of the second power supply stage.

21. The ultrasound wave generating apparatus of claim 1, wherein the power supply includes a user interface conFigured to permit an operator to independently adjust the first terminal clamping voltage and the second terminal clamping voltage via input of control inputs utilizing the user interface.

22. The ultrasound wave generating apparatus of claim 1, wherein the power source includes a battery power source.

23. The ultrasound wave generating apparatus of claim 1, wherein the power source includes an AC/DC converter.

24. The ultrasound wave generating apparatus of claim 1, wherein the driver circuit includes a MOSFET integrated circuit, and wherein the apparatus includes a housing and printed circuit board for carrying the MOSFET integrated circuit, the printed circuit having a peripheral edge that is proximate the housing when the printed circuit board is disposed in the housing, wherein the MOSFET integrated circuit is disposed on the printed circuit at a location that is more proximate the peripheral edge of the circuit board that a longitudinal centerline of the printed circuit board.

25. The ultrasound wave generating apparatus of claim 1, wherein the driver circuit includes a plurality of transistor pairs and a plurality of pin drivers for providing switching of the plurality of transistor pairs, wherein the driver circuit is conFigured so that each of the plurality of pin drivers for providing switching drives a common number of transistor pairs.

26. The ultrasound wave generating apparatus of claim 1, wherein the apparatus includes a printed circuit board carrying the first and second transistors of the driver circuit and wherein an output of the driver circuit includes common node that combines outputs of the first and second transistors, wherein the common output node is constituted by an output voltage plane having a planar surface area partially defining a surface of the printed circuit board.

27. An ultrasound wave generating apparatus comprising:

a power supply having a power source, a timing circuit, and a transistor based driver circuit for output of a drive signal, wherein the driver circuit includes a transistor pair including first and second transistors, and first and second clamping voltage terminals, the first and second transistors having respective first and second gates, wherein the timing circuit is operative to output a timing signal for controlling timing of the drive signal output by the driver circuit;

a hand held housing for housing the power supply;

an ultrasound transducer conFigured to emit ultrasound energy, the ultrasound transducer being coupled to the driver circuit so that the drive signal output by the driver circuit drives the ultrasound transducer, wherein a frequency at which the ultrasound transducer emits maximum power when driven by the output drive signal defines a resonant frequency of the ultrasound transducer;

wherein the driver circuit is operative to output a drive signal having a frequency corresponding to the resonant frequency; and

wherein the apparatus is conFigured so that the transducer has an associated load voltage when the driver circuit outputs the drive signal to drive the transducer at a frequency corresponding to the resonant frequency, wherein the apparatus is further conFigured so that driver circuit has an associated source voltage when the driver circuit outputs the drive signal at a frequency corresponding to the resonant frequency, and wherein the apparatus is conFigured so that the amplitude of the load voltage is at least 90 percent of the amplitude of the source voltage when the driver circuit outputs a drive signal at a frequency corresponding to the resonant frequency;

wherein the ultrasound transducer is operative so that compression force is imparted to the ultrasound transducer when the drive signal is of a first voltage polarity, and further so that an expansion force is imparted to the ultrasound transducer when the drive signal is of a second voltage polarity, and further so that the drive signal is an imbalanced continuous bipolar drive signal so that both of compression forces and expansion forces are imparted to the ultrasound transducer, and further so that the compression forces are of greater magnitude than the expansion forces;

wherein the driver circuit is operative so that the drive signal has an output current capacity of greater than 50 amperes.

wherein the power supply includes a capacitive coupling circuit coupling the timing signal to the first and second gates of the transistor pair, wherein the timing signal is a unipolar timing signal, and wherein the capacitive coupling circuit converts the unipolar timing signal into a bipolar input signal for input into the driver circuit;

wherein the transistor based driver circuit includes a plurality of transistor pairs connected in parallel, each of the transistor pairs having first and second transistors,

wherein each of the transistor pairs is coupled to the first and second clamping voltage terminals;

wherein the ultrasound wave generating apparatus includes a user interface and is adapted so that the ultrasound transducer is incorporated in a replaceable ultrasound transducer assembly that is one of a plurality of candidate ultrasound transducer assemblies that can be associated to the ultrasound wave generating apparatus, wherein the ultrasound wave generating apparatus is operative so that the drive signal output by the driver circuit is responsive to each of (a) a switching of a candidate transducer assembly, and (b) a control input that is input by an operator utilizing the user interface;

wherein the apparatus further includes a housing for housing the ultrasound transducer, the housing having a distal end at which the ultrasound transducer is disposed, wherein there is further disposed at the distal end a standoff component defining a cavity for carrying ultrasound coupling medium, the standoff component having a light transmissive wall adapted to permit visual viewing of an interior of the cavity through the light transmissive wall;

wherein the apparatus includes a transmission line coupling the driver circuit and the transducer, the transmission line including a plurality of coaxial cables arranged in parallel, and further being arranged in one of a braid or twisted configuration;

wherein the power supply has a plurality of power supply stages, each power supply stage having an associated driver circuit and power source, wherein the plurality of the power supply stages include first and second power supply stages, the second power supply stage being successive in relation to the first power supply stage, and wherein an output of the first of the power supply stages is input into a stage ground of the second power supply stage.

wherein the user interface is conFigured to permit an operator to independently adjust the first terminal clamping voltage and the second terminal clamping voltage via input of control inputs utilizing the user interface;

wherein the power source includes a battery power source;

wherein the driver circuit includes a MOSFET integrated circuit, and wherein the apparatus includes a housing and printed circuit board for carrying the MOSFET integrated circuit, the printed circuit having a peripheral edge that is proximate the housing when the printed circuit board is disposed in the housing, wherein the MOSFET integrated circuit is disposed on the printed circuit at a location that is more proximate the peripheral edge of the circuit board that a longitudinal centerline of the printed circuit board;

wherein the driver circuit includes a plurality of transistor pairs and a plurality of pin drivers for providing switching of the plurality of transistor pairs, wherein the driver circuit is conFigured so that each of the plurality of pin drivers for providing switching drives a common number of transistor pairs; and

wherein the apparatus includes a printed circuit board carrying the first and second transistors of the driver circuit and wherein an output of the driver circuit includes common node that combines outputs of the first and second transistors, wherein the common output node is constituted by an output voltage plane having a planar surface area partially defining a surface of the printed circuit board.

28. An ultrasound wave generating apparatus comprising:

a power supply having a timing circuit for outputting a timing signal, and a transistor based driver circuit for output of a drive signal, wherein the driver circuit includes a transistor pair including first and second transistors, and first and second clamping voltage terminals, the first and second transistors having respective first and

second gates, wherein the timing circuit is operative to output a timing signal for controlling timing of the drive signal output by the driver circuit;

an ultrasound transducer conFigured to emit ultrasound energy, the ultrasound transducer being coupled to the driver circuit so that the drive signal output by the driver circuit drives the ultrasound transducer, wherein the ultrasound transducer includes an impedance rating and a frequency rating and wherein the driver circuit is operative to output the drive signal at a frequency of about the frequency rating of the ultrasound transducer; and

wherein the driver circuit includes an output impedance and wherein the apparatus is conFigured so a value of the output impedance of the driver circuit is less than 10 percent of a value of the impedance rating of the ultrasound transducer.

29. The ultrasound wave generating apparatus of claim 28, wherein the ultrasound wave generating apparatus is operative to output more than 50 Watts of ultrasound energy.

30. The ultrasound wave generating apparatus of claim 28, wherein the power supply includes a capacitive coupling circuit coupling the timing signal to the first and second gates of the transistor pair, wherein the timing signal is a unipolar timing signal, and wherein the capacitive coupling circuit converts the unipolar timing signal into a bipolar input signal for input into the driver circuit.

31. The ultrasound wave generating apparatus of claim 28, wherein the transistor based driver circuit includes a plurality of transistor pairs connected in parallel, each of the transistor pairs having first and second transistors, wherein each of the transistor pairs is coupled to the first and second clamping voltage terminals.

32. The ultrasound wave generating apparatus of claim 28, wherein the apparatus includes a battery power source.

33. The ultrasound wave generating apparatus of claim 28, wherein the power supply includes a user interface conFigured to permit an operator to independently adjust the first terminal clamping voltage and the second terminal clamping voltage via input of control inputs utilizing the user interface.

34. An ultrasound wave generating apparatus comprising:

a power supply having a timing circuit for outputting a timing signal, and a transistor based driver circuit for output of a drive signal, wherein the driver circuit includes a transistor pair including first and second transistors, and first and second clamping voltage terminals, the first and second transistors having respective first and second gates, wherein the timing circuit is operative to output a timing signal for controlling timing of the drive signal output by the driver circuit;

an ultrasound transducer conFigured to emit ultrasound energy, the ultrasound transducer being coupled to the driver circuit so that the drive signal output by the driver circuit drives the ultrasound transducer, wherein the ultrasound transducer includes an impedance rating and a frequency rating and wherein the driver circuit is operative to output the drive signal at a frequency of about the frequency rating of the ultrasound transducer;

wherein the driver circuit includes an output impedance and wherein the apparatus is conFigured so a value of the output impedance of the driver circuit is less than 10 percent of a value of the impedance rating of the ultrasound transducer;

wherein the ultrasound wave generating apparatus is operative to output more than 50 Watts of ultrasound energy;

wherein the power supply includes a capacitive coupling circuit coupling the timing signal to the first and second gates of the transistor pair, wherein the timing signal is a unipolar timing signal, and wherein the capacitive coupling circuit converts the unipolar timing signal into a bipolar input signal for input into the driver circuit;

wherein the transistor based driver circuit includes a plurality of transistor pairs connected in parallel, each of the transistor pairs having first and second transistors, wherein each of the transistor pairs is coupled to the first and second clamping voltage terminals;

wherein the apparatus includes a battery power source; and

wherein the power supply includes a user interface configured to permit an operator to independently adjust the first terminal clamping voltage and the second terminal clamping voltage via input of control inputs utilizing the user interface.